Numerical investigations of subglacial hydrology as a direct and indirect driver of glacial erosion

by

Flavien Beaud

M.Sc., Eidgenössische Technische Hochschule Zürich, 2010
B.Sc., École Polytechnique Fédérale de Lausanne, 2008

Thesis Submitted in Partial Fulfillment of the
Requirements for the Degree of
Doctor of Philosophy

in the
Department of Earth Sciences
Faculty of Science

SIMON FRASER UNIVERSITY
Summer 2017

Approval

Name:	**Flavien Beaud**
Degree:	**Doctor of Philosophy (Earth Sciences)**
Title:	***Numerical investigations of subglacial hydrology as a direct and indirect driver of glacial erosion***
Examining Committee:	**Chair:** Dan Gibson Associate Professor

Gwenn Flowers
Senior Supervisor
Associate Professor _____

Jeremy Venditti
Supervisor
Professor
Department of Geography _____

Michele Koppes
Supervisor
Assistant Professor
Department of Geography
University of British Columbia _____

Brent Ward
Internal Examiner
Professor _____

David L. Egholm
External Examiner
Professor
Department of Geoscience
Aarhus University _____

Date Defended: May 26th 2017

Abstract

Glaciers shape high altitude and latitude landscapes in numerous ways. Erosion associated with glacial processes can limit the average height of mountain ranges, while creating the greatest relief on Earth and shaping the highest mountain peaks, but glaciers can also shield pre-existing topography. Glacial erosion processes, though still enigmatic, are central to the evolution of landscapes, particularly since the onset of the Pleistocene. Glacial erosion comprises three fundamental processes: (1) abrasion, (2) quarrying and (3) the direct action of subglacial water flow in sediment transport and bedrock erosion. Glacier sliding and the hydro-mechanical conditions at the ice–bed interface drive erosion processes, and are themselves controlled by the morphology and state of the subglacial drainage system. Although widely acknowledged, the direct and indirect controls of subglacial water flow on glacial erosion have been largely neglected in previous studies. This thesis focuses on exploring these controls using numerical models with an emphasis on sub-annual to annual timescales.

This work has three primary objectives: (1) to investigate how the state and morphology of the subglacial drainage system indirectly drive abrasion and quarrying, (2) to devise the first model of direct bedrock erosion by subglacial water flow and (3) to develop a framework for sediment transport in subglacial channels over a rigid bed. The results show that well-known seasonal variations in subglacial hydrology drive patterns of glacial erosion. Abrasion is favoured where the drainage system is the most dynamic, whereas quarrying calculated using a recently published law is hindered; the latter result is at odds with previous theories. Direct erosion by subglacial water flow can explain bedrock channel excavation, but the resulting erosion rates remain negligible compared to expected basin-wide glacial erosion rates. The models predict a bottleneck in sediment transport near the glacier terminus that is inherent to channel dynamics. The resulting sediment accumulation provides a process-based explanation for esker deposition, and could shape proglacial sediment yields. In focusing on spatial and temporal scales commensurate with subglacial processes, this study challenges some of the common assumptions made in glacial erosion studies and provides a starting point for refining models of landscape evolution.

Keywords: glacial erosion; subglacial hydrology; abrasion; quarrying; subglacial water flow erosion; glacial geomorphology

Acknowledgements

I am particularly obliged to Gwenn Flowers, my senior supervisor, for her patience and dedication that have been instrumental to my academic success and the great learning experience that my Ph.D. has been. I am also grateful to Jeremy Venditti and Michele Koppes for their supervision, support and feedback which have greatly helped to keep my thesis work focused and relevant for the field of glacial geomorphology.

I would like to express my gratitude to the members of the glaciology group at SFU over the six years that I have been working on my thesis: Jeff Crompton, Nat Wilson, Mauro Werder, Sam Pimentel, Adrien Gilbert, Alexandra Pulwicky, Dave Bigelow, Laura Thomson and Leif Anderson, for numerous engaging discussions and for making the atmosphere in the office so enjoyable. Many thanks go to, in no particular order, Ian Hewitt, Christian Schoof, Neal Iverson and Bernard Hallet, for numerous interesting and constructive discussions or comments. I would also like to thank the editors R. A. Marston and Arjen Stroeven for their work in the publication of Chapters 2 and 3, as well as two anonymous referees, David L. Egholm and John D. Jansen for their reviews that helped improve these two manuscripts.

Funding was provided by the Swiss National Cooperative for the Disposal of Radioactive Waste (Nagra) within the framework of investigating ice-age effects related to the long-term safety of radioactive waste disposal. I am particularly grateful to Urs Fischer for making possible and overseeing the projects in collaboration with Nagra. Funding was also provided by the Natural Sciences and Engineering Research Council of Canada (NSERC) and Simon Fraser University (SFU).

Finally, I can't express how thankful I am to my parents, friends and Brittany. They have made this endeavour possible and have been instrumental in making these six years a beautiful life experience despite the many challenges that I have faced.

Table of Contents

List of Tables

List of Figures

Preface

The research conducted in this thesis was lead by the author, Flavien Beaud, and the work presented in Chapters 2–5 was conducted with a number of co-authors: Associate Professor Gwenn E. Flowers, Professor Jeremy G. Venditti, Assistant Professor Sam Pimentel and Assistant Professor Michele Koppes.

Chapter 2 is reprinted from Geomorphology, Vol. 219, F. Beaud, G. E. Flowers, and S. Pimentel, Seasonal-scale abrasion and quarrying patterns from a two-dimensional ice-flow model coupled to distributed and channelized subglacial drainage, Pages 178–191, Copyright 2014, with permission from Elsevier.

Chapter 3 is reprinted from Earth Surface Dynamics, Vol. 4, F. Beaud, G. E. Flowers and J. G. Venditti, Efficacy of bedrock erosion by subglacial water flow, Pages 124–145, Creative Common license 2016 (http://www.earth-surf-dynam.net/4/125/2016/).

Chapter 4 was submitted to Geology as a manuscript titled Excavation of bedrock tunnel valleys and inner gorges by seasonally-produced meltwater with the following author list: F. Beaud, J. G. Venditti, G. E. Flowers and M. Koppes. The manuscript was rejected and is to be reformatted and re-submitted to another journal.

Chapter 5 is destined to be expanded, in particular including some simulations to apply the current framework, and to be submitted for publication within the next few months

Chapter 1

Introduction

The erosive action of glaciers is pivotal to understanding the interactions between tectonics and climate in orogeny (e.g. Brocklehusrt and Whipple, 2002; Brozovic and others, 1997; Egholm and others, 2009; Fox and others, 2015; Herman and others, 2010, 2013; Herman and Champagnac, 2016; Willenbring and Jerolmack, 2016). The imprint of glaciers in high latitude or altitude regions shapes our interactions with the landscape through its impact on infrastructure (e.g. Fischer and others, 2015; Iverson and Person, 2012; Preusser and others, 2010; Vivian, 1970) and civilization (e.g. Cruikshank, 2005). Physical glaciology, however, is a young field and glacial erosion in particular remains mysterious. Process-based theories of glacial erosion were mainly developed in the 1970's, coinciding with the rise of physical theories of glacial processes (e.g. Glen, 1955; Meier, 1958; Weertman, 1964; Lliboutry, 1965; Vivian, 1970; Röthlisberger, 1972; Shreve, 1972; Boulton, 1974; Lliboutry, 1976; Nye, 1976). Since a special issue of the Journal of Glaciology in 1979, theories on the processes of glacial erosion have seldom been explored (Beaud and others, 2016; Cohen and others, 2006; Hallet, 1996, 1981; Hooyer and others, 2012; Iverson, 1990, 1991, 2012; Röthlisberger and Iken, 1981), despite the abundant use of early erosion laws (Hallet, 1979, 1981) by geomorphologists studying the effect of glaciers on the landscape. There is thus a need to further study glacial erosion processes and specifically how subglacial hydrology directly and indirectly drives these processes.

This introduction provides (1) a review of historical developments of the processes and roles of glacial erosion, (2) a summary of glacier flow and subglacial hydrology, (3) a summary of the physical processes of glacial erosion and the associated theories, (4) a summary of the impact of glacial erosion on landscape evolution and (5) the research objectives and questions addressed in this thesis. Throughout the thesis, I use the term "erosion" to indicate bedrock erosion, and the terms "removal" or "transport" when the reworked substrate is sediment.

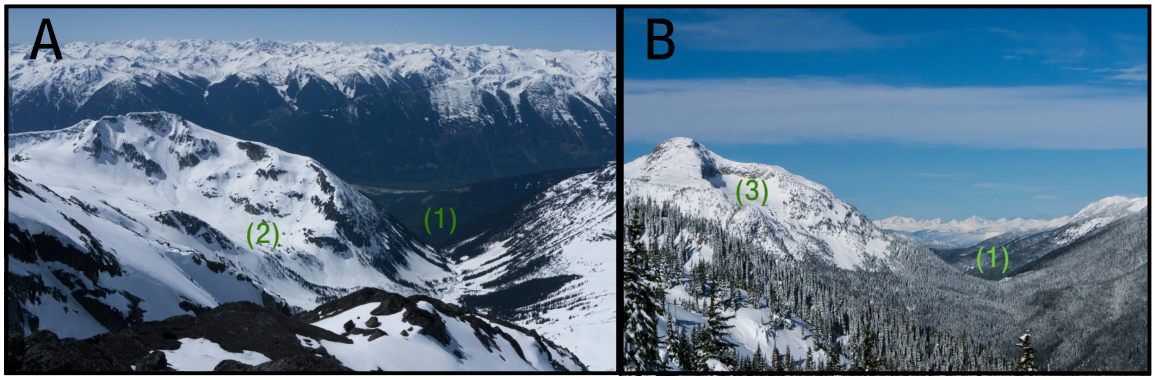

Figure 1.1: Typical features of glacial valleys. (A) View from the west ridge of Mount Sampson towards the south to the Lillooet river, Coast Mountains, British Columbia. (B) View towards the north west from Zoa Peak, Coast Mountains, British Columbia. U-shaped valleys are shown with (1), a hanging valley with (2) and a cirque with (3). Photos were taken by the author.

1.1 History of glacial erosion theory

Scientific theories evolve such that some become obsolete and others build the foundations of new fields of research. Recognizing how theories have evolved through time in a field of research can help current researchers to build new theories. Jules Blache wrote an extensive review of the state of glacial geomorphology in 1952 that he expanded with his own analysis. A thorough historical review of geomorphology from the late 1800s to 1965 can be found in the fourth volume of *The History of the Study of Landforms* (Burt and others, 2008) and, of particular interest for this historical review, the chapter written by Evans (2008), *Glacial Erosional Processes and Forms: Mountain Glaciation and Glacier Geography*. In this section, the evolution of glacial geomorphology is summarized, from its emergence until the mid-1970's, to provide a historical context for how theories of glacial erosion have changed.

At the end of the 19th and beginning of the 20th century, scientists started to describe and explain the shape of landscapes, attributing their formation to the action of hill slopes, rivers and glaciers. Consideration of the action of glaciers specifically arose as some mountain valley profiles could not be explained by fluvial action. Agassiz had established the basis for the theory of ice ages several decades earlier enabling the idea that glaciers had, perhaps, shaped valleys during times of extensive ice cover.

In the first half of the 20th century three different schools arose (Blache, 1952; Evans, 2008): (1) the *protectionists* thought of glaciers as protective blankets; (2) the *glacialists* posited that glaciers were the main agent shaping non-fluvial valleys and (3) the *parisian school* recognized glacial erosion, yet emphasized the necessity of the conjugated para-, pre- or post-glacial, fluvial erosion. The landforms of interest (Fig. 1.1) were cirques, U-shaped

valleys, hanging U-shaped valleys, overdeepened valley profiles and fjords in northern coastal areas. During this period, the strife between the different schools hindered progress:

> What we have gained since 1912 [...] is to recognize [...] that there has been no continuous progress, but different schools that work simultaneously without communicating or acknowledging each-other. The vast majority of authors present the results of their work supposing that the methods that they use, or those of their academic master, are known and accepted. One should instead start by stating explicitly their adherence to such or such school or academic master. However, this would presume that [said school's or academic master's] authority is not universal.
>
> (Blache, 1952, p.33)

Most of what Blache (1952) stated remains true at present: glacial geomorphology, as a field of research, is still divided between studies focusing on observations of formerly glaciated landscapes, present-day observations, physical explanation of specific processes and landscape evolution. Bridging the gaps between these types of studies is one of the overarching challenges in glacial geomorphology and is necessary to further our understanding of both landforms and processes.

The *protectionists*' theories were built around the idea that glaciers cannot leave a significant imprint on alpine valleys due to their sluggish movement, hence should act as protective blankets draped over mountain valleys. This vision is highlighted by a quote from the famous Swiss geologist Albert Heim, related by Preusser and others (2010): "Mit Butter hobelt man nicht (Butter is not an abrasive agent)". Disciples of this school nonetheless thought glaciers were efficient carriers of the sediment that falls onto them or that is laid in their path, and they recognized the action of subglacial meltwater in carving canyons. Blache (1952) unabashedly describes this school as "archaic" and oblivious to the shape of alpine landscapes, as it attempted to explain landforms with geological theories (e.g. folding and faulting of rocks). Evans (2008) suggests that some leading *protectionists* had only been exposed to Alpine glacial landscapes that they perceived as conventional, lacking the perspective that the exposure to landscapes dominated by fluvial processes would have given them.

The *glacialists* also called *école du lit glaciare* by Blache (1952) considered that glaciers leave a unique and specific imprint on the landscape while recognizing the preglacial conditioning by fluvial processes of alpine valleys. The *glacialists* suggested that glaciers should erode following the same guiding principles as rivers, such that glacial erosion is proportional to the work or pressure exerted by the ice on the bed and the speed of the ice mass (e.g. Blache, 1952). The early theory of Gannett in 1898 (Evans, 2008, p.424) proposes that the similarity between fluvial and glacial erosion lies in the shape of the river channel and that of the glacial valley. While a typical river valley has a V-shape, the river channel tends

to be U-shaped. In comparison, the glacier should fill an entire valley during an ice age, thus the valley has the same U-shape as the glacier channel.

The *parisian school*, led by de Martonne, accepted the role of glaciers in shaping landscapes, while emphasizing that rivers are doing at least as much if not more work. de Martonne (1910) was one of the pioneers to propose a physical formula to explain the intensity of glacial erosion, whereby erosion is an inverse function of ice-surface slope. The reasoning is that when ice-surface slope is steep, the base of the glacier loses contact with the rock, hindering the erosive action. This theory was used to explain that glaciers tend to enhance the stepped profile of glacial alpine valleys, as the erosion is inhibited over the steps and accentuated over flatter areas. This was also used to explain hanging valleys: the slope of the tributary is steeper than that of the trunk glacier the latter would thus erode a deeper valley. Similar geometrical considerations have been made in numerical studies of landscape evolution to differentiate erosion by abrasion and quarrying (e.g. Egholm and others, 2012; MacGregor and others, 2009)

During the late 19th and early 20th centuries, it was accepted that glaciers were moving, even if extremely slowly, and could slide over their beds. One of the very first processes to be identified was abrasion (Evans, 2008, and citations therein), likely due to the prevalence of polished and striated outcrops. Quarrying was recognized as a process, but its significance was widely disregarded, and the erosion of subglacial water flow and the slots it carved in glacial valleys was only noted by a few (Evans, 2008). Three scientists made preliminary attempts at quantifying glacial erosion or more generally friction exerted on the bed, as they conceived a direct relation between these two quantities. Pioneering work by McGee in 1894 (Evans, 2008, p. 472) suggested that friction on the bed F_{bed} is a function of the glacier velocity v_{gl}, the weight of the ice w_{ice} and the bed slope α_{bed} such that

$$F_{\mathrm{bed}} = f_1(v_{\mathrm{gl}}) w_{\mathrm{ice}} \cos(\alpha_{\mathrm{bed}}), \tag{1.1}$$

with f_1 a function. Elaborating on McGee's work, de Martonne (1910) proposed

$$F_{\mathrm{bed}} = f_2(v_{\mathrm{gl}}) \cos(\alpha_{\mathrm{surf}}) P_{\mathrm{glb}} h_{\mathrm{i}} A_{\mathrm{bed}}, \tag{1.2}$$

where α_{surf} is the slope of the surface of the glacier, P_{glb} is its bed perimeter, h_{i} is its thickness and A_{bed} is the adherence of the bed. In a similar fashion, "Gilbert related abrasion to basal velocity, pressure exerted against the bed, shape of the bed, hardness of the bed, and the quantity and hardness of striating rocks." (Evans, 2008, p. 472).

Research in Earth sciences was hindered significantly during and between the two World Wars, and it is Lliboutry in the mid-1960's who spearheaded the renewed interest in the physical mechanisms of glacial erosion (Lliboutry, 1962, 1965). During this period a modern understanding of physical processes of glacial erosion emerged. Four mechanisms were identified (Fig. 1.2): (1) quarrying, the detachment of blocks from a bed obstacle, (2) abrasion,

filing of the bedrock by clasts embedded in sliding ice, (3) erosion by subglacial meltwater flow which encompasses the same mechanisms as fluvial erosion but with larger shear stresses and (4) chemical dissolution and weathering. These four mechanisms were clearly identified from field observations, however their relative role in erosion was debated, and still is.

In the 1960's and 1970's several authors proposed their conceptual models of erosion. Vivian (1970) suggested that water flow and abrasion were the main mechanisms of erosion, and that quarrying was only secondary. His inferences are based only on observations of glaciers around Chamonix, in particular the Glacier D'Argentière. A tunnel under the Glacier D'Argentière that was built for hydroelectric purposes and used to test the abrasive resistance of paving material, allowed Vivian (1970) to observe 10 cm of incision in five years in quartzite blocks. He also relates several other instances of such rapid erosion by subglacial waters and suggests that this erosion explains the formation of canyons incised at the bottom of glacial valleys. The sparsity of clasts observed in the cavity led him to conclude that quarrying was inefficient. Vivian (1970), however, failed to recognize how spatially-limited the action of subglacial water was and that the clasts responsible for abrasion had to be produced at the bed by quarrying.

Lliboutry proposed a detailed physical model of glacial erosion in a series of papers (Lliboutry, 1962, 1994, 1965). In 1962 and 1965 he proposed that glacial erosion is composed of two spatial components: (1) erosion by the front of the glacier and (2) subglacial erosion. He argued that annual to multi-annual fluctuations in glacier length are necessary to weaken the bed and then bulldoze the loosened material, leading to erosion by the front of the glacier. For example, over a period of overall melt and retreat of the glacier terminus, the bedrock in front of the glacier can be damaged by subaerial processes and frost-heaving. The next period of advance will bulldoze the loosened material and entrain it in the ice close to the terminus. Lliboutry (1962; 1965) argued that the erosion by the front of the glacier is more important than subglacial erosion, even though this mechanism of proglacial erosion has been disregarded by researchers. For subglacial erosion, he suggested that quarrying is the dominant mechanism and that its action is necessary to produce tools for abrasion. He further suggested that the steps created by quarrying tend to be erased easily by polishing due to abrasion and that quarrying action is underestimated. Lliboutry (1994) made the first, and one of the rare, attempts to produce a model of glacial erosion accounting for abrasion and quarrying based on physical mechanisms. His abrasion model also includes the wearing and rounding of clasts, and how such wear decreases abrasion efficiency.

1.2 Glacier motion and subglacial hydrology

Understanding glacier flow and basal processes is key to understanding glacial erosion mechanisms. I review these processes in more depth in Chapter 2 (see also Cuffey and Paterson,

2010). Glacier flow is driven by pressure gradients and results from the combination of internal viscous deformation, basal sliding and deformation of the bed. Ice is a polycrystalline material whose viscosity decreases with temperature and strain rate, and is a function of composition (e.g. impurities, air bubbles) and crystalline structure (Cuffey and Paterson, 2010). Basal sliding can only occur where the glacier bed is at the pressure melting point and it is controlled by basal shear stress, effective pressure and topographic roughness (e.g. Weertman, 1964; Budd and others, 1979; Iken, 1981; Bindschadler, 1983; Schoof, 2005; Gagliardini and others, 2007) and can occur with or without cavity formation. When no cavity forms on the lee side of an obstacle, sliding is dominated by regelation and enhanced creep. Ice motion across a bed obstacle creates a pressure gradient, the pressure exerted is higher on the stoss (up-flow) side of the obstacle than the lee (down-flow) side. The melting point of ice is pressure-dependent, thus melting will occur on the stoss side where the pressure is higher; pressure gradients then draws the fluid toward the lee side where refreezing occurs. This process causes ice to move past bed obstacles, but can only explain low sliding speeds (e.g. Cuffey and Paterson, 2010). The presence of bed asperities concentrates stress and leads to locally enhanced deformation. If the driving stress is large enough and sliding relatively large a cavity can form in the lee side of an obstacle (e.g. Cohen and others, 2006; Iken, 1981; Iken and others, 1983; Iverson and Petersen, 2011; Kamb, 1987; Vivian, 1970; Vivian and Zumstein, 1973).

Many field studies have shown a positive correlation between basal water pressures and sliding speed (e.g. Anderson and others, 2004; Bartholomaus and others, 2007; Fischer and others, 2011; Iken and Bindschadler, 1986; Lliboutry, 1976; Mair and others, 2002; Müller and Iken, 1973). Fluctuations in sliding velocity and basal water pressure are tied to meltwater production and water delivery to the bed, and these fluctuations occur on daily to seasonal time scales for most valley glaciers and some ice-sheet outlet glaciers (e.g. Bartholomew and others, 2012; Iken and others, 1983; Müller and Iken, 1973; Sole and others, 2011). A typical meltseason leads to three different sliding phases: (1) winter, were velocities are relatively low and often referred to as "background velocities", (2) the spring-speed up that shows a peak in sliding speeds and (3) the end of the summer, where sliding speeds may drop bellow the winter background velocity (e.g. Iken and Bindschadler, 1986; Iken and others, 1983; Müller and Iken, 1973). Any sudden injection of water, for example due to heavy rain-fall, the drainage of a sub-, en-, supra-glacial or ice marginal lake, or subglacial volcanism can also lead to a significant increase in sliding speed (e.g. Anderson and others, 2014; Bartholomaus and others, 2011; Björnsson, 2010; Nye, 1976).

Glacier beds are often classified as one of two types: "hard", when the bed is undeformable, often bedrock, and "soft" when the bed can be deformed by basal shear stresses or reworked by subglacial water flow, often indicative of the presence of a significant layer of till. In the context of bedrock erosion, I will focus on hard-bed conditions. Two main types of drainage systems operate under glaciers (e.g. Fountain and Walder, 1998): a distributed

system characterized by water pressures that increase with water flux, and a channelized system characterised by water pressures that decrease with increasing discharge in steady state. These drainage systems can co-exist, and most glaciers exhibit a spatio-temporal transition between dominant drainage types (e.g. Iken and Bindschadler, 1986). In the absence of substantial water input, the distributed system will dominate. When a significant amount of water reaches the bed (e.g. surface melt or lake drainage) the water pressure rises and water velocity increases. This promotes melting of the ice by viscous heat dissipation and may allow a Röthlisberger channel (R-channel; Röthlisberger, 1972) to form. Rapid water input and abrupt increases in pressure are usually associated with an increase in ice velocity and accompanied by a transition to a subglacial drainage system dominated by flow in channels (e.g. Bartholomew and others, 2012; Mair and others, 2002, 2003; Sole and others, 2011). As long as there is a significant water supply to the bed, the R-channels will continue to enlarge and will migrate up-glacier. The efficiency in water evacuation associated with a well established channelized drainage system leads to reduced basal water pressure and reduced basal sliding. When the water supply decreases too much to sustain the R-channels, they close by ice creep and a slow drainage system becomes dominant again.

Subglacial water flow over a soft bed is widely associated with distributed drainage systems, because basal water pressure generally increase with water flux (see Flowers, 2015; Fountain and Walder, 1998; Greenwood and others, 2016, for reviews). If a soft bed is sufficiently permeable or mobilizable, water may be evacuated without channel formation (e.g. Flowers, 2008; Walder and Fowler, 1994). To describe subglacial water flow over soft beds, a number of drainage systems have been proposed: canals (e.g. Ng, 2000a; Walder and Fowler, 1994), a layer of till (e.g. Clarke, 1996; Le Brocq and others, 2009), a macroporous sheet (e.g. Creyts and Schoof, 2009; Flowers and Clarke, 2002), so-called subglacial swamps (e.g. Kyrke-Smith and Fowler, 2014) or a groundwater system (e.g. Boulton and others, 1995; Flowers and Clarke, 2002). Sediment evacuation by water flow over a soft bed may be limited to sand-sized particles and smaller, as the shear stresses produced by the water flow are significantly smaller than in an R-channel (e.g. Beaud and others, 2016; Creyts and others, 2013; Kyrke-Smith and Fowler, 2014; Ng, 2000a; Walder and Fowler, 1994, see also Appendix B), although water at the ice–till interface can be crucial for sediment accretion to basal ice and sediment removal (e.g. Alley and others, 2003; Creyts and others, 2013; Le Brocq and others, 2009). However, in the scenario where a glacier drainage system is dominated by soft-bed conditions, a significant layer of till is expected which would protect the bedrock from glacial erosion (Hindmarsh, 1996). In Chapters 2–5, I discuss the role of soft-bed drainage in the context of each study. The sub-annual evolution of subglacial drainage controls spatio-temporal patterns of ice sliding and basal water pressure, quantities that are critical for glacial erosion. Exploring these controls and the effect on spatio-temporal patterns of glacial erosion is the goal of Chapter 2.

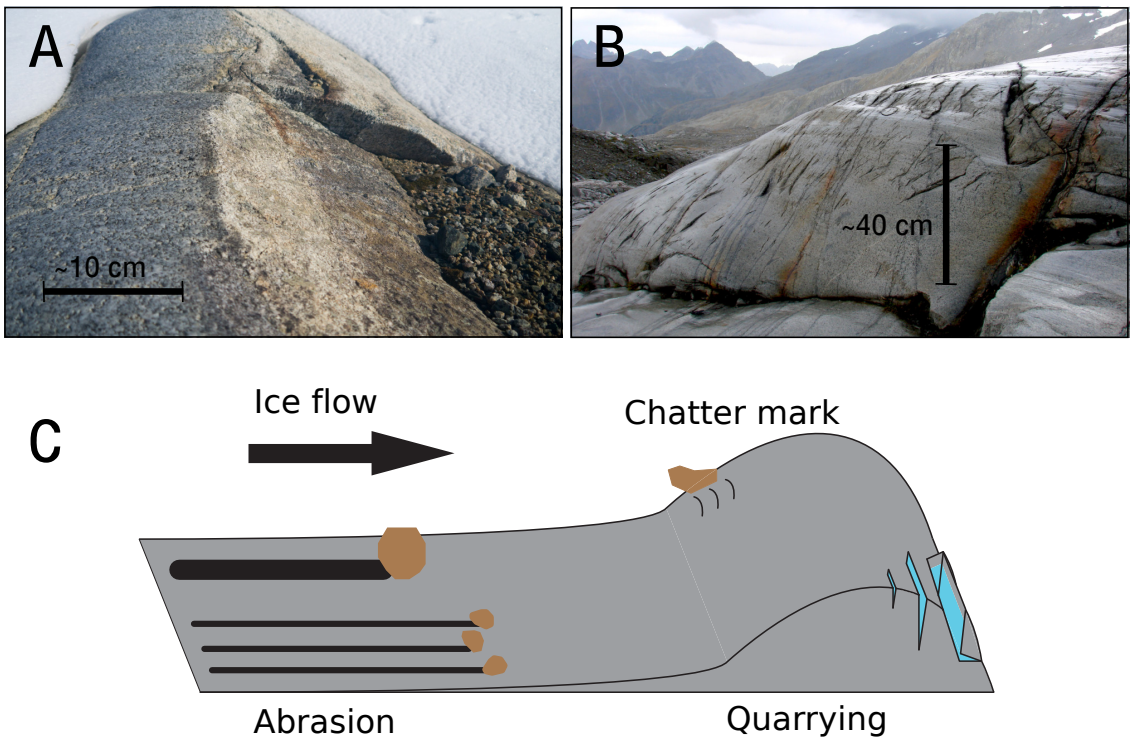

Figure 1.2: Typical small-scale features created by glacial erosion and associated processes. (A) Bedrock hump showing a polished side and a quarried side; ice flow was from left to right. (B) Bedrock obstacle showing polishing, striations and chatter marks or gouges. Ice flow was from right to left and towards the picture. (C) Conceptual summary of the processes of glacial erosion. Photos were taken by the author.

1.3 Processes of glacial erosion

1.3.1 Abrasion

Abrasion was the first glacial erosion process identified (Evans, 2008) and is the most studied. In-situ observations of abrasion remain rare (Anderson and others, 1982; Boulton, 1974, 1979; Lister and others, 1968; McCall, 1960; Vivian, 1970), yet they were crucial in developing physical theories (e.g. Boulton, 1979; Lliboutry, 1962, 1965). Mathews (1979) used abrasion mill experiments to study the mechanism at the mineral scale. He describes abrasion as a grain-scale plucking mechanism whereby minerals are either dislodged along their boundaries or broken with a preference for breaking along cleavage planes when they exist. Boulton (1979) suggests that the abrasion rate $\dot{e}_\mathrm{a}$ should be proportional to the concentration of abrading particles in ice c_a1, the velocity of the particle v_p, the effective pressure at the particle–bed contact N_pb and the bed hardness h_b:

$$\dot{e}_\mathrm{a} \propto \frac{c_\mathrm{a1} v_\mathrm{p} N_\mathrm{pb}}{h_\mathrm{b}}. \tag{1.3}$$

In Boulton (1979) the effective pressure at the particle–bed contact is assumed to be the same as the effective pressure at the ice–bed interface.

Hallet (1979) proposes a very similar law, but argues that the contact force between the particle and the bed is independent of the ice thickness, as long as the ice thickness is greater than $\sim 30\,\mathrm{m}$ (McCall, 1960). Hallet (1979) suggests that this contact force is a function of the bed-normal velocity of the clast in the ice and that such motion is the result of basal melting. The erosion rate by abrasion can then be expressed as

$$\dot{e}_\mathrm{a} = c_\mathrm{a2} {u_\mathrm{b}}^l, \tag{1.4}$$

where c_a2 is a constant accounting for the hardness of the bedrock or clasts as well as the concentration of clasts, u_b is the basal sliding speed and l is an exponent close to 2. Hallet (1981) extended his early theory to account more explicitly for the concentration of clasts. The theory that clast–bed contact force is a function of the bed-normal velocity of the clast was later validated by laboratory experiments (Byers and others, 2012; Iverson, 1990; Lister and others, 1968). A value of l close to but less than 2 was also confirmed by laboratory experiments of ice–bed friction (Byers and others, 2012). Cohen and others (2005), however, challenge the findings of Hallet (1981) that clast–bed friction is relatively small. Through a combination of subglacial measurements and theory, Cohen and others (2005) show contact forces two orders of magnitude larger than that expected from Hallet's (1981) calculations, attributed to near-Newtonian rheology of the ice close to the bed and around clasts. If the ice rheology follows Glen's (1955) flow-law in this environment, the results are expected to remain close to Hallet's (1981) predictions. The contact forces between the glacier sole, clasts and bed are central to understanding ice sliding and erosion; the controls on these forces however remain uncertain.

Abrasion rates are largely controlled by sliding speeds, which are dependent on the state and morphology of the subglacial drainage system. Because of the difficulty of observing the relationships between these processes in the field, numerical modelling is a tool of choice. The choice of sliding law (e.g. Gagliardini and others, 2007; Schoof, 2005) may therefore also be crucial to computed abrasion patterns. Most studies addressing the role of subglacial hydrology in glacial erosion do so with a highly simplified representation of the drainage system (Egholm and others, 2012; Herman and others, 2011; Hildes and others, 2004; Ugelvig and others, 2016). The dependence of calculated erosion rates on the sliding law has only been addressed in the absence of subglacial hydrology (Brædstrup and others, 2016). In Chapter 2 I attempt to bridge this gap by using a numerical model to address how the type of subglacial drainage system and sliding law affect erosion pattern.

1.3.2 Quarrying

The quarrying of a block occurs through the following series of events: (1) growth of fractures present in a bedrock obstacle (size on the order of a metre) caused by subglacial processes, (2) dislodgement of the block and (3) entrainment of the block by ice flow (Röthlisberger and Iken, 1981). Quarrying was first recognized in well fractured bedrock where the glacier drag was sufficient to dislodge blocks extensively (e.g. Evans, 2008; Iverson, 1991, and references therein). Scientists in the mid-20th century did not recognize that the action of the ice could lead to the enlargement of fractures in bedrock, thus frost-heaving was a good candidate to explain the loosening of blocks (e.g. Lliboutry, 1962, 1965). Lliboutry (1962) stresses the potential effect of sub-seasonal to daily fluctuations in water pressure to enhance fracture growth such that these fluctuations are conducive to larger quarrying rates. The refreezing of subglacial water in fractures is, however, unlikely in this context as water pressure is expected to remain high and the water temperature above the pressure melting point (Hallet, 1996; Iverson, 1991; Lliboutry, 1962). Robin (1976) proposed a heat-pump mechanism triggered by large pressure fluctuations in cavities that could lead to the freezing of blocks to the glacier sole, facilitating their evacuation.

The modern conceptual model of quarrying was first suggested by Röthlisberger and Iken (1981), who proposed specific processes for each of the three steps listed above. They used the numerical model of cavity formation developed by Iken (1981) to calculate stresses caused by ice sliding over the bedrock. Their results corroborate Lliboutry's (1962; 1965) postulate that water-pressure fluctuations in cavities dramatically increase stresses imposed on the bed. In an earlier effort Morland and Morris (1977) also used a numerical model to explore stress gradients in a bedrock hump caused by sliding ice, but in the absence of a cavity. They calculate relatively large stress gradients, although not sufficient to break unfractured rock. Iverson (1991) developed a numerical model to calculate stresses in a bedrock step in the presence of a lee-side cavity and corroborated the theory that water-pressure fluctuations may be the main control on quarrying. Hallet (1996) used a similar numerical model to calculate micro-crack growth and concluded that low effective pressures (ice pressure minus water pressure) and high sliding speeds, in addition to the water-pressure fluctuations, were the conditions most conducive to quarrying.

Only a few observations of quarrying events have been reported in conjunction with glacier sliding (Anderson and others, 1982; Cohen and others, 2006). The exceptional experiment conducted by Cohen and others (2006) consisted of monitoring stresses on and in the vicinity of a bedrock obstacle at the bed of Engabreen, Norway. The intact bedrock obstacle withstood the stresses; it is only when a notch was cut in the obstacle that quarrying of the ledge occured. Observations of quarried surfaces (Hooyer and others, 2012; Krabbendam and Bradwell, 2011) unequivocally show that failure occurs along pre-existing planes of

weakness, supporting the postulate that ice-induced stresses are not able to fracture intact bedrock (Cohen and others, 2006; Morland and Morris, 1977).

Iverson (2012) developed a law to include quarrying in landscape evolution models using a theory of adhesive wear and accounting for the heterogeneity of bedrock fractures. This model captures increased quarrying rates with increased sliding for a fixed effective pressure. For a fixed sliding speed, the role of the effective pressure is not monotonic and depends highly on the heterogeneity of bedrock fractures. The effect of water pressure fluctuations is also omitted from the model because of the target time-scale of more than tens of thousands of years.

As for abrasion rates, the subglacial drainage system is crucial to understanding quarrying patterns because it drives sliding and water pressure patterns. Numerical modelling is again a tool of choice to study quarrying patterns, yet the role of subglacial hydrology on quarrying has only been addressed with very simple models of water flow (Hildes and others, 2004; Ugelvig and others, 2016). In Chapter 2 I explore how the type of subglacial drainage system and sliding law affect modelled quarrying patterns.

1.3.3 Subglacial melt-water erosion and chemical weathering

Subglacial melt-water erosion (SME)

The ability of subglacial melt-water erosion (SME) to carve bedrock is well recognized (e.g. Glasser and Bennett, 2004; Vivian, 1970), but the physical processes responsible for such bedrock erosion have never been studied. Sediment evacuation rates by subglacial water flow are often assumed to represent glacier-catchment-wide erosion rates (e.g. Bogen, 1996; Gurnell and others, 1996; Hallet and others, 1996; Herman and others, 2015; Koppes and Montgomery, 2009; Koppes and others, 2015; Riihimaki and others, 2005), despite the lack of process-based studies of such evacuation. Intuitively, erosion and sediment transport caused by subglacial water flow should encompass the same processes as in fluvial systems. As water flows over a rough bed, it produces shear stresses that can mobilize sediment if these shear stresses exceed a threshold that depends on particle size and buoyant weight (e.g. Shields, 1936). Once mobilized a particle can then roll, saltate or be entrained in suspension with increasing shear stress (e.g. Lamb and others, 2008a; Sklar and Dietrich, 2004). Saltation and suspension are the transport regimes of interest for erosion, as particles subject to such regimes can abrade bedrock upon impact (e.g. Cook and others, 2013; Lamb and others, 2008a; Scheingross and others, 2014; Sklar and Dietrich, 2001, 2004). Plucking can also occur in fluvial environments if blocks of rocks are loose enough to be dislodged and entrained by the stresses caused by water flow or impacting particles (e.g. Chatanantavet and Parker, 2009; Dubinski and Wohl, 2013; Lamb and others, 2015; Whipple and others, 2000, 2013). The loosening of blocks is thought to occur due to chemical weathering in pre-existing cracks (e.g. Chatanantavet and Parker, 2009), although in some lithologies, such as

columnar basalt, the joints could be sufficiently developed for flood events to dislodge blocks (e.g. Baynes and others, 2015; Bretz, 1969; Dubinski and Wohl, 2013; Lamb and Fonstad, 2010; Lamb and others, 2015). For both abrasion and plucking, if enough sediment is present, it will shield the bed from erosion.

Landforms at a wide range of scales (centimetre to several kilometres) have been attributed to SME and used to infer past conditions at the bed of glaciers and ice sheets (e.g. Bennett and Glasser, 2009; Glasser and Bennett, 2004; Kor and others, 1991). For example, tunnel valleys are channel-like features that can be up to a few kilometres wide and tens of kilometres long. They are the largest features attributed to SME. Recent improvements in geophysical techniques have led to numerous observations of these features, yet their origins remains controversial (e.g. Ó Cofaigh, 1996; Kehew and others, 2012; van der Vegt and others, 2012). The origin of inner gorges, which are V-shaped incisions into an otherwise glacial landscape are also controversial. Their formation was first attributed to fluvial erosion during inter-glacial periods, however they can persist through glaciations (Montgomery and Korup, 2010). Two recent studies show they can be excavated by SME (Dürst-Stucki and others, 2012; Jansen and others, 2014).

Theories about the formation of tunnel valleys and inner gorges are mainly based on observations (e.g. Ó Cofaigh, 1996; Kehew and others, 2012; van der Vegt and others, 2012). In addition, assumptions regarding proglacial observations are based on fluvial sediment transport theories (e.g. Bogen, 1996; Herman and others, 2015; Orwin and Smart, 2004; Østrem, 1975; Riihimaki and others, 2005), but the physical processes responsible for SME and sediment evacuation remain unexplored. Exploring these processes is my goal in Chapters 3–5. I start by creating the first numerical model of SME by combining a model of abrasion caused by water-born particles with a model of subglacial water flow (Chapter 3). I then use this SME model to test the current theories of bedrock channel formation (tunnel valleys and inner gorges; Chapter 4). Finally, I develop the first framework for sediment transport in a channelized drainage system over a hard bed (Chapter 5) that can be used to investigate sediment evacuation and the role of transient sediment fluxes on SME.

Chemical weathering

The role of chemical weathering in the subglacial environment has seldom been studied. Hallet (1976) showed that dissolution and precipitation could be important, but only for specific lithologies relatively easily soluble in water, such as limestone. Anderson (2005) linked erosion with weathering rates, and concluded that solute fluxes represent an insignificant fraction of the total sediment load. These few studies built a case for neglecting chemical weathering in subsequent erosion studies. Recent work by Crompton and others (2015) however suggests that re-precipitation of minerals can account for over 30% of the suspended sediment load in the proglacial stream of an un-named glacier in the Yukon Territory, Canada.

1.3.4 Evolution of conceptual models

Four mechanisms of subglacial erosion have been identified: quarrying, abrasion, erosion by subglacial water flow and chemical weathering, yet their relative importance remains debated and our understanding of them is very contrasted. Abrasion has received the most attention (Anderson and others, 1982; Boulton, 1974, 1979; Hallet, 1979, 1981; Hindmarsh, 1996; Iverson, 1990; Lister and others, 1968; Lliboutry, 1994; Mathews, 1979; Röthlisberger, 1968), and is likely the best understood of glacial erosion processes. The role of quarrying was recognized later (Lliboutry, 1962, 1965) and its physical controls have been studied (Anderson and others, 1982; Cohen and others, 2006; Hallet, 1996; Hooyer and others, 2012; Iverson, 1991, 2012; Röthlisberger and Iken, 1981), yet it is unclear whether these controls have been adequately captured in numerical models (Beaud and others, 2014). Only a handful of studies have examined the two remaining mechanisms (e.g. Anderson, 2005; Beaud and others, 2016; Crompton and others, 2015; Hallet, 1976). Examining the role of subglacial water flow on erosion is a central aspect of my thesis.

The first appearance of what one might consider a modern view of erosion mechanisms was presented by Röthlisberger (1968) in a short paper explaining his conceptual description of the evolution of subglacial relief, in an attempt at sparking further interest in these processes. He discusses the role of different bed conditions on the abrasive efficiency of clasts and the effects on the metre-scale topography of the glacier bed. Röthlisberger (1968) further acknowledges that the supply of clasts from the headwall is not sufficient to sustain the depth of glacial valleys and suggests that these clasts have to be detached from the bed by "other erosive processes". Anderson (2014) develops a basic numerical model encompassing abrasion and quarrying to discuss the evolution of bed roughness and finds that bedrock steps tend to migrate up-glacier. Hildes and others (2004) makes a significant numerical modelling effort by coupling ice and water flow, Hallet's (1979; 1981) abrasion law and a process-based quarrying law where the rates are a function of critical crack growth. They attempt to constrain the erosion parameters for abrasion and quarrying as a function of the rock substrate and discuss their results for the Laurentide and Cordilleran ice sheet. Hildes and others (2004) find that erosion is fastest where water pressure, and thus sliding rate, is high. Water pressure fluctuations are also necessary in this model to lead to critical crack growth and quarrying rates to be large.

A number of authors have made an effort to differentiate abrasion from quarrying in numerical studies of landscape evolution, however these differentiations tend to be ad hoc, and based primarily on simple geometrical considerations of the glacier bed or on the exponent l of an erosion law (e.g. Anderson and others, 2006; Egholm and others, 2012; Kessler and others, 2008; MacGregor and others, 2009, 2000). Numerical models of glacial erosion using a process-based differentiation of abrasion and quarrying thus remain rare (Anderson, 2014; Hildes and others, 2004; Lliboutry, 1994) and the importance of subglacial water is

neglected, with the exception of Hildes and others (2004). In addition, the effect of erosion or sediment evacuation by subglacial water flow is omitted. In this thesis, I start by comparing how abrasion and quarrying patterns are affected the sub-annual evolution of the subglacial drainage system (Chapter 2), although the interactions between these two erosion processes are still omitted. In the remainder of the thesis, I develop numerical models to explore the role of SME (Chapters 3 and 4) and sediment transport by subglacial water flow (Chapter 5). Chapters 3–5 thus provide a physical description of the action of subglacial water flow so that the development of a comprehensive model of glacial erosion encompassing abrasion, quarrying and SME becomes possible.

1.4 Glacial action and landscape evolution

Numerical modelling studies of landscape evolution by glacial processes rely on significant assumptions about the direct and indirect role of subglacial drainage systems. The work presented in this thesis is not directly related to landform excavation (with the exception of Chapter 4) or landscape evolution due to the relatively short timescales considered. This work is, however, key to exploring the assumptions tied to the effect of subglacial water flow on glacial erosion. In this section I review the theories of landscape evolution associated with the action of glaciers. The relevance of this thesis in the context of glacial erosion and landscape evolution is reserved for Chapter 6.

The mechanisms of orogeny and the interactions between tectonic forces and climate-driven erosion are well recognized (e.g. Willett, 1999). Before describing the possible roles of glaciers in orogeny, I will clarify the use and definition of several terms. In the context of erosion in mountain ranges, relief is a key concept. It is the difference in elevation between the highest and lowest surface elevations within a defined areal unit. When analyzing relief (Fig. 1.3), the size of the chosen areal unit is particularly important, as changes in relief can be of opposite sign in the same region for different areal units (e.g. Champagnac and others, 2014). To create relief at the scale of a mountain range, tectonic forces leading to crustal thickening are necessary to create uplift. I will follow the definition of England and Molnar (1990) for surface uplift, rock uplift and exhumation. Surface uplift is the displacement between the Earth surface and the geoid, and is defined as positive when the surface is moving away from the geoid. Similarly to relief, an areal unit has to be defined (e.g. Brozovic and others, 1997), as different points in a given areal unit can show different trajectories. Rock uplift is the displacement of a given block of rock in the Earth's crust relative to the geoid. Exhumation is the positive displacement of a given block of rock relative to the surface, and can be the result of erosion or extensional forces due to tectonic processes. Finally, as stated by England and Molnar (1990):

$$\text{surface uplift} = \text{rock uplift} - \text{exhumation}. \tag{1.5}$$

In this context, thermochronometers yield quantification of exhumation rates from which erosion rates can be estimated (e.g. Fox and others, 2014).

Using these definitions, Molnar and England (1990) explain the intricacies of differentiating surface- and rock uplift, and that climate change could be a factor leading to conditions that can be confused with surface uplift through feedbacks linking tectonic activity, climate change and erosion. These feedbacks are based on the possible interactions between relief production, mean elevation and ridge-line elevations. Assuming a two-dimensional vertical slice of crust of thickness T that shows a relatively flat topography and that its surface is at an mean elevation h above the geoid, has a width w and has a density of $\rho_c = 2700\,\mathrm{kg\,m^{-3}}$ overlying the mantle of density $\rho_m = 3300\,\mathrm{kg\,m^{-3}}$. The isostatic adjustment resulting from the removal of an area $\Delta T w$ would be $\Delta T \frac{\rho_m - \rho_c}{\rho_m} \approx \Delta \frac{5}{6} T$. If differential erosion removes an area $h \times w$ from the crust such that peaks are shielded and deep valleys created, the isostatic adjustment would yield a rock uplift of $\frac{5}{6}h$ bringing the peaks to an elevation $h + \frac{5}{6}h \approx 1.8h$, but the resulting new mean elevation $\bar{h}$ would be lower: $\bar{h} = h - h/6 \approx 0.83h$.

The creation of relief can thus trigger positive rock uplift although the surface uplift is negative, and the maximum height, or height of peaks and ridges, would increase in this area. The rise of the Himalaya and the exposure of silicate material to weathering has been suggested as a potential mechanism to trap CO_2 and initiate global cooling (Molnar and England, 1990). Molnar and England (1990) propose that if the rise of the Himalaya triggered CO_2 trapping and the onset of Northern hemisphere glaciations, glacial periods would enhance relief production and the rise of peaks and ridges. High mountain ridges perturb atmospheric circulation, enhancing precipitation (e.g. Saint Elias Mountains, Yukon Territory, Canada; Fig. 1.3A) and thus erosion and weathering. Increased erosion and weathering are likely to lead to more CO_2 trapping hence global cooling, and again the intensification of glaciations.

This feedback relies on three key assumptions: (1) weathering-driven CO_2 burial is significant and increases with global denudation, (2) global denudation rates have increased since the onset of glaciations and (3) glacial periods lead to an increase in relief at the scale of mountain ranges. I will omit discussing the first assumption as it is beyond the scope of the current work. Since 1990, a significant effort has been devoted to test the second and third hypotheses leading to the following questions. Have global denudation rates increased since the onset of glaciations in the Northern hemisphere? If these denudation rates increased is it because glacial erosion is faster than fluvial erosion or because the switch between glacial and fluvial conditions prevents an equilibrium state to be reached and erosion is high? How does a glaciation impact the relief of a mountain range? Numerical models of landscape evolution by glacial erosion are often used to discuss changes in relief (e.g. Brædstrup and others, 2016; Brocklehusrt and Whipple, 2002; Egholm and others, 2011b, 2012, 2009; Herman and others, 2011; Herman and Braun, 2008; Pedersen and Egholm, 2013; Tomkin and Braun, 2002; Ugelvig and others, 2016), although subglacial hydrology is rarely

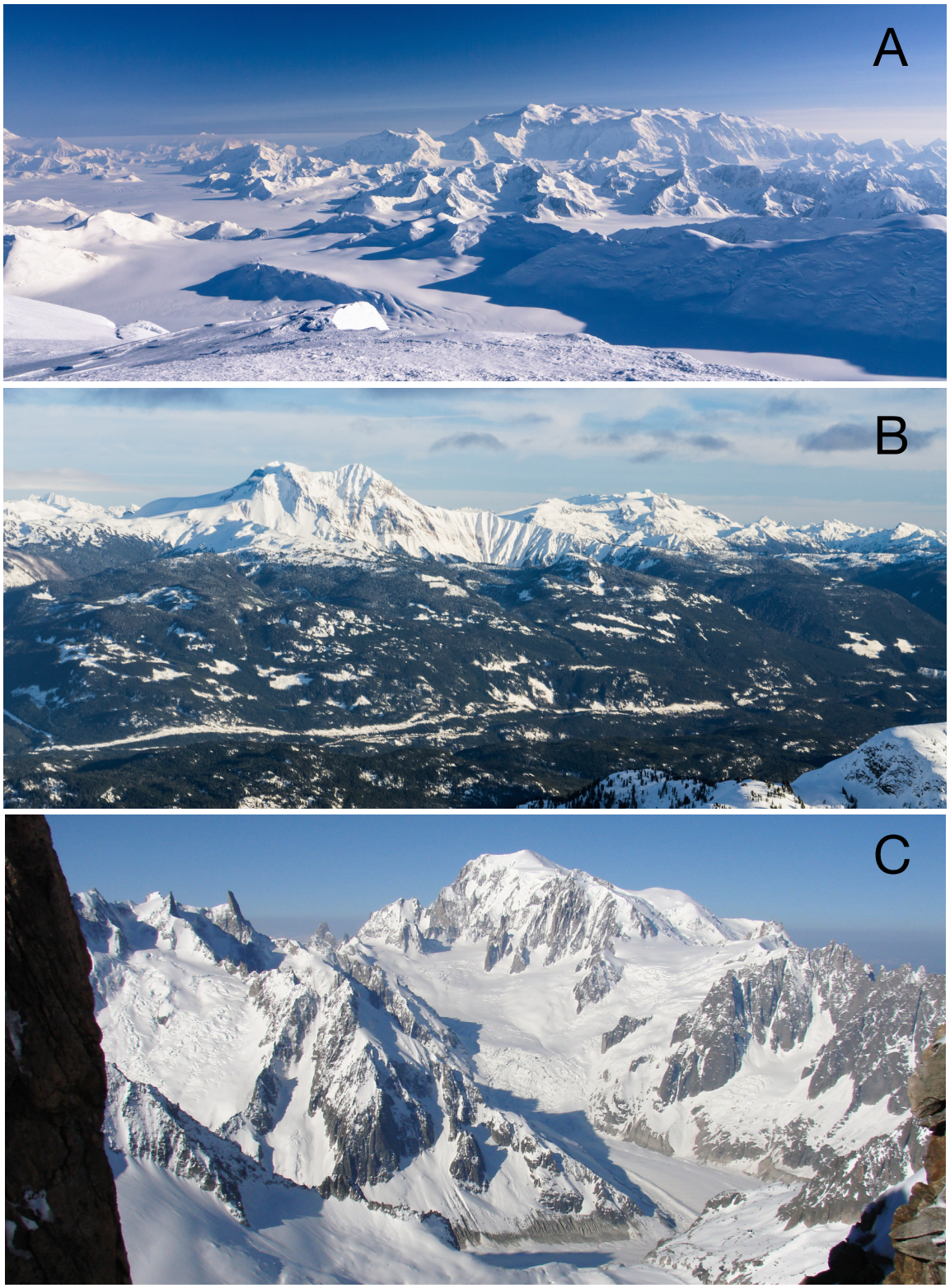

Figure 1.3: *(Caption continued on the following page.)*

Figure 1.3: *(Continued caption)* Different reliefs that are typical of glacial landscapes. These pictures highlight the distribution of elevation in glaciated mountain landscapes, the peaks and ridges are narrow and represent a limited fraction of the areal cover. (A) View looking south towards Mount Logan (5959 m a.s.l., $\sim$ 60 km away from photographer.) from a shoulder next to Mount Steele, St. Elias Mountains, Yukon Territory. The maximum elevation difference is larger than 3500 m. (B) View looking east towards Mount Garibaldi (2678 m a.s.l.) from Pelion Mountain, Coast Mountains, British Columbia. Mount Garibaldi is $\sim$ 25 km away from the photographer and the maximum elevation difference is $\sim$ 2500m. (C) View looking south-west towards Mont Blanc (4810 m a.s.l.) from the south col of les Droites, Mont Blanc massif, France. Mont Blanc is $\sim$ 15 km away from the photographer and the maximum elevation difference is larger than 2500 m.

considered (Egholm and others, 2012; Herman and others, 2011; Ugelvig and others, 2016). Exploring how subglacial hydrology affects erosion patterns to inform the assumptions made in landscape evolution studies is the purpose of Chapter 2. In addition, quantifications of glacial erosion rates over time spans of up to several decades are predominantly derived from measurements of proglacial sediment yields. These sediment yields are driven by water-born subglacial sediment transport, the mechanisms of which are poorly understood. The framework for sediment transport in R-channels proposed in Chapter 5 contributes to refining the interpretation of sediment yields.

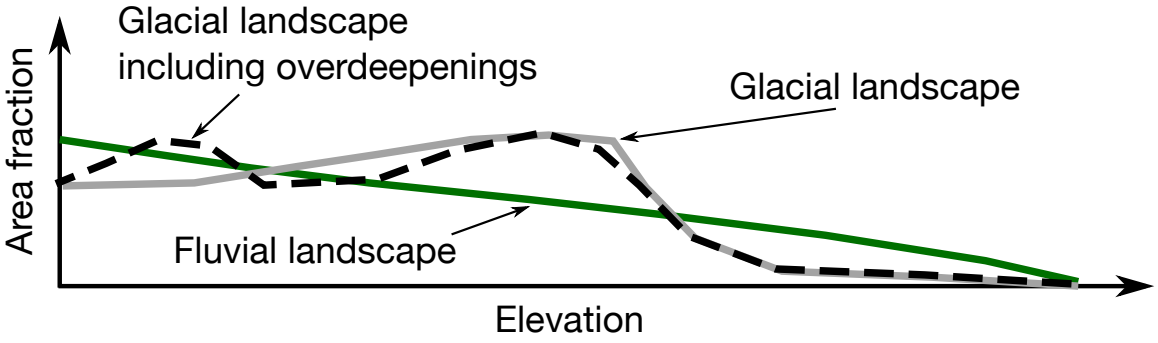

Figure 1.4: Conceptual figure of hypsometry of different landscapes. In glacial landscapes the hypsometric maximum is thought to correlate with the elevation of the ELA. When the bedrock elevation, rather than present day surface, is taken into account another local hypsometric maximum appears where large overdeepenings are present (Dürst-Stucki and Schlunegger, 2013; Herman and others, 2011).

A global increase in denudation rates was first inferred from increased marine sediment deposition (Molnar and England, 1990; Zhang and others, 2001) and such trend is confirmed by thermochronometers showing enhanced exhumation over the past 2–4 Ma (e.g. Herman and others, 2013; Herman and Champagnac, 2016). Some authors argue, however, that such an erosion increase is an artefact due to measurement bias and the increase in

measurement resolution as time approaches the present (Willenbring and Jerolmack, 2016). Willenbring and Jerolmack (2016) suggest that global erosion and sediment deposition rates have remained virtually constant over the past 10 Ma. Although Willenbring and Jerolmack (2016) successfully highlight the potential importance of this measurement bias for sediment deposition and the use of thermochronometers, they fail to quantify its importance in particular regarding Herman and others's (2013) calculation of exhumation rates. A much more detailed discussion of the question can be found in two debate articles Herman and Champagnac (2016) and Willenbring and Jerolmack (2016).

A number of studies support the hypothesis that climate, by enabling glacial erosion, can control the mean elevation of a mountain range regardless of tectonic forces through a mechanism termed "glacial buzzsaw" (e.g. Brocklehusrt and Whipple, 2002; Brozovic and others, 1997; Egholm and others, 2009; Mitchell and Montgomery, 2006). In mid- to low- latitude mountain ranges (e.g. Andes except Patagonia, New Zealand Alps, Himalayas, Cascades, Sierra Nevada) a correlation exists between the distribution of topography and the elevation of the equilibrium line altitude (ELA). The hypsometry, frequency distribution of elevation bins, typical of glacial erosion is different from that of a fluvial landscape (Fig. 1.4). A fluvial landscape will have an increasing area fraction with decreasing elevation, whereas a glacial landscape will show a maximum area fraction at mid-elevations (Fig. 1.4). The ELA is the altitude of the transition between a glacier accumulation (net ice gain), and ablation (net ice loss) areas. At the end of the melt-season the ELA coincides with the snow line, and following theories of glacier flow (Cuffey and Paterson, 2010) the ELA is the location of maximum ice flux. The fact that the hypsometric maximums for glacial landscapes occurs just below present-day areally-averaged ELAs, and several hundred metres above the ELAs of the last glacial maximum, has led to the conjecture that glacial erosion is most efficient around and above the ELA (e.g. Brocklehusrt and Whipple, 2002; Brozovic and others, 1997; Egholm and others, 2009; Mitchell and Montgomery, 2006). Peaks and ridges spared by such dramatic erosion undergo uplift at least due to isostatic adjustment and become particularly elevated (e.g. Nanga Parbat; Brozovic and others, 1997). Fox and others (2015) show that the rate of rock uplift in two regions of the Alps is significantly different because of tectonic processes. The mean elevations of these areas, however, are very similar, suggesting a climatic control on topography. The idea of a "glacial buzzsaw" has been confirmed by numerical modelling (e.g. Brocklehusrt and Whipple, 2002; Egholm and others, 2009; Pedersen and Egholm, 2013), in which glacial erosion is assumed proportional to sliding speed; given the configuration of theses models, the greatest sliding speeds are expected around the ELA. The realism of such modelled distributions of erosion rates might be questionable, as hydrology-enhanced sliding and erosion tend to occur downstream of the ELA (e.g. Beaud and others, 2014; Herman and others, 2011, 2015, see also Chapter 2). I further discuss this point in Chapter 6.

In opposition to the buzzsaw, glaciers can shield topography if they are frozen to their beds (e.g. Ferraccioli and others, 2011; Thomson and others, 2010; Tomkin and Braun, 2002; Ward and others, 2012). Glacial erosion rates have been shown to decrease with increasing latitude (Herman and Brandon, 2015; Koppes and others, 2015; Thomson and others, 2010). This shows the difficulty to generalize the effect of glaciation on the landscape, and highlights that erosion rate gradients that are observed at present due to longitudinal changes could be expected through time during a glacial cycle.

Erosion rates measured over the past several decades suggest that glacial erosion tends to be faster than fluvial erosion, yet this may not hold over longer time periods (Koppes and Montgomery, 2009). It is very likely that glaciations have lead to an increase in erosion rates and relief formation. Landscapes resulting from glacial or fluvial action show significantly different hypsometries, and it has been recognized that disequilibrium between a landscape and a dominant erosion mechanism will yield particularly high erosion rates (e.g. Champagnac and others, 2009; Church and Ryder, 1972; Pedersen and Egholm, 2013). It is thus likely that enhanced global erosion rates could be the result of a switch between glacial and interglacial conditions, rather than the action of glaciers alone. A necessary piece required to solve the conundrum of the effect of glacial action on the landscape will therefore be that we gain a better understanding of the processes of glacial erosion and their drivers.

1.5 Research objectives and questions

Subglacial hydrology has both a direct and indirect effect on glacial erosion. The indirect effect is that the type and morphology of the subglacial drainage system are amongst the main drivers of conditions at the ice–bed interface. These conditions control the processes of glacial erosion, yet studies of the indirect effects of subglacial hydrology on glacial erosion are rare despite being acknowledged as important. There is also a gap in the timescales that have been addressed. The studies in which abrasion and quarrying laws are proposed discuss the parameter space of such erosion rates (e.g. Hallet, 1979, 1981; Iverson, 2012), but these laws are used directly in landscape evolution models with little verification (e.g. Cohen and others, 2005; Iverson, 1990) or testing at timescales relevant to glacier processes (sub-daily to multi-annual). The field verification of individual erosion laws is extremely challenging and laboratory experiments are rare (Iverson, 1990; Mathews, 1979). An argument often used to validate erosion laws is the ability of numerical models to reproduce realistic glacial landscapes (e.g. Egholm and others, 2011b, 2012; Harbor and others, 1988; Harbor, 1992; Herman and others, 2011; Kessler and others, 2008; MacGregor and others, 2000, 2009; Tomkin and Braun, 2002). Although this reproducibility is clear, alone it remains too weak to show that processes of erosion are adequately captured.

Numerical modelling is a tool of choice to study glacial erosion processes and their spatio-temporal evolution. Recent developments in numerical models of (1) subglacial water flow (e.g. Flowers, 2008; Hewitt, 2011; Schoof, 2010; Werder and others, 2013), (2) ice flow (e.g. Blatter, 1995; Egholm and others, 2011a), (3) basal sliding (e.g. Gagliardini and others, 2007; Schoof, 2005), (4) the interactions between subglacial hydrology, sliding and ice flow (e.g. Hewitt, 2013; Pimentel and others, 2010; Pimentel and Flowers, 2011), (5) fluvial erosion (e.g. Chatanantavet and Parker, 2009; Lamb and others, 2008a; Sklar and Dietrich, 2004) and (6) fluvial sediment transport in mixed bedrock / alluvial channels (e.g. Inoue and others, 2014; Nelson and Seminara, 2012; Zhang and others, 2015) made available the components necessary to assemble numerical models capable of exploring processes of glacial erosion.

My approach is that of process-based numerical modelling at sub-seasonal to annual timescales to explore how subglacial hydrology directly and indirectly drives glacial erosion, to address the following questions. (1) What are the indirect effects of subglacial hydrology on abrasion and quarrying patterns? (Chapter 2) (2) How important is the direct effect of subglacial hydrology on bedrock erosion? (Chapters 3 and 4) (3) What are the dynamics of sediment transport in a channelized drainage system over a hard bed? (Chapter 5)

In Chapter 2 (see also Beaud and others, 2014), I use a numerical model of coupled ice and water flow to test the effect of transient subglacial hydrology and the choice of sliding law on patterns of erosion by abrasion and quarrying. In Chapter 3 (see also Beaud and others, 2016), I assemble the first process-based model of bedrock erosion by subglacial water flow and discuss the implications for overall glacial erosion and subglacial landform formation. In Chapter 4, I use the model from Chapter 3 with a simple model of ice flow to investigate the formation of tunnel valleys and inner gorges over a glacial cycle. In Chapter 5, I develop the first model of morphodynamics in R-channels suited for both bedrock and alluvial bed conditions. Sediment fluxes can thus be modelled which provides with tools to discuss esker formation and some underlying assumptions made in interpreting proglacial sediment yields. Finally, in Chapter 6, the results from Chapters 2–5 are summarized and the three research questions addressed. I further explain how the work presented impacts our current understanding of glacial erosion processes, the implications of the work for landform genesis and landscape evolution and how to incorporate these findings into future work.

Chapter 2

Seasonal-scale abrasion and quarrying patterns from a two-dimensional ice-flow model coupled to distributed and channelized subglacial drainage

Abstract

Field data and numerical modelling show that glaciations have the potential either to enhance relief or to dampen topography. We aim to model the effect of the subglacial hydraulic system on spatiotemporal patterns of glacial erosion by abrasion and quarrying on time scales commensurate with drainage system fluctuations (e.g., seasonal to annual). We use a numerical model that incorporates a dual-morphology subglacial drainage system coupled to a higher-order ice-flow model and process-specific erosion laws. The subglacial drainage system allows for a dynamic transition between two morphologies: the distributed system, characterized by an increase in basal water pressure with discharge, and the channelized system, which exhibits a decrease in equilibrium water pressure with increasing discharge. We apply the model to a simple synthetic glacier geometry, drive it with prescribed meltwater input variations, and compute sliding and erosion rates over a seasonal cycle. When both the distributed and channelized systems are included, abrasion and sliding maxima migrate $\sim 20\%$ up-glacier compared to simulations with distributed drainage only. Power-law sliding generally yields to a broader response of abrasion to water pressure changes along the flowline compared to Coulomb-friction sliding. Multi-day variations in meltwater input elicit a stronger abrasion response than either diurnal- or seasonal variations alone for the

same total input volume. An increase in water input volume leads to increased abrasion. We find that ice thickness commensurate with ice sheet outlet glaciers can hinder the up-glacier migration of abrasion. Quarrying patterns computed with a recently published law differ markedly from calculated abrasion patterns, with effective pressure being a stronger determinant than sliding speeds of quarrying rates. These variations in calculated patterns of instantaneous erosion as a function of hydrology-, sliding-, and erosion- model formulation, as well as model forcing, may lead to significant differences in predicted topographic profiles on long time scales.

2.1 Introduction

Erosion rates measured or inferred in highly glaciated catchments vary over four to five orders of magnitude (Hallet and others, 1996; Koppes and Montgomery, 2009). Accordingly, glaciated environments can be highly erosive (e.g., Molnar and England, 1990; Hallet and others, 1996; Shuster and others, 2005; Valla and others, 2011) or can protect the pre-glacial landscape (e.g., Thomson and others, 2010; Ferraccioli and others, 2011). Since the Pliocene, most mountain ranges worldwide have undergone large modifications because of the action of glaciers and ice sheets. The extent and rate of these modifications is still highly debated, however (e.g., Molnar and England, 1990; Brozovic and others, 1997; Koppes and Montgomery, 2009; Herman and others, 2010; Montgomery and Korup, 2010; Thomson and others, 2010; Steer and others, 2012). The formation of large erosional features (greater than kilometre-scale, e.g., overdeepenings and tunnel valleys) is still poorly explained, although recent comprehensive descriptions of such features (Dürst-Stucki and others, 2010; Preusser and others, 2010; Cook and Swift, 2012) support the original hypothesis that subglacial water is a key control on the initiation and evolution of an overdeepening (Hooke, 1991) or a tunnel valley (Dürst-Stucki and others, 2010). Using a numerical model of coupled ice and water flow (Pimentel and Flowers, 2011) and equipped with erosion laws (Hallet, 1979; Iverson, 2012), we make a preliminary assessment of the relative rates and patterns of glacial erosion on subseasonal to annual time scales.

It is well established that glaciers and ice sheets erode through three main mechanisms: abrasion, quarrying (or plucking), and the action of subglacial streams (e.g., Boulton, 1974, 1979; Hallet, 1979; Alley and others, 1997; Cohen and others, 2006). Abrasion takes place when clasts dragged by the overriding ice carve grooves in the bedrock. This process is controlled primarily by the sliding velocity (Hallet, 1979). Quarrying results from the lee-side failure of bedrock obstacles caused by stress gradients imparted by sliding (e.g., Iverson, 1991; Hallet, 1996). When ice overrides an obstacle, a lee-side cavity can form and the deviatoric stresses in the bedrock increase on the stoss side. This stress gradient can be accentuated by water pressure fluctuations in the cavity. Increasing water pressure enlarges the cavity, by lifting the roof and by enhancing sliding, thus reducing the contact

area; when the water pressure drops, local deviatoric stresses in the bed then increase dramatically (Iverson, 1991; Hallet, 1996; Cohen and others, 2006). If, in addition, cracks are present on the stoss side or top of the obstacle, the obstacle will experience fatigue and may eventually fracture. A positive feedback can arise if the cracks are sufficiently small that their hydraulic conductivity is low compared to that of the subglacial drainage system. In such a case, cracks can sustain high water pressures even when the cavity is drained, enhancing the fatigue of the step (Iverson, 1991; Cohen and others, 2006).

The role of subglacial streams is often treated as being limited to flushing sediments from the ice–bedrock interface (e.g., Humphrey and Raymond, 1994; Alley and others, 1997; Riihimaki and others, 2005). These streams, however, are known to have a significant effect on the dissolution of highly water-soluble bedrock (Walder and Hallet, 1979). Moreover, they may have an even greater erosive power and higher flushing efficiency than subaerial rivers owing to the high water pressures that can be achieved subglacially (Alley and others, 1997). Creyts and others (2013) apply sediment transport equations to a subglacial drainage system formulated as a macroporous sheet (Creyts and Schoof, 2009) and show that strong diurnal cycles in water input enhance sediment transport efficiency. Despite the potential importance of subglacial streams to overall glacial erosion, we reserve their treatment for future study and focus exclusively on abrasion and quarrying here.

To date, studies employing numerical models of glacial erosion almost exclusively use the abrasion law developed by Hallet (1979), in which the abrasion rate is proportional to the sliding velocity raised to a power equal to or greater than one (e.g., MacGregor and others, 2000; Tomkin and Braun, 2002; Anderson, 2005; Herman and Braun, 2008; Egholm and others, 2009). Some efforts have been made to add a parameterization of the bedrock slope to the aforementioned law in order to simulate quarrying (e.g., MacGregor and others, 2009; Egholm and others, 2012), but few studies include a process-based plucking law (e.g., Hildes and others, 2004). In nearly all the literature, therefore, both abrasion and quarrying are proportional to sliding speed.

Sliding of an ice mass is highly influenced by the basal water pressure (e.g., Müller and Iken, 1973; Lliboutry, 1976; Iken, 1981), which in turn is jointly controlled by the rate of water influx to the bed and the morphology of the drainage system (e.g., Iken, 1981; Nienow and others, 1998). When the drainage system is 'distributed' (e.g., Fountain and Walder, 1998), water flow is relatively slow and the water pressure rises with increasing input. Different formulations have been proposed to describe a distributed drainage system, including flow through subglacial till (e.g., Clarke, 1987), a network of linked cavities (e.g., Lliboutry, 1976; Kamb, 1987) or a macroporous sheet with laminar (e.g., Flowers and Clarke, 2002) or turbulent flow (e.g., Creyts and Schoof, 2009). In contrast, a 'channelized' drainage system transports water through a network of Röthlisberger (R)-channels, Nye (N)-channels, or canals (Röthlisberger, 1972; Nye, 1976; Walder and Fowler, 1994). The most commonly used conceptual model is that of a network of R-channels, which at equilibrium exhibits a

decrease in water pressure with increasing discharge. The transition between the distributed and channelized drainage systems is responsible for the up-glacier migration and eventual termination of the 'spring speed-up event' observed at the onset of the melt season in many glaciers (e.g., Iken and Bindschadler, 1986; Mair and others, 2003; Anderson and others, 2004; Bartholomaus and others, 2007; Fischer and others, 2011).

Numerical modelling of the dynamic transition between distributed and channelized subglacial drainage systems is still nascent (Flowers and others, 2004; Kessler and Anderson, 2004; Flowers, 2008; Schoof, 2010; Pimentel and Flowers, 2011; Hewitt and others, 2012; Hewitt, 2013; Werder and others, 2013) with the coupling to ice flow rarely included (c.f. Arnold and Sharp, 2002; Flowers and others, 2011; Pimentel and Flowers, 2011; Hewitt, 2013). Attempts to include the role of subglacial hydrology in erosion models have thus far been limited to treatments of distributed drainage (MacGregor and others, 2009; Herman and others, 2011; Egholm and others, 2012), largely because of the complexity of combining drainage system types and the computational burden of representing processes varying on highly disparate time scales. However, the models above have been successful in demonstrating a role for hydrology in the formation of overdeepenings (Herman and others, 2011; Egholm and others, 2012) as originally suggested by Hooke (1991), even with simple representations of the drainage system.

Here we take a first step in exploring the potential influence of a dual-morphology subglacial drainage system on modelled patterns of glacial erosion. We employ the hydrologically coupled, two-dimensional model of Pimentel and Flowers (2011) — which integrates a higher-order flowband representation of ice dynamics (Blatter, 1995; Pattyn, 2002) — with distributed and channelized subglacial drainage (Flowers, 2008). The model returns the sliding and water pressure patterns, which enable us to calculate erosion rates through process-specific laws: abrasion as formulated by Hallet (1979) and quarrying as recently derived by Iverson (2012). We restrict our investigation to examining instantaneous erosion rates with a stationary glacier geometry in order to isolate the influence of the melt season and glacier hydrology on seasonal patterns of erosion. In a first set of experiments, we explore the influence of the representation of basal drainage and sliding on calculated erosion by comparing (i) distributed-only to distributed and channelized drainage systems, and (ii) Coulomb-friction sliding to power-law (Weertman-type) sliding. In a second set of experiments, we examine the model response to changes in the frequency, amplitude, and total volume of meltwater forcing, with the aim of determining whether subannual fluctuations in glacier hydrology and dynamics are important for erosion modelling (c.f. Herman and others, 2011). We also touch on the role of glacier size to highlight differences between glacier– versus ice sheet–scale problems.

2.2 Methods

Model governing equations for ice dynamics and subglacial drainage are presented below, including boundary and initial conditions, followed by the implementation of erosion laws in the model. The strategy is then outlined to define the model tests.

2.2.1 Ice and water flow

Ice flow

Egholm and others (2011b) demonstrated the importance of the implementation of membrane stresses (lateral and longitudinal) in modelling the flow and erosion of valley glaciers. The implementation of subglacial hydrology can lead to large gradients in effective pressure and, thus, sliding velocity (e.g., Pimentel and Flowers, 2011), reinforcing the need for membrane stresses. Accordingly, we use the common Stokes flow approximation from Blatter (1995) and Pattyn (2002) rather than the extensively used 'shallow-ice approximation'. Readers interested in the model details are referred to Pimentel and Flowers (2011) and Pimentel and others (2010). The conceptual model for ice and water flow is illustrated in Fig. 2.1, with variables defined in Table 2.1.

Writing the momentum balance according to Blatter's (1995) model, i.e., assuming cryostatic conditions, the acceleration term and the vertical stress gradients can be neglected. Including a parameterization of lateral drag (Pimentel and others, 2010; Pimentel and Flowers, 2011), the horizontal stress balance can be written

$$4\frac{\partial}{\partial x}\left(\nu\frac{\partial u}{\partial x}\right)+2\frac{\partial}{\partial x}\left(\frac{\nu u_{\mathrm{L}}}{W}\frac{\partial W}{\partial x}\right)+\frac{\partial}{\partial z}\left(\nu\frac{\partial u}{\partial z}\right)-\frac{\nu\left(u-u_{\mathrm{L}}\right)}{W^{2}}=\rho_{\mathrm{i}}g\frac{\partial h_{\mathrm{i}}}{\partial x} \tag{2.1}$$

with $u=u(x,z)$ the horizontal velocity, $u_{\mathrm{L}}=u_{\mathrm{L}}(x,z)$ the velocity along the valley walls, W the flow unit half-width, $h_{\mathrm{i}}(x)$ the ice thickness, ρ_{i} the density of ice, g the acceleration caused by gravity, and x and z (respectively) the horizontal and vertical coordinates. The strain-rate-dependent viscosity $\nu(x,z)$ is

$$\begin{aligned}\nu=\frac{1}{2}A^{-1/n}\Bigg[&\left(\frac{\partial u}{\partial x}\right)^{2}+\left(\frac{u_{\mathrm{L}}}{W}\frac{\partial W}{\partial x}\right)^{2}+\frac{u_{\mathrm{L}}}{W}\frac{\partial u}{\partial x}\frac{\partial W}{\partial x}\\&+\frac{1}{4}\left(\frac{\partial u}{\partial z}\right)^{2}+\frac{1}{4}\left(\frac{u-u_{\mathrm{L}}}{W}\right)^{2}+\dot{\epsilon}_{0}^{2}\Bigg]^{(1-n)/2n}\end{aligned} \tag{2.2}$$

where A is the flow law coefficient, $n=3$ the flow law exponent (Glen, 1955), and $\dot{\epsilon}_0$ a constant to prevent vanishing strain rates at the surface (Meier, 1958). A no-stress boundary condition is applied at the ice surface and a Coulomb-friction (Schoof, 2005; Gagliardini and others, 2007) sliding law forms the basal boundary condition.

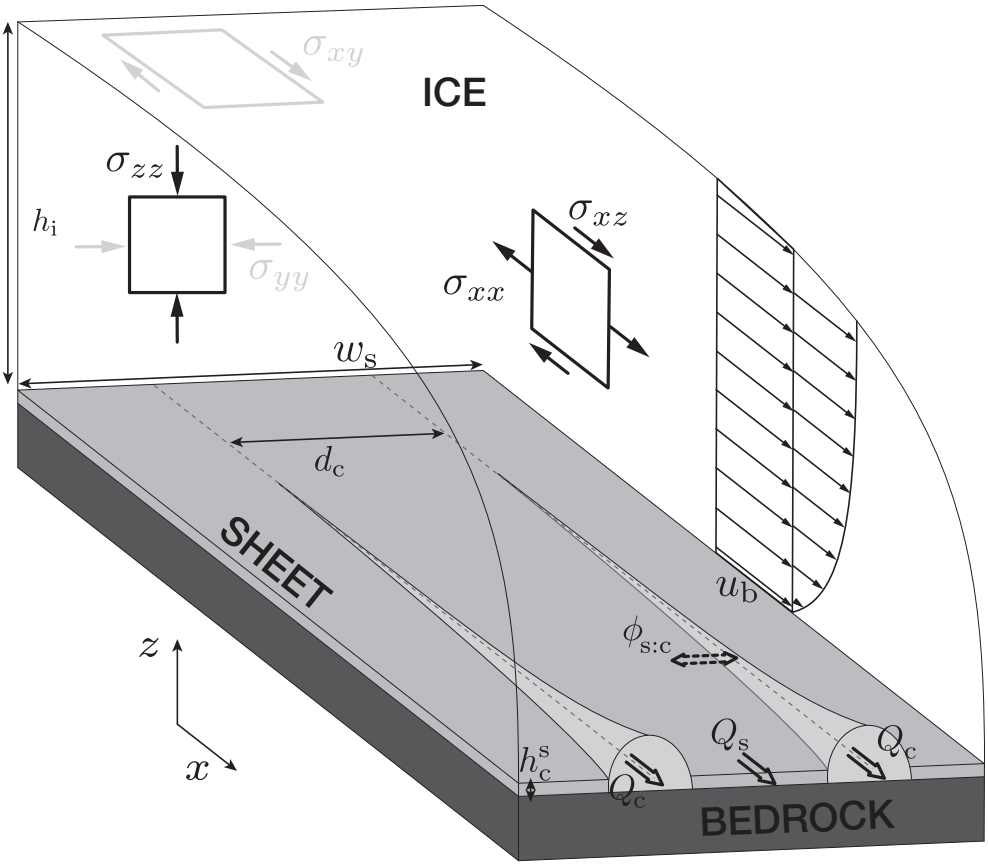

Figure 2.1: Conceptual model for ice and water flow (modified from Flowers, 2008). The distributed drainage system is represented by a macroporous sheet of critical thickness h_c^s and width w_s carrying a discharge $Q_\mathrm{s} = q_\mathrm{s} w_\mathrm{s}$. The channelized system is represented by a system of parallel semi-circular R-channels with a latent spacing d_c and each carrying a discharge Q_c. The exchange rate between sheet and channels is $\phi_{\mathrm{s:c}}$. Broken lines in the upper part of the bed represent incipient channels whose cross-sectional area corresponds to the vestigial size S_ϵ. The glacier has a thickness $h_\mathrm{i}(x)$, and ice flow includes basal sliding u_b and deformation. Stresses included in the momentum balance are shown in black (σ_{xx}, σ_{xz}, and σ_{zz}) and those resulting from the parametrization of the lateral extent in grey (σ_{yy} and σ_{xy}).

Table 2.1: Model variables

Symbols	Names	Units
General		
h_i	Ice thickness	m
N	Effective pressure	Pa
p_i	Ice overburden pressure	Pa
t	Time	s
x	Horizontal coordinate	m
z	Vertical coordinate	m
z_b	Elevation of glacier bed	m
z_s	Elevation of glacier surface	m
Ice		
A_s	Ice flow law coefficient corrected for bed roughness	$\mathrm{Pa}^{-3}\,\mathrm{s}^{-1}$
u	Horizontal velocity	$\mathrm{m\,a}^{-1}$
u_b	Sliding velocity	$\mathrm{m\,a}^{-1}$
n_i	Unit vector normal to the surface	-
ν	Strain rate-dependent viscosity of ice	$\mathrm{Pa\,s}$
τ_b	Basal shear stress	Pa
σ_{ij}	Stress tensor	Pa
σ_n	Bed-normal stress	Pa
Water		
$\dot{b_\mathrm{s}}$	Source term to sheet system	$\mathrm{m\,s}^{-1}$
$\dot{b_\mathrm{c}}$	Source term to channel system	$\mathrm{m\,s}^{-1}$
f_R	Darcy-Weisbach roughness coefficient	$\mathrm{m}^{2/3}\,\mathrm{s}^{-2}$
h_s	Water-sheet thickness	m
$h_\mathrm{s:c}$	Water-sheet thickness at sheet-channel interface	m
p_c	Water pressure in channels	Pa
p_s	Water pressure in the sheet	Pa
$p_\mathrm{s:c}$	Water pressure at sheet-channel interface	Pa
P_w	Wetted perimeter of channels	m
q_s	Water flux in the sheet	$\mathrm{m}^2\,\mathrm{s}^{-1}$
Q_c	Channel discharge	$\mathrm{m}^3\,\mathrm{s}^{-1}$
R_c	Channel radius	m
R_H	Hydraulic radius of channels	m
S	Channel cross-sectional area	m^2
$\phi_\mathrm{s:c}$	Sheet–channel water exchange rate	$\mathrm{m\,s}^{-1}$
ψ_c	Fluid potential in channels	Pa
ψ_s	Fluid potential in the sheet	Pa
Erosion		
$\dot{e_\mathrm{a}}$	Abrasion rate	$\mathrm{m\,a}^{-1}$
$\dot{e_\mathrm{q}}$	Quarrying rate	$\mathrm{m\,a}^{-1}$
F	Contact force between a clast and bedrock	Pa
$\mathscr{P}$	Probability of bedrock step failure	-
s_bc	Length of basal cavities	m
$\varepsilon_{\dot{e}_\mathrm{a}}$	Excess of abrasion due to the melt-season	-
σ'_bed	Deviatoric stress in the bed	Pa

Table 2.2: Model constants and parameters

Symbols	Names	Values	Units
General			
n	Glen's flow law exponent	3	-
ρ_{w}	Water density	1000	$\mathrm{kg\,m^{-3}}$
ρ_{i}	Ice density	910	$\mathrm{kg\,m^{-3}}$
A	Ice flow law coefficient	2.4×10^{-24}	$\mathrm{Pa^{-3}\,s^{-1}}$
$h_{\xi_{\mathrm{f}}}$	Horizontal grid cell length	200–1000	m
W	Flow band half-width	0.5–1.0	km
y_{s}	Number of seconds in one year	31556926	$\mathrm{s\,a^{-1}}$
Ice			
C	Bed roughness constant	$0.84 \times m_{\max}$	-
C_{s}	Power law sliding constant	2.5×10^{-9}	$\mathrm{m\,a^{-1}\,Pa^{-p+q}}$
$m_{\max}$	Maximum slope of bed asperities	0.25–0.45	-
r	Roughness of the bed	0.04–0.07	-
u_{L}	Horizontal velocity along valley walls	0	$\mathrm{m\,a^{-1}}$
$\dot{\epsilon}_0$	Constant for vanishing strain rates	10^{-30}	$\mathrm{a^{-1}}$
$\lambda_{\max}$	Specific wavelength of the bed	8–12	m
Water			
c_{t}	Pressure melting coefficient	9.8×10^{-8}	$\mathrm{K\,Pa^{-1}}$
c_{w}	Specific heat capacity of water	4.22×10^{3}	$\mathrm{J\,kg^{-1}\,K^{-1}}$
d_{c}	Latent channel spacing	1–2	km
$h_{\mathrm{c}}^{\mathrm{s}}$	Critical sheet thickness	0.35–2.0	m
K_{s}	Hydraulic conductivity	0.027–0.07	$\mathrm{m\,s^{-1}}$
L	Latent heat of fusion	3.35×10^{5}	$\mathrm{J\,kg^{-1}}$
n'	Manning roughness of channel	0.032	Pa
q	Water pressure exponent	7/2	-
Q_{G}	Geothermal flux	0.07	$\mathrm{W\,m^{-2}}$
S_{ϵ}	Vestigial cross-sectional area	2×10^{-2}	$\mathrm{m^2}$
w_{s}	Width of the sheet	1–2	km
δ_{H}	Hydrology time step	600	s
γ	Numerical compressibility parameter	10^{-9}	$\mathrm{Pa^{-1}}$
$\chi_{\mathrm{s:c}}$	Sheet-channel coupling coefficient	1	-
Erosion			
B	Viscosity parameter ($B = A^{-1/n}$)	73.3×10^{6}	$\mathrm{Pa\,s^{1/3}}$
c	Scaling factor	0.1	-
C_{a}	Abrasion scaling constant	5×10^{-5}	$\mathrm{m^{1-l}\,a^{l-1}}$
h_{bs}	Height of bedrock step	0.1–2.0	m
l	Abrasion law exponent	1–3	-
l_{bs}	Length of bedrock step	1–20	m
m	Quarrying law exponent	3	-
V_0	Characteristic rock volume	10	$\mathrm{m^3\,m^{-1}}$
α	Empirical exponent for the contact force F	-	-
σ_0	Weibull scale parameter	10	MPa
σ_{n}^{*}	Stress threshold for ice crushing	10	MPa
κ	Weighting factor	0.33	-

In the sliding law initially suggested by Weertman (1964) and later corrected for effective pressure (here defined as the ice overburden pressure minus the water pressure: $N = p_\mathrm{i} - p_\mathrm{s}$) (e.g., Budd and others, 1979; Bindschadler, 1983), the sliding velocity is proportional to the basal shear stress τ_b and the inverse of the effective pressure:

$$u_\mathrm{b} = C_\mathrm{s} {\tau_\mathrm{b}}^p / N^q \tag{2.3}$$

where C_s, p, and q are empirical constants. When using this 'Weertman-type' law to describe sliding, along with a model of subglacial hydrology, two issues arise: (i) $u_\mathrm{b} \to \infty$ when $N \to 0$ leading to a singularity, and (ii) τ_b increases monotonically with u_b (c.f. Iken, 1981). To prevent this monotonic increase in τ_b, one can use a regularized Coulomb-friction law (Schoof, 2005; Gagliardini and others, 2007):

$$\tau_\mathrm{b} = C \left(\frac{u_\mathrm{b}}{u_\mathrm{b} + C^n N^n A_\mathrm{s}} \right)^{1/n} N \tag{2.4}$$

with $C = 0.84 \times m_\mathrm{max}$ a constant related to bed roughness, m_max the maximum slope of a bed obstacle, and A_s Glen's flow law parameter corrected for the shape of bedrock obstacles (Gagliardini and others, 2007):

$$A_\mathrm{s} = A \lambda_\mathrm{max} \frac{-0.00002 + 0.013r + 0.0262r^2}{r^2}. \tag{2.5}$$

Here λ_max and r are, respectively, the wavelength and roughness of the bed and are prescribed in the model. The use of such a law is motivated by the fact that the maximum theoretical resistance produced by the bed, and hence the maximum shear stress, is dictated by the maximum slope of bedrock obstacles. When sliding speed and water pressure are sufficiently high, cavities form on the lee side of bedrock obstacles. With enhanced water pressure, cavities grow until a threshold is reached where they engulf the maximum slopes of bed obstacles. This then leads to a decrease in basal shear stress while the sliding speed continues to rise.

Water flow

The conceptual model of water flow is illustrated in Fig. 2.1. Water flow through the channelized drainage system is assumed to occur in saturated R-channels (Röthlisberger, 1972; Nye, 1976). Discharge in an individual channel is given by (Röthlisberger, 1972)

$$Q_\mathrm{c} = - \left(\frac{8S^3}{P_\mathrm{w} \rho_\mathrm{w} f_\mathrm{R}} \right)^{1/2} \frac{\partial \psi_\mathrm{c}}{\partial x} \left| \frac{\partial \psi_\mathrm{c}}{\partial x} \right|^{-1/2} \tag{2.6}$$

with S the channel cross-sectional area, $P_\mathrm{w} = (\pi + 2) R_\mathrm{c}$ the wetted perimeter, R_c the radius of the channel, $f_\mathrm{R} = 8gn'/R_\mathrm{H}^{1/3}$ the Darcy-Weisbach roughness as a function of the Manning

roughness n', $R_\mathrm{H} = \pi R_\mathrm{c}/(2\pi + 4)$ the hydraulic radius, x the coordinate along water flow, $\psi_\mathrm{c} = p_\mathrm{c} + \rho_\mathrm{w} g z_\mathrm{b}$ the fluid potential in the channel, p_c the water pressure in the channel, and $z_\mathrm{b}(x, y)$ the elevation of the bed. Röthlisberger channels open by melting of the channel walls and from close by ice creep (Röthlisberger, 1972). Their evolution in time is derived using the principle of mass conservation for water in the channels and ice and leads to the following partial differential equations for channel cross-sectional area S (Nye, 1976) and water pressure (Clarke, 2003):

$$\frac{\partial S}{\partial t} = -\frac{Q_\mathrm{c}}{\rho_\mathrm{i} L}\left(\frac{\partial \psi_\mathrm{c}}{\partial x} - c_\mathrm{t}\rho_\mathrm{w} c_\mathrm{w}\frac{\partial p_\mathrm{c}}{\partial x}\right) - 2AS\left(\frac{p_\mathrm{i} - p_\mathrm{c}}{n}\right)^n \tag{2.7}$$

and

$$\frac{\partial p_\mathrm{c}}{\partial t} = -\frac{1}{\gamma S}\left(\frac{\partial S}{\partial t} + \frac{\partial Q_\mathrm{c}}{\partial x} + \frac{Q_\mathrm{c}}{\rho_\mathrm{w} L}\left(\frac{\partial \psi_\mathrm{c}}{\partial x} - c_\mathrm{t}\rho_\mathrm{w} c_\mathrm{w}\frac{\partial p_\mathrm{c}}{\partial x}\right) - \left(\dot{b}_\mathrm{c} + \phi_\mathrm{s:c}\right)\right) \tag{2.8}$$

with L the latent heat of fusion of ice, c_t the pressure melting coefficient, c_w the heat capacity of water, A the flow law coefficient, n Glen's flow law exponent, γ a compressibility parameter to prevent numerical stiffness (Clarke, 2003), d_c a latent channel spacing, $\dot{b_\mathrm{c}}$ a source term directly to the channel system, and $\phi_\mathrm{s:c}$ a source term arising from the exchange between distributed and channelized drainage systems (elaborated below).

For distributed flow through a porous sheet (e.g., Flowers and Clarke, 2002; Creyts and Schoof, 2009) or through a network of cavities (e.g., Kamb, 1987; Schoof and others, 2012), mass continuity reads:

$$\frac{\partial h_\mathrm{s}}{\partial t} + \nabla \cdot \boldsymbol{q_\mathrm{s}} = \frac{Q_\mathrm{G}}{\rho_\mathrm{w} L} + \dot{b}_\mathrm{s} - \phi_\mathrm{s:c} \tag{2.9}$$

with h_s the areally averaged water volume or equivalent sheet thickness, $\boldsymbol{q_\mathrm{s}}$ the water flux through the sheet or cavity network, Q_G the geothermal flux, ρ_w the density of water, and $\dot{b_\mathrm{s}}$ a direct source term to the sheet.

Here we assume that water flows through a macroporous sheet with the flux described by (e.g., Clarke, 1996; Flowers and Clarke, 2002)

$$q_\mathrm{s} = -\frac{K_\mathrm{s} h_\mathrm{s}}{\rho_\mathrm{w} g}\frac{\partial \psi_\mathrm{s}}{\partial s} \tag{2.10}$$

with K_s the hydraulic conductivity of the sheet or cavity system, $\psi_\mathrm{s} = p_\mathrm{s} + \rho_\mathrm{w}\, g\, z_\mathrm{b}$ the fluid potential, and p_s the water pressure in the sheet. We adopt the sheet pressure parametrization of Flowers and Clarke (2002): $p_\mathrm{s} = p_\mathrm{i}\,(h_\mathrm{s}/h_\mathrm{c}^\mathrm{s})^k$, where p_i is the ice overburden pressure, h_c^s a critical sheet thickness, and k is an adjustable exponent. The coupling between the sheet and channel systems is expressed in terms of a rate of water exchange that depends on the fluid potential gradient between the two systems (e.g., Flowers, 2008):

$$\phi_\mathrm{s:c} = \chi_\mathrm{s:c}\frac{K_\mathrm{s:c}\, h_\mathrm{s:c}}{\rho_\mathrm{w}\, g\, {d_\mathrm{c}}^2}\,(p_\mathrm{s} - p_\mathrm{c}) \tag{2.11}$$

where $\chi_{\mathrm{s:c}}$ is a dimensionless sheet–channel coupling coefficient. The exchange of water is controlled by the transmissivity of the sheet–conduit interface $K_{\mathrm{s:c}}h_{\mathrm{s:c}}$. The conductivity at the interface is taken as that of the sheet ($K_{\mathrm{s:c}} = K_{\mathrm{s}}$), and the effective water thickness $h_{\mathrm{s:c}}$ is calculated by inverting the relation for $p_{\mathrm{s}}(h_{\mathrm{s}})$ above with $p_{\mathrm{s:c}} = \max(p_{\mathrm{s}}, p_{\mathrm{c}})$, leading to $h_{\mathrm{s:c}} = h_{\mathrm{c}}^{\mathrm{s}} \left(p_{\mathrm{s:c}}/(\rho_{\mathrm{i}} g h_{\mathrm{i}})\right)^{1/k}$. Variable $p_{\mathrm{s:c}}$ is taken as the larger, rather than the mean, of the sheet and channel water pressures because the mean value was found to introduce unrealistic bottlenecks in system exchange. Mass conservation in the system requires that the effective width w_{s} of the distributed system be specified, along with the channel density per unit width n_{c} or latent channel spacing $d_{\mathrm{c}} = 1/n_{\mathrm{c}}$. The treatment above permits different pressures in the distributed and channelized systems and parameterizes water exchange as a function of these pressure differences. In contrast, the finely resolved two-dimensional network structure of the channelized system in Hewitt (2013) and Werder and others (2013) motivates the enforcement of a uniform pressure between channel segments and the adjacent sheet. In their formulation of the numerical model (Hewitt, 2013; Werder and others, 2013), the exchange between sheet and channels need not be explicitly calculated as it is here.

Initial and boundary conditions

The basal boundary condition for ice flow $u_{\mathrm{b}}(x,t)$ is dictated by the Coulomb friction law (Eq. 2.4) (Schoof, 2005; Gagliardini and others, 2007), with no sliding permitted at the upstream end of the domain: $u_{\mathrm{b}}(x = 0, t) = 0$. At the ice surface a stress-free boundary is assumed $\sigma_{ij}(z = h_{\mathrm{i}}, t)n_j = 0$, where n_j is the unit vector. On the valley walls, a no slip condition is applied: $u_{\mathrm{L}}(x, z) = 0$. Glacier geometry, defined by bed elevation $z_{\mathrm{b}}(x)$ and ice thickness $h_{\mathrm{i}}(x)$, is prescribed and assumed not to change appreciably over the course of the annual simulations. Water pressure in the sheet and channels at the glacier terminus is atmospheric and approximated as $p_{\mathrm{s}}(x = L, t) = p_{\mathrm{c}}(x = L, t) = 0$. A no-flux condition is imposed on both the sheet and channel system at the up-stream boundary: $Q_{\mathrm{c}}(x = 0, t) = q_{\mathrm{s}}(x = 0, t) = 0$. At the up-stream boundary the pressure in the sheet and channel ($p_{\mathrm{s,c}}(x = 0, t)$) is free. We prescribe $\partial S/\partial x(x = L, t) = 0$ for channel cross-sectional area at the glacier terminus. The evolution of the subglacial drainage system and water pressure are sensitive to the system's initial state, in part defined by the prescribed incipient channel cross section S_ϵ. We therefore use a one-year spin-up for the hydrology model in which ice flow is decoupled from subglacial drainage prior to each coupled simulation. Model constants and parameters are listed in Table 2.2.

2.2.2 Erosion

Abrasion

We use the most common law for abrasion, developed by Hallet (1979), where the abrasion rate is written:

$$\dot{e}_{\mathrm{a}} = C_{\mathrm{a}} {u_{\mathrm{b}}}^{l} \tag{2.12}$$

where C_{a} serves to combine parameters such as clast and bedrock hardness and clast shape, u_{b} is the basal sliding speed, and l is an empirical exponent often set to 1 or 2 (e.g., Humphrey and Raymond, 1994; MacGregor and others, 2000; Tomkin and Braun, 2002; Anderson and others, 2006; Herman and Braun, 2008; Egholm and others, 2009; MacGregor and others, 2009; Egholm and others, 2011b; Herman and others, 2011; Egholm and others, 2012).

Quarrying

Following the adhesive wear theory, Iverson (2012) developed the following law for plucking:

$$\dot{e}_{\mathrm{q}} = \frac{u_{\mathrm{b}} \mathscr{P} h_{\mathrm{bs}}}{2 l_{\mathrm{bs}}} \left(1 - \frac{s_{\mathrm{bc}}}{l_{\mathrm{bs}}}\right) \tag{2.13}$$

where $\mathscr{P}$ describes the probability of failure of the bedrock step (below), h_{bs} is the step height, l_{bs} is the step wavelength and s_{bc} is the cavity length parametrized as (Iverson and Petersen, 2011)

$$s_{\mathrm{bc}} = 4 \left(\frac{u_{\mathrm{b}} h_{\mathrm{bs}}}{2\pi y_{\mathrm{s}}}\right)^{1/2} \left(\frac{B}{N}\right)^{n/2} \tag{2.14}$$

with the number of seconds per year y_{s}, the effective pressure at the ice–bed contact N, the viscosity parameter $B = A^{-1/n}$ in Glen's flow law and the flow law exponent n. The step failure probability $\mathscr{P}$ follows a Weibull distribution:

$$\mathscr{P} = 1 - \exp\left(-\frac{h_{\mathrm{bs}}(l_{\mathrm{bs}} - s_{\mathrm{bc}})}{V_0} \left(\frac{\sigma'_{\mathrm{bed}}}{\kappa \sigma_0}\right)^{m}\right) \tag{2.15}$$

with V_0 a characteristic rock volume large enough to contain the largest crack of the rock mass, σ_0 the Weibull scale parameter weighted by a factor κ, and m an exponent accounting for the homogeneity of the bed. The larger the value of m the more homogeneous the bedrock. The deviatoric stress in the bed σ'_{bed} is given by (Hallet, 1996; Iverson, 2012)

$$\sigma'_{\mathrm{bed}} = c\,(\sigma_{\mathrm{n}} - p_{\mathrm{s}}) = c\,N \left(\frac{1}{1 - s_{\mathrm{bc}}/l_{\mathrm{bs}}}\right) \tag{2.16}$$

where c is a scaling factor, $N\left(\frac{1}{1-s_{\mathrm{bc}}/l_{\mathrm{bs}}}\right) \leq \sigma^*_{\mathrm{n}}$, and σ^*_{n} is the stress threshold at which ice crushes. This parameterization requires the assumption that the stresses in the bed are

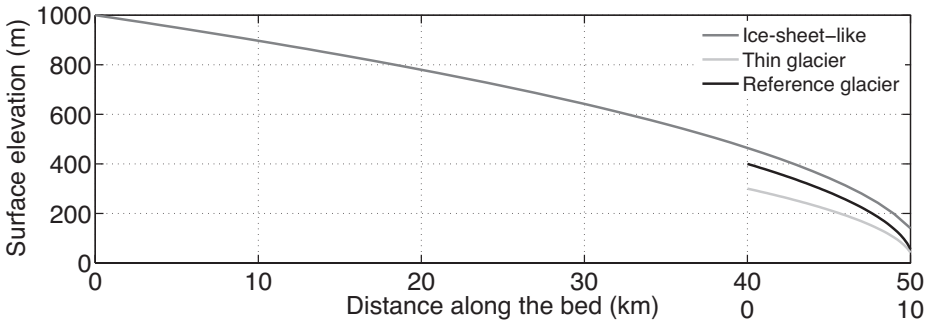

Figure 2.2: Parabolic ice geometries used in simulations. The reference geometry is shown in black (400 m maximum thickness, 10 km long), a thin glacier in light grey (300 m maximum thickness, 10 km long), and an ice sheet outlet-glacier in dark grey (1000 m maximum thickness, 50 km long).

averaged over the whole ice–bedrock contact area. Note that the deviatoric stress in the bed cannot be calculated directly from the ice model as bridging stresses are neglected (in making the cryostatic assumption) and the model is not resolved at the scale of individual cavities. A consequence of this law is the bounding of the quarrying $\dot{e}_{\mathrm{q}}$ for a given step size (Iverson, 2012). When a cavity grows to the point that it engulfs a given step, quarrying is prevented as the step becomes drowned.

Erosion law parameters

The value of the abrasion law exponent is usually taken as $l = 1$ (e.g., MacGregor and others, 2000; Herman and Braun, 2008; Egholm and others, 2009) or $l = 2$ (e.g., MacGregor and others, 2009; Egholm and others, 2012). Harbor (1992) suggested a range from 1 to 4, although he was considering a general erosion rule and not abrasion specifically. Hallet's (1979) model could be interpreted as taking $l = 2$ through the dependence of both particle flux and contact force on sliding speed. We use $l = 1$ for most of the simulations in order to be conservative in evaluating the influence of basal hydrology on modelled erosion. Following Iverson (2012), we present quarrying rates for bedrock steps that have a length-to-height ratio of 10. Although Iverson (2012) used statistical distributions of step sizes, we use five different step sizes that cover the same range of lengths (1-20 m). We set the exponent $m = 3$ in Eq. (2.15), the central value used in the tests by Iverson (2012). The erosion rate obtained for each step size is then summed to obtain the total erosion rate (Iverson, 2012, supplementary material). Values of erosion parameters are given in Table 2.2.

2.3 Strategy

The simulations we present comprise two experiments: one in which we explore the effects of model formulation in terms of drainage system representation and the choice of sliding

Simulation	Purpose	Hydrology	Frequency	h_c^s(m)	K_s(m s^{-1})	m_{max}	λ_{max}(m)
SH_ref	Reference	Sheet only	SD	0.50	0.067	0.25	12
SC_ref	Reference	Sheet & channels	SD	0.35	0.027	0.25	12
SH_PLS	Power law sliding	Sheet only	SD	0.50	0.067	$C_s = 2.5 \times 10^{-9}$	
SC_PLS	Power law sliding	Sheet & channels	SD	0.35	0.027	$C_s = 2.5 \times 10^{-9}$	
SC_S	Forcing frequency	Sheet & channels	S	0.35	0.027	0.45	12
SC_SD	Forcing frequency	Sheet & channels	SD	0.35	0.027	0.45	12
SC_SW	Forcing frequency	Sheet & channels	SW	0.35	0.027	0.45	12
SC_SWD	Forcing frequency	Sheet & channels	SWD	0.35	0.027	0.45	12
SC_SD_amp	Forcing amplitude	Sheet & channels	SD	0.35	0.027	0.30	12
SC_S2D	Forcing amplitude	Sheet & channels	S2D	0.35	0.027	0.30	12
SC_VolUp5	↑ meltwater volume	Sheet & channels	SD	0.35	0.027	0.45	12
SC_VolUp10	↑ meltwater volume	Sheet & channels	SD	0.35	0.027	0.45	12
SC_VolUp15	↑ meltwater volume	Sheet & channels	SD	0.35	0.027	0.45	12
SC_VolDwn5	↓ meltwater volume	Sheet & channels	SD	0.35	0.027	0.45	12
SC_VolDwn10	↓ meltwater volume	Sheet & channels	SD	0.35	0.027	0.45	12
SC_IS	Ice-sheet-like geometry	Sheet & channels	SD	2.0	0.070	0.45	12
SC_TG	Thin glacier geometry	Sheet & channels	SD	0.50	0.075	0.40	8

Table 2.3: Summary of simulations. Model nomenclature: SH = Sheet only; SC = Sheet and Channel; ref = reference run, PLS = Power Law for Sliding; IS = ice-sheet-like geometry; TG = Thin Glacier. Forcing nomenclature: VolUp15 = 15% increase in meltwater volume; VolUp10 = 10% increase in meltwater volume; VolUp5 = 5% increase in meltwater volume; VolDwn5 = 5% decrease in meltwater volume; VolDwn10 = 10% decrease in meltwater volume; S = Seasonal, W = Weekly, D = Diurnal, 2D = Diurnal with twice the amplitude compared to D (Fig. 2.3). Key model parameters are tabulated for the drainage system (h_c^s, K_s) and the sliding law (m_{max}, λ_{max} for Coulomb friction and C_s for power-law sliding).

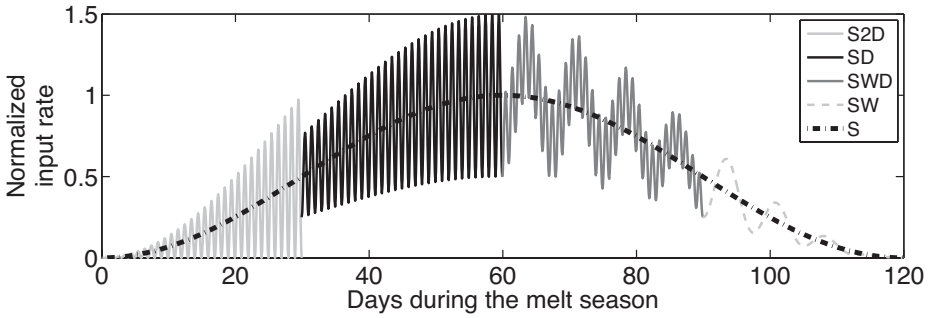

Figure 2.3: Subseasonal modulation of the water input to the bed ($\dot{b}_\mathrm{s}$), with magnitude normalized to conserve total volume over the four-month melt season. The sinusoidal baseline (S) is modulated with sinusoids of different frequencies. Nomenclature: S = Seasonal (black dot-dashed), SD = Seasonal + Diurnal (black), S2D = Seasonal + Diurnal with a doubled amplitude compared to SD (light grey), SW = Seasonal + Weekly (light grey dashed), SWD = Seasonal + Weekly + Diurnal (grey). Each forcing is shown for only a fraction of the melt season here for clarity, but is applied over the entire 120-day period in a simulation.

law, and a second in which we examine the role of model forcing in terms of water input fluctuation frequency and amplitude, total water input volume, and changes in ice geometry (Table 2.3). In keeping with our focus on the influence of subseasonal to annual glacier processes, we confine our presentation to instantaneous erosion rates calculated under the above conditions. We do not evolve the surface or bed geometry during the course of the simulations. To isolate the influence of the melt season through the incorporation of hydrology into the model, we introduce a metric to quantify the erosion excess attributable to the melt season and its attendant processes. We define excess erosion, $\varepsilon_{\dot{\mathrm{e}}}(x)$, as

$$\varepsilon_{\dot{e}}(x) = \frac{\int_\mathrm{yr} \dot{e}(x) - \int_\mathrm{yr} \dot{e}^\mathrm{dry}(x)}{\int_\mathrm{yr} \dot{e}(x)} \tag{2.17}$$

with $\int_\mathrm{yr} \dot{e}(x)$ the erosion rate integrated over one model year for any given simulation, and $\int_\mathrm{yr} \dot{e}^\mathrm{dry}(x)$ the erosion rate integrated over one model year for the equivalent simulation without hydrology and with $N = p_\mathrm{i} - 0$ in either sliding law (Eqs. 2.3 and 2.4). The quantity $\dot{e}$ could represent abrasion, quarrying, or their sum, depending on the application.

2.3.1 Reference model configuration

Unless otherwise noted, the simulations presented use a static parabolic ice surface resting on a flat bed (Fig. 2.2). Water impinges on the distributed drainage system during a four-month 'summer' period, where the water input rate is prescribed as a diurnal sinusoid superimposed on a seasonal sinusoid (Fig. 2.3, black line). This forcing function is not meant to be realistic, but rather to test the response of the system to forcings with clearly established amplitudes and frequencies inspired by natural processes. The prescribed water input rate varies as a

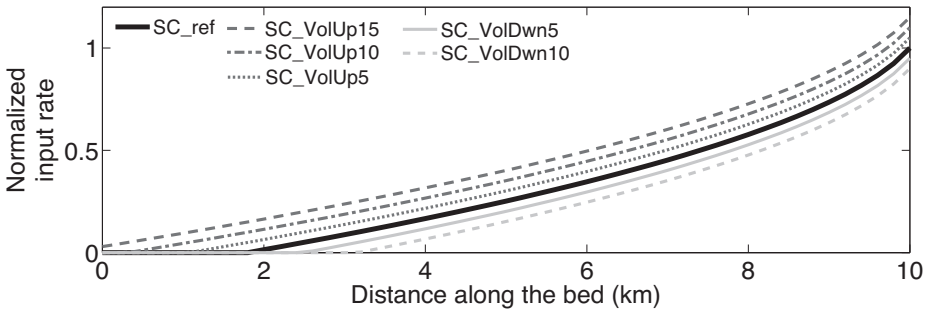

Figure 2.4: Longitudinal profile of the normalized water input rate. An increase or decrease in the total volume of water in the simulations is accomplished by shifting the reference profile (solid black) up or down by increments of 5% with a maximum of +15% (dashed dark grey) and minimum of −10% (dashed light grey).

function of ice-surface elevation (Fig. 2.4, black line); no account is taken of supraglacial or englacial drainage (c.f. Flowers and Clarke, 2002), so the water input rate can be thought of as the fraction of surface meltwater that reaches the glacier bed. No surface water input is prescribed during the eight-month 'winter'. We include distributed and channelized drainage in the reference model (Eqs. 2.6–2.11), and for simplicity we assume the latent channel spacing d_c is identical to the width of the distributed system w_s (and the glacier itself). This restriction is not required by the model formulation. The Coulomb friction law (Eq. 2.4) is used to describe sliding in the reference model, and the glacier bed is assumed to be sufficiently clean for erosion to take place; sediments are assumed to be removed instantaneously. See Table 2.2 for model constants and parameters.

2.3.2 Formulations of subglacial hydrology and sliding

Drainage system morphology

These simulations are designed to compare the influence of hydrology on erosion as a function of the model representation of the drainage system. We first employ the distributed system alone (SH_ref; Eqs. 2.9–2.10) and compare this with the interacting distributed and channelized systems (SC_ref; Eqs. 2.6–2.11). To facilitate model comparisons, we hold the bed characteristics (m_{max} and λ_{max} in the Coulomb friction law) fixed for these simulations. Owing to the differences in model physics, the sheet transmissivity ($h_c^s K_s$) varies but is tuned to produce a similar melt season acceleration. We use this comparison to assess and discuss the importance of integrating a channelized drainage system in glacial erosion models.

Sliding law

To date, models of landscape evolution almost uniquely use a power law for sliding (with $p = 3$ and $q = 1$, Eq. 2.3) whether or not hydrology is considered. We investigate this

choice by comparing the reference simulations (SC_ref and SH_ref), which use a Coulomb friction law, to simulations SC_PLS and SH_PLS (Table 2.3), which employ power-law sliding instead.

2.3.3 Changes in model forcing and geometry

Frequency and amplitude of water input fluctuations

The timesteps required to resolve seasonal to subseasonal processes in models of landscape evolution are prohibitive. Glacier seasonal cycles are therefore usually neglected (e.g., Egholm and others, 2012). Hewitt (2013) found only small differences in modelled ice velocity patterns between simulations forced with a seasonal sinusoid versus one including diurnal modulation; this difference increased when a more realistic forcing was tested.

In order to assess the validity of averaging or omitting subseasonal variations in water input when driving models over longer time scales, we test the model response to varying water input. Various forcings are constructed by superimposing fluctuations of different frequency and amplitude on the seasonal sinusoid (Fig. 2.3). The bed characteristics ($m_{\max}$ and $\lambda_{\max}$) for the Coulomb friction law and the transmissivity ($h_{\mathrm{c}}^{\mathrm{s}} K_{\mathrm{s}}$) of the sheet are held constant in each test to permit a fair comparison (Table 2.3). Seasonal and diurnal frequencies were chosen on the basis of natural observed fluctuations of melt rates. Six-day-period fluctuations (referred to as weekly for convenience) were introduced as a test of intermediate variability inspired by, for example, synoptic weather variations. We also compare simulations with variable amplitude fluctuations (see Fig. 2.3 and Table 2.3). All of the above tests conserve the total volume of water input to the drainage system during the melt season.

Total volume of water input

Glaciers are likely to be more erosive during phases of retreat than advance, owing to the increased volume of available meltwater potentially reaching the bed (e.g., Koppes and Hallet, 2002, 2006). Though we restrict ourselves to seasonal simulations here, we conduct a test to mimic modest increases or decreases in water input that might be associated, respectively, with glacier retreat or advance. The prescribed water input profiles are shown in Fig. 2.4 and are modulated in time using the reference Seasonal + Diurnal (SD) forcing (Fig. 2.3). Other model parameters are again held constant. Simulations cover a shift in the prescribed profile from −10% (SC_VolDwn10) to +15% (SC_VolUp15) in increments of 5%.

Ice thickness

Hallet and others (1996) suggested that large glaciers tend to erode more efficiently than small ones. The extent to which ice sheet outlet glaciers exhibit seasonal behaviour similar to

their smaller cousins is in the process of being defined by current research (e.g., Bartholomew and others, 2011; Meierbachtol and others, 2013). To investigate the role of ice thickness in a very simple experiment, we apply the reference forcing to the glacier geometries in Fig. 2.2. The large differences in ice thickness require simulation-specific model tuning (Table 2.3). Provided a seasonal cycle exists in each simulation, these variations in tuning do not substantially alter the pattern of calculated erosion. We are therefore able to compare patterns of normalized erosion rate between simulations. Identical water input profiles are applied to the reference glacier geometry (SC_ref) and to the ice sheet outlet glacier geometry (SC_IS), yielding identical rates of water input as a function of normalized flowline distance between these two simulations. Identical water input functions are used for the reference and 'thin-glacier' (SC_TG) cases, yielding 1.7 times greater total water input volume for the thin glacier given its lower surface elevation. The width of the thin and reference glaciers is 1 km (i.e., $w_s/2 = W = 500\,\mathrm{m}$) and that of the ice sheet outlet glacier is 4 km (i.e., $w_s/2 = W = 2000\,\mathrm{m}$).

2.4 Results

We focus our analysis on the patterns of erosion rather than the absolute rates, as the former are less sensitive to poorly constrained parameter values and therefore offer a more robust basis for comparison between simulations. For our default choice of $l = 1$ in the abrasion law (Eq. 2.12), abrasion patterns precisely mimic sliding patterns; we therefore omit sliding patterns from the presentation.

2.4.1 Effects of drainage system morphology

Sheet only (SH_ref)

The introduction of subglacial hydrology with a distributed system (sheet) only (Eqs. 2.9 – 2.10) permits the simulation of a seasonal cycle in sliding speed when forced with Seasonal + Diurnal (SD) meltwater input (Fig. 2.3, black line). This spring speed-up is concentrated between kilometres 6 and 10 along the flowline (Fig. 2.5, grey shading) and has a duration of $\sim$30 days in the simulation. With increasing water input to the bed, the water pressure increases, thus lowering the effective pressure and leading to enhanced sliding and abrasion rates (Fig. 2.5). Abrasion rates, which directly reflect sliding patterns, show more than a threefold increase at 8 km along the flowline (Fig. 2.5A), where water input is sufficient to produce low effective pressure at the bed (Fig. 2.5C). The maximum abrasion rate is reached 9 days after the maximum rate of water input, which peaks on day 60 of the simulation (Fig. 2.3). The combination of sheet transmissivity ($h_c^s K_s$) and water input rate lead to a maximum in subglacial storage (h_s) around day 69 of the simulation.

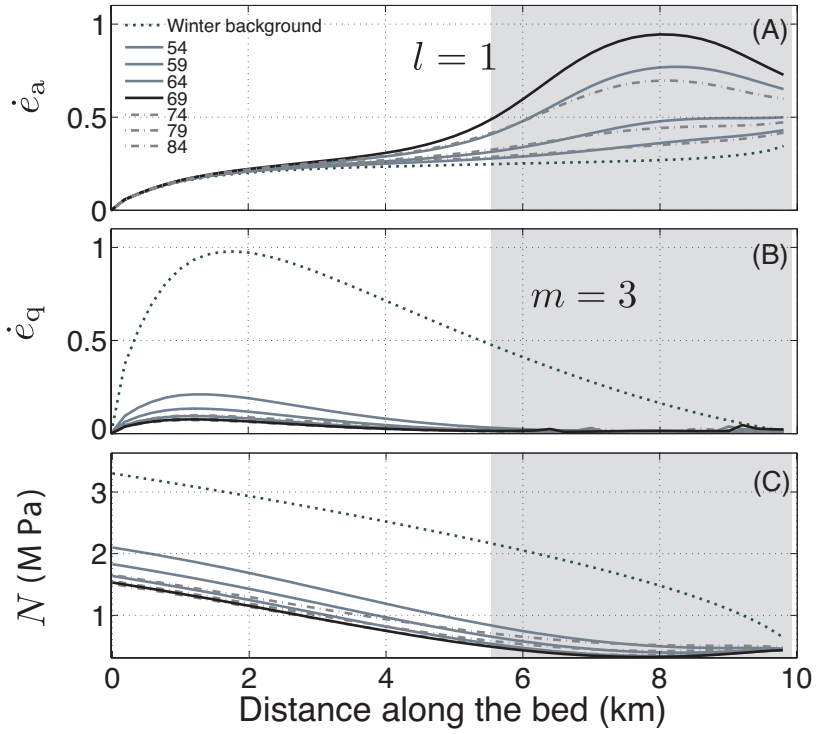

Figure 2.5: Profiles of normalized abrasion rate, normalized quarrying rate, and basal effective pressure during the seasonal sliding enhancement in sheet-only simulation SH_ref. (A) Abrasion rates $\dot{e}_a$ for $l = 1$; (B) quarrying rates $\dot{e}_q$ for $m = 3$; (C) effective pressure $N = p_i - p_s$. Lines are snapshots corresponding to different sliding phases (day number during melt season in legend): increasing sliding (solid grey), maximum sliding (solid black), decreasing sliding (dot-dashed grey), and winter background (dotted). Shading highlights region most affected by spring 'speed-up'.

Quarrying rates decrease during the period of enhanced sliding in this simulation (Fig. 2.5B), instead responding more strongly to effective pressure (Fig. 2.5C). Although sliding speed is positively correlated with quarrying rates (Eqs. 2.4 , 2.13–2.16), the relative importance of sliding speed remains modest compared to that of effective pressure. The drop in effective pressure of about an order of magnitude between the winter background and the time of maximum sliding leads to a large decrease in the deviatoric stress in the bed $\sigma_{\mathrm{d}}^{\mathrm{bed}}$ (Eq. 2.16). In addition, the speed-up enables other feedbacks that act to decrease quarrying rates in this model (Eq. 2.13): when the length of a cavity increases, the volume of quarried rock decreases, and the area of ice–bed contact is reduced thus lowering the probability of step failure (Eqs. 2.13, 2.15, 2.16). This result contrasts with the notion that quarrying should be more efficient in areas of large sliding and abundant water (e.g., Hooke, 1991; Iverson, 1991; Cohen and others, 2006).

Sheet and channels (SC_ref)

The introduction of channelized drainage in the model (Eqs. 2.6–2.11) elicits qualitatively distinct behaviour from the distributed system alone (Fig. 2.6). The abrasion rate maximum migrates up-glacier over time, with the position of the seasonal maximum abrasion rate being $\sim$2 km further up-glacier than in the sheet-only simulation (c.f. black lines in Figs. 2.6A and 2.5A). Accordingly, the effects of the spring transition are most pronounced between kilometres 4 and 8 along the flowline (Fig. 2.6A, grey shading), rather than near the glacier terminus as in SH_ref. The duration of the speed-up is also shorter in this case: $\sim$20 rather than $\sim$30 days. The migration of the abrasion maximum, as well as the more limited duration of the spring speed-up, is a consequence of the development of channelized drainage. Where the distributed system dominates, effective pressure decreases with water input; when a channel begins to form, water is drawn out of the sheet, thus increasing the effective pressure in the system (Fig. 2.6C). The lowest effective pressures in simulation SC_ref occur just upstream from the incision point of the headward-growing channel (Fig. 2.6D). In SC_ref, the abrasion rate exhibits an increase of $\sim$fivefold relative to the winter background value, greater than that in the distributed-only case. This result is partly a function of the different transmissivities used in SH_ref versus SC_ref. The implementation of a distributed-only system to describe subglacial drainage necessitates a higher effective transmissivity (e.g., Flowers, 2008) (see values in Table 2.3), allowing a more prolonged increase in subglacial storage and a delay in the maximum sliding and abrasion rates (day 69 in SH_ref, Fig. 2.5A versus day 46 in SC_ref, Fig. 2.6A).

In contrast to abrasion, quarrying patterns in Fig. 2.6B are similar to those in Fig. 2.5B. Small perturbations in quarrying rates appear at high sliding speeds (Fig. 2.6B) because the sliding speeds obtained lead to elongated cavities (Eq. 2.14) that begin to engulf the bedrock steps. When a step is nearly drowned, the deviatoric stress in the bed (Eq. 2.16) increases enough to produce a small peak in the quarrying rate (Eqs. 2.13 and 2.15). These

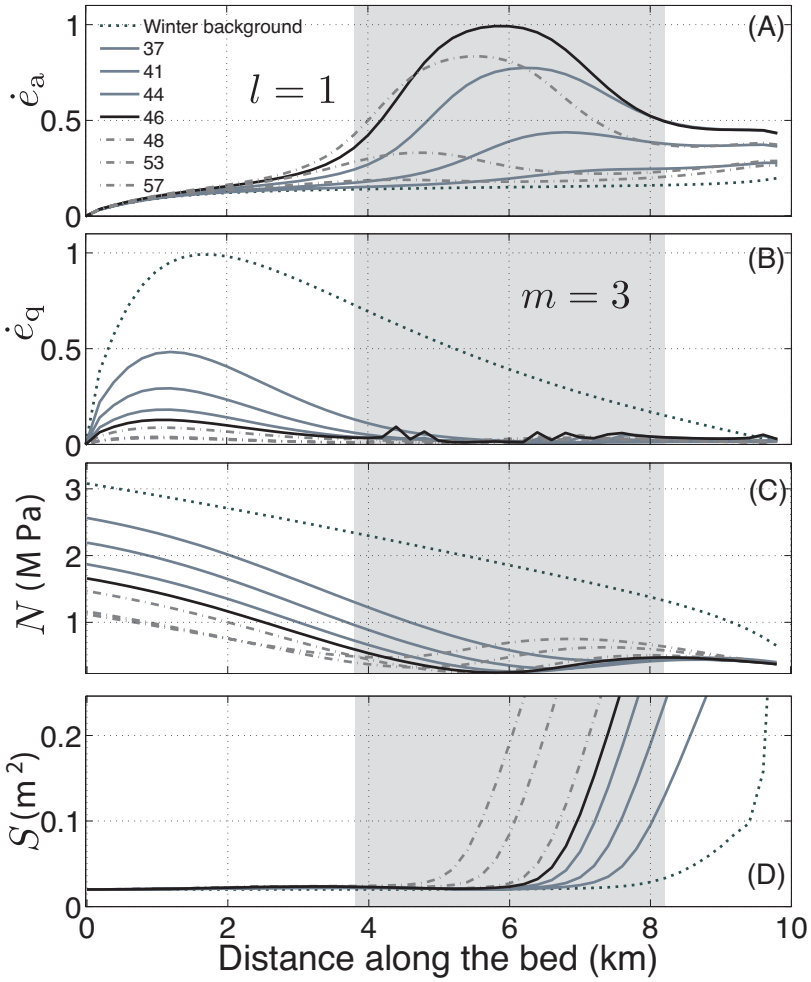

Figure 2.6: Profiles of normalized abrasion rate, normalized quarrying rate, basal effective pressure and channel cross-sectional area during the seasonal sliding enhancement in coupled sheet-channel simulation SC_ref. (A) Abrasion rates $\dot{e}_a$ for $l = 1$; (B) quarrying rates $\dot{e}_q$ for $m = 3$; (C) effective pressure $N = p_i - p_s$; (D) cross-sectional channel area S. Lines are snapshots corresponding to different sliding phases (day number during melt season in legend): increasing sliding (solid grey), maximum sliding (solid black), decreasing sliding (dot-dashed grey), and winter background (dotted). Shading highlights region most affected by spring 'speed-up'. Note the retreat of the abrasion peak compared to SH_ref in Fig. 2.5 caused by channel formation. The effective pressure minimum is located just up-stream from the channel head.

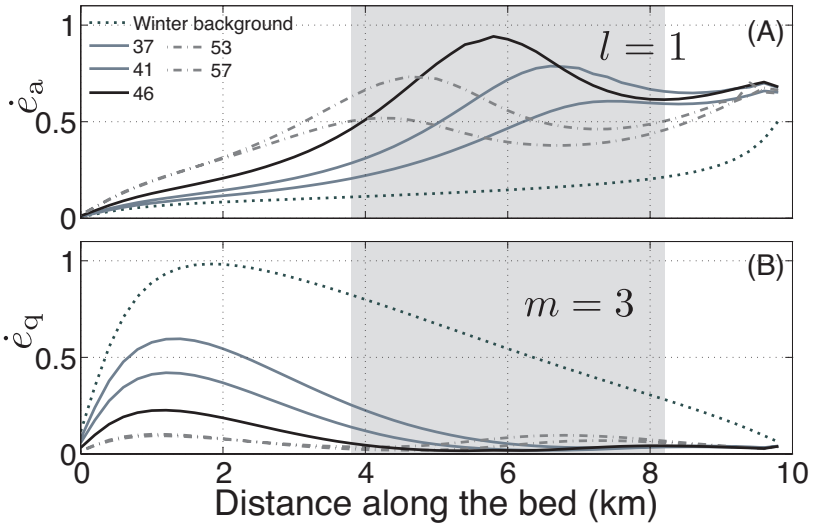

Figure 2.7: Profiles of normalized abrasion and quarrying rates during the seasonal sliding enhancement in the coupled sheet-channel simulation SC_PLS. (A) Abrasion rates $\dot{e}_a$ for $l = 1$; (B) quarrying rates $\dot{e}_q$ for $m = 3$. Lines are snapshots corresponding to different sliding phases (day number during melt season in legend): increasing sliding (solid grey), maximum sliding (solid black), decreasing sliding (dot-dashed grey), and winter background (dotted). Shading highlights region most affected by spring 'speed-up' in the reference simulation SC_ref and is shown here for comparison. Note that enhanced abrasion rates are no longer limited to the shaded area as in Fig. 2.6.

peaks occur on either side of the region of maximum sliding and are of a discrete nature in Fig. 2.6B because the conditions above are obtained for only two of the five bedrock step heights in the quarrying model (Eq. 2.16).

2.4.2 Sliding law

Substitution of power-law sliding (SC_PLS) for Coulomb-friction sliding, as in the reference model (SC_ref), has significant impacts on modelled abrasion patterns, but not on quarrying (Fig. 2.7). Simulations SC_PLS and SC_ref differ only in the choice of sliding law; both employ the coupled sheet–channel drainage system and SD (Seasonal + Diurnal) forcing. The incision and migration of subglacial channels again drive an up-glacier migration of the abrasion rate maximum, while quarrying rates again decrease during the interval of enhanced sliding. In contrast to the reference model, the seasonal acceleration is observed along the entire length of the flowline rather than being confined to several kilometres (Fig. 2.6A). This broad response reflects the relatively simple behaviour of power-law sliding as a function of effective pressure (Eq. 2.3), as well as the decoupled nature of sliding and deformation when the sliding is described by such a power law (see also discussion).

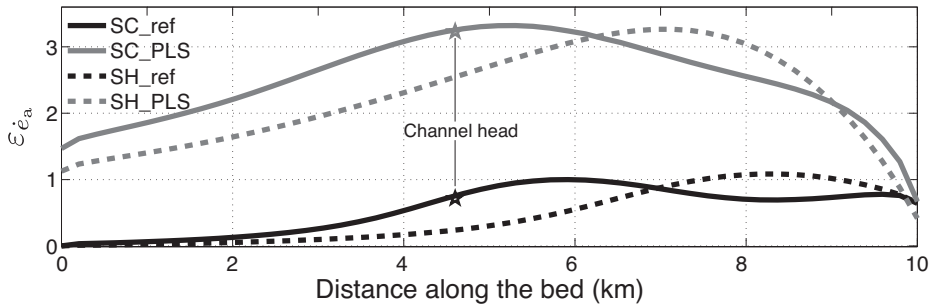

Figure 2.8: Comparison of excess abrasion $\varepsilon_{\dot{e}_a}$ (Eq. 2.17) for different sliding laws (black = Coulomb friction, grey = power law) and distributed-only (dashed) and distributed-channelized (solid) representations of basal drainage. Stars mark maximum up-glacier position of channel head (here defined as $S(x) = 0.1\,\mathrm{m}^2$) in multi-morphology simulations.

2.4.3 Importance of the seasonal cycle to annually integrated abrasion

The combined influence of drainage system representation and the choice of sliding law are illustrated in Fig. 2.8 in terms of 'excess abrasion' $\varepsilon_{\dot{e}_a}$ (Eq. 2.17). We omit quarrying from the results displayed and elaborate on that choice in the discussion. While the incorporation of hydrology and the seasonal cycle alter annually integrated erosion patterns for the sheet-only and for the coupled sheet-channel simulations, the conceptual model adopted to describe the drainage system has implications for the predicted patterns of erosion. Model tuning can produce comparable magnitudes, but not patterns of erosion. With power-law sliding, excess abrasion is more than three times greater than with Coulomb-friction sliding. In addition to this difference in magnitudes of excess abrasion, the position of maximum $\varepsilon_{\dot{e}_a}$ differs slightly ($\sim$10%) between simulations with the two sliding laws.

2.4.4 Erosion law exponent and model formulation

To illustrate the change in model behaviour when $l > 1$ in the abrasion law (Eq. 2.12), we plot integrated and excess abrasion (Eq. 2.17) for the reference simulation SC_ref for $l = 1$, 2, and 3 (Fig. 2.9). Integrated abrasion is compared to the 'dry' simulation in which hydrology is excluded and we set $N = p_\mathrm{i} - 0$ in the Coulomb friction law (Eq. 2.4). In models of landscape evolution, the value of l is generally set equal to 1 or 2 (e.g., MacGregor and others, 2000; Tomkin and Braun, 2002; Herman and Braun, 2008; Egholm and others, 2009; MacGregor and others, 2009; Herman and others, 2011; Egholm and others, 2012), though values up to 4 have been suggested for the evolution of transverse valley profiles (Harbor, 1992). Our choice of $l = 1$, along with our reference model parameters, leads to a conservative estimate of the influence of hydrology and the melt season on integrated abrasion rates. Comparison of dotted and dashed black lines in Fig. 2.9A shows little excess abrasion $\varepsilon_{\dot{e}_a} < 0.1$ (solid black line, Fig. 2.9B). In contrast, the influence of hydrology and the melt

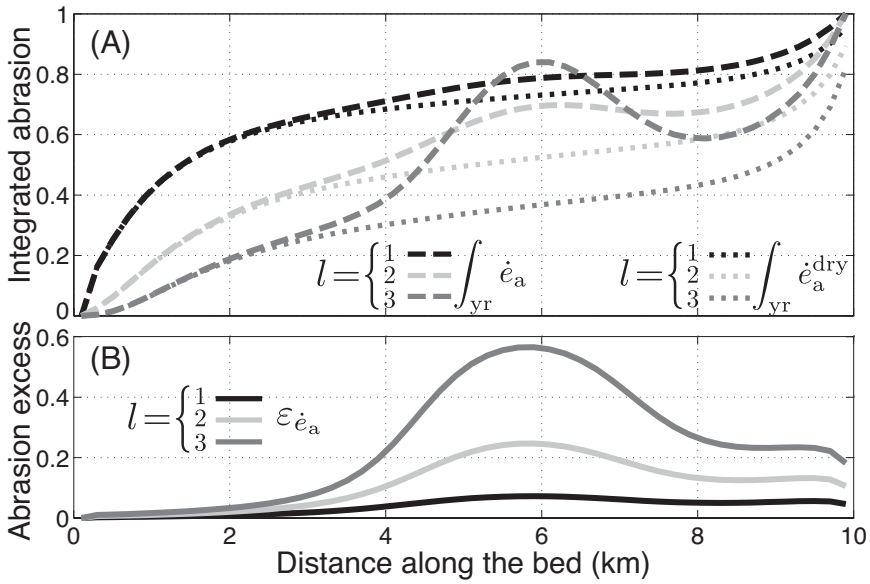

Figure 2.9: Comparison of integrated and excess abrasion (Eq. 2.17) for different values of exponent l (Eq. 2.12): $l = 1$ (black), $l = 2$ (light grey), and $l = 3$ (dark grey). (A) Integrated abrasion $\int_{\mathrm{yr}} \dot{e}_{\mathrm{a}}(x)$ for reference simulation SC_ref (dashed lines) compared with the same quantity for 'dry' simulations $\int_{\mathrm{yr}} \dot{e}_{\mathrm{a}}^{\mathrm{dry}}(x)$ (dotted lines). (B) Resulting excess abrasion $\varepsilon_{\dot{e}_{\mathrm{a}}}$ (solid lines). We choose to disregard the increase in integrated abrasion over the last kilometer in our interpretations of the results; The steep ice-surface gradients lead to significant increase in driving stress and thus in sliding speed. This increase is thus specific to the glacier geometry used.

season become significantly more pronounced for $l > 1$ (grey curves in Figs. 2.9A,B), with $\varepsilon_{\dot{e}_a} > 0.5$ for $l = 3$ (solid dark grey line, Fig. 2.9B). An additional test using the surface and bed geometry of Haut Glacier d'Arolla with a sheet-only hydrology yields $\varepsilon_{\dot{e}_a} \sim 0.6$ for $l = 1$ (not shown), hinting at potentially significant feedbacks in the presence of real topography (c.f. Herman and others, 2011).

2.4.5 Influence of model forcing and geometry

Importance of changes in water input

Excess abrasion is used to examine model sensitivity to meltwater forcing frequency in Fig. 2.10A and amplitude in Fig. 2.10B (see Table 2.3 for summary of simulations and Fig. 2.3 for forcings) while conserving total water input volume. Meltwater input variability has been seized upon as a key driver of ice-flow variations (e.g., Schoof, 2010), though quantity and delivery seem to matter when observations are examined in a holistic manner. With our reference model formulation, little difference in excess erosion is evident when comparing simulations forced with seasonal (S) versus seasonal plus diurnal (SD) input variations (Fig. 2.10A). An elevated response is observed when weekly variations are added to the seasonal plus diurnal variations (SWD), while seasonal plus weekly (SW) variations produce a dramatically increased response with a nearly eightfold increase in $\varepsilon_{\dot{e}_a}$ compared to those for the S and SW simulations.

Although the precise amplitudes of $\varepsilon_{\dot{e}_a}$ in these simulations are influenced by the particulars of the model, the sensitivity to intermediate forcing frequencies can be explained in terms of the duration and magnitude of maximum basal water pressures. Meltwater input variability is greatest for forcings that include diurnal variations (SD, SWD); nevertheless the high water pressures sustained with these forcings are short-lived. Short-lived periods of high water pressure, and therefore high sliding rates, produce short-lived peaks in abrasion rate that may not integrate to annually significant values. A slowly varying seasonal forcing (S) allows ample time for drainage system adjustment, thus avoiding the high peak water pressures and sliding rates that accompany the higher-frequency forcings. Weekly modulation of the seasonal forcing (SW) introduces sustained periods of high water input to which the drainage system can only partially adjust. Over a melt season, this leads to a greater integrated ice displacement by sliding and therefore to greater excess abrasion. Despite these differences in the magnitudes of excess abrasion, the position of maximum $\varepsilon_{\dot{e}_a}$ appears insensitive to input frequency. This can be explained by the extent of channel formation in response to the initial period of elevated basal water pressures during the melt season. Sliding and abrasion rates are sufficiently high during this initial period that their influence is significant enough on the seasonal scale.

Figure 2.10B compares simulations that differ only in forcing amplitude (SC_SD_amp versus SC_S2D in Table 2.3 and Fig. 2.3). Doubling the amplitude of diurnal variations,

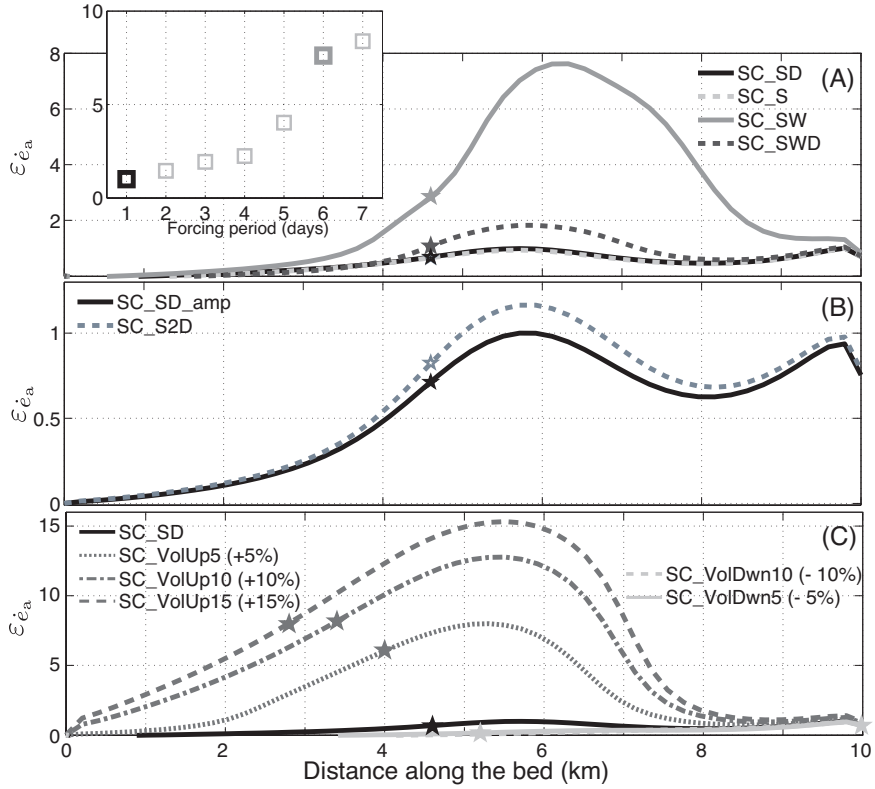

Figure 2.10: Sensitivity of excess abrasion $\varepsilon_{\dot{e}_a}$ to meltwater input frequency, amplitude and total volume. All simulations are shown for $l = 1$. (A) Sensitivity to water input frequency (see Fig. 2.3): S = Seasonal (dashed grey), SD = Seasonal + Diurnal (solid black), SW = Seasonal + Weekly (solid grey), SWD = Seasonal + Weekly + Diurnal (dashed dark grey). The inset shows maximum excess abrasion versus the period of forcing added to the seasonal sinusoid. Bold black and grey boxes represent, respectively, SC_SD and SC_SW in (A). (B) Sensitivity to water input amplitude (see Fig. 2.3): SD = Seasonal + Diurnal (solid black), S2D = Seasonal + Diurnal with a doubled amplitude compared to SD (dashed grey). (C) Sensitivity to total water input volume (see Fig. 2.4): Seasonal + Diurnal (SD), SD + 15% (VolUp15), SD + 10% (VolUp10), SD + 5% (VolUp5), SD - 5% (VolDwn5), SD - 10% (VolDwn10). Stars mark maximum up-glacier position of channel head (here defined as $S(x) = 0.1\,\mathrm{m}^2$) in each simulation. Excess abrasion in all the panels is normalized with respect to the relevant reference model; magnitudes of $\varepsilon_{\dot{e}_a}$ are comparable between (A) and (C) but not (B) because of the use of different values of $m_{\max}$ in the Coulomb friction law for (B) (see Table 2.3).

while preserving total water input volume, leads to a maximum increase of $\sim 15\%$ in excess abrasion over the melt season, though the increase is confined to a limited section of the flowline. Doubling the forcing amplitude leads to higher maximum water pressures and thus to higher sliding rates and more abrasion, though this difference is much less than that achieved by altering the forcing frequency. The migration of the channel head is again the same for the two simulations.

Figure 2.10C compares simulations SC_SD, SC_VolUp5, 10 and 15, and SC_VolDwn5 and 10 (Table 2.3) in which water input is varied in increments of 5% (see profiles in Fig. 2.4) but modulated identically between simulations with the seasonal plus diurnal (SD) forcing. The larger the water input volume, the greater the maximum excess abrasion. Between SC_SD and SC_VolUp5 the peak excess abrasion is ~ 7 times higher for a 5% shift in melt rates and about two times between SC_VolUp5 and SC_VolUp15. Increasing the total water input volume in the manner prescribed here leads to water accessing the bed farther up the flowline, as well as more sustained periods of high water pressure. Up-glacier migration of the channel head therefore occurs in response to the quantity of water input volume (stars in Fig. 2.10).

The position of the excess abrasion maximum along the flowline corresponds to the location of the water pressure peak at the beginning of the melt season, i.e. a combination of water input distribution and size of the channel. Although the one-year model initialization runs are simulation-specific and yield significantly different channel sizes before the onset of the melt season, the location of the channel heads at the end of the winter is similar. As a result, simulations with a sharper increase in water pressure (e.g., SC_SW) show large excess abrasion down-glacier from kilometre 6 (solid grey line, Fig. 2.10A).

Changes in ice thickness

Figure 2.11 shows markedly different patterns of excess abrasion depending on the scale of the ice mass investigated. Thicker more extensive ice (SC_IS in Fig. 2.11) yields a more localized peak in $\varepsilon_{\dot{e}_a}$ closer to the glacier terminus, while thinner less extensive ice (e.g., SC_TG in Fig. 2.11) yields a broad maximum in excess abrasion peaking halfway along the flowline in this simulation. Examination of the maximum location of the channel head in each simulation (stars in Fig. 2.11) shows a more extensive channel system under thin ice (SC_TG) compared to the reference model (SC_ref) and a very limited channel migration in the case of the ice sheet outlet glacier (SC_IS). Thick ice hinders channel formation in general because of the higher rates of creep closure (Eq. 2.7). In the thin glacier case, channelized drainage operates over $\sim 60\%$ of the flowline, compared to $\sim 55\%$ in the reference case and $\sim 22\%$ in the ice sheet case. The peak in excess abrasion retreats $\sim 35\%$ farther up-glacier and is roughly four times wider in the thin glacier case than the ice sheet case. Though independent parameter tuning was required for each of the three simulations in Fig. 2.11 owing to significant differences in ice thickness (see Table 2.3), the

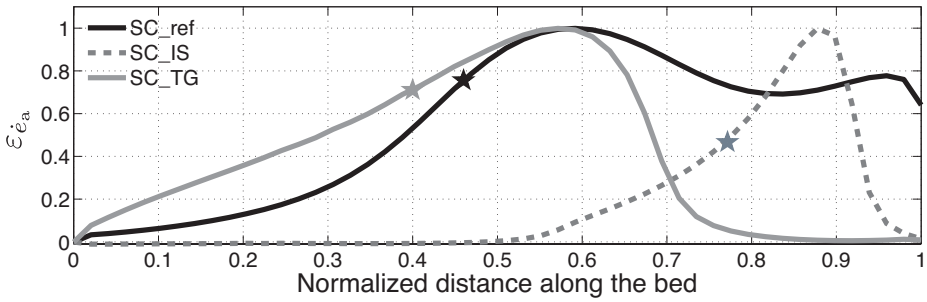

Figure 2.11: Excess abrasion $\varepsilon_{\dot{e}_a}$ calculated for different ice geometries: IS = ice sheet outlet glacier (dashed grey), ref = reference geometry (solid black), TG = thin glacier (solid grey). Note that thickness and length of IS are greater than for ref and TG (see Fig. 2.2). Owing to differences in hydrology and sliding law parameters (Table 2.3), $\varepsilon_{\dot{e}_a}$ is normalized independently for each simulation. Stars mark maximum up-glacier position of channel head (here defined as $S(x) = 0.1\,\mathrm{m}^2$) in each simulation. All simulations are shown for $l = 1$ with Seasonal + Diurnal (SD) forcing.

emergent patterns are still robust. An $\sim$22% coverage of the channelized drainage system for SC_IS corresponds to $\sim$11 km, which would coincide with suggested valley-glacier-like behaviour of the ice sheet outlet glacier near its terminus (e.g., Bartholomew and others, 2011; Meierbachtol and others, 2013).

2.5 Discussion

2.5.1 Limitations of the model

The success and limitations of the model in terms of reproducing observed drainage system behaviour have already been discussed by Flowers (2008). Of relevance here is the failure of the model to produce winter water pressures commensurate with observations. In most simulations, the model predicts flotation fractions of $\sim$30–40% in winter, whereas observations show that winter water pressures can be much higher, for example 80% (e.g., Mathews, 1964; Vivian and Zumstein, 1973). Modelled winter sliding speeds would be higher with higher winter water pressures. In reality, however, limited winter water volumes and decreased drainage system connectivity ordinarily prevent high sliding rates that might otherwise be associated with such high water pressures in a well-connected and supplied system. The issue of under-predicted winter water pressures is not unique to this model (e.g., Hewitt, 2013; Werder and others, 2013) and thus remains a modelling challenge.

Although the model includes only a one-dimensional representation of basal drainage that neglects lateral variations and interactions between channels, the results of Hewitt (2013) and Werder and others (2013) suggested that a drainage system comprising parallel and quasi-regularly spaced channels develops when more sophisticated two-dimensional

network models are executed on simple topography. In the presence of significant bed topography, numerical stability issues often arise for channel models, some of which may be circumvented with treatments of over- and underpressure (e.g., Hewitt and others, 2012). Applications of subglacial hydrology models that include channel systems to real topography have thus far been limited to settings with low bed slopes (e.g., Flowers and others, 2004; Werder and others, 2013).

We use a representation of the distributed drainage system that omits an important feedback between glacier hydrology and sliding (c.f. Kessler and Anderson, 2004). Cavity-based representations of the distributed system (e.g., Schoof, 2010) include this feedback, whereby sliding contributes to cavity opening, thus increasing the capacity of the distributed drainage system. This feedback provides an important stabilizing mechanism in the system in cases where water pressures are high enough to promote sliding, but where volumes are too low to pressurize growing cavities. A model that includes this feedback should also more faithfully reproduce the inferred phasing between subglacial water volume and sliding speed, and thus the observed phasing between horizontal and vertical glacier velocities (e.g., Iken, 1981; Hewitt, 2013). Our omission of this feedback, as well as any type of additional (e.g., englacial) storage, suggests possible phasing errors in variations of diurnal water pressure, sliding, and abrasion. We performed a set of additional simulations (not shown) with a cavity-based distributed drainage system and found little difference in the phasing of diurnal water-pressure fluctuations compared to simulations using the sheet-based formulation. We did, however, find differences in phasing on the seasonal scale, and therefore in the timing of the spring speed-up. These differences led to a slightly sharper peak in the profile of annual excess abrasion with the cavity system, though the general conclusion drawn in this study remain unaffected.

Our implementation of the quarrying model lacks a statistical distribution of bedrock steps as proposed by Iverson (2012), yet our choice of step sizes preserves Iverson's (2012) length-to-height ratio and absolute range. When only a single step size is considered, the local water pressure and sliding speed may combine in such a way that cavities fully engulf the steps and arrest quarrying altogether. Introducing multiple step sizes, as we have done, partially though imperfectly guards against this possibility. We find that the quarrying patterns calculated for individual step sizes (not shown) are similar to those obtained by summing over all five step sizes (Figs. 2.5B, 2.6B, and 2.7B). In our results, low rates of quarrying are largely a function of low effective pressures rather than the limited number of step sizes employed. One minor consequence, however, of the small and discrete number of step sizes is the presence of small disturbances in the quarrying profile (Fig. 2.6). These disturbances are the result of basal conditions producing cavity sizes that approach a given step size. These conditions are rarely attained in our simulations and only persist for 1–2 days when present.

Finally, we have neglected sediment production and transport by the ice and subglacial streams. The presence of clasts is necessary for abrasion to take place (e.g., Boulton, 1974, 1979; Hallet, 1979) and the clast concentration directly affects abrasion patterns (Hallet, 1981). If the bed is completely covered with sediment, abrasion will be significantly reduced (e.g., Cuffey and Alley, 1996) or inhibited altogether (e.g., Egholm and others, 2012). Therefore the results we present should be interpreted qualitatively. Sediment transport is highly controlled by sliding speed (e.g., Iverson, 1993; Iverson and Iverson, 2001), thus enhanced sliding would facilitate sediment evacuation. A related process that might play an important role for the distribution of erosion is the interplay between quarrying and abrasion. The clasts present at the bed of a glacier are most likely produced *in situ*, i.e., by quarrying, and then act as abrasive tools (e.g., Röthlisberger, 1968; Iverson, 2002). Moreover, abrasion tends to smooth bedrock steps while quarrying enlarges them (e.g., Röthlisberger, 1968; Iverson, 2002). Thus, in order to create bedforms such as roches moutonées, both processes must coexist (Iverson, 2002).

2.5.2 Implications for glacial erosion modelling

The formation of subglacial channels and resulting up-glacier migration of the ice surface velocity, attributed to changes in basal sliding speed, has been documented for alpine glaciers (e.g., Nienow and others, 1998; Mair and others, 2002; Anderson and others, 2004; Bartholomaus and others, 2007, 2011) and for northern hemisphere ice-cap and ice sheet margins (e.g., Nye, 1976; Sole and others, 2011; Bartholomew and others, 2012; Meierbachtol and others, 2013). We thus suggest that the implementation of a subglacial channel system should influence models of landscape evolution by glacial erosion. Issues of computational power for the implementation of channels on highly variable topography (Hewitt and others, 2012; Werder and others, 2013) and of dependency of the channel network on the mesh structure (Werder and others, 2013) remain. Parameterization of coupled drainage (e.g., Arnold and Sharp, 2002) may bridge that computational gap where fully resolved models are prohibitive.

Despite the small effect of superimposing diurnal cycles on the seasonal sinusoid, input variations with a period longer than a few days significantly alter the amplitude of excess abrasion. In considering the addition of subglacial forcing in glacial erosion models, the stochastic nature of melt arising from variable weather may drive the most significant seasonal amplification of abrasion.

Hewitt (2013) found only a small difference in surface velocity patterns with a Coulomb-friction or power-law sliding for an ice sheet-like geometry. Longitudinal stress gradients in an ice-flow model damp some of the surface velocity response to a change in sliding, thus implications for erosion cannot be reasonably judged from perturbations to surface velocities. Hewitt (2013) furthermore used exponents for the power-law sliding (Eq. 2.3) equivalent to $p = q = 1$ or $p = q = 1/3$, whereas we use $p = 3$ and $q = 1$ (e.g., Budd

and others, 1979; Bindschadler, 1983; Herman and others, 2011; Egholm and others, 2012) (Table 2.2). What may seem superficially to be contrasting results between our study and that of Hewitt (2013) are not contradictory; we maintain that the choice of sliding law has a significant effect on sliding and abrasion patterns.

Another significant difference between power-law and Coulomb-friction sliding is that the latter exhibits a behavioural threshold related to cavitation, which is controlled in part by bed roughness. At low water pressures, the Coulomb-friction law leads to viscous-drag-like behaviour, while at high water pressures (when cavitation occurs) it leads to Coulomb-slip-like behaviour (Schoof, 2005; Gagliardini and others, 2007; Hewitt, 2013). Power-law sliding, in contrast, responds to changes in water pressure across the full range of effective-pressure regimes. In tuning model parameters to obtain comparable seasonal speed-ups in simulations with power-law sliding versus Coulomb-friction sliding, we found a consistently broader spatial response of power-law sliding to changes in basal water pressure. The response of the Coulomb-friction law tended to be more spatially localized, though this is not independent of the chosen bed roughness parameters. While general conclusions are difficult to draw from our experiments, these findings highlight the more complex behaviour of the Coulomb-friction sliding law.

The comparison of integrated and excess abrasion obtained with different exponents l (Eq. 2.12; Fig. 2.9) the similar patterns obtained in the 'dry' simulations for all three values of l (Fig. 2.9A, dotted lines). When a subglacial drainage system is implemented, the role of l becomes more significant as it amplifies the seasonal enhancement of abrasion. Excess abrasion computed with $l = 3$ is ~ 7 times higher than with $l = 1$ (Fig. 2.9B); however, to our knowledge no data exist to either validate or invalidate these results. In previous studies, the choice of $l = 1$ (e.g., MacGregor and others, 2000; Herman and Braun, 2008; Egholm and others, 2011b) is justified by the linear relationship between sliding speed and sediment evacuation found by Humphrey and Raymond (1994). This case study of Humphrey and Raymond (1994) may not be broadly representative, as they measure the sediment evacuation during the 1982-1983 surge of Variegated Glacier, Alaska. When $l = 2$ is chosen (e.g., MacGregor and others, 2009; Egholm and others, 2012), the common justification is Hallet's (1979) derivation of $\dot{e}_\mathrm{a} \propto u_\mathrm{b} F^\alpha$, where $F \propto u_\mathrm{b}$ is the contact force between a clast and the bed and α is an empirical exponent. Hence $\dot{e}_\mathrm{a} \propto u_\mathrm{b}^2$ if $\alpha = 1$. The value that should be prescribed for α is still unclear, yet probably close to 1, as shown with a ring shear device by Byers and others (2012). Harbor (1992) suggested that $1 \leq l \leq 4$ produces realistic cross-sectional shapes for a glacial valley, although this study considers a generalized erosion rule rather than an abrasion rule in particular. Herman and others (2011) compared results for $l = 1$ and $l = 2$ for the evolution of the long valley profile and also found that the larger l leads to more localized erosion (see Herman and others, 2011; Figs. 3 and 4). Thus more work is required to examine the influence of l on modelled glacial erosion over long time scales.

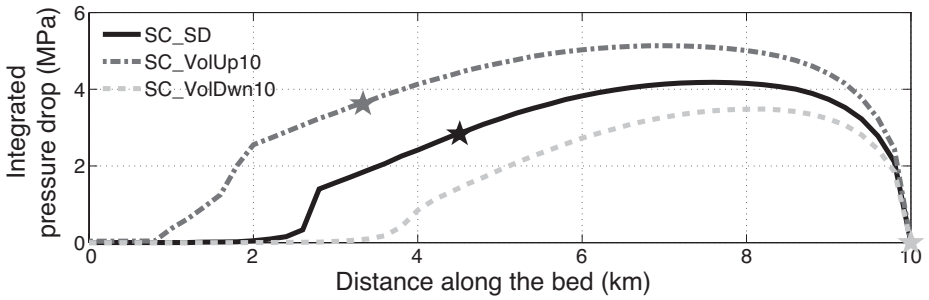

Figure 2.12: Time integrated daily reduction in water pressure shown for three simulations in which the total water input volume is varied (see Figs. 2.4 and 2.10C): Seasonal + Diurnal (SC_SD), SC_SD + 10% (SC_VolUp10), SC_SD - 10% (SC_VolDwn10). Stars mark maximum up-glacier position of channel head (here defined as $S(x) = 0.1\,\mathrm{m}^2$) in each simulation.

2.5.3 Quarrying rates and water pressure fluctuations

Iverson (2012) suggests that an implementation of sliding as a function of water pressure may counteract the importance of the effective pressure alone and enhance quarrying. In our calculations, this effect appears to be overshadowed by the importance of changes in effective pressure. The modelled quarrying rates therefore show little sensitivity to sliding, with quarrying maxima being obtained in winter when modelled effective pressures are highest. For a quarrying event to happen, the stresses in the bed need to exceed those required for critical crack growth (e.g., Iverson, 1991; Hallet, 1996; Hildes and others, 2004). Stresses produced under a thick column of ice are large, but might not be large enough to exceed this threshold. When a cavity forms over a bedrock obstacle, the stresses close to the ledge of the obstacle increase substantially (Iverson, 1991), in some cases enough to exceed the threshold for critical crack growth (Cohen and others, 2006).

According to what was originally proposed by Iverson (1989), used to explain cirque and overdeepening formation by Hooke (1991), later corroborated with numerical models (Iverson, 1991; Hallet, 1996) and recently illustrated through a subglacial experiment (Cohen and others, 2006), quarrying is generally enhanced by water pressure fluctuations, which occur preferentially during the melt season. Cohen and others (2006) demonstrated a correlation between fracture growth and water pressure reduction (i.e. effective pressure increase). They argued that during cavity growth caused by increasing water pressure, the contact surface between bedrock and ice diminishes. With a reduction in cavity water pressure, a greater fraction of the ice load is transferred to the bed-contact area, creating stresses that may surpass the threshold for critical crack growth (Hallet, 1996). Sufficiently large stresses of this kind seem to require large changes in water pressure, not just large overburden pressures. With this in mind, we compute the daily to sub-daily water pressure reductions that occur in the simulations shown in Fig. 2.10C where the total water input

volume is varied. The annually integrated profiles of these water-pressure variations we shown in Fig. 2.12 as an extremely crude proxy for quarrying patterns. In our simulations, maximum cumulative water pressure fluctuations occur closer to the glacier terminus than the upstream boundary and below the maximum up-glacier position of the channel head, when water input is large enough for a significant channel to form. Collectively, these results point to the need for further study of the quarrying process, its underpinnings, and how best to represent it in numerical models.

2.6 Conclusion and outlook

We use a flowband model of coupled ice and water flow to test the effects of different representations of the subglacial drainage system and sliding law on calculated erosion rates. We also examine the influence of water input frequency, amplitude, and volume with an eye to evaluating whether seasonal or subseasonal processes need to be accounted for in models of glacial erosion. To our knowledge this is the first study to combine a multimorphology basal hydrology model with Coulomb-friction sliding, subseasonal water input fluctuations, and process-specific laws for abrasion and quarrying. The principal conclusions of our study are:

- The peaks in instantaneous and integrated abrasion migrate up-glacier when the coupled sheet-channel drainage system is implemented, as compared to the sheet-only drainage system.
- Excess abrasion rates calculated with power-law sliding are larger, and enhanced over a larger portion of the bed, than those computed with Coulomb-friction sliding.
- Sliding and abrasion rates are very sensitive to the period of subseasonal fluctuations in meltwater input, suggesting that capturing multiday variations in meltwater input may be more important than resolving diurnal fluctuations.
- With increases in total water input volume, excess abrasion increases, notably upstream from its maximum value. This suggests that inter-annual variations in melt may have a significant effect on erosion.
- Calculations with the quarrying law of Iverson (2012) produce quarrying patterns markedly different than those for abrasion, with maxima coincident with high effective pressures (thick ice) rather than high sliding speed.
- If water pressure fluctuations drive the quarrying process (Cohen and others, 2006), our calculations hint at quarrying being most efficient below the maximum extent of the channelized system, with a pattern distinct from that of abrasion.

The full implications of the results above can only be realized when long-term simulations that permit an evolving bedrock are conducted to explore the sign and significance of feedbacks within the system. Until such studies are undertaken, we highlight several potential avenues for exploration that may prove important in realistic modelling of glacial erosion. Though the representation of channel networks is computationally out of reach for current landscape evolution models, the relevant effects of a channel network and its seasonal evolution could conceivably be parameterized at the subgrid scale (Arnold and Sharp, 2002). Furthermore, the quasi-instantaneous response time of the basal drainage system (order days to weeks), as compared to the time scales relevant to changes in glacier geometry (order decades to century) invites asynchronous model coupling in which ice flow and erosion models need not adopt the minuscule timesteps required for a subseasonally resolved hydrology.

A second result that seems intuitively important is the suggestion that intermediate forcing frequencies (i.e., multiday variations in meltwater input) may be important in driving erosion. Although Herman and others (2011) argued that subseasonal fluctuations have little effect on erosion owing to the rapid response time of the subglacial drainage system compared to erosion, we may have failed to adequately emulate realistic meltwater input variations in models to date (e.g., Pimentel and others, 2010; Hewitt, 2013). In a similar way that high-frequency stochastic fluctuations in climate can drive significant variations in glacier extent (e.g., Roe and O'Neal, 2009; Roe, 2011) or that individual extreme mass-balance years can influence glacier health, subseasonal variations in hydrology and sliding may prove important for erosion even when integrated over longer time scales.

Though not investigated here, the erosive agency of the subglacial water system itself may also be important in the formation of large erosional features such as tunnel valleys (e.g., Dürst-Stucki and others, 2010). Moreover, subglacial sediment evacuation is intimately linked to subglacial drainage (e.g., Riihimaki and others, 2005; Creyts and others, 2013) and would be influenced by the high water pressures obtained subglacially (e.g., Alley and others, 1997; Creyts and others, 2013). These remain important avenues for investigation as we seek to better understand glacial landscapes and model their evolution.

Acknowledgements

We are grateful to the Swiss National Cooperative for the Disposal of Radioactive Waste (Nagra), the Natural Sciences and Engineering Research Council of Canada (NSERC), and Simon Fraser University (SFU) for providing funding. We would like to thank Neal Iverson for his constructive comments, Nat Wilson for numerous interesting discussions, and D.L. Egholm and an anonymous referee for their comments that helped improve the manuscript. We also thank R.A. Marston for his thorough editorial work.

Chapter 3

Efficacy of bedrock erosion by subglacial water flow

Abstract

Bedrock erosion by sediment-bearing subglacial water remains little-studied, however the process is thought to contribute to bedrock erosion rates in glaciated landscapes and is implicated in the excavation of tunnel valleys and the incision of inner gorges. We adapt physics-based models of fluvial abrasion to the subglacial environment, assembling the first model designed to quantify bedrock erosion caused by transient subglacial water flow. The subglacial drainage model consists of a one-dimensional network of cavities dynamically coupled to one or several Röthlisberger channels (R-channels). The bedrock erosion model is based on the tools and cover effect, whereby particles entrained by the flow impact exposed bedrock. We explore the dependency of glacial meltwater erosion on the structure and magnitude of water input to the system, the ice geometry and the sediment supply. We find that erosion is not a function of water discharge alone, but also depends on channel size, water pressure and sediment supply, as in fluvial systems. Modelled glacial meltwater erosion rates are one to two orders of magnitude lower than the expected rates of total glacial erosion required to produce the sediment supply rates we impose, suggesting that glacial meltwater erosion is negligible at the basin scale. Nevertheless, due to the extreme localization of glacial meltwater erosion (at the base of R-channels), this process can carve bedrock (Nye) channels. In fact, our simulations suggest that the incision of bedrock channels several centimetres deep and a few metres wide can occur in a single year. Modelled incision rates indicate that subglacial water flow can gradually carve a tunnel valley and enhance the relief or even initiate the carving of an inner gorge.

3.1 Introduction

Textbook descriptions of glacial erosion detail mechanisms of abrasion and quarrying, but mention erosion by subglacial meltwater as a potential, unquantified, additional incision mechanism (e.g., Bennett and Glasser, 2009; Anderson and Anderson, 2010). This imbalance reflects the deficiency in our understanding of the latter. In fact, subglacial meltwater loaded with sediment has been inferred to carve metre-scale channels in bedrock (e.g., Glasser and Bennett, 2004), often called Nye channels (N-channel; Weertman, 1972) and kilometre-scale tunnel valleys (e.g., Ó Cofaigh, 1996; Glasser and Bennett, 2004; Jørgensen and Sandersen, 2006; Dürst-Stucki and others, 2010; Kehew and others, 2012), and more recently its role has been invoked as a necessary mechanism in the carving and deepening of inner gorges (Dürst-Stucki and others, 2012; Jansen and others, 2014).

Although the ability of subglacial water flow to flush subglacial sediment is well established (e.g., Humphrey and Raymond, 1994; Gurnell and others, 1996; Hallet and others, 1996; Willis and others, 1996; Alley and others, 1997; Koppes and Hallet, 2002, 2006; Riihimaki and others, 2005; Koppes and Montgomery, 2009), there has been little work quantifying subglacial sediment transport (Creyts and others, 2013), and no work on bedrock erosion by subglacial meltwater. Most studies of glacial erosion that use measurements of proglacial sediment yield rely on the hypothesis that subglacial meltwater flow is the most important process removing sediment from the glacier bed (e.g., Gurnell and others, 1996; Koppes and Hallet, 2002, 2006; Orwin and Smart, 2004; Riihimaki and others, 2005). In numerical models of glacial erosion, sediment transport by subglacial water flow is usually neglected (e.g., MacGregor and others, 2000, 2009; Brocklehusrt and Whipple, 2002; Tomkin and Braun, 2002; Anderson and others, 2006; Herman and Braun, 2008; Egholm and others, 2009, 2011a,b, 2012; Herman and others, 2011; Beaud and others, 2014), often under the assumption that sediment is removed instantaneously. Bedrock erosion resulting from subglacial water is likewise neglected. A better understanding of the processes that lead to the formation of tunnel valleys or inner gorges is also important for the evaluation of deep geological repositories for nuclear waste in regions facing a potential future glaciation (e.g., Iverson and Person, 2012).

Subglacial water flows through two main types of drainage systems: distributed and channelized. In numerical models (see Flowers (2015) for a review), a distributed drainage system is typically represented by a network of connected cavities (e.g., Lliboutry, 1968; Iken, 1981; Kamb, 1987; Schoof, 2010; Bartholomaus and others, 2011), a macroporous sheet of sediment (e.g. Clarke, 1996; Creyts and Schoof, 2009) or a water film (e.g., Weertman, 1972; Le Brocq and others, 2009). These representations reflect field observations of an increase in water pressure with discharge (e.g. Iken and Bindschadler, 1986; Nienow and others, 1998). A channelized drainage system is most often described by a single Röthlisberger channel or a network thereof (e.g., Röthlisberger, 1972; Nye, 1976; Flowers and

others, 2004; Kessler and Anderson, 2004; Schoof, 2010; Hewitt and others, 2012). Water velocities are relatively high in the channelized system and, under steady-state conditions, water pressure decreases with increasing discharge (Röthlisberger, 1972). Conduits carved both in sediment and ice, so-called canals (e.g., Walder and Fowler, 1994; Ng, 2000a; Kyrke-Smith and Fowler, 2014), have properties closer to those of a distributed system as pressure often increases with discharge (Walder and Fowler, 1994). In winter, the distributed drainage system evacuates most basal water, and water pressures tend to be relatively high. As surface melt becomes significant, the water input becomes too large for the distributed drainage system alone, water pressure increases and R-channels start to form. Once an efficient drainage system is established, meltwater is routed relatively quickly downstream and baseline water pressures are generally lower than in winter, with large daily fluctuations. As surface melt decreases, channels are reduced in size by ice creep and may eventually close. We hypothesize that this cycle may have a significant effect on bedrock erosion by subglacial meltwater flow (e.g., Willis and others, 1996; Swift and others, 2005).

Three main processes produce bedrock erosion in rivers: abrasion, macro-abrasion and quarrying (e.g., Whipple and others, 2000, 2013). Abrasion is the result of particles entrained by the flow (saltating or in suspension) colliding with the bedrock and is governed by the tools and cover effect, whereby particles (i.e., tools) entrained by the flow impact exposed bedrock but can also shield it if they are immobile (i.e., cover; e.g., Whipple and others, 2000, 2013; Sklar and Dietrich, 2001, 2004; Turowski and others, 2007; Lamb and others, 2008a; Cook and others, 2013; Scheingross and others, 2014). Macro-abrasion and quarrying both result from dislodgement of blocks and require a relatively high joint density in the bedrock. Macro-abrasion occurs when blocks are dislodged as a result of the impact of moving particles, while quarrying is the result of dislodgement by pressure gradients caused by water flow (Whipple and others, 2000, 2013). Over highly jointed bedrock, quarrying and macro-abrasion can produce large canyons under extreme flow conditions (e.g., Bretz, 1969; Lamb and Fonstad, 2010; Baynes and others, 2015). In this study, we limit our analysis to abrasion (Whipple and others, 2000, 2013; Cook and others, 2013) and use well-established models to estimate the erosion due to total sediment load (Lamb and others, 2008a) and saltating load only (Sklar and Dietrich, 2004).

Alley and others (1997) suggest that the sediment transport capacity of an R-channel is most affected by changes in water discharge and hydraulic potential gradient and further posit that in most cases, the hydraulic potential gradient increases downstream (due to steep ice-surface slopes close to the terminus) so that the transport capacity should also increase. Dürst-Stucki and others (2012) calculate an erosional potential of subglacial water based on the hydraulic potential gradient under a valley glacier and find that the erosional potential increases toward the terminus and could explain the deepening of inner gorges during a glaciation (e.g., Jansen and others, 2014). Both studies are, however, quite speculative regarding the processes behind subglacial meltwater erosion. Creyts and others (2013) were

the first to couple subglacial water flow in a distributed drainage system, basal refreezing and sediment transport in a numerical model to explore the evolution of bed slopes adverse to ice flow close to the terminus. They demonstrate strong feedbacks between sediment deposition / entrainment and hydraulic conditions as well as the importance of daily fluctuations in water input on the sediment flux.

In proglacial studies of seasonal sediment yield, hysteresis between sediment and water discharge is often observed (e.g., Willis and others, 1996; Swift and others, 2005; Mao and others, 2014). It is usually attributed to changes in sediment availability, tapping of new areas of the bed by the developing drainage system, or increased mobilization caused by sudden changes in the subglacial hydraulic system (e.g., Willis and others, 1996). An event during which sediment transport peaks before discharge is usually defined as clockwise hysteresis and is interpreted as the manifestation of an unlimited sediment source (e.g., Mao and others, 2014). The opposite is true for counter-clockwise hysteresis. In a study of bedload transport by a proglacial stream in the Italian Alps, Mao and others (2014) identify a transition throughout the melt-season from hysteresis dominated by clockwise events to hysteresis dominated by counter-clockwise events. The authors infer that this transition is due to the activation of different sediment sources across the drainage basin.

Evidence of the erosional action of subglacial meltwater flow is widespread in formerly glaciated regions and appears in the form of N-channels, tunnel valleys and inner gorges. Tunnel valleys are large (few hundred metres to kilometres wide and up to tens of kilometres long) channel-like features found within the limits of former continental ice sheets (e.g., Ó Cofaigh, 1996; Glasser and Bennett, 2004; Jørgensen and Sandersen, 2006; Dürst-Stucki and others, 2010; Kehew and others, 2012) or in Antarctica (e.g., Denton and Sugden, 2005; Rose and others, 2014) in substrata varying from loosely consolidated sediment to bedrock. Their formation is attributed to the action of pressurized subglacial meltwater, and three particular mechanisms have been proposed (e.g., Ó Cofaigh, 1996; Glasser and Bennett, 2004; Kehew and others, 2012): (1) sediment creep toward preferential groundwater flow paths, (2) carving by sediment-loaded subglacial water flow or (3) erosion caused by large subglacial water floods.

Inner gorges are narrow canyons incised at the bottom of an otherwise U-shaped valley (e.g., Montgomery and Korup, 2010), and are found extensively in formerly glaciated mountain ranges like the Alps (e.g., Montgomery and Korup, 2010; Dürst-Stucki and others, 2012). The origin of inner gorges was originally entirely attributed to postglacial fluvial erosion, although Montgomery and Korup (2010) conclude that such features persist through repeated glaciations instead of being reset by glacial erosion. For example, Valla and others (2010) find that fluvial incision rates on the order of a centimetre per year occurred during at least the past four thousand years in a gorge in the French Western Alps. Recently Dürst-Stucki and others (2012) showed that pressurized water flow is necessary to explain the longitudinal profile of an inner gorge in the foothills of the Alps, and Jansen and others

(2014) infer from cosmogenic nuclide exposure that the timing of carving of seven inner gorges in the Baltic Shield matches the timing of glacial cover. Inner gorges are therefore most likely the combined product of fluvial erosion during interglacial periods and subglacial meltwater erosion during glacial periods, although the importance of fluvial versus glacial conditions is probably dependent on surrounding topography. Nye channels, tunnel valleys and inner gorges share some characteristics suggesting a common genetic origin, although the specific combination of processes responsible for their evolution may differ slightly.

We implement a one-dimensional (1-D) model of subglacial water flow in which a network of cavities is dynamically coupled to one or a few channels. We then compute the shear stress exerted on the bed and use it to compute transport stages and bedrock erosion rates by abrasion caused by particle impacts. We compare the results of models that treat erosion by saltating particles only (Sklar and Dietrich, 2004) and erosion by both the saltating and suspended particles (Lamb and others, 2008a). We use the word "erosion" only to describe the carving of bedrock while "transport", "mobilization" or "entrainment" refer to the movement of unconsolidated sediments.

We first perform steady-state simulations with the channelized drainage system alone to demonstrate basic model behaviour. We investigate the role of ice geometry, surface melt and sediment supply. We then introduce the coupled (distributed and channelized) hydraulic system and water forcing with sub-seasonal fluctuations to test the importance of transients in the subglacial drainage system. Finally, we discuss the implications of our results for the formation of N-channels and consequently of tunnel valleys over bedrock and the persistence of inner gorges through repeated glaciations. Our specific research questions are: 1) What are the major controls on subglacial meltwater erosion? 2) How important is subglacial meltwater erosion compared to overall glacial erosion? 3) Can ordinary seasonal melt processes lead to subglacial bedrock channel incision (and potentially the formation of an incipient tunnel valley or persistence of an inner gorge)? 4) What are the implications of the water flow regime in channels for hysteresis and sediment transport?

3.2 Modelling approach

3.2.1 Subglacial water flow

We use a 1-D model of coupled cavity and channelized drainage styled after previous models (e.g., Werder and others, 2013), with the numerical distensibility parameter of Clarke (2003) and the water exchange term of Hewitt and Fowler (2008). The system of equations describing R-channels admits both a wave-like solution and the solution for water flow which introduces numerical stiffness. To circumvent this problem, Clarke (2003) proposed to treat water as a slightly compressible fluid and he introduced a numerical distensibility parameter, γ. The water exchange term is required as the channelized and distributed

Table 3.1: Summary of hydrological model parameters (see Appendix B for extended list).

Parameter	Description	Value
M	Number of grid points	101
$\mathrm{d}x$	Cell size	500 m
$\mathrm{d}t$	Time step	600 s
W	System width	1000 m
X_L	Glacier length	50 km
ρ_w	Water density	$1000\,\mathrm{kg\,m^{-3}}$
ρ_i	Ice density	$910\,\mathrm{kg\,m^{-3}}$
L	Latent heat of fusion	$3.34 \times 10^5\,\mathrm{J\,kg^{-1}}$
n	Flow-law exponent	3
k_ex	Exchange coefficient	$5 \times 10^{-13}\,\mathrm{m^{3/2}\,kg^{-1/2}}$
e_v	Englacial void ratio	1×10^{-3}
γ	Numerical compressibility	$10^{-9}\,\mathrm{Pa^{-1}}$

drainage systems are otherwise defined as two independent systems (Flowers and others, 2004; Hewitt and Fowler, 2008).

Channelized drainage

As in most subglacial drainage models, we assume the channelized system to be a network of semi-circular Röthlisberger channels (Röthlisberger, 1972; Nye, 1976). The channels are assumed to be linear (along the x coordinate) and parallel to one another if more than one is considered. The conservation of water mass is given by (Clarke, 2003):

$$-\gamma S\frac{\partial \phi_\mathrm{ch}}{\partial t} = \frac{\partial Q_\mathrm{ch}}{\partial x} + \frac{\Xi - \Pi}{L}\left(\frac{1}{\rho_\mathrm{i}} - \frac{1}{\rho_\mathrm{w}}\right) - v_\mathrm{cc} - (\dot{b}_\mathrm{ch} + \varphi)W, \tag{3.1}$$

where S is the cross-sectional area of the R-channel, ϕ_ch is the hydraulic potential, Q_ch is the water discharge, ρ_w and ρ_i are the densities of water and ice respectively, v_cc is the rate of creep closure of the channel walls, $\dot{b}_\mathrm{ch}$ is a water source term to the channel, φ is the exchange rate between the distributed and channelized drainage systems, W is the width of the catchment drained by the R-channel, γ is a numerical compressibility parameter (Clarke, 2003), x is the coordinate along the flow line and t is time. Note that we assume changes in bed topography with time are small enough to be neglected. Therefore $\partial\phi_\mathrm{b}/\partial t = 0$ and $\partial p_\mathrm{ch}/\partial t = \partial(\phi_\mathrm{ch} - \phi_\mathrm{b})/\partial t = \partial\phi_\mathrm{ch}/\partial t$, where p_ch is the water pressure in the channel and ϕ_b the hydraulic potential at the bed. The evolution of channel cross-sectional area S with time is

$$\frac{\partial S}{\partial t} = \frac{\Xi - \Pi}{\rho_\mathrm{i} L} - v_\mathrm{cc}, \tag{3.2}$$

where Ξ is the dissipation of potential energy, Π is the energy to maintain the water at the pressure melting point, L is the latent heeat of fusion, thus $(\Xi - \Pi)/(\rho_\mathrm{i} L)$ is the rate of

channel opening by viscous heat dissipation. We refer the reader to the Supplement for the description of Ξ, Π, v_{cc} and Q_{ch}.

Distributed drainage

The distributed drainage system is treated as a network of connected cavities (Kamb, 1987) undergoing turbulent flow. Assuming that water can be stored englacially or subglacially, the conservation of water mass can be written (Werder and others, 2013)

$$\frac{e_{\mathrm{v}}}{\rho_{\mathrm{w}} g}\frac{\partial \phi_{\mathrm{ca}}}{\partial t} + \nabla \cdot \boldsymbol{q}_{\mathrm{ca}} + v_{\mathrm{o}} - v_{\mathrm{c}} - (\dot{b}_{\mathrm{ca}} - \varphi) = 0 \tag{3.3}$$

where ϕ_{ca} is the hydraulic potential in the cavity network, e_{v} is the englacial void ratio, $\boldsymbol{q}_{\mathrm{ca}}$ is the water flux in the cavity network, g is the gravitational acceleration, v_{o} and v_{c} are the opening and closure rate, respectively, $\dot{b}_{\mathrm{ca}}$ is a water source term to the cavity network. The evolution of the average cavity height h_{ca} with time is:

$$\frac{\partial h_{\mathrm{ca}}}{\partial t} = v_{\mathrm{o}} - v_{\mathrm{c}}. \tag{3.4}$$

We refer the reader to the Supplement for the description of v_{o}, v_{c} and $\boldsymbol{q}_{\mathrm{ca}}$.

Coupled channelized and distributed drainage

To couple the two drainage systems we use a term to describe water exchange between cavities and channels as a function of their respective pressure differences (e.g., Flowers and others, 2004; Hewitt and Fowler, 2008):

$$\varphi = k_{\mathrm{ex}}(N_{\mathrm{ch}} - N_{\mathrm{ca}}), \tag{3.5}$$

where k_{ex} is an exchange coefficient (Table 3.1) and N_{ch} and N_{ca} are the effective pressures in the channelized and cavity systems, respectively (see Appendix B). The system formed by Eqs. (3.1), (3.2), (3.3) and (3.4) is solved with the MATLAB `pdepe` solver.

Shear stress partitioning

Following Clarke (2003) we write the shear stress exerted on the bed by subglacial water flow as:

$$\tau_{\mathrm{b}} = \frac{1}{8} f_{\mathrm{b}} \rho_{\mathrm{w}} u^2, \tag{3.6}$$

where f_{b} is the Darcy-Weisbach friction coefficient for the bed and u is the depth-averaged water flow velocity defined as $u = Q_{\mathrm{ch}}/S$ in a channel and $u = q_{\mathrm{ca}}/h_{\mathrm{ca}}$ in the network of cavities. Details pertaining to the shear stress calculation are described in the Supplement.

Subglacial water flow model simplifications

We implement the model in a 1-D continuum such that the drainage system is assumed to be fully connected. Distributed and channelized drainage systems are assumed to be saturated. The bed is impermeable and undeformable. We also neglect the routing of supra- and englacial water, the effect of particles or refreezing on water flow constriction and the feedbacks between sliding speed and water pressure.

Boundary and initial conditions

Atmospheric pressure defines the downstream boundary condition for both the network of cavities and the R-channels: $\phi_{\mathrm{ch}}(x = X_{\mathrm{L}}, t) = \phi_{\mathrm{b}} + 1000\,\mathrm{Pa}$. For most simulations, a no-flux condition is applied at the upstream boundary such that $Q_{\mathrm{ch}}(x = 0, t) = 0$, $q_{\mathrm{ca}}(x = 0, t) = 0$. Otherwise, for the simulation in which discharge is constant throughout the domain, we apply a Neumann boundary condition at the upstream node of the channel: $Q_{\mathrm{ch}}(x = 0, t) = 18\,\mathrm{m}^3\,\mathrm{s}^{-1}$. We use a one-year model spin-up for all the transient simulations as we find no significant difference in results using one- and two-year spin-ups.

3.2.2 Erosion by saltating and total load

In river reaches where bedrock fracture density is low (i.e. blocks are larger than 1–2 metres in size), abrasion is the primary erosional process (Whipple and others, 2000, 2013). Particles that are mobilized by the flow and move by saltation or in suspension can impact the bed, and the energy released upon impact can cause erosion. To erode its bed, a river therefore requires tools (particles available for transport) and an exposed bed.

Saltation erosion model (SEM) (Sklar and Dietrich, 2004)

The rate of erosion caused by a saltating load can be expressed as:

$$\dot{e}_{\mathrm{salt}} = I_{\mathrm{r}} V_{\mathrm{i}} F_{\mathrm{e}}, \tag{3.7}$$

where I_{r} is the rate of particle impact with the bed, V_{i} is the volume of bed material removed upon impact and F_{e} the fraction of the bed exposed. The impact rate (I_{r}) is a function of the number of particles and their saltation trajectories. The more particles and the shorter the saltation length, the higher the impact rate. The volume removed upon impact (V_{i}) is a function of the energy released on impact and therefore of the particle mass, its speed normal to the bed and the physical properties of the bed and the particle. The fraction exposed (F_{e}) determines the areal extent of bedrock vulnerable to erosion and represents the cover effect. All the quantities described here are given per unit width. Values of V_{i}, I_{r}

and F_e are computed as:

$$V_i = \frac{\pi \rho_s D^3 w_{si}^2 Y}{6 k_v \sigma_T^2}, \tag{3.8}$$

where ρ_s is the sediment density, D is the particle diameter, w_{si} is the particle velocity upon impact, Y is the Young's modulus of the bedrock, k_v is an empirical rock erodibility coefficient and σ_T is the rock tensile strength;

$$I_r = \frac{6 q_s}{\pi D^3 L_s}, \tag{3.9}$$

where q_s is the sediment supply rate and L_s is the hop length of particles;

$$F_e = 1 - \frac{q_s}{q_{tc}}, \text{ for } q_s \leq q_{tc}, \tag{3.10}$$

where q_{tc} is the sediment transport capacity. Substituting Eqs. (3.8), (3.9) and (3.10) into (3.7) and simplifying yields:

$$\dot{e}_{salt} = \frac{\rho_s q_s w_{si}^2 Y}{L_s k_v \sigma_T^2} \left(1 - \frac{q_s}{q_{tc}}\right). \tag{3.11}$$

Note that when $q_s/q_{tc} > 1$ the erosion rate becomes $\dot{e}_{salt} = 0$ because the bed is completely covered with sediment. Constants and parameters are listed in Table 3.2, and the formulations of L_s and w_{si} are described in the Supplement. We follow Sklar and Dietrich (2004) in using the Fernandez-Luque and van Beek (1976) formulation of transport capacity:

$$q_{tc} = 5.7 (r g D^3)^{1/2} (\tau^* - \tau_c^*)^{3/2}, \tag{3.12}$$

where $r = \rho_s/\rho_w - 1$ is the buoyant density of sediment and τ_c^* the critical value of the Shields stress. The Shields stress τ^* is computed as:

$$\tau^* = \frac{\tau_b}{(\rho_s - \rho_w) g D}. \tag{3.13}$$

Total load erosion model (TLEM) (Lamb and others, 2008a)

The total load erosion model (TLEM) is based on the original model of Sklar and Dietrich (2004) and extended by Lamb and others (2008a) to account for the impact of particles in suspension close to the bed. The total load erosion rate is calculated as:

$$\dot{e}_{tot} = \frac{A_1 \rho_s Y}{k_v \sigma_T^2} c_b w_{i,eff}^3 \left(1 - \frac{q_b}{q_{tc}}\right), \tag{3.14}$$

where $A_1 < 1$ is a coefficient to account for the upward lifting of particles close to the bed by turbulent eddies (here $A_1 = 0.36$), c_b is the near-bed sediment concentration, $w_{i,eff}$ is the effective impact velocity, and q_b is the volumetric flux of sediment transported as bed-load.

Table 3.2: Summary of parameter values for the saltation (Sect. 3.2.2) and total load (Sect. 3.2.2) erosion models.

Parameter	Description	Value
A_1	Coefficient for upward lifting of particles †	0.36
D	Diameter of particles	60 mm
σ_T	Rock tensile strength †	7.0 MPa
Y	Young's modulus of bedrock †	5.0×10^4 MPa
k_v	Rock erodibility coefficient †	1.0×10^6
τ_c^*	Critical Shields stress †	0.03
ρ_s	Sediment density	2650 Kg m^{-3}
$q_{s,ref}$	Ref. sediment supply per unit width (Steady-state – transient)	$3.6 - 9.1 \times 10^{-3}$ m^2 s^{-1}

†Parameter values from Lamb and others (2008a)

The calculation of these quantities is explained in the Supplement. By analogy with the saltation-erosion model, c_b is similar to the impact rate I_r, $w_{i,eff}$ to the volume removed upon impact V_i, and $(1 - q_b/q_{tc})$ to the fraction of the bed exposed (F_e). Similarily to the SEM, when $q_b/q_{tc} > 1$ the erosion rate becomes $\dot{e}_{tot} = 0$ because the bed is completely covered with sediment. Constants and parameters used for the TLEM are the same as in the SEM and are listed in Table 3.2.

The major differences between the TLEM and the SEM are that: (1) the effective impact velocity $w_{i,eff}$ (TLEM) increases monotonically with transport stage as it accounts for the effect of turbulence causing particle collisions with the bed whereas w_{si} tends to 0 at large transport stages (and therefore $\dot{e}_{salt}$ approaches 0) as particle trajectories become parallel to the bed, and (2) the fraction of the bed exposed in the TLEM $(1 - q_b/q_{tc})$ uses the bed load flux (q_b) as contributing to the cover. This means that as the transport stage increases, the fraction of bedrock exposed in the TLEM is higher than in the SEM, provided a significant portion of the sediment is transported in suspension.

Erosion model simplifications

We calculate erosion rates with a constant particle diameter ($D = 60$ mm) and assume that this particle size is representative of the median grain size in an R-channel. This choice is consistent with Riihimaki and others (2005) who report a median grain size corresponding to very coarse gravel in the proglacial area of Bench Glacier, Alaska. We assume that the bedrock has a uniform resistance to erosion, erosion occurs uniformly across the width of a channel, abrasion is the main erosion mechanism and that the cover effect is linear. A linear cover effect means that as long as the bed is partially exposed, newly deposited particles are

assumed to cover bedrock rather than previously deposited sediment, hence the exponent of one on the "cover" fraction q_s/q_{tc} (cf. Turowski and others, 2007). We also neglect sediment transport and the effect of downstream fining.

3.3 Modelling strategy and rationale

The model outlined above involves numerous variables and parameters leading to feedbacks. Applications of the model of erosion by abrasion in rivers (e.g. Sklar and Dietrich, 2004, 2006, 2008; Turowski and others, 2007; Lamb and others, 2008a; Chatanantavet and Parker, 2009; Nelson and Seminara, 2011; Egholm and others, 2013) show that the primary dependencies are: the transport stage, the relative sediment supply and the hydraulic potential gradient. Numerical modelling studies of subglacial water flow emphasize the importance of the frequency and amplitude of the water input forcing and of the ice and bed geometry (e.g., Flowers, 2008; Creyts and Schoof, 2009; Schoof, 2010; Hewitt, 2013; Werder and others, 2013; Beaud and others, 2014), although few studies have discussed the shear stress on channel walls (e.g., Clarke, 2003). In an effort to identify the key variables, parameters and feedbacks, we start with simple experiments and build up the complexity. The simulations are separated in two subsections: (1) steady-state decoupled simulations of a channelized drainage system only (Table 3.3) and (2) transient simulations of a coupled channelized and distributed drainage system (Table 3.4).

In the steady-state simulations (Table 3.3), we first assess the erosion pattern resulting from a constant discharge along the glacier bed. Then we introduce a water forcing that increases with decreasing ice-surface elevation and test the effect of ice geometry and sediment supply. Additional experiments assessing the effect of water flow through a network of cavities, water input, sediment size, and channel wall and bed roughness are shown in the Supplement. In the transient simulations (Table 3.4) we first analyze the role of a synthetic melt season, then use water forcing following realistic melt seasons and test the role of ice geometry, channel density and sediment supply.

As per the theory on which the SEM (Sklar and Dietrich, 2004) and TLEM (Lamb and others, 2008a) are based, sediment supply, through the tools and cover effects, exerts a major control on erosion rates and patterns by water flow beneath glaciers. Although it is possible to estimate sediment supply to rivers (e.g., Gurnell and others, 1996; Willis and others, 1996; Kirchner and others, 2001; Orwin and Smart, 2004; Sklar and Dietrich, 2004; Riihimaki and others, 2005; Turowski and others, 2009; Mao and others, 2014), no method exists to quantify subglacial sediment supply or transport. In glacierized catchments, measurements are usually made in the proglacial stream, relatively close to the terminus (e.g., Warburton, 1990; Gurnell and others, 1996; Willis and others, 1996; Orwin and Smart, 2004; Riihimaki and others, 2005; Swift and others, 2005; Mao and others, 2014), where water flow is subaerial and potentially influenced by channel dynamics between the glacier

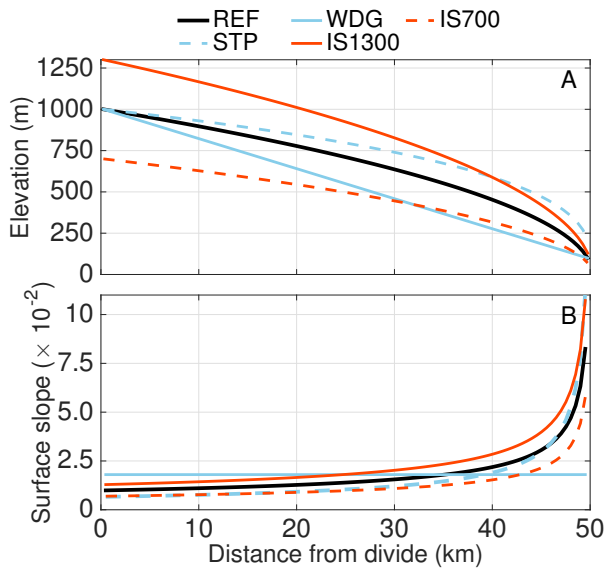

Figure 3.1: (A) Different ice geometries considered (see Tables 3.3 and 3.4) and (B) corresponding ice-surface slopes. The geometries REF, IS1300 and IS700 are parabolas such that the surface elevation is given by $z_s(x) = z_{s,max}\sqrt{x}$, where $z_{s,max}$ is the maximum ice-surface elevation and $x \in [1, 0]$. In order to obtain the steeper front in STP we use a cubic root instead of the square root: $z_s(x) = z_{s,max}x^{1/3}$. The wedge-like geometry WDG is defined by a straight line with the same elevation change as REF.

terminus and the measurement station (Warburton, 1990; Orwin and Smart, 2004; Mao and others, 2014). In the steady-state simulations we impose a sediment supply that leads to an interesting and diverse range of simulations illustrating most processes and their feedbacks, whereas in the transient simulations we choose a sediment supply that leads to a sediment yield at the last node equivalent to a few millimetres of glacial erosion per year.

We use a flat bed and a parabolic surface for all but two geometries: STP and WDG (Fig. 3.1). The STP geometry aims at reproducing the steep front of an advancing ice sheet, while the WDG geometry has a wedge shape that resembles the profile of a thinning and retreating ice sheet margin. We assume that water input is distributed uniformly (no moulins) along the bed except for the simulation S_MOULIN. For almost all simulations we fix the sediment supply per unit width; the total sediment supply therefore increases with channel size. This is similar to the assumption of a uniform till distribution across the width of the glacier in which the channelized water flow sources its sediment.

3.4 Results

All quantities related to the erosion model are given per unit width of flow. The cross-sectional area of a subglacial channel (S), thus its width ($W_{ch} = 2\sqrt{2S/\pi}$), changes more rapidly with distance along the flow path than a typical subaerial river. We need to account

Table 3.3: Summary of steady-state simulations. For simulations in which meltwater input is a function of ice-surface elevation z_s, we compute $f(z_s(x)) = \dot{b}_{ss\,max} \times (1 - (z_s(x) - z_{s,min})/z_{s,max})$, where $\dot{b}_{ss\,max} = 8.5 \times 10^{-7}\,m\,s^{-1}$ is the maximum melt water input rate to the channelized drainage system, and $z_{s,min}$ and $z_{s,max}$ are respectively the minimum and maximum ice-surface elevations. Note that $\dot{b}_{ss\,max} = 8.5 \times 10^{-7}\,m\,s^{-1}$ corresponds to 7.6 cm of ice melt per day assuming $\rho_i = 910\,kg\,m^{-3}$. The reference sediment supply used for the steady-state simulations is: $q_{s,ref} = 3.6 \times 10^{-3}\,m^2\,s^{-1}$ (Table 3.2).

Simulation	Purpose	Forcing	Difference from reference run	Section
S_MOULIN	R-channel only	$Q_{ch}(x = 0, t) = 4.25\,m^3\,s^{-1}$	Localized input upstream boundary	3.4.1
S_REF	Reference	$\dot{b}_{ch,ref}(x, t) = f(z_s(x))$		3.4.1
S_WDG	Ice geometry	$\dot{b}_{ch}(x, t) = \dot{b}_{ch,ref}$	Constant ice-surface slope $d\phi_0/dx = cst$	3.4.1
S_STP	Ice geometry	$\dot{b}_{ch}(x, t) = \dot{b}_{ch,ref}$	Steeper and thicker terminus	3.4.1
S_1300	Ice geometry	$\dot{b}_{ch}(x, t) = \dot{b}_{ch,ref}$	$z_{s,max} = 1300\,m$	3.4.1
S_700	Ice geometry	$\dot{b}_{ch}(x, t) = \dot{b}_{ch,ref}$	$z_{s,max} = 700\,m$	3.4.1
S_SSP	Sediment supply	$\dot{b}_{ch}(x, t) = \dot{b}_{ch,ref}$	$q_s = q_{s,ref}/20 - q_{s,ref} \times 25$	3.4.1

for these changes when displaying the results, and therefore introduce three quantities: the total transport capacity $Q_{tc} = q_{tc} W_{ch}\,(m^3\,s^{-1})$, the total erosion computed with the TLEM $E_{tot} = \dot{e}_{tot} W_{ch}\,(m^2\,s^{-1})$ and the total erosion computed with the SEM $E_{salt} = \dot{e}_{salt} W_{ch}\,(m^2\,s^{-1})$.

3.4.1 Steady-state decoupled simulations

We examine basic steady-state behaviour of key model variables such as R-channel cross-sectional area (S), transport capacity (q_{tc}), impact velocity (w_{si} and $w_{i,eff}$), transport stage (τ^*/τ_c^*) and relative sediment supply (q_s/q_{tc}). In the steady-state simulations, the drainage system is composed of a single R-channel. Simulations are terminated once dependent variables (S and ϕ_{ch}) reach steady-state. In this series of simulations, unless stated otherwise, we impose the sediment supply $q_s = 3.6 \times 10^{-3} m^2\,s^{-1}$ to produce an interesting and diverse range of model behaviour.

R-channel with constant discharge

In the S_MOULIN simulation we use the reference glacier geometry (Fig. 3.1, REF) and the water input is imposed at the uppermost node only, i.e. as if a moulin were feeding the system. This permits us to drive the system with a constant water discharge and to analyse the resulting relation between discharge, channel cross-sectional area, velocity, instantaneous erosion rates and transport capacity patterns.

Table 3.4: Summary of transient simulations. In this series of simulations the basal sliding speed is $u_b = 5\,\mathrm{m\,a^{-1}}$ and the reference sediment supply is $q_{s,ref} = 9.1 \times 10^{-3}\mathrm{m^2\,s^{-1}}$ (Table 3.2). Water is fed to the network of cavities rather than the channel, hence $\dot{b}_{ch} = 0\,\mathrm{m\,s^{-1}}$, and the function of surface elevation is that of the steady-state simulations (Table 3.3).

Simulation	Purpose	Description	Section
T_REF	Reference transient	Reference geometry and synthetic water input	3.4.2
T_2007	Realistic forcing	2007 surface-melt time series	3.4.2
T_2008	Realistic forcing	2008 surface-melt time series	3.4.2
T_1300	Ice geometry	$z_{s,max} = 1300\,\mathrm{m}$	3.4.2
T_700	Ice geometry	$z_{s,max} = 700\,\mathrm{m}$	3.4.2
T_W500	Drainage catchment width	$W = 500\,\mathrm{m}$, i.e. 2 R-channels	3.4.2
T_W333	Drainage catchment width	$W = 1000/3\,\mathrm{m}$, i.e. 3 R-channels	3.4.2
T_W250	Drainage catchment width	$W = 250\,\mathrm{m}$, i.e. 4 R-channels	3.4.2
T_SSP/4	Sediment supply	$q_s = q_{s,ref}/4$	3.4.2
T_SSP/2	Sediment supply	$q_s = q_{s,ref}/2$	3.4.2
T_SSPOPT	Sediment supply	Optimized erosion; $q_s = 0.6 \times q_{tc}$	3.4.2

Although discharge is constant (Fig. 3.2a), the cross-sectional area of the R-channel changes along the profile (Fig. 3.2a) due to the ice geometry (Fig. 3.1). Over the first 46 km, the cross-sectional area decreases in response to the steepening hydraulic potential gradient (Fig. 3.2b), the latter being a function of ice-surface slope (Fig. 3.1). Close to the terminus (last 4 km of the profile), the ice thins significantly, the hydraulic potential gradient shallows (by a factor 3) and the cross-sectional area increases. The average water velocity assumes the opposite pattern (Fig. 3.2b). Because the grain size is kept constant, $q_{tc} \propto (\tau^* - \tau_c^*)^{3/2}$, the rate of sediment transport (Fig. 3.2c) is amplified relative to the velocity (q_{tc} drops by a factor 6 while u is reduced by about 50%); both have maxima at 46 km and decrease sharply near the terminus. In this simulation the sediment transport capacity is always larger than the supply rate (Fig. 3.2c), exposing most of the bed ($F_e > 0.5$).

In both the TLEM and SEM, near-bed sediment concentration and impact rate are described as a function of the sediment supply and the hop trajectory of a particle, so they are similar (Fig. 3.2d). As the velocity increases (km 0–46) the sediment is transported faster and further from the bed and the near-bed sediment concentration and impact rate decrease.

Impact velocities (Fig. 3.2e) vary depending on the model. In the SEM the impact velocity tends toward zero as the hop length increases and the particles approach transport in suspension, which leads to a local minimum around km 46. The TLEM accounts for the effect of turbulent eddies on the trajectory of particles close to the bed, thus the effective impact velocity is commensurate with the velocity and peaks around km 46.

Erosion rates (Fig. 3.2f) in both the SEM and TLEM show a minimum at 46 km and a maximum close to the terminus. The minimum and maximum correspond respectively to the minimum and sharp rise in near-bed sediment concentration or impact rate. Even

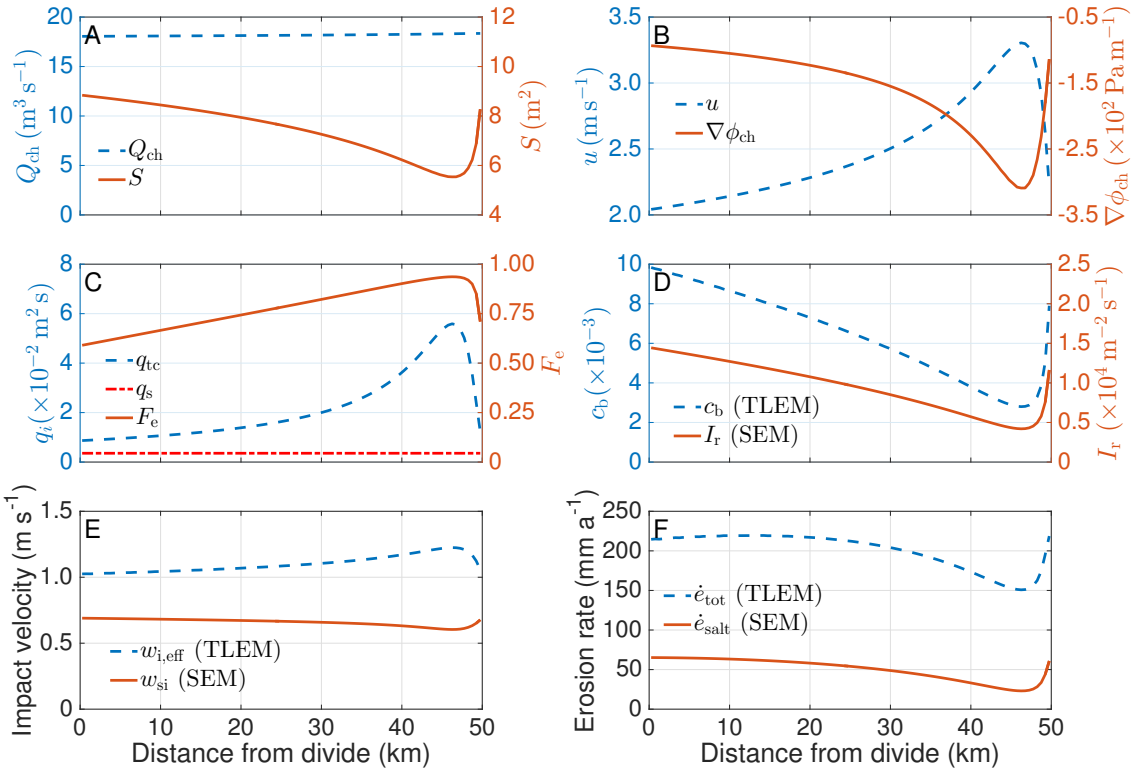

Figure 3.2: Relationship between the hydraulic and erosion variables in a steady-state R-channel with constant discharge (Table 3.3, S_MOULIN; Sect. 3.4.1). Components of the TLEM and SEM models are also compared. (A) R-channel discharge, Q_{ch} and cross-sectional area S; (B) Velocity, u and gradient in hydraulic potential, $\nabla\phi_{ch}$; (C) Sediment transport capacity, q_{tc}, prescribed sediment supply rate, q_s and fraction of bed exposed, F_e; (D) Near-bed sediment concentration, c_b (TLEM) and impact rate, I_r (SEM); (E) Impact velocity in the TLEM, $w_{i,eff}$ and the SEM, w_{si}; (F) Erosion rate calculated with the TLEM, $\dot{e}_{tot}$ and the SEM, $\dot{e}_{salt}$.

under a constant discharge, ice surface slope and channel size produce a peak in velocity just upstream of the terminus. At this peak, the flow has the power to lift particles far enough from the bed to reduce erosion in both the SEM and TLEM. Erosion rates are higher with the TLEM than the SEM due to the difference in impact velocities when the sediment transport regime approaches suspension. For the transport stages we obtain, impact velocities with the TLEM are consistently higher than with the SEM. Moreover for relatively large transport stages, more of the bed is exposed in the TLEM: when some fraction of the total load travels in suspension, i.e. $q_s > q_b$.

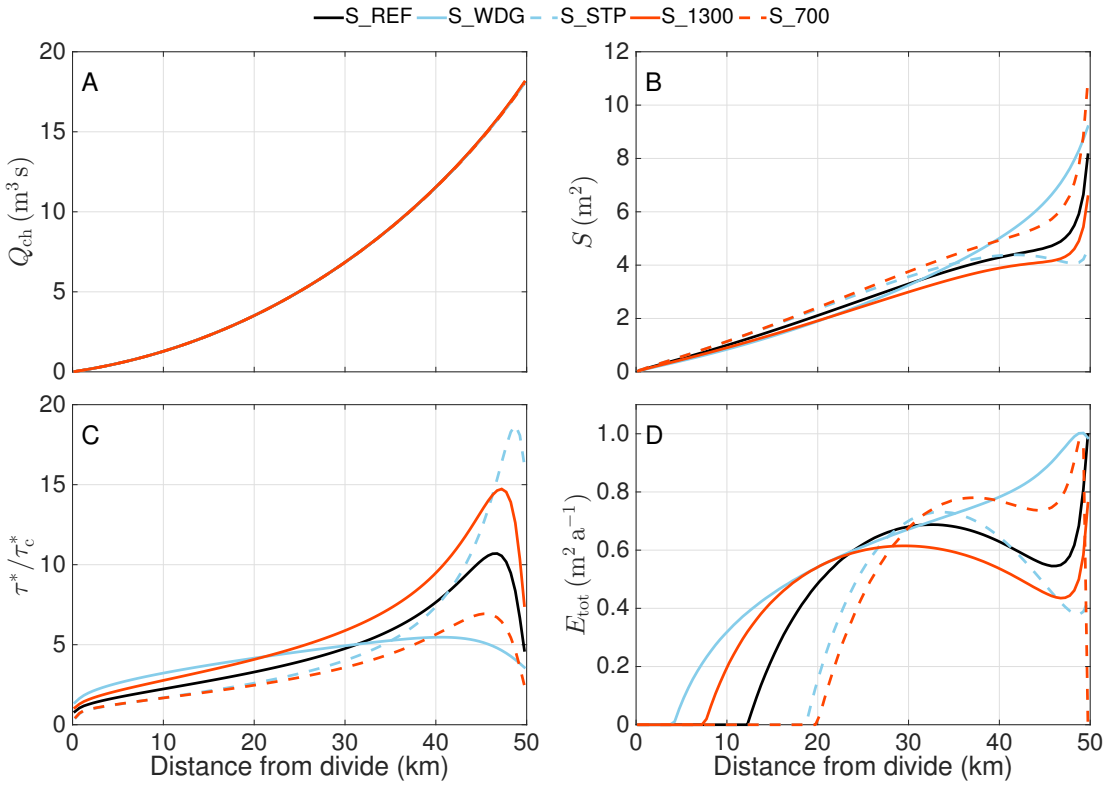

Figure 3.3: Comparison of steady-state simulations with varying ice geometries, reference water input and drainage through a single R-channel (Table 3.3). (A) Discharge in the channel, Q_{ch} (all curves overlap); (B) Channel cross-sectional area, S; (C) Transport stage, τ^*/τ_c^*; (D) Total erosion computed with the TLEM (E_{tot}).

Ice geometry

The surface slope of a glacier is a first-order control on subglacial water flow (Eqs. (3.1)–(3.2)). We experiment with thicker ice (IS1300, Fig. 3.1), thinner ice (IS700, Fig. 3.1) and steeper ice-surface slopes close to the terminus (STP, Fig. 3.1), all compared to the reference ice geometry (REF, Fig. 3.1). Shallower surface slopes close to the terminus are tested with a wedge-like geometry of constant surface slope (WDG, Fig. 3.1). All these simulations (Fig. 3.3; see Table 3.3) employ the surface melt profile of S_REF and therefore yield nearly identical discharge profiles (Fig. 3.3a). The water input is a function of the ice-surface elevation (Table 3.3), hence the discharge is largest close to the terminus.

The thinner the ice close to the terminus the larger the channel (Fig. 3.3b) and the lower the transport stage (Fig. 3.3c). In the case of S_STP, the combination of a particularly steep hydraulic potential gradient and relatively thick ice near the terminus inhibits channel enlargement over the last 5–10 km as observed in other simulations (Fig. 3.3b). Since the discharge profile is the same for the simulations presented, the smaller the channel, the faster

the flow and hence the larger the transport stage. The maximum transport stage for the simulation with the steepest terminus (S_STP, $\tau^*/\tau_c^* \approx 18.5$, Fig. 3.3c) is almost four times larger than that for the simulation with the shallowest terminus (S_WDG, $\tau^*/\tau_c^* \approx 5.5$, Fig. 3.3c; see Fig. 3.1 and Table 3.3). Over the first 25 km of the profile the simulation with a constant ice-surface slope (S_WDG) shows the steepest hydraulic potential gradient, creating comparatively higher transport stages than other models.

Erosion begins around km 4 for S_WDG (Fig. 3.3d), and around km 19–20 for S_STP and S_700 (Fig. 3.3d), because for the prescribed sediment supply, the bed becomes exposed for transport stages $\tau^*/\tau_c^* \gtrsim 2.5$. All simulations but S_WDG have a local maximum in total erosion (E_{tot}, Fig. 3.3d) between km 30 and 37 and a local minimum between km 45 and 49. The sediment supply per unit width is constant, therefore the relative sediment supply decreases as the transport stage increases. The erosion rate per unit width thus decreases when $q_s/q_{tc} < 0.5$ because the number of tools decreases. For simulation S_WDG the increase in channel size compensates for the small decrease in erosion rate per unit width (not shown) because the transport stage remains relatively low ($\tau^*/\tau_c^* < 6$). Over the last few kilometres of the profile, total erosion increases again for the simulations in which transport stage drops to moderate values (S_REF and S_1300). Total erosion drops sharply at the terminus for S_700 as the transport stage drops below 2.5. When the transport stage remains relatively high ($\tau^*/\tau_c^* > 15$) the number of tools remains low, as does total erosion (S_STP, Fig. 3.3c and 3.3d). Ice geometry exerts a primary influence on transport stage and erosion patterns via its control on hydraulic potential gradients and channel size. Simulation S_WDG yields the most erosion, despite relatively low transport stages, illustrating the importance of the tools effect (e.g., Sklar and Dietrich, 2006).

Sediment supply

Tools and cover compete so that both a lack and an overabundance of tools hinder erosion. Sklar and Dietrich (2004) and Lamb and others (2008a) have shown that erosion peaks for a given flow regime at an optimum relative sediment supply. We thus investigate how varying sediment supply ($q_s = 1.8 \times 10^{-4}$ to $8.9 \times 10^{-2}\,m^2\,s^{-1}$) affects the rates and patterns of subglacial meltwater erosion, while the subglacial hydraulic regime remains that of S_REF (Fig. 3.3; Table 3.3).

For sediment supply rates $q_s \leq q_{s,ref} \times 2$ (Fig. 3.4a) the patterns of total erosion with the TLEM and SEM (Fig. 3.4b and 3.4c) show the same features as in Fig. 3.3: no erosion in the uppermost part of the profile followed by a local maximum around mid-profile, a local minimum around km 46–47 and a sharp rise in the last 3 km. For larger sediment supply $q_s \geq q_{s,ref} \times 5$, the patterns change and have a single maximum only. If the relative sediment supply satisfies $q_s/q_{tc} > 0.3$ (Fig. 3.4a) the number of tools remains high enough for total erosion to increase with transport stage (τ^*/τ_c^*) as the increase in channel size compensates for the small drop in erosion per unit width $\dot{e}_{tot}$ when $q_s/q_{tc} < 0.5$.

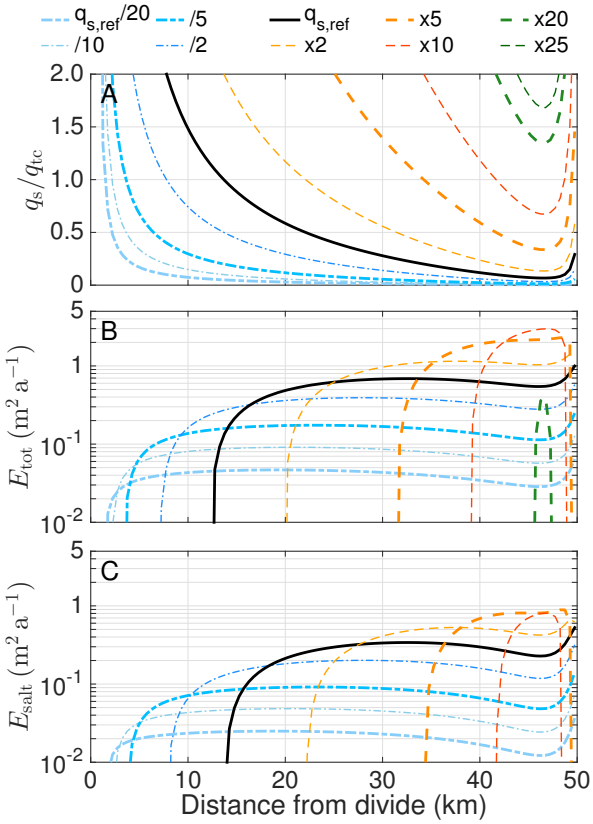

Figure 3.4: Influence of sediment supply rate q_s (S_SSP, Table 3.3) on total erosion with the TLEM and SEM for the same hydrology as the reference simulation (S_REF, Table 3.3). The legend applies to all panels. (A) Relative sediment supply (q_s/q_{tc}); (B) Total erosion rate computed with the TLEM (E_{tot}); (C) Total erosion rate computed with the SEM (E_{salt}). Note the logarithmic scale on the y-axis of (B) and (C).

Erosion occurs over 48 km of the bed (S_SSP, $q_{s,ref}/20$) in both the SEM and TLEM for the lowest sediment supply, whereas the bed is almost completely shielded for the second largest sediment supply (S_SSP, $q_{s,ref} \times 20$) and erosion occurs only between km 46 and 48 in the TLEM (Fig. 3.4). The SEM treats the whole sediment supply as participating in the cover effect, and the bed is shielded as soon as $q_s/q_{tc} \leq 1$. The TLEM discriminates between transport as bedload and in suspension, therefore if $q_b < q_s$ the bed can remain partially exposed even for a relative sediment supply $q_s/q_{tc} \geq 1$. The erosion window is therefore larger for the TLEM (Fig. 6 in Lamb and others, 2008a). The fact that erosion rates computed with the TLEM are higher than those computed with the SEM is inherent to the model formulation (Lamb and others, 2008a).

An interesting conclusion arising from Fig. 3.4 is that total erosion is significant over most of the bed (Fig. 3.4b and 3.4c) when the sediment supply rate is relatively low ($q_s \leq q_{s,ref} \times 2$; Fig. 3.4a). Total erosion becomes more localized at higher relative sediment supply

rates. Changing the particle diameter (D), instead of sediment supply (q_{s}), leads to similar changes in relative sediment supply and therefore in erosion patterns (see Supplement). The transport stages calculated are large enough to produce significant differences between the SEM and TLEM for large relative sediment supplies. Hereafter, we focus on the TLEM only in the results as it is more appropriate for the flow conditions encountered beneath glaciers.

3.4.2 Transient coupled simulations

Arguably, most erosion and sediment transport in fluvial systems occur during flood events (e.g., Whipple and others, 2000, 2013; Kirchner and others, 2001; Sklar and Dietrich, 2004; Lamb and others, 2008a; Turowski and others, 2009; Lamb and Fonstad, 2010; Cook and others, 2013). In glacial environments large daily variations in melt-water input to the glacier bed can be likened to periodic flooding (e.g., Willis and others, 1996). We perform a series of transient simulations with a cavity network coupled to an R-channel (Eqs. (3.1), (3.2), (3.3) and (3.4)) to explore how the transience in subglacial water flow is affected by changes in ice thickness, surface melt and sediment supply, and how this transience impacts instantaneous and annually integrated erosion rates. In this series of simulations, we choose the sediment supply ($q_{\mathrm{s,ref}} = 9.1 \times 10^{-3}\mathrm{m}^2\,\mathrm{s}^{-1}$) such that the modelled sediment yield ($\int \min(q_{\mathrm{s}}(X_{\mathrm{L}})W_{\mathrm{ch}}(X_{\mathrm{L}}), Q_{\mathrm{tc}}(X_{\mathrm{L}}))\mathrm{d}t$) corresponds to an inferred basin-wide erosion rate of a few millimetres of erosion per year (e.g., Gurnell and others, 1996; Hallet and others, 1996; Koppes and Montgomery, 2009).

Reference model

The reference model uses a synthetic forcing in the form of water supply to the distributed system ($\dot{b}_{\mathrm{ca}}$, Eq. (3.3); sinusoid with a period of 120 days on which we superimpose daily fluctuations) and the reference glacier geometry (Fig. 3.1, REF; Table 3.4, T_REF). The sediment supply rate per unit width is assumed to be uniform along the bed. With this simple test we explore how the transience in water input and response of the subglacial drainage system affect transport stage and erosion rate. Modelling subglacial water flow through coupled distributed and channelized drainage systems has been described extensively in recent literature (see Table 3 in Flowers, 2015), so we omit a discussion of the drainage system itself and focus instead on how subglacial hydrology affects transport stage and erosion.

Since the sediment supply is fixed, transport stage (Fig. 3.5a) and relative sediment supply (Fig. 3.5b) are anti-correlated. The time transgression in transport stage and relative sediment supply is a result of the upglacier incision of R-channels. Once a channel is well developed, water pressure decreases in the channel, as does water velocity and transport stage (Fig. 3.5a). Daily fluctuations are only detectable close to the terminus, where a

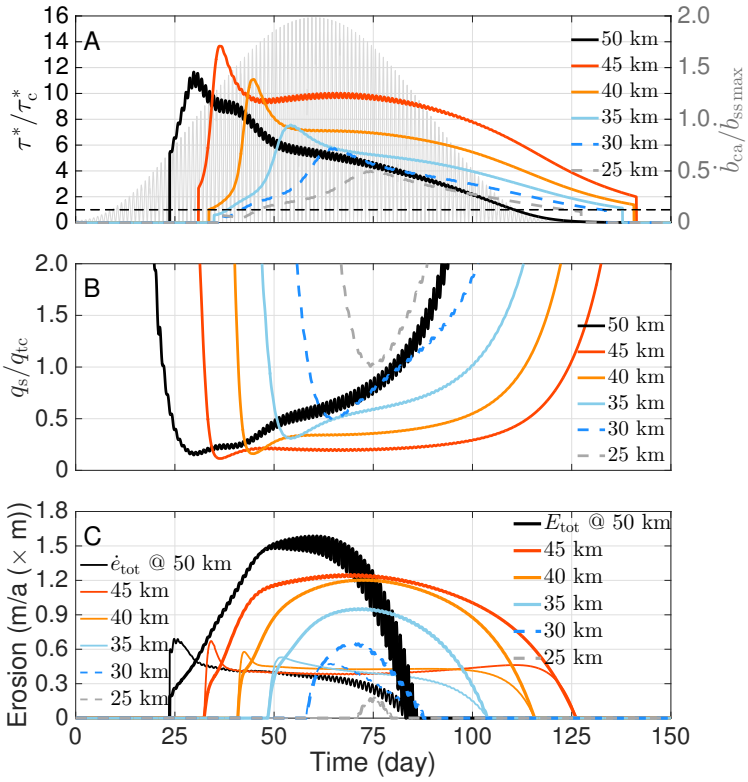

Figure 3.5: Timeseries at six different distances from the divide (km 50, 45, 40, 35, 30 and 25) for simulation T_REF (Table 3.4). (A) Transport stage (τ^*/τ_c^*) and normalized meltwater input ($\dot{b}_{ca}/\dot{b}_{ss\,max}$) at the terminus (light grey). The dashed line represents the threshold for sediment motion: $\tau^*/\tau_c^* = 1$. (B) Relative sediment supply q_s/q_{tc}. (C) Erosion per unit width $\dot{e}_{tot}$ ($m\,a^{-1}$, thin lines) and total erosion E_{tot} ($m^2\,a^{-1}$, thick lines) computed with the TLEM.

channel is relatively well developed. Similar to what we find in the steady-state simulations, the largest transport stages are found a few kilometres up-glacier from the terminus. The bed remains shielded over the first 25 km from the ice divide. The time window during which erosion occurs ($q_s/q_{tc} \lesssim 1 - 1.5$) is longest at km 45 and decreases up- and down-glacier. The size of the R-channel at the terminus (km 50) after day 80 becomes large enough that the transport stage (Fig. 3.5a) is insufficient to maintain an exposed bed. Further upstream from km 45, the hydraulic potential gradient shallows and the discharge decreases so that the bed is exposed for a shorter time.

Erosion per unit width ($\dot{e}_{tot}$, Fig. 3.5c) peaks when the relative sediment supply satisfies $0.25 \leq q_s/q_{tc} \leq 0.4$, i.e. at the onset of R-channel formation, even before the peak in transport stage for the lowermost 15 km (km 35–50 in Fig. 3.5). The peak in erosion is followed by relatively constant values and eventually an abrupt drop. At the terminus,

erosion ceases due to low shear stress in the relatively large channel, while upstream erosion ceases due to declining water supply. Note that erosion can occur after the melt season ends (day 120) at km 45 because water remains stored englacially and subglacially (Eq. (3.3)). Further up-glacier (km 25–30) the maximum erosion per unit width coincides with the minimum in relative sediment supply, as the latter remains larger than 0.5 and enough tools are available close to the bed.

Patterns of total erosion (E_{tot}, Fig. 3.5c, thick lines) all peak between day 65 and 75, except at the terminus (km 50). The initial peak in erosion per unit width occurs while the channel is small, thus total erosion is largely controlled by channel size over most of the record. Simulations with transient meltwater input highlight the role of channel size in controlling transport stages and erosion close to the terminus.

Surface melt

We vary the amount of water reaching the bed to explore the differences between using synthetic and realistic melt records. The realistic melt records come from the ablation area of an unnamed glacier in the Saint Elias Mountains, Yukon, Canada, in 2007 and 2008 (Wheler and others, 2014). We scale the 2007 melt record (T_2007, Table 3.4) so that the total volume of water is identical to the synthetic input. The melt timeseries from 2008 (T_2008, Table 3.4) is then scaled such that the ratio of 2007 to 2008 melt volumes is preserved. This test is intended to highlight the importance of total melt volume and the temporal structure of meltwater input.

When we apply the realistic forcing from 2007 (T_2007), the transport stage exhibits four to five peaks (Fig. 3.6a) at km 35, 42.5 and 50. At these three locations, the first peak occurs once enough water is supplied to the bed to form a channel (Fig. 3.6a; after 45 days at 42.5 km and 50 km, and after 75 days at 35 km). The subsequent peaks in transport stage (after day 60 at 42.5 km and 50 km and after day 80 at 35 km) follow periods of high melt. After day 45, the transport stage remains highest at 42.5 km because creep closure prevents R-channels from becoming too large and water discharge is high enough to maintain high velocities. At km 20 and 27.5 it takes about 60 days for the first peak in transport stage to occur. The subsequent peaks at these two locations (around day 90, 105 and 129) lag high melt periods even further.

Given the prescribed sediment supply rate, the bed is only exposed at transport stages larger than 3.5. Erosion (Fig. 3.6b; $\dot{e}_{\text{tot}}$ and E_{tot}) at km 27.5 and 50 therefore only occurs during peaks in transport stage; at km 20 the bed is always covered. Erosion rate per unit width ($\dot{e}_{\text{tot}}$, Fig. 3.6b) plateaus at moderate transport stages, thus it remains relatively constant once the bed is partially exposed. On the other hand, total erosion (E_{tot}, Fig. 3.6b) peaks with transport stage (Fig. 3.6a). Similar results are obtained for T_2008 (Fig. 3.6c and 3.6d), where a different melt timeseries is employed. While the amplitudes of the fluctuations of meltwater input are a few times larger in T_2008 than T_2007 (Fig. 3.6a

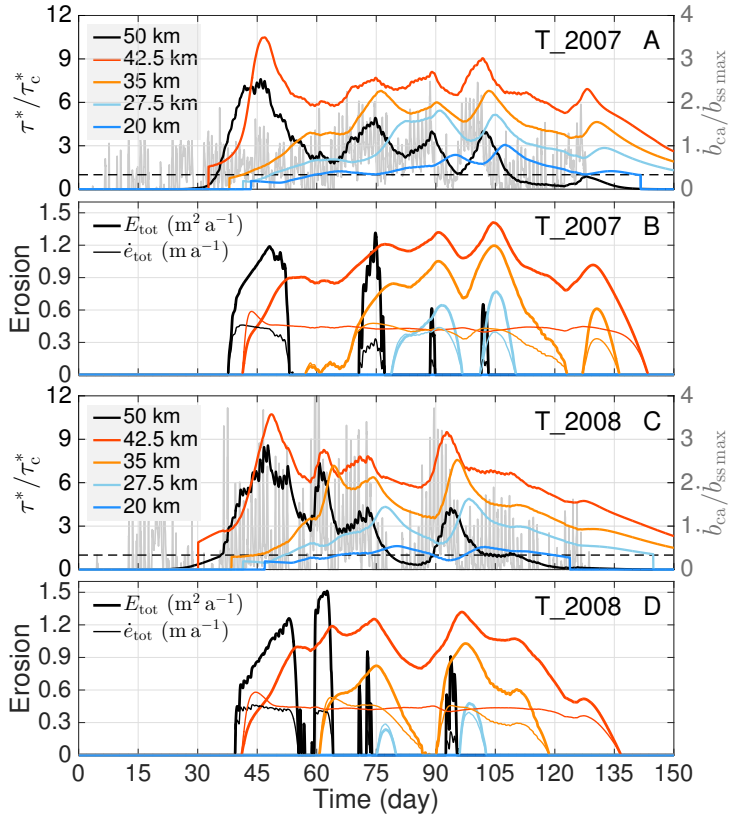

Figure 3.6: Timeseries of transport stage and erosion rates for two realistic water input timeseries (Table 3.4, T_2007 and T_2008) at five different distances from the divide (km 20, 27.5, 35, 42.5 and 50). (A) Transport stage (τ^*/τ_c^*) and normalized meltwater input ($\dot{b}_{ca}/\dot{b}_{ss\,max}$) at the terminus (light grey) for simulation T_2007. (B) Erosion rate per unit width $\dot{e}_{tot}$ (thin lines) and total erosion E_{tot} (thick lines) for simulation T_2007. (C) Transport stage (τ^*/τ_c^*) and normalized meltwater input ($\dot{b}_{ca}/\dot{b}_{ss\,max}$) at the terminus (light grey) for simulation T_2008. (D) Erosion rate per unit width $\dot{e}_{tot}$ (thin lines) and total erosion E_{tot} (thick lines) for simulation T_2008. The dashed lines in (A) and (C) represent the threshold for sediment motion: $\tau^*/\tau_c^* = 1$.

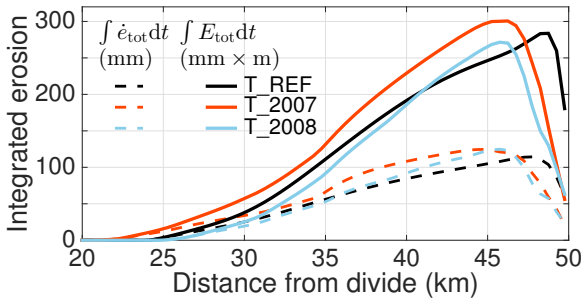

Figure 3.7: Comparison of time-integrated erosion per unit width ($\int \dot{e}_{\mathrm{tot}}\mathrm{d}t$) and total erosion ($\int E_{\mathrm{tot}}\mathrm{d}t$) for different water inputs. The first 20 km of the profile are not shown because the bed is alluviated and erosion rates are negligible.

and 3.6c), the total melt in T_2008 is about 80% that of T_2007. These realistic meltwater forcings produce episodic variations in transport stage and erosion rate that suggest multi-day fluctuations in meltwater input are important.

These multi-day variations in water input also lead to a succession of channel enlargement events (Fig. 3.6a and 3.6c), represented by multiple peaks in transport stage (τ^*/τ_c^*). On the time scale of several days, creep closure near the terminus is low enough that a channel is sustained between the melt events, leading to an up-glacier migration of relatively large transport stages and integrated erosion. Thus, the pressure in the channel close to the terminus, and hence transport stage, is low. This results in the integrated total erosion ($\int E_{\mathrm{tot}}\mathrm{d}t$) being about three times lower for realistic inputs (Fig. 3.7, T_2007 and T_2008) than for the synthetic one (Fig. 3.7, T_REF) at the terminus. For the same total water input (T_REF and T_2007), the realistic melt-season produces more erosion averaged over the glacier bed than the synthetic input (8×10^{-2} mm for T_2007 versus $\sim 7 \times 10^{-2}$ mm for T_REF).

Ice geometry

Studies of sediment yield from glacierized catchments (e.g., Hallet and others, 1996; Koppes and Hallet, 2002, 2006; Koppes and Montgomery, 2009) conclude that glaciers are more erosive during retreat than during advance due to the amount of meltwater production. Glacier thinning (or thickening) during a phase of retreat (or advance) will also impact the development of the subglacial drainage system and hence its ability to flush sediments and erode the bed. In this series of model tests we hold the sediment supply fixed and vary the glacier geometry by changing the maximum ice thickness (Fig. 3.1, T_REF, T_1300, T_700, Table 3.4), while the water input remains the same. As we have already described the principal mechanisms responsible for fluctuations in erosion rates in previous sections, we now focus on annually integrated erosion.

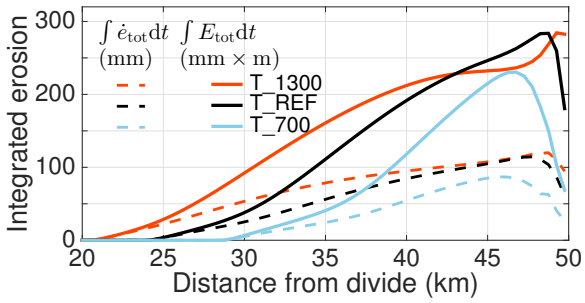

Figure 3.8: Comparison of time-integrated erosion per unit width ($\int \dot{e}_{\mathrm{tot}} \mathrm{d}t$) and total erosion ($\int E_{\mathrm{tot}} \mathrm{d}t$) for different ice geometries. The first 20 km of the profile are not shown because the bed is alluviated and erosion rates are negligible.

For all ice geometries tested in Fig. 3.8 (T_1300, T_700 and T_REF, Table 3.4), significant erosion only occurs downglacier of km 20. The thicker the ice, the further upglacier significant erosion (both $\int \dot{e}_{\mathrm{tot}} \mathrm{d}t$ and $\int E_{\mathrm{tot}} \mathrm{d}t$) occurs (up to km 21 for T_1300 and km 29 for T_700). In these tests, thicker ice also means steeper surface slopes (Fig. 3.1). Since water input is identical for these simulations, steeper surface slopes lead to faster water flow and the possibility of initiating sediment motion further up glacier. At the terminus almost four times as much erosion occurs for T_1300 than T_700 because thick ice prevents the growth of a large channel.

Subglacial drainage catchment width of a channel

Hydraulic properties of the distributed drainage system determine the density of channels that form (e.g., Werder and others, 2013). The smaller the channel spacing, the lower the discharge in a single channel. A smaller channel, at equilibrium, yields larger water pressures, so we expect that more water would be evacuated through the cavity network. In this test we fix the total glacier width at 1000 m and allow two, three or four channels to form such that channel catchment widths (W) are, respectively, 500, 333 and 250 m (T_W500, T_W333, T_W250; Table 3.4).

If we consider the erosion in a single R-channel per simulation (Fig. 3.9a), the smaller the drainage catchment width, the smaller the discharge, and the smaller the time-integrated erosion (Fig. 3.9a; $\int \dot{e}_{\mathrm{tot}} \mathrm{d}t$ and $\int E_{\mathrm{tot}} \mathrm{d}t$). The feedback causing erosion rate per unit width to decrease at large transport stages (cf. Fig. 3.2) is such that even for the simulations where the drainage catchment width is relatively small, erosion rates are comparable ($\int \dot{e}_{\mathrm{tot}} \mathrm{d}t$, Fig. 3.9a) despite the lower transport stages. The differences are, however, relatively large for the annually integrated total erosion (maximum $\int E_{\mathrm{tot}} \mathrm{d}t$ for T_REF is more than twice that of T_W250, Fig. 3.9a) because of the effect of channel size.

The hierarchy in total integrated erosion is inverted when all R-channels within a fixed glacier width are accounted for (Fig. 3.9b, between km $\sim$ 37 and $\sim$ 48). Once the number of

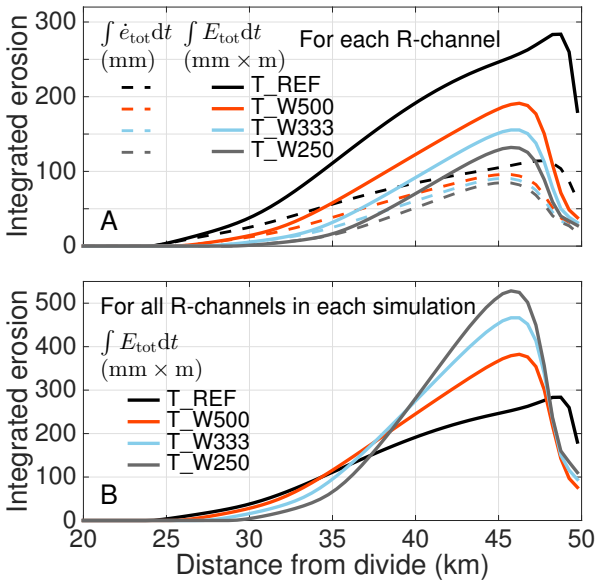

Figure 3.9: Influence of drainage catchment width (W) on time-integrated erosion. (A) Time-integrated erosion per unit width ($\int \dot{e}_{\mathrm{tot}}\mathrm{d}t$) and total erosion ($\int E_{\mathrm{tot}}\mathrm{d}t$) for an individual R-channel. (B) Time-integrated total erosion ($\int E_{\mathrm{tot}}\mathrm{d}t$) summed over all R-channels in each simulation. The first 20 km of the profile are not shown because the bed is alluviated and erosion rates are negligible.

R-channels present is taken into account, integrated total erosion is largest for the smallest channel catchment (almost twice as large for T_W250 than T_REF, Fig. 3.9b). In this case, numerous small channels therefore produce more erosion than few large ones.

At the terminus (km 50), the simulations with a catchment width per channel smaller than that in T_REF show values of annually integrated erosion ($\int E_{\mathrm{tot}}\mathrm{d}t$) of about half that of the reference simulation (Fig. 3.9b). The relatively smaller R-channels in these simulations remain more pressurized and thus drain less water from the cavity network (Eq. (3.1)); the relative discharge in the cavity network near the terminus is therefore larger than in the reference simulation (T_REF), further diminishing transport stage near the terminus (cf. Figs. 3.2–3.3).

Sediment supply

In the present model the values and patterns of sediment supply are amongst the key unknowns. Most till is produced subglacially (e.g., Sanders and others, 2013) and the amount and size distribution of till depends on the history and patterns of production (quarrying) and comminution (abrasion). We test the sensitivity of erosion rates and patterns to different values of input sediment supply. In two simulations (T_SSP/2 and T_SSP/4; Table 3.4) the sediment supply rate per unit width is constant in space and time and is

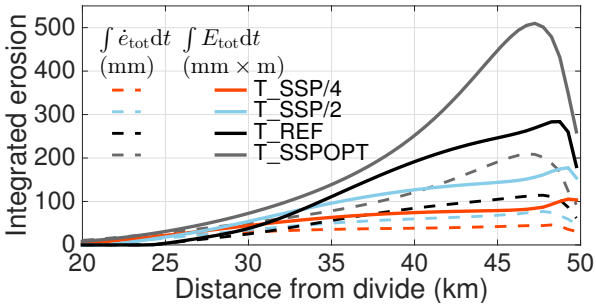

Figure 3.10: Time-integrated erosion per unit width ($\int \dot{e}_{tot} dt$) and time-integrated total erosion ($\int E_{tot} dt$) as a function of sediment supply rate (q_s) (Table 3.4). The first 20 km of the profile are not shown because the bed is alluviated and erosion rates are negligible.

taken as a fraction of the reference supply rate in T_REF (Table 3.4). The largest erosion rate in the SEM occurs when the relative sediment supply is $q_s/q_{tc} = 0.5$. For the TLEM and transport stages $\tau^*/\tau_c^* < 100$, maximum erosion rate is obtained for a relative sediment supply of $0.5 \leq q_s/q_{tc} < 0.8$ (Lamb and others, 2008a). We determine a ratio q_s/q_{tc} close to optimum and examine the resulting erosion rates and patterns (T_SSPOPT; Table 3.4). This provides us an upper bound on subglacial meltwater erosion rates. The hydraulic conditions in this suite of simulations are that of T_REF (Fig. 3.5).

Decreasing the sediment supply leads to a decrease in the maximum integrated erosion (Fig. 3.10, T_SSP/2 and T_SSP/4; $\int \dot{e}_{tot} dt$ and $\int E_{tot} dt$) and to the bed being eroded further up-glacier. For a relatively low sediment supply (T_SSP/4), the peak in annually integrated erosion per unit width ($\int \dot{e}_{tot} dt$, Fig. 3.10) is hardly discernible and the peak in annually integrated total erosion ($\int E_{tot} dt$, Fig. 3.10) is controlled by channel size. In order to estimate the maximum erosion that can occur under the given hydraulic conditions and sediment size, we optimize the sediment supply rate by expressing it as a function of the transport capacity ($q_s/q_{tc} \approx 0.6$). The resulting patterns of annually integrated erosion ($\int \dot{e}_{tot} dt$ and $\int E_{tot} dt$, Fig. 3.10, T_SSPOPT) mimic the transport stage patterns (see τ^*/τ_c^*, Fig, 3.5A), and peak at nearly twice the values of T_REF.

3.5 Discussion

3.5.1 Significance of model simplifications

We have detailed the simplifications and underlying assumptions of the model while describing the model and the strategy, we therefore focus on the potential implications of the most important simplifications. At the onset of the melt season, sliding is expected to accelerate as a response to increased water supply to a distributed drainage system (e.g., Iken, 1981; Hooke and others, 1989; Mair and others, 2003; Anderson and others, 2004; Sole and

others, 2011; Meierbachtol and others, 2013; Hewitt, 2013; Hoffman and Price, 2014) which would promote cavity enlargement and water flow through the distributed rather than the incipient channelized drainage system. This sliding feedback alone could produce a small decrease in water pressure (e.g., Hoffman and Price, 2014), hence a decrease in transport stage.

In this study, we treat only the case of bedrock erosion by abrasion and we neglect the effect of quarrying. Although the latter can lead to erosion rates up to an order of magnitude larger than abrasion, it requires that the bedrock be highly jointed (Whipple and others, 2000, 2013). Quarrying is a two-step process: (1) loosening of blocks around pre-existing cracks (or possibly opening of new cracks) and (2) mobilization and transport of loose blocks (Whipple and others, 2000, 2013; Chatanantavet and Parker, 2009; Dubinski and Wohl, 2013; Lamb and others, 2015). The depth of loose cracks could be related to sediment availability (Chatanantavet and Parker, 2009) and mobilization and transport of quarried blocks scale with the transport stage (Dubinski and Wohl, 2013; Lamb and others, 2015). Therefore we expect that the patterns of quarrying would be similar to the transport stage, yet limited by the thickness of the loosened layer.

We compute erosion with only a single particle size that is assumed to be the median size of the sediment mixture (e.g. Sklar and Dietrich, 2004, 2006, 2008; Turowski and others, 2007; Lamb and others, 2008a; Chatanantavet and Parker, 2009; Nelson and Seminara, 2011). The SEM (Sklar and Dietrich, 2004) was generalized for a grain-size distribution by Egholm and others (2013), a study in which they however omit a discussion of the implications of the generalization of the SEM. As for the TLEM, Lamb and others (2008a) suggest that a generalization to grain-size distributions would require re-evaluation of some of the equations to account for the interactions between particles of different sizes within the bedload layer. A decrease in median sediment size would probably result in an erosion profile more spread out along the bed and an increase in median sediment size would result in a localization of erosion (see Supplement). The changes in erosion would be quantitatively similar to a decrease in sediment supply (q_s) and thus a decrease in relative sediment supply ($q_\mathrm{s}/q_\mathrm{tc}$), which strongly controls erosion patterns.

We make the assumption of a supply-limited glacier bed, hence neglect the effect of sediment transport and the interactions between sediment thickness and water flow. The mobilization and particularly deposition of sediment affect the flow regime by enlarging or reducing the cross-section of flow (Creyts and others, 2013). On a timescale of days, when sediment is mobilized, the cross-section of flow is enlarged and could result in a drop in channel water pressure and a corresponding loss of flow strength. The opposite effect, leading to flow strengthening, could occur when sediment is deposited. We do not treat the case of transport-limited conditions, where the channelized drainage system would more closely resemble canals (Walder and Fowler, 1994; Ng, 2000a; Kyrke-Smith and Fowler, 2014). To implement sediment transport adequately, it is necessary to improve existing

models for subglacial water flow through canals (Walder and Fowler, 1994; Ng, 2000a; Kyrke-Smith and Fowler, 2014) with time-evolving effective pressure. Alley and others (1997), however, argue that in the case of subglacial water flow through canals, the water pressure remains relatively high and very little water would be drained from the distributed system, limiting the capacity of canals to transport sediment. In contrast, the steady-state water pressure in an R-channel decreases with increasing discharge, favouring water flow in the channelized system and enhancing transport and erosion.

Accounting for the production of sediment and the evolution of particle diameter at the glacier bed would also largely influence sediment supply patterns. For example, we can speculate that if the sediment sources are localized in areas of more easily eroded bedrock (e.g., Dühnforth and others, 2010), tools would only be present downstream from these areas. If instead of fixing the sediment supply per unit width, we fix the total sediment supply (simulation not shown), tools are less available at peak flows, reducing erosion, whereas the cover effect is enhanced for a relatively small channel. We also tested a simple power-law downstream fining function (e.g., Sklar and Dietrich, 2006; simulation not shown). The results were very similar to those obtained with a decrease in relative sediment supply, because particles were smaller than the reference size of 60 mm in the region of the bed where channels form. Another means of obtaining insight into sediment supply rates and patterns would be through the use of a comprehensive model of glacial erosion, i.e. a model encompassing transient subglacial hydrology (between distributed and channelized systems), ice dynamics, glacial abrasion and quarrying. Such a model has yet to be developed, as patterns of glacial erosion remain poorly understood (cf. Beaud and others, 2014). Finally, subglacial water flow evacuates a significant volume of sediment despite the small area over which R-channels operate and the tendency of these channels to remain stably positioned in association with moulins (e.g., Gulley and others, 2012). The mechanism by which large volumes of sediment are delivered to the channels remains elusive. More work is therefore required to quantify subglacial sediment production patterns.

3.5.2 What are the major controls on subglacial meltwater erosion?

We rank the transient simulations by glacier-area-averaged erosion rate in Fig. 3.11a. Because we prescribe water input rates sufficient to form a channelized drainage system, it stands out from the model formulation that sediment supply is the most important parameter. A lack or overabundance of tools inhibits erosion. In our results this is shown by the fact that T_SSPOPT (sediment supply optimized for erosion; Table 3.4) produces the most erosion and T_SSP/4 (smallest sediment supply; Table 3.4) the least. Changing the ice geometry also leads to a relatively large range of averaged erosion rates as T_1300 (thick ice; Table 3.4) yields twice as much erosion as T_700 (thin ice; Table 3.4; Fig. 3.11a). Larger hydraulic potential gradients in T_1300 cause the shear stress be large enough over larger portions of the bed to create erosion (Fig. 3.9). Subglacial drainage catchment width,

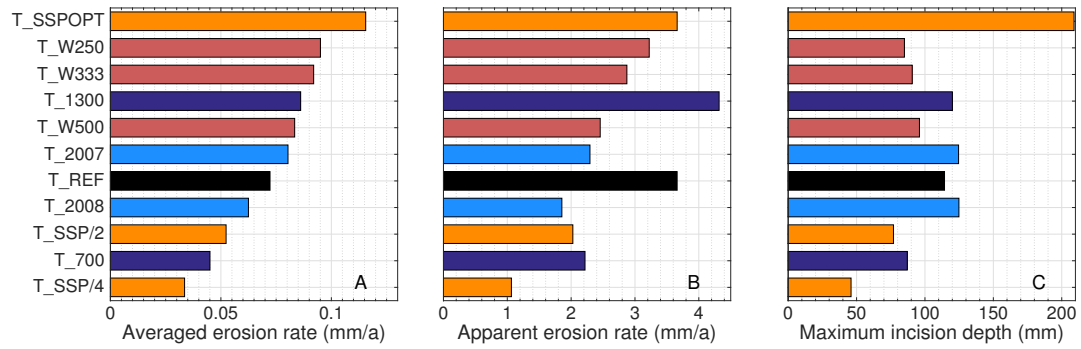

Figure 3.11: Synthesis of transient simulations (Table 3.4) through comparison of the following quantities calculated for one model year: (A) Erosion rate averaged over the whole glacier bed ($\int\int E_{\mathrm{tot}}\mathrm{d}t\mathrm{d}x$); (B) Apparent erosion rate calculated as the volume of sediment that is transported across the last grid node, i.e. terminus, ($\int \min(q_{\mathrm{s}}W_{\mathrm{ch}}, Q_{\mathrm{tc}})\mathrm{d}t$) averaged over the glacier area. This quantity corresponds to what one would measure as the sediment flux in a proglacial stream. (C) Maximum incision depth ($\max\left(\int \dot{e}_{\mathrm{tot}}\mathrm{d}t\right)$). Simulations are ranked by averaged erosion rate and the colours represent different simulation suites: black for "reference", blue for "water input", purple for "ice geometry", red for "drainage width" and orange for "sediment supply" (Table. 3.4).

within the range tested, plays a lesser role than sediment supply or ice geometry although the averaged erosion rate in T_W250 (four channels; Table 3.4) is $\sim 30\%$ more than that of T_REF. The fact that T_2007 (realistic melt season from 2007 record; Table 3.4) produces more averaged erosion than T_REF suggests that an increase in the multi-day variability of the water input enhances erosion.

The relations are different for apparent erosion rate (Fig. 3.11b), here defined as the equivalent thickness of bed material evacuated by the integrated sediment flux ($\int \min(q_{\mathrm{s}}W_{\mathrm{ch}}, Q_{\mathrm{tc}})\mathrm{d}t$) at the terminus (km 50). The apparent erosion rate corresponds to the quantity estimated by studies of sediment yield in proglacial channels, lake or fjords. Relatively large hydraulic potential gradients and relatively thick ice close to the terminus, both of which inhibit R-channels growth, compete against the loss of transport capacity. Therefore the largest apparent erosion occurs for the thickest ice (T_1300, Fig. 3.3). Interestingly, the lowest drainage density (T_REF) yields more apparent erosion than the highest (T_W250). Discharge through the cavity network close to the terminus increases with R-channel density; the smaller the channel, the larger the water pressure and the lower the pressure gradient between the two systems. This feedback, in addition to the discharge in the R-channel being smaller due to the R-channel drainage catchment size, reduces the transport stage close to the terminus.

The results in Fig. 3.11b suggest that, despite the increase in apparent erosion that accompanies an increase in meltwater input (e.g., the total melt in T_2007 is about 1.25

times that of T_2008), the thinning associated with the retreat of an ice mass would have a competing effect by decreasing the hydraulic potential gradient (see Fig. 3.3). The flushing power of subglacial water flow is conducive to the removal of subglacial sediment enabling glacial abrasion and quarrying to be efficient. Our results hint that the subglacial drainage conditions most favourable for glacial erosion occur where significant surface melt and relatively steep surface slopes occur simultaneously, i.e. during an ice sheet maximum advance or during early phases of retreat. This corroborates the hypothesis of Jørgensen and Sandersen (2006) that some Danish tunnel valleys were excavated during the stagnation of the Scandinavian ice sheet. However, these findings challenge the hypothesis that glaciers deliver more sediment to proglacial areas during retreat than during advance (e.g., Hallet and others, 1996; Koppes and Hallet, 2002, 2006; Koppes and Montgomery, 2009), yet more work is required to explore this hypothesis. The lack of flow strength in the upper reaches of the glacier (upstream from km 20 for most simulations) suggests that subglacial sediment in the accumulation area is transported almost solely by entrainment due to sliding at the ice-bed interface.

In the steady-state simulations we find that significant erosion can occur in a network of cavities (see Supplement). In the transient simulations, however, the coupling with R-channels prevents large shear stresses from developing in the distributed drainage system, and the threshold for sediment motion is not even reached for particles of 1 mm diameter. We thus argue that bedrock erosion in the distributed drainage system is limited unless specific conditions are satisfied, for example a subglacial flood or a surge.

3.5.3 How important is subglacial meltwater erosion compared to overall glacial erosion?

In most literature on modelling landscape evolution by glacial erosion it is assumed that subglacial meltwater efficiently removes sediment from the glacier bed, while its effect on bedrock erosion is neglected (e.g., MacGregor and others, 2000, 2009; Brocklehusrt and Whipple, 2002; Tomkin and Braun, 2002; Anderson and others, 2006; Herman and Braun, 2008; Egholm and others, 2009, 2011a,b; Herman and others, 2011). On the other hand, in formerly glaciated landscapes, erosional features like tunnel valleys (e.g., Glasser and Bennett, 2004; Denton and Sugden, 2005; Dürst-Stucki and others, 2010, 2012; Kehew and others, 2012; Jansen and others, 2014) indicate that subglacial water can produce significant bedrock erosion. The results we obtain with our simple ice geometries and water input forcings indicate that the areally averaged bedrock erosion produced by subglacial water flow is on the order of $10^{-1} - 10^{-2}\,\mathrm{mm\,a^{-1}}$ (Fig. 3.11) while glacial erosion rates are often on the order of $1 - 10\,\mathrm{mm\,a^{-1}}$ (e.g., Gurnell and others, 1996; Hallet and others, 1996; Koppes and Montgomery, 2009; Riihimaki and others, 2005). Bedrock erosion by abrasion from sediment-bearing subglacial water thus appears negligible compared to reported erosion rates in proglacial areas. Our results corroborate the assumption that subglacial meltwater

efficiently removes sediment from the bed and we postulate that this flushing action is necessary for glacial abrasion and quarrying to access an exposed bed and remain efficient.

3.5.4 Can ordinary seasonal melt processes lead to subglacial bedrock channel incision?

We find maximum modelled vertical bedrock incision ranging from ~ 50 to $\sim 200\,\mathrm{mm\,a^{-1}}$ (Fig. 3.11c). Assuming that over a period of 20 years climate is relatively steady and the bedrock does not change significantly, the location of moulins would remain relatively fixed laterally and so would the channel paths (Gulley and others, 2012). Using the lowest incision rate (T_SSP/4), a Nye channel almost a metre deep, a few metres wide and tens of kilometres long could be carved near an ice sheet margin in 20 years. A similar N-channel would be carved in only five years assuming the largest incision rate (T_SSPOPT).

Landforms created by former continental ice sheets indicate that subglacial water ways can occupy persistent paths throughout a deglaciation. Eskers deposited by the retreating Laurentide ice sheet can be traced for up to several hundred kilometres and show a dendritic pattern almost as far upstream as the former divide (e.g., Storrar and others, 2014). Some tunnel valleys show several cut-and-fill structures suggesting different excavation events; moreover, tunnel valleys carved during different glaciations tend to follow the same paths (e.g., Jørgensen and Sandersen, 2006). Eskers also commonly lie inside tunnel valleys (e.g., Jørgensen and Sandersen, 2006; Kehew and others, 2012). Assuming an incision rate of $100\,\mathrm{mm\,a^{-1}}$ (e.g., Fig. 3.7), a simple volume calculation suggests that it would take about 15000 years to carve a 30 m deep and 100 m wide V-shaped tunnel valley, similar to the dimensions of tunnel valleys observed in Ireland (Knight, 2003).

In the context of an alpine glacier, valley geometry tends to focus subglacial water flow paths toward the thalweg. Assuming that a glacier occupies topography strongly imprinted by fluvial processes, erosion by subglacial water flow may tend to preserve if not enhance the pre-existing fluvial features along the valley centreline. For an alpine glacier eroding its bed at a pace of $2\,\mathrm{mm\,a^{-1}}$ (e.g., Hallet and others, 1996; Riihimaki and others, 2005; Koppes and Montgomery, 2009), in the case of simulation T_2008 (Table 3.3, apparent erosion of $\sim 2\,\mathrm{mm\,a^{-1}}$; ice geometry comparable to that of a large valley glacier), the maximum incision depth in one year is $\sim 125\,\mathrm{mm}$ (Fig. 3.11c). The relief of a canyon with the maximum width of the N-channel ($\sim 4.5\,\mathrm{m}$, for T_2008) would increase by more than $\sim 120\,\mathrm{mm\,a^{-1}}$ (rate of vertical bedrock incision minus rate of surrounding glacial erosion). If the canyon were five times as wide ($\sim 22.5\,\mathrm{m}$), the maximum rate of relief increase would still be $\sim 24\,\mathrm{mm\,a^{-1}}$ about twice the measured incision rates in a metres-wide gorge in the French Western Alps (e.g., Valla and others, 2010), highlighting the erosional power of localized subglacial meltwater action.

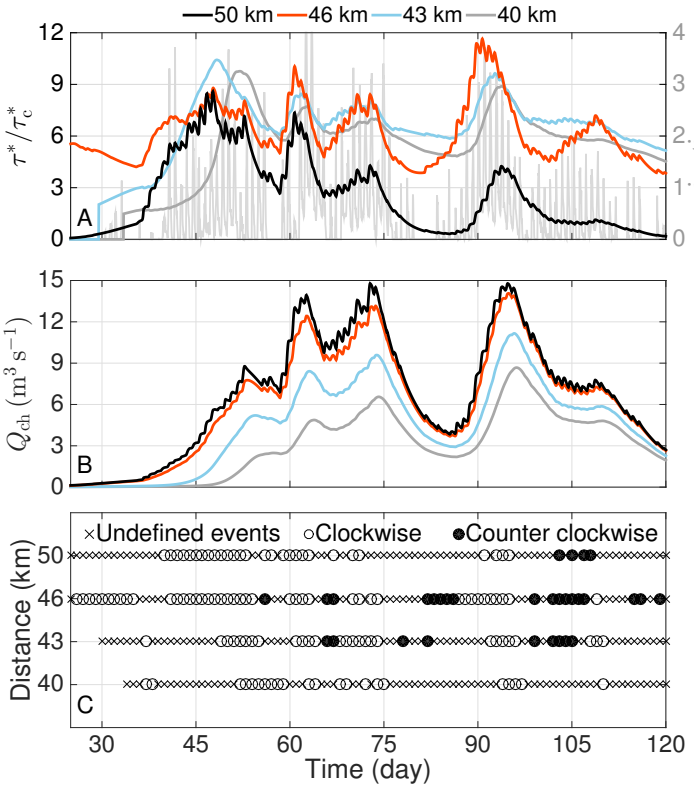

Figure 3.12: Hysteresis between water discharge and transport stage for simulation T_2008 (see Table 3.4 and Fig. 3.6). Timeseries at four locations (km 40, 43, 46 and 50) distributed over the last 10 kilometres of the glacier profile of: (A) Transport stage (τ^*/τ_c^*) and normalized water input ($\dot{b}_{ca}/\dot{b}_{ss\,max}$) at the terminus (light gray); (B) Discharge in the channel, Q_{ch}; (C) Calculated direction of the daily hysteresis when transport stage is plotted against water discharge. The hysteresis is clockwise when transport stage peaks before discharge over a daily cycle. Undefined events represent days where the fluctuations in transport stage or discharge are either simultaneous or not strong enough to produce hysteresis.

3.5.5 What are the implications of the water-flow regime in channels for hysteresis and sediment transport?

We calculate the direction of daily hysteresis between modelled transport stage (Fig. 3.12a) and water discharge (Fig. 3.12b) at four locations within the last 10 km of the glacier profile (Fig. 3.12c) for simulation T_2008 (Table 3.4; Fig 3.6). Overall, hysteresis is dominated by clockwise events, with counter-clockwise events only occurring during the second half of the melt season. Clockwise hysteresis correlates well with the rising limb of multi-day water discharge and transport stage peaks, while counter-clockwise hysteresis correlates with the falling limb, particularly at km 46 (Fig. 3.12). During the rising limb of a multi-day melt event, changes in channel size are dominated by enlargement; the pressure in the channel

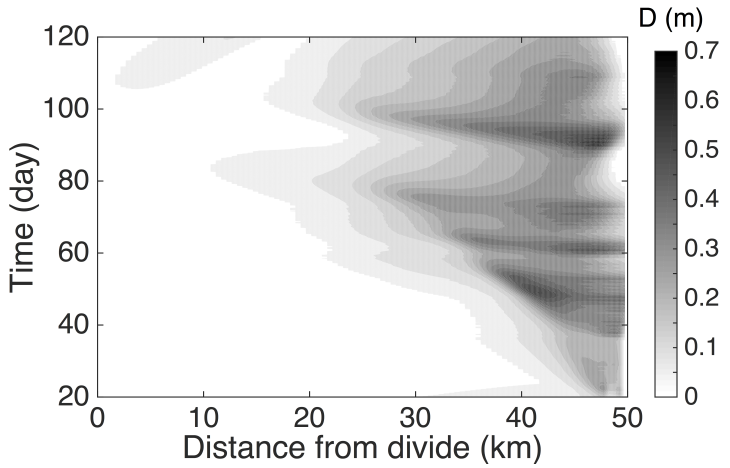

Figure 3.13: Maximum particle diameter for which movement would be initiated in simulation T_2008 assuming $\tau_c^* = 0.03$ (see Table 3.4 and Fig. 3.6).

therefore peaks before the discharge, as do the averaged water-flow velocity and transport stage. During the falling limb of the melt event, if the channelized drainage is relatively well established, changes in channel size are dominated by closure, and the pressure peak can occur after the peak in discharge. In the case of a proglacial stream carrying a sediment load smaller than its transport capacity, peaks in transport stage would act as mobilizing events propagating sediment pulses downstream. We therefore surmise that the direction of hysteresis in sediment transport and discharge is not necessarily linked to changes in sediment supply conditions or the tapping of new sediment sources, but may be the result of changes in subglacial sediment mobilization in the vicinity of the glacier terminus.

In coarse-bedded streams, grain hiding has a significant effect on sediment transport (e.g., Yager and others, 2012; Scheingross and others, 2013), as mobile grains can be trapped behind larger immobile particles. We calculate the maximum particle diameter for which movement would be initiated in simulation T_2008 (Fig. 3.13) and find that boulders of up to 70 cm in diameter can be transported within the last 10 km of the profile and would correspond to flood-like conditions in rivers. The analogy to river systems might have influenced the interpretation of glacial deposits such as eskers, where the presence of boulders or lack of fines is often used to infer emplacement during flood events (e.g., Brennand, 1994; Burke and others, 2012).

For simulation T_2008, we find that transport stage exhibits a sharp decrease close to the terminus (Figs. 3.5A, 3.6A and 3.6C) which leads to a correspondingly sharp decrease in the size of particles transported (Fig. 3.13) and could lead to a bottleneck in sediment transport. This bottleneck effect could lead to the deposition of sediment, filling the channel toward the end of the melt season. A similar process, but operational over a longer time

scale, would be consistent with time-transgressive deposition of eskers near the mouths of R-channels beneath retreating ice margins (e.g., Brennand, 1994; Burke and others, 2012).

3.6 Conclusions

This study is the first attempt to quantify bedrock erosion rates by transient subglacial water flow with a numerical model. We implement a 1-D model of subglacial drainage in which a network of cavities and R-channels interact. We compute the shear stress exerted on the bed and the resulting bedrock erosion by abrasion (saltation erosion, after Sklar and Dietrich (2004), and total load erosion after Lamb and others (2008a)). Because of the large calculated transport stage we argue that in the case of subglacial meltwater erosion it is probably more appropriate to use the TLEM than the SEM. Assuming that a significant amount of meltwater is produced and reaches the bed, the main drivers of subglacial water erosion that we isolate are: the rate of sediment supply, particularly the relative sediment supply, and ice geometry.

From this exercise, we conclude that:

1. Bedrock erosion and transport stage in the subglacial drainage system do not scale directly with water discharge. Instead, transport stage and erosion are related to the hydraulic potential gradient and hence a combination of water discharge, ice-surface slope and channel (or cavity) cross-sectional area. In our simulations, this combination of discharge, slope and channel cross-sectional area leads to a drop in transport stage close to the terminus as water pressure approaches atmospheric.

2. Erosion rates due to the action of subglacial water flow averaged over the whole glacier bed are negligible compared to the rates of glacial erosion necessary to produce the sediment supply rates we impose.

3. In our transient simulations, a bedrock channel a few to several decimetres in depth could be carved over a single melt season as erosion is concentrated at the base of R-channels.

4. The vertical incision rates we calculate are a few to several times larger than published rates of fluvial incision in gorges. Therefore, this mechanism may explain the gradual excavation of tunnel valleys in bedrock and the preservation or even initiation of inner gorges.

Though we have demonstrated the potential for subglacial water flow to incise bedrock on seasonal timescales, site-specific and quantitative assessments of its importance will require more realistic 2-D hydrology models (e.g., Hewitt, 2013; Werder and others, 2013) and simulations over timescales of glacial advance and retreat.

Acknowledgements

We are grateful to the Swiss National Cooperative for the Disposal of Radioactive Waste (Nagra) for providing funding within the framework of investigating ice-age effects related to the long-term safety of radioactive waste disposal. We are particularly grateful to Urs Fischer for overseeing this project and we would like to thank Michelle Koppes for insightful discussions. We would also like to thank John D. Jansen, an anonymous reviewer and the handling associate editor, Arjen Stroeven for their comments. Funding was also provided by the Natural Sciences and Engineering Research Council of Canada (NSERC), the Canada Research Chairs Program, and Simon Fraser University (SFU).

Chapter 4

Excavation of bedrock tunnel valleys and inner gorges by seasonally-produced meltwater

Abstract

Subglacial water flow drives the excavation of a variety of bedrock channels including tunnel valleys and inner gorges. Subglacial floods of various magnitudes are often invoked to explain the erosive power of water flowing under ice. In this study we examine whether subglacial floods are necessary to carve bedrock channels, or if more frequent melt season events (e.g. daily production of meltwater) can, over a glacial cycle, explain the formation of substantial bedrock channels. We use a 1-D numerical model of bedrock erosion by subglacial meltwater, where water flows through interacting distributed and channelized drainage systems. The shear stresses produced drive bedrock erosion by bed- and suspended-load abrasion. We show that seasonal meltwater discharge produces shear stresses that are large enough to erode bedrock channels. Large-scale floods are less erosive because the sediment that carves channels is carried in suspension and there are fewer contacts with the bed. We also demonstrate that seasonal meltwater discharge can, over a glacial cycle, lead to the excavation of bedrock channels of the range of sizes and shapes commensurate with published observations.

4.1 Introduction

Bedrock channels carved by subglacial meltwater erosion (SME), such as tunnel valleys (TV) and inner gorges (IG), are common features of formerly glaciated landscapes. Their formation is often attributed to subglacial floods of various magnitudes (e.g. Kehew and others, 2012; van der Vegt and others, 2012; Wright, 1973). Deciphering the role of mag-

nitude and frequency of events in the formation of landscapes has been a central focus of geomorphology for more than 60 years. There remains discussion about whether events of moderate frequency and magnitude (e.g. annual to decadal return times; Wolman and Miller, 1960) or rare events of very large magnitude (e.g. millennial return time; Kirchner and others, 2001) exert the dominant control on the evolution of landscapes. Here we investigate whether the formation of subglacial bedrock channels requires floods or may be accomplished solely by seasonal-scale meltwater processes.

In the context of subglacial water flow, high frequency, small magnitude events are those that occur more than tens of times per year (e.g. days of surface melting) and that are capable of forming an R-channel where sediment transport may take place. These seasonal melt water flows have discharges of a few tens to a few hundreds of cubic metres per second. Moderate frequency and magnitude floods would have return periods of one year to several decades and have discharges of several hundred to a few tens of thousands of cubic metres per second. Rare events would be mega-floods with peak discharges greater than $\sim 5 \times 10^4\,\mathrm{m^3\,s^{-1}}$ (see Appendix C for further rational).

Tunnel valleys are channel-like features, up to a few kilometres wide and tens of kilometres long, that are common in areas of low relief overridden by continental ice sheets. They exhibit an adverse sloping (overdeepened) longitudinal profile that terminates abruptly, close to the maximum extent of the former ice sheet (see Ó Cofaigh (1996); Kehew and others (2012); van der Vegt and others (2012) for reviews). Subglacial meltwater is widely accepted to be the dominant process driving TV excavation, with most studies suggesting TVs are formed during the maximum still-stand or early retreat phase of an ice sheet. However, there is no consensus on the magnitude of subglacial discharge required for their excavation. Tunnel valley formation has been variously linked to basal melting excavating canals in subglacial sediment (e.g. Boulton and Hindmarsh, 1987), to seasonal meltwater release (Mooers, 1989), to intermittent moderate-scale floods (e.g. Jørgensen and Sandersen, 2006; Kehew and others, 2012; van der Vegt and others, 2012; Wingfield, 1990), and to mega-floods (e.g. Denton and Sugden, 2005; Sharpe, 2005; Shaw and Gilbert, 1990; Wright, 1973). Evidence for water reservoirs sufficient to supply mega-flood events is often lacking (e.g. Clarke and others, 2005; Mooers, 1989). Nevertheless, for erosion to be significant, most of these studies assume that the release of water must be sudden (e.g. Kehew and others, 2012; van der Vegt and others, 2012).

Inner gorges, as treated here, are V-shaped incisions in an otherwise glacially sculpted landscape, often a U-shaped valley. They were initially thought to be incised by fluvial action during interglacial periods (e.g. Korup and Schlunegger, 2007), however, more recent studies suggest that IGs in the Swiss Alps persisted through multiple glaciations (e.g. Montgomery and Korup, 2010) and that some IGs in Switzerland and Scandinavia are subglacial in origin (Dürst-Stucki and others, 2012; Jansen and others, 2014). It therefore appears that

IGs are the result of a combination of subglacial and non-glacial fluvial erosion, although the relative efficacy of these processes remains unclear.

Here, we explore the excavation of TVs and IGs using a one-dimensional numerical model of bedrock erosion by impacting sediment entrained in subglacial water flow. Our specific research questions are: 1) Is flood-SME or seasonal-SME more effective at carving bedrock channels? 2) Can seasonal-SME over a glacial cycle explain the formation of the range of bedrock channels we observe in glaciated terrain?

4.2 Model and Simulations

In the SME model, the channelized drainage system is represented by a semi-circular Röthlisberger channel (R-channel; Nye, 1976; Röthlisberger, 1972), the distributed drainage system by a network of connected cavities (e.g. Kamb, 1987) and the exchange between systems by a function of the water pressure gradient between the two (Hewitt and Fowler, 2008, see Appendix for further details). The subglacial water flow model is used to calculate the shear stress on the bed of the R-channels. The shear stress and channel dimensions are then used to model erosion by abrasion (Beaud and others, 2016) using the tools and cover principle (Sklar and Dietrich, 2004) whereby particles entrained by the flow as bed- or suspended load impact and erode exposed bedrock (Lamb and others, 2008a). An overabundance of particles shields the bed from impacts. Erosion rate is a function of a particle's kinetic energy upon impact, the concentration of particles available close to the bed and the fraction of bedrock exposed. Hence, erosion rates are highly sensitive to both the supply and size of available sediment. Plucking is omitted from the model, although it is the dominant erosion mechanism in highly fractured bedrock (e.g. Lamb and Fonstad, 2010; Whipple and others, 2000, 2013) and can yield erosion rates an order of magnitude higher than from abrasion (e.g. Whipple and others, 2000, 2013).

To compare the relative efficacy of flood- versus seasonal SME in carving bedrock channels, we model floods corresponding to moderate frequency and magnitude events with a wide range of duration (10–60 days) and total water volume (0.1–10 times the integrated volume of our reference seasonal meltwater simulation, $\sim 1 \times 10^8\,\mathrm{m}^3$). We assume flood flow, and hence erosion, occurs only in R-channels, and therefore omit the distributed system in the flood simulations (e.g. Clarke, 2003). We use the general shape of the outburst flood hydrograph described in Nye (1976), and scale the duration and total volume of water released to create synthetic floods of different magnitudes. The hydrograph is imposed as a flux boundary condition at the upstream end of the model domain. We choose our reference flood so that its duration is 20 days and the total volume of water released is 10 times the integrated seasonal meltwater volume (resulting in a peak discharge of $\sim 5 \times 10^3\,\mathrm{m}^3\,\mathrm{s}^{-1}$), in accordance with jökulhlaups described by Björnsson (2002). For these simulations we use

a 50-km long synthetic glacier with a parabolic surface profile, a flat bed and a maximum ice thickness of 1000 metres (Beaud and others, 2016).

We perform two long-term simulations using seasonal meltwater flows, which correspond to high-frequency small-scale events: one for a TV and a second for an IG. In both simulations, we use a model of ice dynamics to produce surface-elevation profiles that emulate the growth and decay of an ice sheet. The prescribed mass balance is a function of ice-surface elevation, and at any given point, varies sinusoidally with a period of 20 kyrs. We select a time window of a few thousand years around the period of maximum ice extent and focus on the lower reaches of the profile, where surface meltwater production is most likely. Within this time window we select time slices of ice thickness, mass balance and sliding speed every 250–300 yrs to drive the SME model. Lateral migration of the R-channel is crudely accounted for by randomly selecting annual channel positions from a Gaussian distribution (see Appendix C) of prescribed width. In this way, we mimic the lateral spatial distribution of erosion with a one-dimensional longitudinal model. For the TV scenario, we consider a large continental ice sheet resting on a gently inclined bed. In the IG scenario we consider a large valley glacier by superimposing the synthetic glacier-surface profile on a real valley-bottom profile from the Berner Alps, Switzerland. See Appendix C for further details of the modelling approach.

4.3 Subglacial erosion by seasonal meltwater versus floods

The seasonal-SME model produces an incipient bedrock channel (i.e., Nye channel) up to four metres wide and 12 centimetres deep (Fig. 4.1A); in the flood simulation, the channel is almost 50 metres wide but only 1.4 centimetres deep (Fig. 4.1B). Maximum discharge during the reference flood is two orders of magnitude higher than maximum discharge during the synthetic melt season and has a two-fold impact. The R-channel becomes much larger during the flood, enabling erosion over a wider area. Higher shear stresses, however, result in more sediment in suspension; erosion per unit width therefore remains small, as fewer particles impact the bed (Beaud and others, 2016; Lamb and others, 2008a; Scheingross and others, 2014).

When bedrock erosion is spatially averaged across the glacier bed, the erosion for flood-SME is twice as large ($\sim 0.15\,\mathrm{mm}$) as for seasonal-SME ($0.07\,\mathrm{mm}$). Despite this difference, the depth of the channel carved by seasonal-SME is almost 10 times greater (with a width-to-depth ratio two orders of magnitude smaller), greatly increasing the likelihood that it will persist through the next glacial advance (Fig. 4.1C). Between flood events, glacial erosion by abrasion and quarrying, which we expect for a temperate glacier would average $1 - 2\,\mathrm{mm\,a^{-1}}$ (e.g. Hallet and others, 1996), would reduce the relief of the flood-generated channel. Furthermore, the maximum depth of bedrock channels excavated during a flood decreases with increasing shear stress (Fig. 4.2). The larger the volume and the faster the

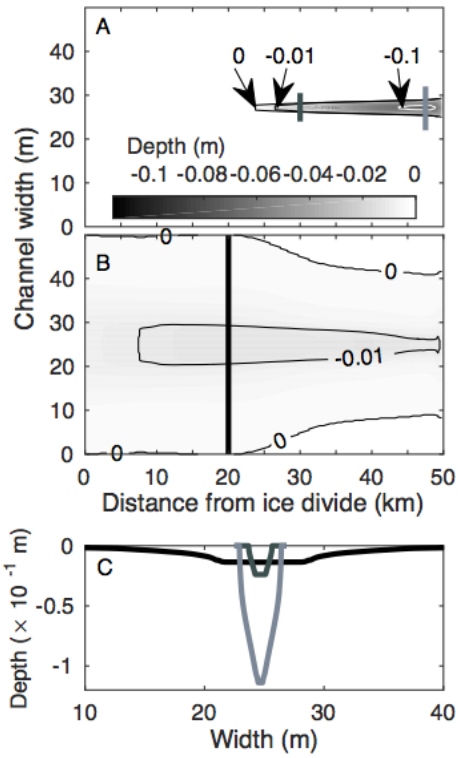

Figure 4.1: Topography of simulated bedrock channels along the longitudinal profile of the glacier bed. (A) Seasonal-SME. (B) Flood-SME. (C) Cross-sectional profiles of the incipient bedrock channels at locations marked by the vertical lines of matching color in (A) and (B). See Beaud and others (2016) (or Chapter 3) for a discussion of the importance of model parameters on seasonal-SME.

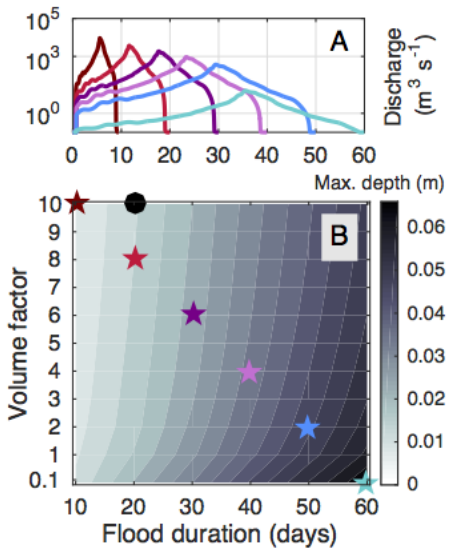

Figure 4.2: (A) Discharge hydrographs (log-scale) for six synthetic floods representing the range of total volume and flood duration simulated. (B) Maximum simulated bedrock channel depth as a function of flood duration and volume factor. The volume factor is the number by which the integrated volume of seasonal meltwater is multiplied to obtain the total flood volume. Stars represent the floods plotted in (A) with matching colors. The black circle represents the reference flood.

release of water (Fig. 4.2A), the larger the resulting R-channel and the greater the shear stress. The resulting erosion is distributed over a wider area, but sediment suspension is enhanced and erosion per unit width reduced. The deepest simulated bedrock channel carved by flood-SME is half as deep (Fig. 4.2B; ~ 0.06 m) as that carved by seasonal-SME (~ 0.12m).

4.4 Discharge frequency and erosional efficiency

We find three main characteristics can be used to differentiate the effect of flood- versus seasonal-SME: (1) the total volume of bedrock eroded, (2) the cross-sectional profile of the incipient bedrock channel (Fig. 4.1), and (3) the maximum depth of incision (Figs. 4.1 and 4.2). In both IG and TV scenarios, the total volume of bedrock eroded is negligible compared to expected rates of glacial erosion by abrasion and quarrying (Beaud and others, 2016). Few quantitative observations of Nye channels exist, but the width-to-depth ratio of the observed channels varies between 1 and ~ 100 (Kor and others, 1991); by this metric, seasonal-SME yields more realistic simulated bedrock channels (width-to-depth ratios of ~ 40 versus ~ 4000 for flood-SME; Fig. 4.1). The maximum depth of incision, relative to the background rate of glacial erosion, will determine whether a bedrock channel persists over a glacial cycle.

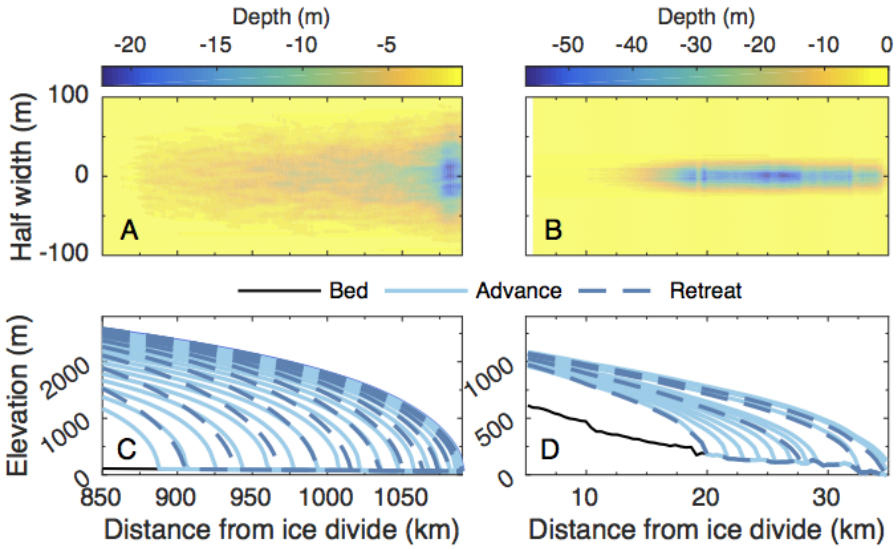

Figure 4.3: Excavation of bedrock channels by seasonal-SME over a glacial cycle. (A) Depth of erosion in the TV scenario; erosion is distributed over 200m laterally to mimic the migration of R-channels and obtain a width-to-depth ratio of 10 (van der Vegt and others, 2012). (B) Depth of erosion in the IG scenario; erosion is distributed over 50m as valley walls are expected to constrain R-channel migration. (C) Ice profiles shown every 250 years for the TV scenario over a time interval of 7500 years. (D) Ice profiles shown every 300 years for the IG scenario over a time interval of 4500 years.

In the absence of intense geothermal activity, the recharge of a subglacial reservoir from surface and basal melting required to produce the modelled floods would likely take years to decades, a period during which seasonal-SME would continue to erode a bedrock channel. The deepest bedrock channel we simulate by flood-SME (Fig. 4.2) would be erased in a few decades assuming continued glacial erosion rates of 2 $\mathrm{mm\,a^{-1}}$ between floods (Hallet and others, 1996; Koppes and Montgomery, 2009), whereas it would take >60 years for the ice to erase a channel carved by seasonal-SME after the cessation of subglacial water flow (Fig. 4.1C). We suggest that seasonal subglacial meltwater processes produce shear stresses sufficient to drive bedrock channel formation by abrasion, and hence seasonal meltwater production can explain the formation of both inner gorges and tunnel valleys.

4.5 Bedrock channel excavation over a glacial cycle

When exploring the long-term effects of seasonal-SME, our model produces bedrock channels with characteristics similar to observed inner gorges and tunnel valleys (Fig. 4.3). The bedrock channels have an overdeepened profile and an abrupt termination (Fig. 4.3A and B) within several kilometres of the maximum extent of the ice (Fig. 4.3C and D). The deepest part of the channel corresponds to the reach near the ice margin that would sustain

the longest period of channelized water-flow (Beaud and others, 2016). The IG scenario (Fig. 4.3B and D) leads to a volume of bedrock eroded per unit length similar to the TV scenario, but the channels are deeper. This happens even though the total volume of water released is several times smaller in the IG scenarios. The reason this occurs is that the valley glacier ice is thinner, which permits channelized water flow to persist for twice as long over certain reaches of the bed. In both scenarios, we calculate shear stresses > 600 Pa for $\sim 20 - 65$ days over a melt season, large enough to cause suspension and hence limit erosion, as in the flood simulations.

4.6 Formation of bedrock channels in glaciated terrain

A qualitative comparison of cross-sectional areas between our model results and field-observations of bedrock channels shows good visual agreement (Appendix Fig. C.1). Ultimately, the width of the bedrock channels is imposed by the size of the R-channels and how we distribute their migration across a fixed width. Larger R-channels and particularly migration widths will lead to wider bedrock channels similar to TVs and smaller R-channels and migration widths will lead to more narrow channels. How the R-channel migration is distributed across a fixed width is not trivial (Appendix Fig. C.2). Mimicking lateral R-channel migration using a normal probability distribution creates a multi-channel structure as observed in TVs (Jørgensen and Sandersen, 2006) and also allows slot canyon incision in IGs (Sanders and others, 2014).

Our simulations show that channels of dimensions comparable to observed bedrock TVs and IGs can be excavated over 1–3 kyr by seasonal-SME. The location of deepest channel excavation in the TV scenario (Fig. 4.3A) is consistent with the interpretation that TVs form just upstream of the maximum extent of an ice sheet. Tunnel valleys are perhaps best identified in these areas where they have greatest relief, but could be formed anywhere that channelized subglacial water flow persists, as shown in our simulations. We stress that our model is limited to the formation of channels in bedrock; in order to investigate the formation of TVs in poorly consolidated sediments, different governing equations (e.g. Walder and Fowler, 1994) are required. For IGs, we acknowledge that in many cases fluvial erosion during inter-glacial periods can also play a significant role (e.g. Korup and Schlunegger, 2007; Montgomery and Korup, 2010). Nevertheless, we find that IGs can be formed by seasonal-SME alone, i.e. in the absence of floods (e.g. Dürst-Stucki and others, 2012; Jansen and others, 2014). Ultimately, the balance between non-glacial and subglacial fluvial erosion in the formation of IGs is tied to the glacial history of the valley, including the ice-thickness profiles, the rate and total volume of meltwater delivery to the bed, and the duration over which channelized conditions can be sustained in the subglacial drainage system. We suggest that seasonal subglacial meltwater processes may shape both bedrock TVs and IGs, with differences in scale arising from the extent of ice cover and the

ability of the subglacial drainage system to migrate laterally due to the presence or absence of strongly confining bed topography.

4.7 Conclusions

We use a 1-D numerical model of bedrock abrasion by subglacial meltwater flow to explore the magnitude and frequency of discharge necessary to carve subglacial bedrock channels. Our results suggest that, for channelized subglacial water flow, high frequency and small magnitude discharge events, in the form of seasonal meltwater processes, are able to drive bedrock channel excavation more effectively than less frequent, higher magnitude floods. Seasonal flows produce sufficiently high shear stresses to cause incision, whereas flood flows produce even higher shear stresses, which drive particles into suspension and thereby decrease abrasion. By considering the influence of seasonal processes over a glacial cycle, we simulate bedrock channels commensurate with the tunnel valleys and inner gorges that are ubiquitous in glaciated terrain. Rare, mega-flood flows are not necessary to produce tunnel valleys or inner gorges. On this basis, we suggest that these landforms share the same seasonal subglacial meltwater origin.

Acknowledgements

Funding was provided by the Swiss National Cooperative for the Disposal of Radioactive Waste (Nagra) within the framework of investigating ice-age effects related to the long-term safety of radioactive waste disposal. Funding was also provided by the Natural Sciences and Engineering Research Council of Canada (NSERC), the Canada Research Chairs Program, and Simon Fraser University (SFU).

Chapter 5

A framework for studying sediment transport in R-channels

Abstract

The role of glaciers in shaping the landscape is central to the interactions between climate and tectonic forces at high latitudes and in mountainous regions, and to understand the origin of landforms that attest to past glacial action. Sediment yields from glacierized basins are used to quantify contemporary erosion rates on seasonal to decadal timescales, often under the assumption that subglacial water flow is the main contributor to these yields. Two recent studies have used such sediment fluxes to calibrate a glacial erosion rule, where erosion rate scales with ice sliding speed raised to a power greater than one. Eskers hold valuable information about past subglacial hydraulic conditions in their spatial organization, geometry and sedimentary structures. The relations between hydraulic conditions and esker properties are nevertheless intricate as the formation of eskers has been mainly inferred from descriptive theories, on which a consensus has yet to be reached. Eskers are prevalent in areas of rigid bed and with a thin till cover and their formation is thought to be predominantly controlled by either water or sediment availability. Subglacial sediment transport by water flow has, however, seldom been studied, thus the controls on sediment yield from glacierized basins remain enigmatic. To bridge this gap, we develop a 1-D model of morphodynamics in semi-circular bedrock-floored subglacial channels. We adapt a sediment conservation law from the fluvial literature, developed for both mixed bedrock / alluvial and alluvial conditions, to subglacial channels. Channel evolution is a function of melt-opening due to viscous heat dissipation from the water flow, and creep closure of the overlying ice, to which we add the closure or enlargement due to sediment deposition or removal, respectively. We apply the model to an idealized land-terminating glacier and find that temporary sediment accumulation, or the formation of an incipient esker, is inherent to the dynamics of the channelized water flow. The interactions between sediment transport

and water flow in a semi-circular ice-walled channel exert greater control on the pattern of sediment delivery to the proglacial area than does the sediment availability at the bed. Hysteresis cycles between sediment transport and water discharge may not be correlated to sediment availability, as is assumed for river systems.

5.1 Introduction

Observations of water-born sediment fluxes in proglacial areas (e.g. Gurnell and others, 1996; Hallet and others, 1996; Herman and others, 2015; Humphrey and Raymond, 1994; Koppes and Hallet, 2006, 2002; Koppes and Montgomery, 2009; Koppes and others, 2015; Loso and others, 2004; Mao and others, 2014; Orwin and Smart, 2004; Riihimaki and others, 2005; Sanders and others, 2013; Willis and others, 1996), as well as subglacial landforms (e.g. Bennett and Glasser, 2009; Brennand, 1994; Burke and others, 2015; Ó Cofaigh, 1996; Denton and Sugden, 2005; Dürst-Stucki and others, 2010, 2012; Jansen and others, 2014; Jørgensen and Sandersen, 2006; Kehew and others, 2012; Knight, 2003; Storrar and others, 2014; Stumm, 2010; van der Vegt and others, 2012), are used to infer conditions at the ice–bed interface of contemporary and former glaciers and ice sheets. The interpretation of such observations relies on descriptive theories of sediment transport and bedrock erosion by subglacial water flow, yet a physical model combining such processes is still lacking. In this study, we propose the first model of morphodynamics in semi-circular bedrock-floored Röthlisberger channels (R-channels; Röthlisberger, 1972) in an attempt to bridge the gap between observations and physical processes.

Measurements of sediment fluxes in proglacial areas are widely used to quantify contemporary glacial erosion rates (e.g. Hallet and others, 1996; Herman and others, 2015; Koppes and Hallet, 2006, 2002; Koppes and Montgomery, 2009; Koppes and others, 2015; Loso and others, 2004; Riihimaki and others, 2005; Sanders and others, 2013). These measurements rely on the assumption that subglacial sediment storage is negligible and that subglacial water flow is the primary agent responsible for sediment evacuation, as sediment evacuation caused by sliding ice is assumed to be much smaller (e.g. Alley and others, 1997; Cowton and others, 2012). This assumption of minimal storage can also lead to the suggestion that sediment fluxes are representative of sediment production, and thus direct glacial erosion (Herman and others, 2015). Furthermore, sediment transport in the channelized region of a subglacial drainage system is often assumed to be subjected to similar flow regimes along its profile at a given point in time, namely local changes in flow regime are expected to be caused by temporal variations. In contrast, a recent numerical modelling study suggests that a bottleneck in sediment transport can occur in the vicinity of the terminus (Beaud and others, 2016).

Erosional and depositional features attributed to subglacial water flow (e.g. tunnel valleys, inner gorges and eskers) offer a unique window into the basal conditions of past

ice sheets (e.g. Bennett and Glasser, 2009; Brennand, 1994, 2000; Burke and others, 2012, 2015; Clark and Walder, 1994; Ó Cofaigh, 1996; Denton and Sugden, 2005; Dürst-Stucki and others, 2010, 2012; Jansen and others, 2014; Jørgensen and Sandersen, 2006; Kehew and others, 2012; Knight, 2003; Storrar and others, 2014; Stumm, 2010; van der Vegt and others, 2012). Their origins are nonetheless the centre of much debate (e.g. Chapter 4; Brennand, 1994; Beaud and others, 2016; Burke and others, 2015; Ó Cofaigh, 1996; Dürst-Stucki and others, 2010, 2012; Greenwood and others, 2016; Jansen and others, 2014; Kehew and others, 2012; Storrar and others, 2014; van der Vegt and others, 2012). Deciphering the the formation of erosional features created by subglacial water flow is also key to the planning of safe repositories for nuclear wastes in countries susceptible of experiencing large scale glaciations in the next million of years (e.g. Fischer and others, 2015). Subglacial flood flows are often invoked in order to explain the erosive power of water (Kehew and others, 2012; van der Vegt and others, 2012; Wright, 1973), the size of clasts found in eskers or the large changes in flow regimes inferred from esker sediment (e.g. Brennand, 1994; Burke and others, 2012). The formation of eskers has been attributed to either the geology of the substrate (Clark and Walder, 1994), the availability of meltwater (e.g. Storrar and others, 2014) or the availability of sediment (e.g. Burke and others, 2015). While Burke and others (2015) acknowledge the importance of a tradeoff between sediment and water availability, they emphasize the importance of the quantity of sediment present. In general it is well accepted that eskers form predominantly during later stages of ice retreat over a rigid bed (e.g. crystalline bedrock), but where till is present (Brennand, 2000; Clark and Walder, 1994).

Water flow mobilizes particles only if the shear stress it imparts on the bed exceeds a certain threshold (Shields, 1936). The value of this threshold depends on the characteristics of the channel floor and of the sediment mixture, for example: particle size, the size distribution of particles in the sediment mixture, the slope of the channel or the roughness of the bed (e.g., Einstein, 1950; Garcia, 2000; García, 2008; Lamb and others, 2008b; Meyer-Peter and Müller, 1948; Shields, 1936). Most equations describing the transport of sediment rely on the relationship between the Shields stress, a non-dimensional expression of the shear stress, and its critical value above which sediment movement is initiated (Shields, 1936). As a result, whether water flow tends to mobilize and remove or deposit sediment is a function of the ratio between the rate of sediment transport and that of sediment supply. As a result, for an esker to be deposited by subglacial water flow, a mechanism leading to either a drop in transport rate or increase in sediment supply is required.

The study of physical processes involved in sediment transport and bedrock erosion by subglacial water flow is limited to a handful of papers. Early work by Fowler and Walder (1993) and Walder and Fowler (1994) exploring the formation of subglacial canals excavated both in till and ice paved the way for the study of water-born subglacial sediment transport. Theoretical studies of canals however assume an equilibrium in sediment transport such

that the removal of sediment is equal to the sum of sediment supply by deposition and deformation. In addition the bed conditions are always transport limited (Fowler and Walder, 1993; Walder and Fowler, 1994; Ng, 2000a). Two recent studies (Creyts and others, 2013; Kyrke-Smith and Fowler, 2014) implement sediment transport in a macro-porous sheet (Creyts and Schoof, 2009) under transport-limited conditions. A macro-porous sheet is typically used as a representation of the distributed drainage system in which water pressure increases with water flux, in contrast to the R-channel theory used here in which, at equilibrium, water pressure decreases with increasing water discharge (see Flowers, 2015, for a review). Although Kyrke-Smith and Fowler (2014) do not specifically discuss the evolution of the sediment surface or flux, Creyts and others (2013) describe sediment fluxes and accretion by refreezing at the glacier bed in a macroporous water sheet and discuss how such sediment transport controls bed slopes close to the terminus of the glacier. Creyts and others (2013) show the importance of water discharge fluctuations for sediment transport and discuss the implications for the evolution of bed slope. The body of work exploring the formation of canals in till (Fowler and Walder, 1993; Ng, 2000a,b; Walder and Fowler, 1994) or sediment transport in a macroporous sheet (Creyts and others, 2013; Kyrke-Smith and Fowler, 2014) is restricted to transport-limited bed conditions, and these environments are often related to distributed or slow drainage systems. Considering hard-bed conditions, Beaud and others (2016) developed a model of bedrock erosion by subglacial water flow using a fluvial abrasion law (Lamb and others, 2008a). This study shows that such abrasion rates are negligibly small compared to expected glacial erosion rates, although the localization of erosion to the bed of subglacial channels can lead to the excavation of significant bedrock channels (Beaud and others, 2016), especially over the time scale of a glacial cycle (Chapter 4). These two studies (Beaud and others, 2016; Chapter 4) are limited by the assumption of supply-limited conditions and the omission of sediment transport. Beaud and others (2016) nevertheless suggest that the large spatio-temporal fluctuations in water flow regimes can lead to a bottleneck in sediment transport in the vicinity of the glacier terminus.

We develop a numerical model of sediment transport in R-channels, assuming that subglacial drainage occurs over a hard bed, till cover is relatively thin and patchy and the surrounding distributed drainage system plays a negligible role in sediment transport. We combine equations describing water flow in a semi-circular ice-walled bedrock-floored subglacial channel (Nye, 1976; Röthlisberger, 1972) with a law for sediment conservation suited for both alluvial and mixed bedrock / alluvial channels (e.g. Inoue and others, 2014; Nelson and Seminara, 2012; Zhang and others, 2015). After showing the basic behaviour of the model, we address the following questions. (1) How does the frequency of water input affect sediment transport near the terminus? (2) How does a melt-season affect sediment delivery to the proglacial area? We then discuss the implications of the model results for

the interpretation of proglacial sediment yields and their meaning for glacial erosion rates, as well as the implications of the results on esker formation.

5.2 Methods

5.2.1 Governing equations

In this study, we focus on sediment transport in straight ice-walled bedrock-floored semi-circular Röthlisberger channels (R-channels). In a semi-circular R-channel the conservation of water is given by

$$-\gamma S_{\mathrm{ch}} \frac{\partial p_{\mathrm{ch}}}{\partial t} = \frac{\partial Q_{\mathrm{ch}}}{\partial x} + \frac{\Xi - \Pi}{L}\left(\frac{1}{\rho_{\mathrm{i}}} - \frac{1}{\rho_{\mathrm{w}}}\right) - v_{\mathrm{cc}} - \dot{b}_{\mathrm{ch}}, \tag{5.1}$$

where t and x are, respectively, time and position along the channel, γ is a fluid compressibility factor introduced for numerical purposes (Clarke, 2003), Q_{ch} is the water discharge in the channel, p_{ch} is the water pressure in the channel, Ξ is the dissipation of potential energy, Π is the change in sensible heat of the water, L is the latent heat of fusion, ρ_{i} and ρ_{w} are, respectively, the density of ice and water, v_{cc} is the creep closure rate of the channel and $\dot{b}_{\mathrm{ch}}$ is a local water source term. The evolution of channel cross-sectional area S_{ch} with time is

$$\frac{\partial S_{\mathrm{ch}}}{\partial t} = v_{\mathrm{oc}} - v_{\mathrm{cc}} - v_{\mathrm{s}}, \tag{5.2}$$

where v_{s} is the sedimentation rate in the channel (e.g. Creyts and others, 2013; Ng, 2000a; Walder and Fowler, 1994) defined as positive when sediment is being deposited and negative when it is removed. The opening rate of a channel by viscous heat dissipation is

$$v_{\mathrm{oc}} = \frac{\Xi - \Pi}{\rho_{\mathrm{i}} L}. \tag{5.3}$$

The creep closure rate is

$$v_{\mathrm{cc}} = \tilde{A} S_{\mathrm{ch}} |N_{\mathrm{ch}}|^{n-1} N_{\mathrm{ch}}, \tag{5.4}$$

where $\tilde{A}$ is a factor that includes Glen's flow-law coefficient and the shape of the channel, and $N_{\mathrm{ch}} = p_{\mathrm{i}} - p_{\mathrm{ch}}$ is the effective pressure in the channel, with p_{i} taken as the ice-overburden pressure. For turbulent flow in a semi-circular channel, the discharge is

$$Q_{\mathrm{ch}} = -\left(\frac{8 S_{\mathrm{ch}}^3}{P_{\mathrm{W}} \rho_{\mathrm{w}} f_{\mathrm{R}}}\right)^{1/2} \nabla \phi_{\mathrm{ch}} |\nabla \phi_{\mathrm{ch}}|^{-1/2}, \tag{5.5}$$

where $\phi_{\mathrm{ch}} = \rho_{\mathrm{w}} g z_{\mathrm{b}} + p_{\mathrm{ch}}$ is the hydraulic potential in the channel, h_{i} is the ice thickness, g is the acceleration due to gravity, P_{W} is the wetted perimeter and the Darcy-Weisbach roughness is expressed as $f_{\mathrm{R}} = (8g\langle n' \rangle^2)/(R_{\mathrm{H}}^{1/3})$, with $\langle n' \rangle$ the Manning roughness averaged over the channel perimeter and R_{H} the hydraulic radius. We prescribe different roughnesses

for the bed and the ice, and for each material $f_a = (8gn'^2_a)/(R_{\mathrm{H}}^{1/3})$, where a can represent the ice or bed. The dissipation of potential energy is expressed as

$$\Xi = \left| Q_{\mathrm{ch}} \frac{\partial \phi_{\mathrm{ch}}}{\partial x} \right| \tag{5.6}$$

and the change in sensible heat of the water is given by

$$\Pi = -c_{\mathrm{t}} c_{\mathrm{w}} \rho_{\mathrm{w}} Q_{\mathrm{ch}} \frac{\partial p_{\mathrm{ch}}}{\partial x}, \tag{5.7}$$

where c_{t} is the pressure-melting coefficient and c_{w} is the heat capacity of water.

The case of alluvial and mixed alluvial / bedrock channels has seldom been treated in the literature (c.f. Inoue and others, 2014; Nelson and Seminara, 2012; Zhang and others, 2015). The general form of Exner's equation for alluvial rivers reads

$$(1-\lambda)\frac{\partial \eta_{\mathrm{a}}}{\partial t} + \frac{\partial q_{\mathrm{t}}}{\partial x} = 0, \tag{5.8}$$

where λ is the porosity of the sediment layer, η_{a} its thickness and q_{t} the volumetric sediment flux per unit width. In channels with a patchy alluvial cover (i.e. mixed bedrock / alluvial channels) the thickness of sediment at rest can be nil, though sediment is being transported above the bed. Exner's equation fails to capture such behaviour, thus a term must be added to account for the volume of sediment being transported. The sediment flux is smaller than the transport capacity and must be calculated as a function of the volume of available sediment. Several different formulations have been proposed to treat mixed bedrock / alluvial channels (Inoue and others, 2014; Nelson and Seminara, 2012; Zhang and others, 2015); we build on that of Inoue and others (2014) where the volume of sediment in transit per unit channel width and unit grid cell length is V_{b} and

$$\frac{\partial V_{\mathrm{b}}}{\partial t} + (1-\lambda)F_{\mathrm{c}}\frac{\partial \eta_{\mathrm{a}}}{\partial t} + \frac{\partial q_{\mathrm{t}}}{\partial x} = 0, \tag{5.9}$$

where F_{c} is the fraction of the macro-topography of the bed covered by sediment. Sediment can be located in topographic lows, while topographic highs remain exposed bedrock or the macro topography can be fully covered in which case the bed is fully covered, $F_{\mathrm{c}} = 1$. In Inoue and others (2014), F_{c} is related to the macro-roughness of the bed; we omit this level of complexity in the current study. Inoue and others (2014) define the volumetric sediment flux per unit width as:

$$q_{\mathrm{t}} = \begin{cases} \dfrac{V_{\mathrm{b}}}{V_{\mathrm{tc}}} q_{\mathrm{tc}}, & 0 \leq \dfrac{V_{\mathrm{b}}}{V_{\mathrm{tc}}} < 1 \\ q_{\mathrm{tc}}, & \dfrac{V_{\mathrm{b}}}{V_{\mathrm{tc}}} \geq 1 \end{cases}, \tag{5.10}$$

where q_{tc} is the volumetric transport capacity per unit width (Fernandez-Luque and van Beek, 1976):

$$q_{\mathrm{tc}} = 5.7 \left(rgD^3 \right)^{1/2} \left(\tau^* - \tau_{\mathrm{c}}^* \right)^{3/2}, \tag{5.11}$$

with τ^* the Shields stress and τ_{c}^* its critical value. The saturation volume of sediment per unit area (Inoue and others, 2014), i.e. the threshold above which the volume of sediment in transport is sufficiently high that alluvial conditions start to develop, is

$$V_{\mathrm{tc}} = \frac{q_{\mathrm{tc}}}{u_{\mathrm{s}}} \tag{5.12}$$

and the sediment saltation velocity u_{s} is defined according to Sklar and Dietrich (2004):

$$u_{\mathrm{s}} = 1.56 \left(\frac{\tau^*}{\tau_{\mathrm{c}}^*} - 1 \right)^{0.56} \sqrt{rgD}, \tag{5.13}$$

with $r = \rho_{\mathrm{s}}/\rho_{\mathrm{w}} - 1$ the buoyant density of a particle of diameter D. Note that with this empirical expression (Eq. 5.13) u_{s} must be capped at the water flow velocity (Beaud and others, 2016; Lamb and others, 2008a). To allow for the width of the channel and the flow regime to change over an order of magnitude in space and time, we use the total volume of sediment in a channel reach per unit length V_{s}, instead of the sediment thickness η_{a} which is a width averaged quantity, such that

$$V_{\mathrm{s}} = \left(V_{\mathrm{b}} + (1 - \lambda) F_{\mathrm{c}} \eta_{\mathrm{a}} \right) W_{\mathrm{ch}}, \tag{5.14}$$

where W_{ch} is the width of the R-channel. Accounting for the macro-roughness of the bed is beyond the scope of this study (see Inoue and others, 2014; Zhang and others, 2015) and we replace the fraction covered F_{c} by the ratio between the volume of sediment available and that available to be transported:

$$r_{\mathrm{V}} = \begin{cases} \dfrac{V_{\mathrm{s}}}{V_{\mathrm{tc}} W_{\mathrm{ch}}}, & 0 \leq \dfrac{V_{\mathrm{s}}}{V_{\mathrm{tc}} W_{\mathrm{ch}}} < 1 \\ 1, & \dfrac{V_{\mathrm{s}}}{V_{\mathrm{tc}} W_{\mathrm{ch}}} \geq 1 \end{cases}, \tag{5.15}$$

and thus the total sediment flux in a given reach is

$$q_{\mathrm{tt}} = q_{\mathrm{tc}} r_{\mathrm{V}} W_{\mathrm{ch}}. \tag{5.16}$$

We also define the sediment transport capacity in a reach as

$$q_{\mathrm{ttc}} = q_{\mathrm{tc}} W_{\mathrm{ch}}. \tag{5.17}$$

The conservation of sediment becomes

$$\frac{\partial V_{\mathrm{s}}}{\partial t} + \frac{\partial q_{\mathrm{tt}}}{\partial x} - \frac{q_{\mathrm{ls}}}{\mathrm{d}x} = 0, \tag{5.18}$$

where q_{ls} is a local sediment source term. The rate of change of channel cross-sectional area due to sediment deposition or removal is found by calculating the change in equivalent sediment cross-sectional area resulting from the change in sediment volume

$$v_{\mathrm{s}} = \frac{\partial V_{\mathrm{s}}}{\partial t} \frac{1}{(1-\lambda)}. \tag{5.19}$$

5.2.2 Summary and solution of the system of equations

We solve the system of equations comprising the conservation of water (Eq. 5.1), the evolution of the channel cross-sectional area (Eq. 5.2) and the evolution of sediment volume (Eq. 5.18):

$$-\gamma S_{\mathrm{ch}} \frac{\partial p_{\mathrm{ch}}}{\partial t} = \frac{\partial Q_{\mathrm{ch}}}{\partial x} + \frac{\Xi - \Pi}{L} \left(\frac{1}{\rho_{\mathrm{i}}} - \frac{1}{\rho_{\mathrm{w}}} \right) - v_{\mathrm{cc}} - \dot{b}_{\mathrm{ch}}, \tag{5.20}$$

$$\frac{\partial S_{\mathrm{ch}}}{\partial t} = v_{\mathrm{oc}} - v_{\mathrm{cc}} - v_{\mathrm{s}}, \tag{5.21}$$

$$\frac{\partial V_{\mathrm{s}}}{\partial t} = -\frac{\partial q_{\mathrm{tt}}}{\partial x} + \frac{q_{\mathrm{ls}}}{\mathrm{d}x}, \tag{5.22}$$

for p_{ch}, S_{ch} and V_{s} with the Matlab `ode15s` solver and the parameters summarized in Table 5.1.

5.2.3 Initial and boundary conditions

We prescribe the water discharge at the upstream end of the domain ($Q_{\mathrm{ch}}(x = 0)$) and we set the water pressure at the downstream end to be atmospheric ($p_{\mathrm{ch}}(x = X_{\mathrm{L}}) = 1000\,\mathrm{Pa}$). We prescribe the sediment input at the upstream end of the domain ($q_{\mathrm{ls}}(x = 0)$) or a no-flux boundary ($(\frac{\partial q_{\mathrm{tt}}}{\partial x}(x = 0) = 0)$ condition if no input is prescribed. For the channel cross-sectional area we impose that the gradient in the temporal derivative is constant at the terminus. We spin-up every simulation for a sufficient time that the results are independent of initial conditions. The spin-ups are described individually for each simulation.

5.3 Simulation set-up and results

5.3.1 Model set-up

The model domain comprises a single R-channel fed by a moulin. Our reference glacier geometry is defined by a constant ice surface slope and a flat bed (Fig. 5.1A). All the simu-

Table 5.1: Summary of model constants and parameters

Parameter	Description	Value
M	Number of grid points	101
$\mathrm{d}x$	Cell size	$300\,\mathrm{m}$
$\mathrm{d}t$	Output time step	$3600\,\mathrm{s}$
X_L	Glacier length	$30\,\mathrm{km}$
ρ_w	Water density	$1000\,\mathrm{kg\,m^{-3}}$
ρ_i	Ice density	$910\,\mathrm{kg\,m^{-3}}$
c_w	Heat capacity of water	$4.22 \times 10^3\,\mathrm{J\,kg^{-1}\,K^{-1}}$
c_t	Pressure melting coefficient	$7.5 \times 10^{-8}\,\mathrm{K\,Pa^{-1}}$
D	Particle diameter	0.17 m
L	Latent heat of fusion	$3.34 \times 10^5\,\mathrm{J\,kg^{-1}}$
$\tilde{A}$	Flow-law coefficient for channels	$5 \times 10^{-25}\,\mathrm{Pa^{-n}\,s^{-1}}$
n	Flow-law exponent	3
$\langle n' \rangle$	Manning roughness averaged	0.0321
n'_i	Manning roughness for ice	0.01
n'_b	Manning roughness for bed	0.05
γ	Numerical compressibility parameter	$10^{-9}\,\mathrm{Pa^{-1}}$
λ	Porosity of sediment	0.35

lations feature a constant sediment supply ($q_\mathrm{ls}(x=0) = \mathrm{cst}$) and a constant sediment size ($D = 0.17\,\mathrm{m}$), assuming that this is a representative grain size for the subglacial sediment. We first present simulations where sediment transport and water flow are decoupled ($v_\mathrm{s} = 0$ in Eq. 5.21) and the water input is constant. We then present results with the coupled model and then test the role of temporal fluctuations in water input.

5.3.2 Constant water input

Decoupled simulations

To test the effect of a simple shear-stress field and channel-size profile on sediment transport we perform a simulation with constant water ($Q_\mathrm{ch}(x=0) = 50\,\mathrm{m^3\,s^{-1}}$) and sediment input ($q_\mathrm{ls}(x=0) = 0.1\,\mathrm{m^3\,s^{-1}}$), both prescribed at the upstream boundary. The sediment is only added once the hydrologic system (p_ch and S_ch) has reached a steady state, i.e. the conditions shown in Fig 5.1.

With a constant ice-surface slope, a flat bed and a constant discharge (Fig 5.1A–B), the water velocity decreases monotonically towards the terminus; this decline is enhanced over the last 10 km of the profile (Fig 5.1C) as a result of the increase in channel size (Fig 5.1D). As the ice thins, the creep closure rate of the R-channel decreases, enlarging the channel. The shear stress pattern follows that of the water velocity, suggesting a bottleneck close to the glacier terminus (Fig 5.1E). In this scenario, it only takes about 4 hours for a wave of sediment to travel through the 30-kilometre domain and for the sediment volume (V_s) to

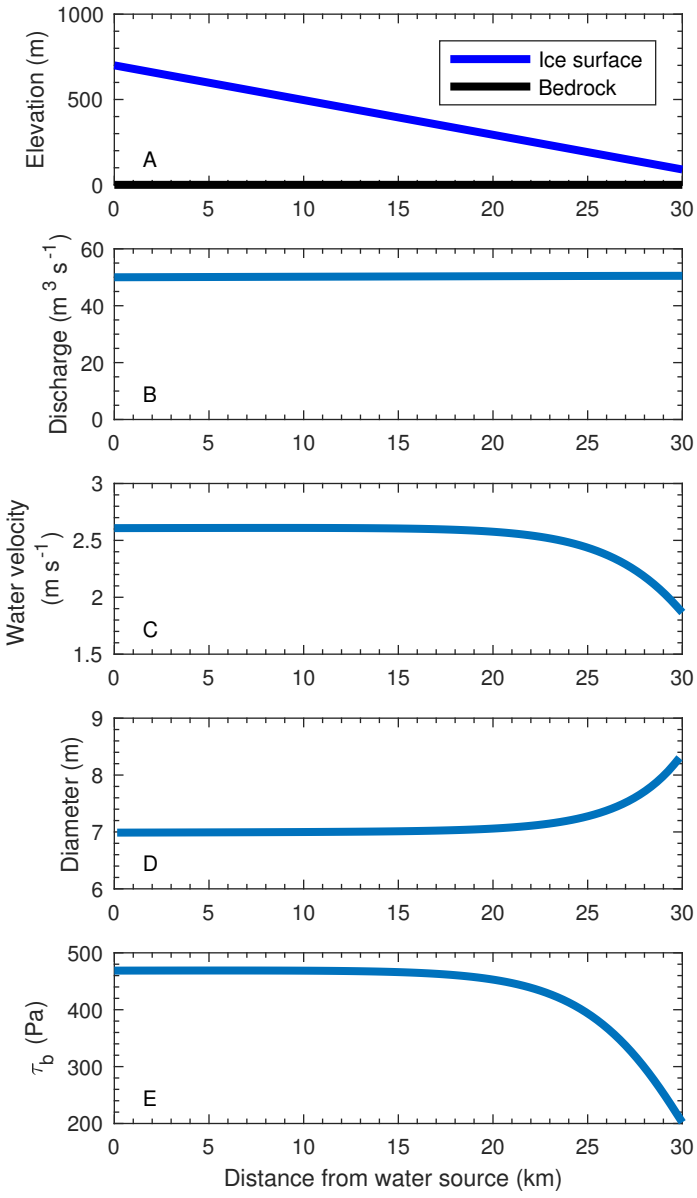

Figure 5.1: Hydraulic quantities computed when steady state has been reached with a constant discharge $Q_{\mathrm{ch}}(x = 0) = 50\,\mathrm{m}^3\,\mathrm{s}^{-1}$ in the absence of sediment. (A) Ice surface z_{i} and bedrock elevation η_{br}; (B) Water discharge Q_{ch}; (C) Water velocity $v = Q_{\mathrm{ch}}/S_{\mathrm{ch}}$; (D) R-channel diameter W_{ch}; (E) Shear stress exerted on the bed τ_{b}.

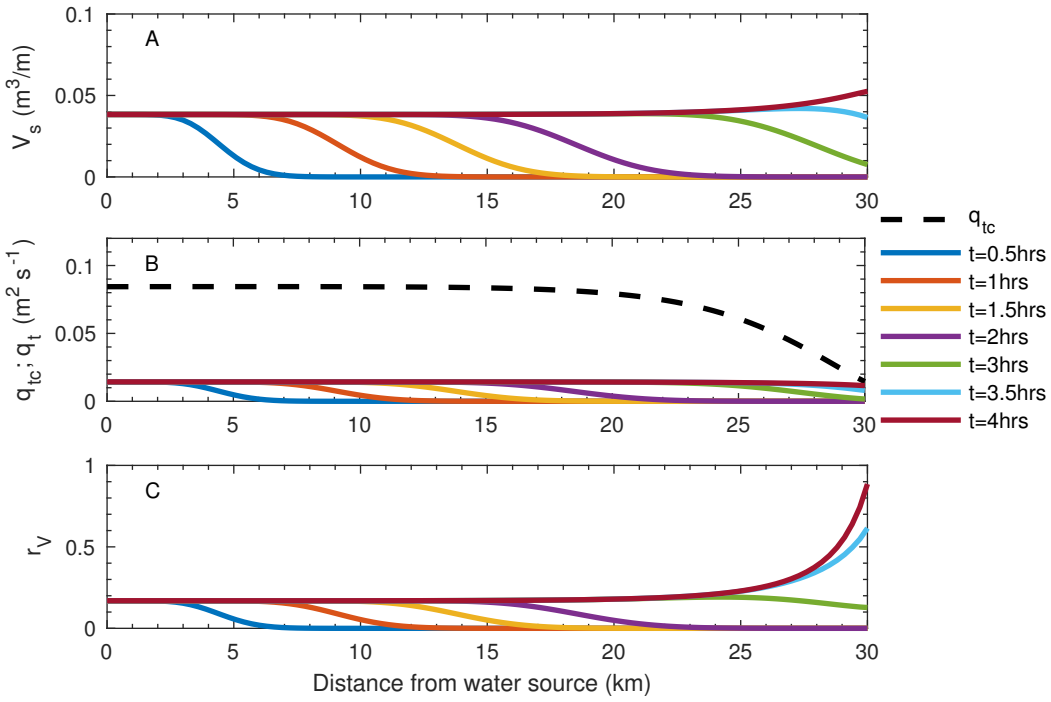

Figure 5.2: Evolution of sediment transport in an uncoupled simulation with steady-state hydrology (Sect. 5.3.2; Fig. 5.1). (A) Volume of sediment per unit length V_s; (B) Volumetric transport capacity q_{tc} (dashed) and sediment flux q_t (solid lines) per unit width; (C) Ratio between volume of sediment in a reach and volume transported at capacity r_V.

reach a steady state (Fig. 5.2A). During this simulation the conditions are always supply limited and the sediment flux remains a fraction of the transport capacity (Fig. 5.2B and C). The slight increase in sediment volume over the last 5 km of the profile is the result of the drop in water-flow velocity and therefore sediment velocity (Fig 5.1C).

Coupled simulations with constant water input

In order to test the effect of coupling between sediment transport and water flow we perform a series of simulations with different rates of sediment input ($q_{\mathrm{ls}}(x = 0)$; Table 5.2). The prescribed rates of sediment input are guided by the transport capacity at the terminus for an uncoupled steady-state simulation. The value of $q_{\mathrm{ls}}(x = 0)$ is increased until the system fails to reach a steady state (Table 5.2). In this series of simulations, the sediment and water input are constant from the beginning of the simulations, in contrast to the previous simulations where the sediment input was only introduced once the hydrology had reached a steady state. In this experiment the interest of the uncoupled simulation (R6; Table 5.2) is two-fold. It shows the same evolution of the hydraulic variables (ϕ_{ch} and S_{ch}) as a simulation where sediment transport is completely omitted and it highlights the role of the coupling or lack thereof on the sediment dynamics when compared to simulation R3, for which the rate of sediment input is the same.

All the coupled simulations (R1–R5; Table 5.2) exhibit a damped oscillation in sediment volume at the terminus until steady state is reached (Fig. 5.3A), as the transport capacity must adjust to changes in channel cross-sectional area caused by changes in sediment volume (Fig. 5.3B). This behaviour can be seen in space as well in the last 1.5 km of the profile once steady state has been reached (Fig. 5.3C–F). The larger the sediment input, the higher the wedge of sediment that accumulates at the terminus (Fig. 5.3C) and the smaller the cross-sectional area of the channel (Fig. 5.3D). The hydraulic potential gradient thus steepens (Fig. 5.3E) and the transport capacity of the water flow increases (Fig. 5.3F). The area of sediment deposited in the channel ($V_{\mathrm{s}}/(1 - \lambda)$) is larger than the associated reduction in channel cross-sectional area (S_{ch}). When comparing the hydrology of R5 to that of the uncoupled simulation R6, the deposition of a sediment cross-section of $\sim 11\,\mathrm{m}^2 = 7/(1-\lambda)$ (Fig. 5.3C), once the porosity is accounted for, results in a channel constriction of only $\sim 1.5\,\mathrm{m}^2$ (Fig. 5.3D). This constriction enhances water flow velocities, thus a smaller cross-sectional area is needed to evacuate the prescribed discharge, but the viscous heat dissipation is also enhanced. In the uncoupled simulation (R6; Table 5.2), this stabilizing feedback is inhibited and the sediment volume at the terminus increases monotonically during the simulation. If the sediment supply is too large, with the uncoupled model, the sediment accumulation at the terminus is large enough that the numerical integration fails.

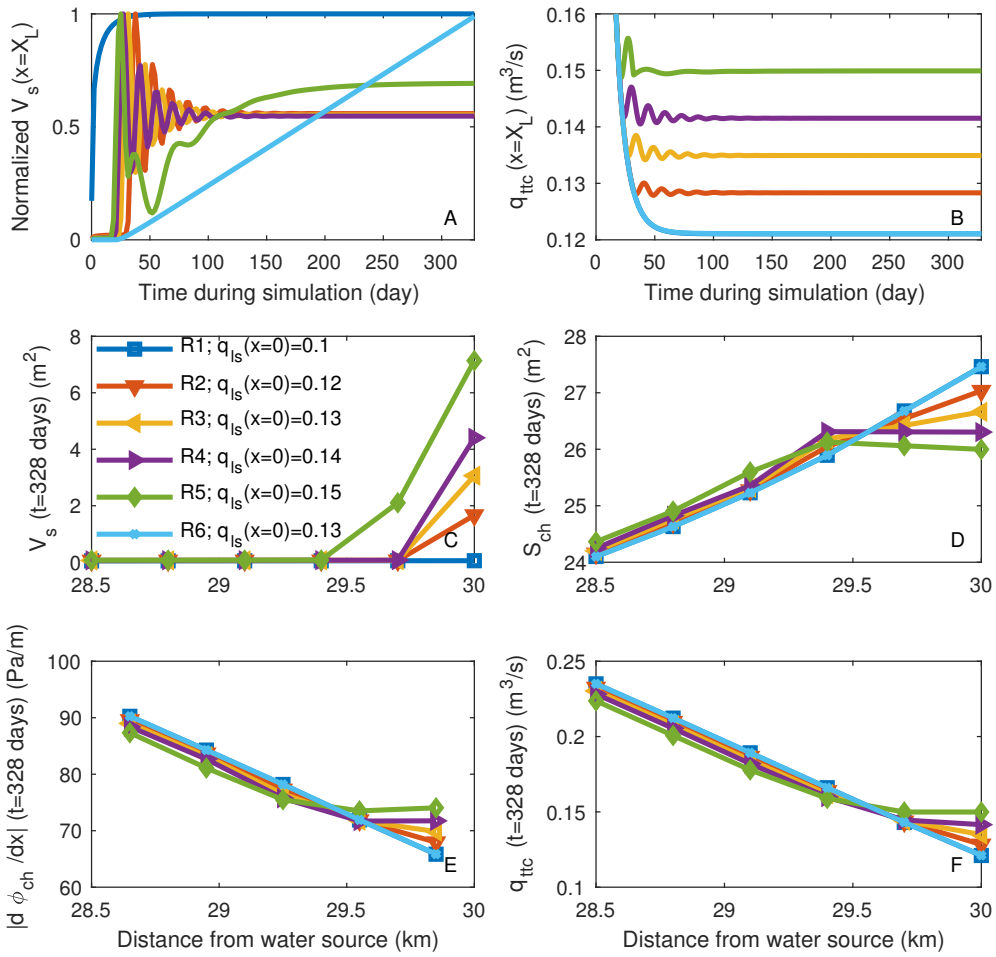

Figure 5.3: Temporal and spatial variations in selected variables showing the interaction between sediment bottleneck and hydrology under steady state conditions. Temporal evolution of (A) normalized sediment volume and (B) transport capacity at the terminus ($q_{\mathrm{ttc}} = q_{\mathrm{tc}} \times W_{\mathrm{ch}}$). The sediment volume is normalized with respect to the largest value encountered during the simulation so that patterns are easier to compare. Spatial changes within the last 1.5 km of the profile at the end of each simulation of: (C) sediment volume per unit length V_{s} , (D) cross-sectional area of the channel S_{ch}, (E) absolute value of the hydraulic potential gradient $|\partial\phi_{\mathrm{ch}}/\partial x|$ and (F) sediment transport capacity q_{ttc}. In all the simulations but R6, the hydrology and sediment transport are coupled (Table 5.2). The uncoupled simulation (R6) is omitted from the volume plot (C) as values of V_{s} close to $400\,\mathrm{m}^2$ are calculated, in comparison to the V_{s} remaining smaller than $8\,\mathrm{m}^2$ for R1–R5.

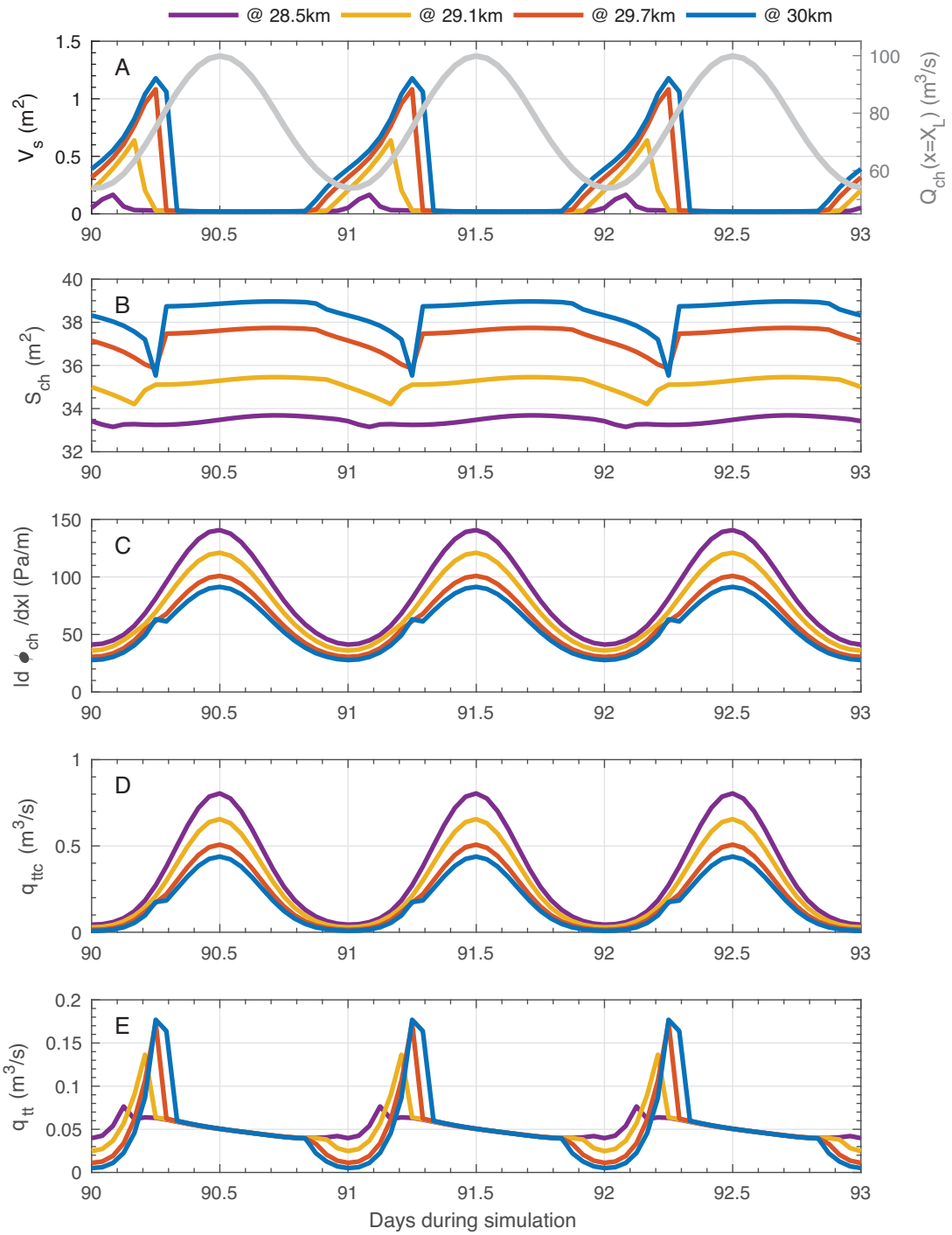

Figure 5.4: Temporal evolution of key quantities near the terminus for a sinusoidal water input with a period of one day. (A) Volume of sediment per unit length and outlet water discharge; (B) Channel cross-sectional area; (C) Absolute value of the hydraulic potential gradient; (D) Transport capacity; (E) Volumetric discharge of sediment. Quantities are shown at 28.5, 29.1, 29.7 and 30 kilometres from the water source for 3 forcing cycles after a 90-day spin-up.

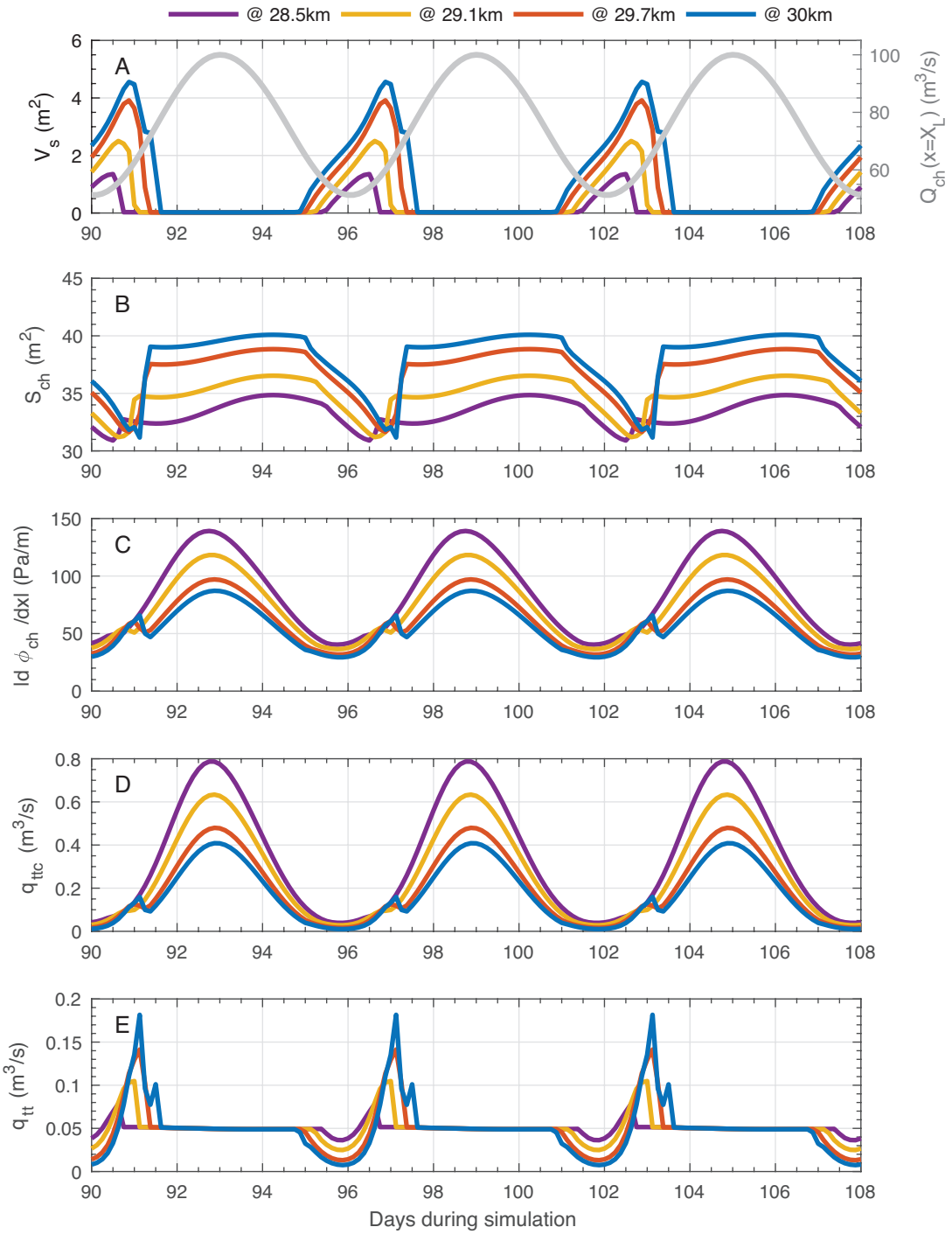

Figure 5.5: Temporal evolution of key quantities near the terminus for a water input forcing period of 6 days. (A) Volume of sediment per unit length and outlet water discharge; (B) Channel cross-sectional area; (C) Absolute value of the hydraulic potential gradient; (D) Transport capacity; (E) Volumetric discharge of sediment. Quantities are shown at 28.5, 29.1, 29.7 and 30 kilometres from the water source for 3 forcing cycles after a 90-day spin-up.

Table 5.2: Summary of simulations run to achieve steady state with constant water and sediment input (see Fig. 5.3).

Simulation	Water-sediment coupling	$q_{\mathrm{ls}}(x=0)\,(\mathrm{m}^3/\mathrm{s})$
R1	Yes	0.10
R2	Yes	0.12
R3	Yes	0.13
R4	Yes	0.14
R5	Yes	0.15
R6	No	0.13

Table 5.3: Summary of simulations with different forcing periods shown in Figs. 5.4–5.8.

Water forcing period	Water-sediment coupling	$q_{\mathrm{ls}}(x=0)\,(\mathrm{m}^3/\mathrm{s})$	Figure
1 day	Yes	0.05	Fig. 5.4
6 days	Yes	0.05	Fig. 5.5
1 month	Yes	0.05	Fig. 5.6
1 month	No	0.05	Fig. 5.7
3 months	Yes	0.05	Fig. 5.8

5.3.3 Water forcing frequency

The timescale for channel cross-sectional area adjustment is on the order of a few hours for sediment transport, but on the order of several days for viscous heat dissipation and creep combined. In order to identify how these processes interact despite such different response times, we perform four simulations with sinusoidal fluctuations in water input of identical amplitude, but four different arbitrary periods: one day, six days, one month and three months. Sediment input remains constant and unchanged for these simulations. To highlight the importance of the coupling between hydrology and sediment transport, we also show a simulation with a period of one month, but where hydrology and sediment transport are uncoupled ($v_{\mathrm{s}} = 0$). These simulations are spun up for 90 days to allow for the system to reach a dynamic steady state.

When we prescribe a daily oscillation in water input (Fig. 5.4), a daily accumulation of sediment begins (~ 0.8 day into the oscillation) as the discharge is nearing its lowest values. This accumulation continues until ~ 0.3 day into the next oscillation. The resulting sediment bottleneck is strongest and lasts longest at the terminus, and decreases in size upglacier (Fig. 5.4A). The channel cross-sectional area changes predominantly as a result of sediment accumulation and removal (Fig. 5.4B), rather than by adjustements via melting and creep closure. Oscillations in hydraulic potential gradient (Fig. 5.4C) and transport

capacity (Fig. 5.4D) thus mainly follow changes in discharge. The decrease in hydraulic potential gradient accompanied by a decrease in discharge while the cross-section remains almost constant leads to the accentuation of the bottleneck in sediment transport (Fig. 5.4E) and the deposition of sediment near the terminus. The channel therefore undergoes alternating alluvial and bedrock conditions between 28.5 and 30 km. At low discharge the bed is alluviated and the system transport limited ($q_{\mathrm{tt}} = q_{\mathrm{ttc}}$), but as the water discharge increases and stored sediment is flushed away, the system becomes supply limited (q_{tt} is controlled by V_{s} as $r_{\mathrm{V}} \leq 1$; Eqs. 5.15 and 5.16).

A very similar behaviour occurs with a forcing period of 6 days (Fig. 5.5), although the changes in channel cross-sectional area are $\sim$ 6 times larger. Sediment accumulates at the terminus for about 2.5 days out of a 6-day cycle, and its volume per unit length is four times larger compared to the simulation with a daily oscillation. The timescale at which the channel size adjusts by creep closure and melt-opening is closer to that of the forcing period in this simulation (q_{ttc} peaks only $\sim$ 6 hours earlier than the discharge); the changes in sediment volume are, however, still the dominant driver of the changes in shear stresses.

Increasing the forcing period to one month also leads to sediment accumulation, although the pattern in sediment volume shows multiple peaks at the terminus (Fig. 5.6). The evolution of the ice-walled perimeter of the channel is now the main driver of changes in shear stresses within one kilometre from the terminus and for $\sim$ 20 days out of the 30 of the forcing period. When examined at a timescale of one month, transport capacity peaks two to four days (at 28.5 and 30 kilometres, respectively) before the discharge. Water discharge and sediment transport interact such that an initial deposition of sediment (e.g. day $\sim$ 115) reduces the channel size (Fig. 5.6B), steepens the hydraulic potential gradient slightly (Fig. 5.6C), and increases the transport capacity (Fig. 5.6D). This interaction results in a rapid removal of sediment that rapidly increases the channel size, and the initiation of the opposite feedback whereby sediment is deposited again. Such a feedback is, for example, responsible for the sediment volume (V_{s}) peak at 95, 125 and 155 days at the terminus (Fig. 5.6A). The discharge increase at the onset of the following cycle leads to rapid removal of sediment and an enlargement of the channel cross-section of $\sim 7\,\mathrm{m}^2$ (i.e. 25% increase in channel cross-sectional area) in less than a day. The sediment flux decreases by a factor $\sim$ 3 and sediment accumulates rapidly again. This sediment layer is subsequently flushed out in a couple of days.

The results from the uncoupled simulation with a one-month period (Fig. 5.7) highlight the importance of the feedbacks between hydrology and sediment transport. A similar alternation of sediment deposition / removal is observed (V_{s} in Fig. 5.7A) as in the coupled simulation (Fig. 5.6). The amount of sediment deposited is, however, several times larger (6-fold at 30 km and 13-fold at 28.5 km), because the sediment bottleneck has no effect on hydraulic conditions. It is interesting to note that by comparing Figs. 5.6 and 5.7 we

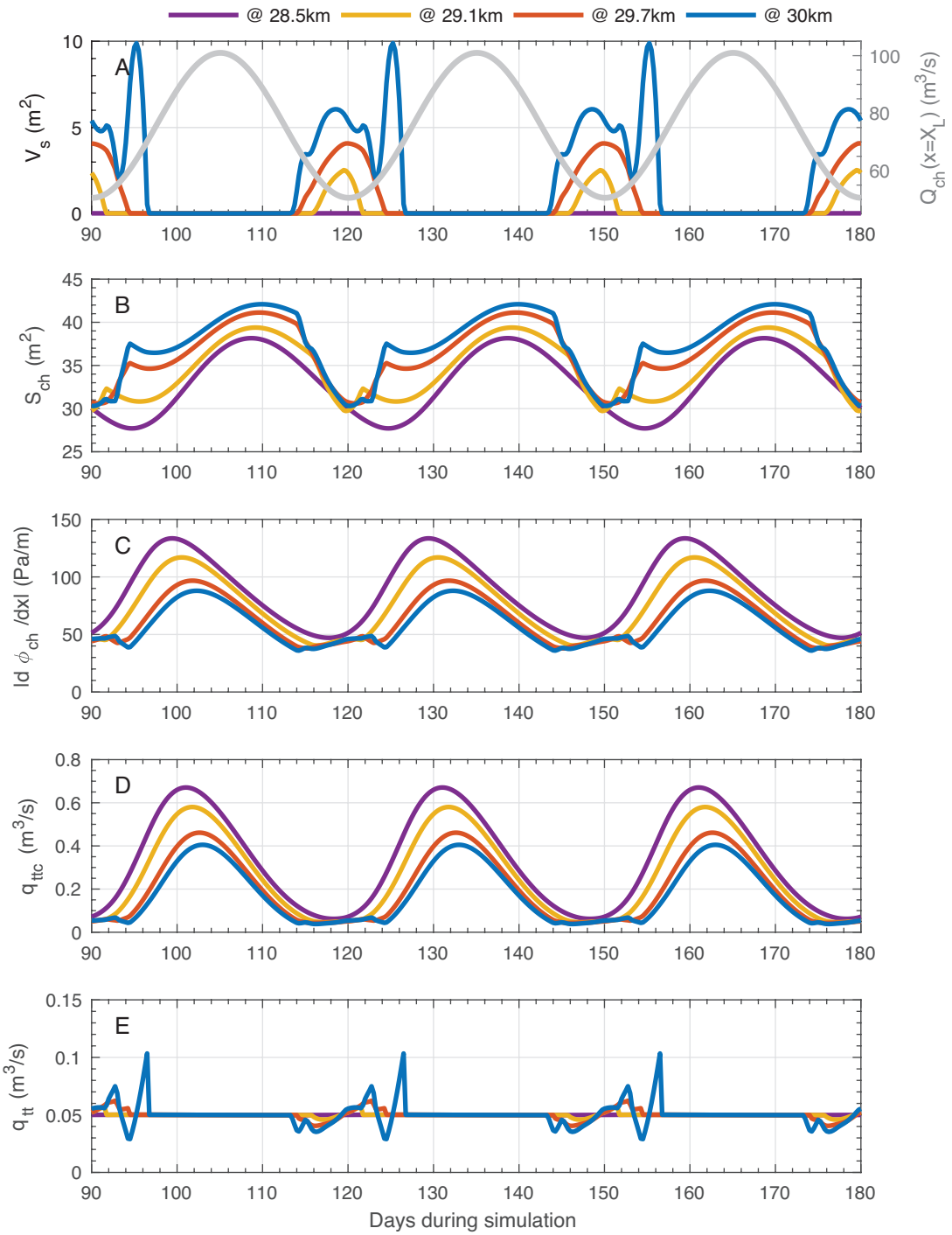

Figure 5.6: Temporal evolution of key quantities near the terminus for a water input forcing period of one month. (A) Volume of sediment per unit length and outlet water discharge; (B) Channel cross-sectional area; (C) Absolute value of the hydraulic potential gradient; (D) Transport capacity; (E) Volumetric discharge of sediment. Quantities are shown at 28.5, 29.1, 29.7 and 30 kilometres from the water source for three forcing cycles after a 90-day spin-up.

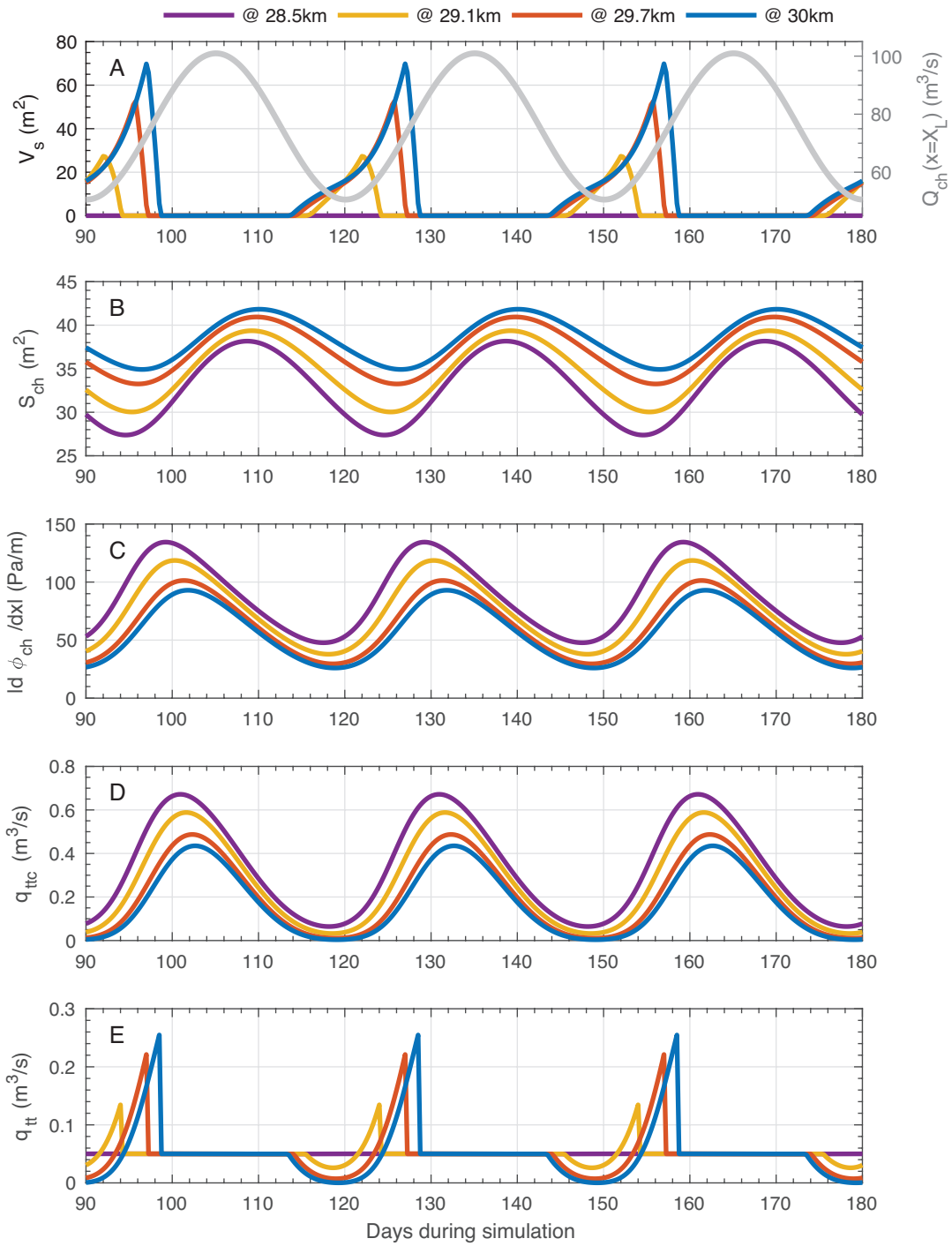

Figure 5.7: Temporal evolution of key quantities near the terminus for a water input forcing period of one month and uncoupled hydrology and sediment transport ($v_s = 0$). (A) Volume of sediment per unit length and outlet water discharge; (B) Channel cross-sectional area; (C) Absolute value of the hydraulic potential gradient; (D) Transport capacity; (E) Volumetric discharge of sediment. Quantities are shown at 28.5, 29.1, 29.7 and 30 kilometres from the water source for three forcing cycles after a 90-day spin-up.

observe that hydraulic conditions (S_{ch} and $\partial\phi_{\mathrm{ch}}/\partial x$) in the coupled model are not impacted by sediment transport upstream from 28.5 km.

Finally, with a forcing period of three months, sediment accumulation only occurs at 30 km (the terminal node), despite maximum values of V_{s} being ~ 3 times larger than in the simulation with a one month period (Fig. 5.8). Hydraulic conditions (S_{ch} and $\partial\phi_{\mathrm{ch}}/\partial x$) are little affected by sediment transport, with the exception of a $\sim$ 20-day time window (e.g. between 160 and 180 days), where the changes in forcing are slow enough that the transport capacity remains at least twice as large as during the other simulations, leaving time for the system to adjust. In all the simulations presented here, the sediment input is such that changes in cross-sectional area due to sediment dynamics are only observed within the last 2 kilometres of the profile; the rest of the bed remains supply-limited.

5.3.4 Seasonal water input

Having established the different responses of the system to a range of water forcing periods, we construct a synthetic discharge time series intended to represent a melt-season (Fig. 5.9A). We explore how the system reacts to a combination of water forcing frequencies and how the forcing influences sediment delivery to the proglacial area. The sediment input is kept constant ($q_{\mathrm{ls}}(x=0) = 0.065\,\mathrm{m^3\,s^{-1}}$) and we again run a simulation with the same forcing but where hydrology and sediment transport are uncoupled ($v_{\mathrm{s}} = 0$). Both simulations are run for two melt-seasons, with the first serving as a spin-up.

During the first part of the melt-season (until day 75), the coupled and uncoupled simulations exhibit supply-limited conditions over the whole profile (Fig. 5.9B). The uncoupled simulation shows an exception at 30 km as the sediment accumulated toward the end of the spin-up requires an additional $\sim$ 8 days to be evacuated. As the channel is sediment-starved, the hydraulic conditions are indistinguishable between the coupled and uncoupled simulations (Fig. 5.9A and C), thus the transport capacity (Fig. 5.9D) is large enough that the sediment transport remains virtually constant (Fig. 5.9E) and matches the sediment input ($q_{\mathrm{ls}}(x=0) = 0.065\,\mathrm{m^3\,s^{-1}}$).

In the second part of the melt-season (after day 75) hydraulic conditions (S_{ch} and $\partial\phi_{\mathrm{ch}}/\partial x$) differ between the coupled and uncoupled simulation over the last kilometre of the profile (Fig. 5.9A and C), concurrent with the onset of sediment accumulation (Fig. 5.9B). Sediment accumulation near the terminus yields steeper hydraulic potential gradients in the coupled simulation, relative to the uncoupled one. Such sediment accumulation is, nevertheless, initiated at similar times in both simulations, coinciding with a significant drop in water discharge (Fig. 5.9A). As discharge drops (day 75) over a couple of days, the creep closure rates are too small to maintain hydraulic potential gradients. Transport capacity thus drops below the rate of sediment input (Fig. 5.9D) leading to sediment deposition (Fig. 5.9B). This accumulation of sediment constricts the channel in the coupled simulation, slightly steepening the hydraulic potential gradients and enhancing sediment

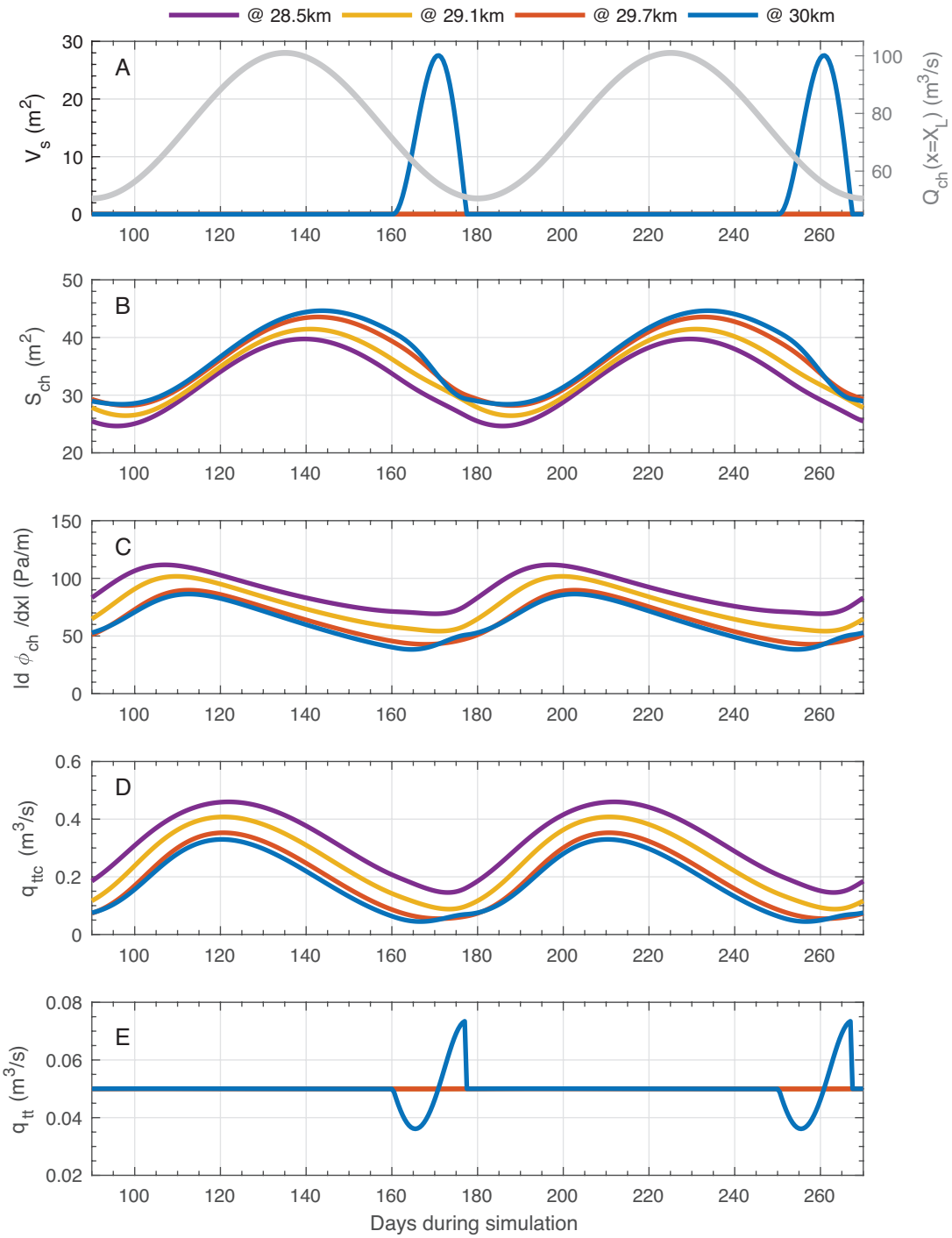

Figure 5.8: Temporal evolution of key quantities near the terminus for a water input forcing period of three months. (A) Volume of sediment per unit length and outlet water discharge; (B) Channel cross-sectional area; (C) Absolute value of the hydraulic potential gradient; (D) Transport capacity; (E) Volumetric discharge of sediment. Quantities are shown at 28.5, 29.1, 29.7 and 30 kilometres from the water source for 2 forcing cycle after a 90-day spin-up.

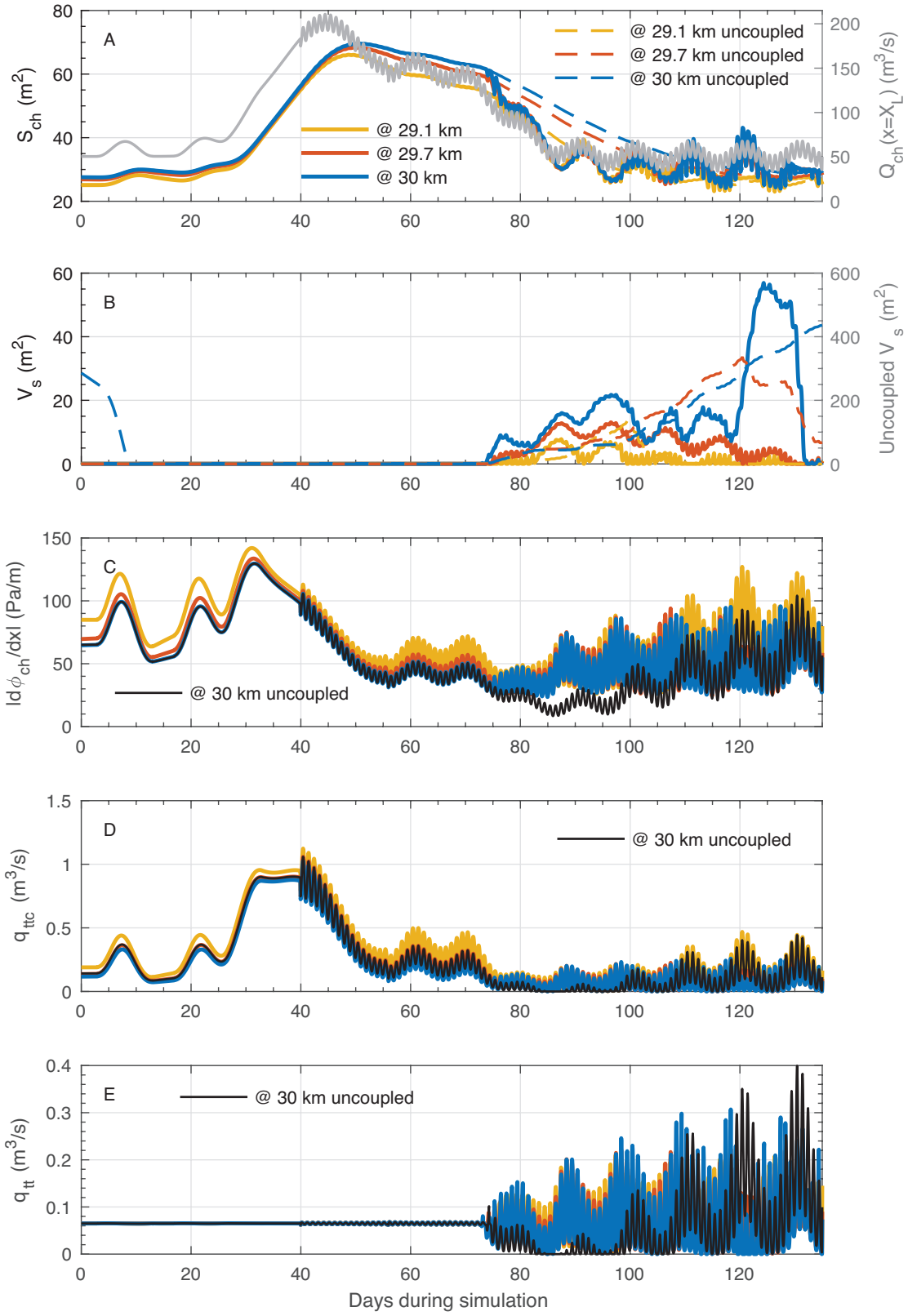

Figure 5.9: *(Caption continued on the following page.)*

Figure 5.9: *(Continued caption)* Temporal evolution near the terminus of: (A) Channel cross-sectional area and water discharge; (B) Sediment volume per unit length; (C) Absolute value of the hydraulic potential gradient; (D) Transport capacity; (E) Volumetric sediment discharge. Quantities are shown for a simulation with a synthetic melt-season and a constant sediment input $q_{\mathrm{ls}}(x = 0) = 0.065\,\mathrm{m}^3/\mathrm{s}$. Dashed lines represent the uncoupled simulation with the same parameters.

transport (Fig. 5.9C–E). Note that sediment transport becomes smaller in the coupled simulation, compared to the uncoupled one, when short events of sediment removal occur as the opposite feedback takes place, enlarging the channel cross-sectional area (days 100–103, 108–110, 117–118 and 125–130).

From day 75 onward, a significant layer of sediment accumulates near the terminus (V_{s}, Fig. 5.9B). The conditions in this part of the profile become mainly transport limited, thus the sediment flux at the terminus exhibits strong daily fluctuations (from no transport to $6 \times q_{\mathrm{ls}}(x = 0)$). As the prescribed sediment supply is constant, sediment delivery to the proglacial area is controlled by sediment dynamics in the vicinity of the terminus.

5.3.5 Implications for pro-glacial sediment yields

The typical method to quantify seasonal pro-glacial sediment yields in the field is to measure water discharge and suspended sediment concentration, since the direct measurement of sediment fluxes can be extremely challenging (e.g. Gurnell and others, 1996; Mao and others, 2014; Orwin and Smart, 2004; Riihimaki and others, 2005; Willis and others, 1996). Bedload flux measurements remain rare (e.g. Mao and others, 2014; Riihimaki and others, 2005), because of the challenge they represent. Hysteresis between sediment transport and water discharge is also widely used to interpret how sediment fluxes relate to subglacial sediment availability. A common assumption is that clockwise hysteresis, defined here as sediment transport peaking before water discharge, indicates that the channel is sediment-starved (e.g. Mao and others, 2014; Riihimaki and others, 2005; Willis and others, 1996).

To relate our results to field measurements, we calculate the sediment mass concentration at the terminus ($[m_{\mathrm{s}}] = (q_{\mathrm{tt}}(x = X_{\mathrm{L}}) \times \rho_{\mathrm{s}})\,/Q_{\mathrm{ch}}$; Fig. 5.10A) and relate it to the outlet water discharge ($Q_{\mathrm{ch}}(x = X_{\mathrm{L}})$, the behaviour of the system during the melt season (c.f. Fig. 5.9), whether the channel close to the terminus is supply- or transport-limited (Fig. 5.10B) and the direction of hysteresis between sediment transport and water discharge (Fig. 5.10C).

The sediment concentration shows a pattern inverse to that of discharge until day 75 (Fig. 5.10A), as is expected for supply-limited transport and constant sediment input (Fig. 5.10B). After day 75, the sediment concentration exhibits strong daily fluctuations as conditions at the channel bed become transport-limited, similar to sediment transport patterns (q_{tt}; Fig. 5.9E).

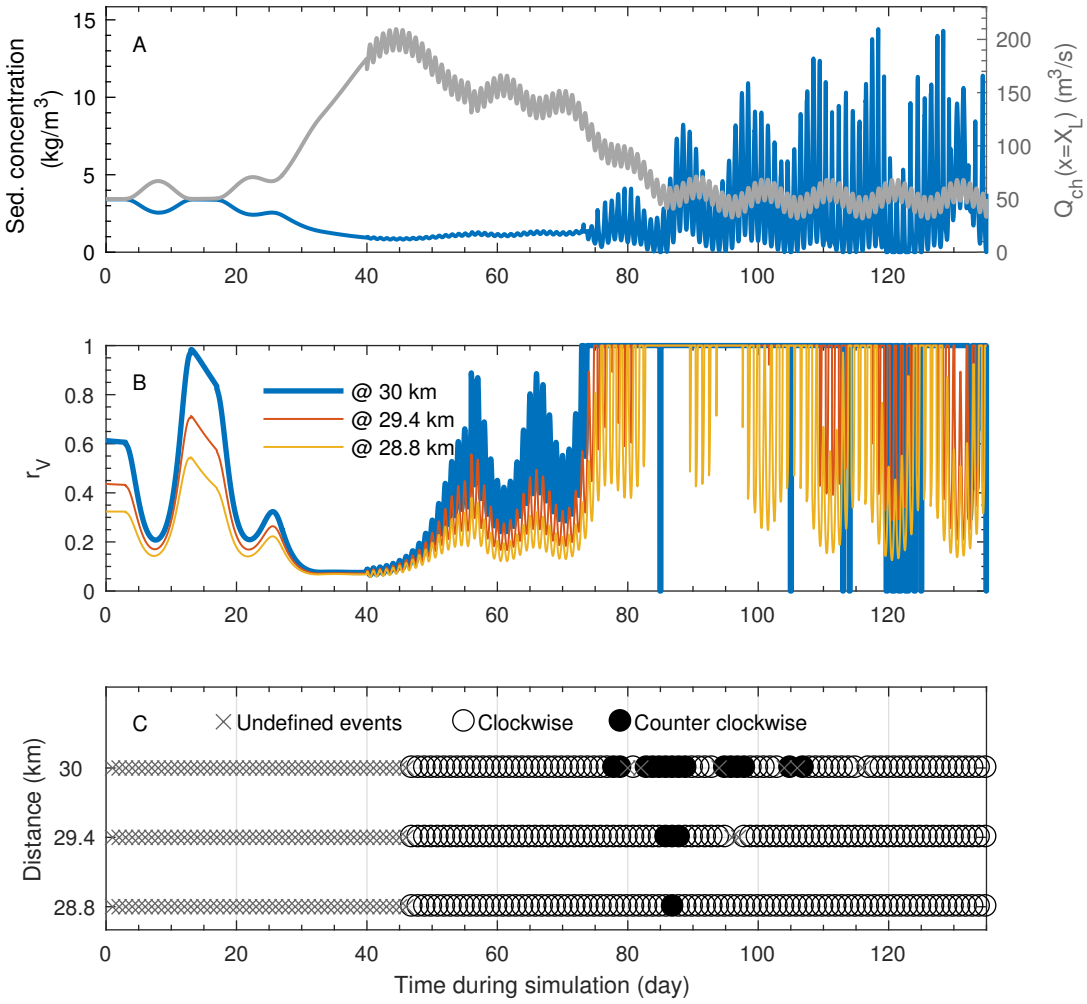

Figure 5.10: Temporal evolution near the terminus of: (A) Sediment concentration and water discharge; (B) Volume ratio r_{V} (transport limited conditions when $r_{\mathrm{V}} = 1$; see Eq. 5.15); (C) Daily hysteresis between sediment transport (q_{tt}) and water discharge (Q_{ch}). We define hysteresis such that a clockwise event is the result of sediment transport peaking earlier than water discharge. We set events as undefined when no daily fluctuations are occurring or when both quantities peak at the same time. Quantities are shown at 28.8, 29.4 and 30 km from the water input. The simulation is the same as that in Fig. 5.9, but with $\mathrm{d}t = 900\,\mathrm{s}$ instead of $\mathrm{d}t = 3600\,\mathrm{s}$ to better resolve the hysteresis.

The conditions at the bed of the channel are increasingly supply-limited with increased distance from the terminus (Fig. 5.10B), coinciding with sediment volume patterns (Fig. 5.9B). Neither supply- nor transport-limited conditions at the bed of the channel are uniquely associated with the direction of hysteresis between sediment and water discharge (Fig. 5.10C). We define clockwise hysteresis when sediment transport (q_{tt}) peaks before the water discharge (Q_{ch}), and vice versa. It appears that hysteresis events are controlled by the water flow regime, with counter clockwise events associated with low transport capacities caused by rapidly decreasing discharge (Fig. 5.9D). As suggested by Beaud and others (2016, see also Chapter 3), the lag between peak shear stress and peak discharge depends on whether the channel is enlarging or contracting on time scales longer than several days. In a growing channel, water velocities peak before discharge, resulting in a clockwise hysteresis between sediment transport and discharge; the opposite is true in a closing channel. This is also the reason that counter-clockwise events are observed primarily at the terminus and their number decreases with distance up-glacier. Ice thickness increases with distance from the terminus, increasing the efficiency of creep closure. The thicker the ice, the more rare it is for the channel to display multi-day periods with a closing trend, because the adaption time of the channel is relatively short.

5.4 Discussion

5.4.1 Model limitations

We treat only the case of water and sediment flow in a semi-circular bedrock-floored R-channel, assuming that the water forcing is applied at the base of a moulin that feeds the channel at its up-stream end. In doing so, we neglect the interactions between the different types of drainage system (see Flowers, 2015; Fountain and Walder, 1998; Greenwood and others, 2016, for reviews). These interactions would be most important at the beginning of the melt-season, when channelized drainage is not established yet.

Sediment transport is only calculated for a single particle diameter, as is common in studies of bedrock erosion (Chatanantavet and Parker, 2009; Inoue and others, 2014; Lamb and others, 2008a; Sklar and Dietrich, 2004, 2006, 2008) or sediment transport over mixed bedrock / alluvial bed conditions (e.g. Inoue and others, 2014; Nelson and Seminara, 2012; Zhang and others, 2015) and we assume that the sediment volume V_{s} is uniformly distributed across the channel width. We choose a particle diameter that produces a wide range of behaviour for the prescribed water input. In addition, the relative sediment supply ($q_{\mathrm{tt}}/q_{\mathrm{ttc}}$) determines whether the channel shows alluvial or mixed alluvial / bedrock conditions and $q_{\mathrm{tt}}/q_{\mathrm{ttc}}$ is a function of both particle diameter and sediment supply (Eq. 5.11). Changing the diameter or sediment supply thus leads to similar feedback mechanisms (Beaud and others, 2016; Lamb and others, 2008a). Observations of glacial hydrology are numerous, while there has been only one attempt at qualifying sediment transport subglacially (Gimbert

and others, 2016). The hydrologic forcing can thus be specified as somewhat realistic, while the sediment supply is much less constrained and has to be tuned as a function of the hydrology.

5.4.2 Sediment delivery to the proglacial environment

Sediment delivery to the proglacial environment has been widely used as a proxy for measuring contemporary erosion rates of glaciers (e.g. Bogen, 1996; Cowton and others, 2012; Hallet and others, 1996; Herman and others, 2015; Humphrey and Raymond, 1994; Koppes and Hallet, 2006, 2002; Koppes and Montgomery, 2009; Koppes and others, 2015; Loso and others, 2004; Riihimaki and others, 2005; Sanders and others, 2013). These studies are based on the assumption that subglacial sediment storage is minimal so that sediment fluxes in the proglacial environment (stream, lake, fjord) reflect erosion rates with little lag (e.g. Bogen, 1996; Cowton and others, 2012; Herman and others, 2015; Riihimaki and others, 2005). The common justifications for this assumption are: (1) the direction of hysteresis between sediment transport and discharge, as supported by studies of fluvial sediment transport (Herman and others, 2015; Mao and others, 2014; Riihimaki and others, 2005; Willis and others, 1996), or (2) an unrealistically thick layer of sediment is required to sustain the measured sediment fluxes (e.g. Koppes and Hallet, 2002). The system is considered supply-limited if sediment transport peaks before water discharge (e.g. Mao and others, 2014; Riihimaki and others, 2005; Willis and others, 1996). We show that hysteresis between sediment transport and water discharge is impacted by the dynamic behaviour of the subglacial channel rather than sediment availability (Fig. 5.10), as a result of the lag between peaks in discharge and shear stress in a channel. We therefore suggest that daily hysteresis cycles are a misleading proxy for subglacial sediment availability.

Despite a constant sediment supply, sediment fluxes at the terminus exhibit two distinct regimes during the modelled melt-season. Although the timing of the regime shift in outlet sediment flux is a function of the model set-up ($q_{\mathrm{ls}}(x = 0)$), $Q_{\mathrm{ch}}(x = 0)$, ice geometry), such a switch is expected in the presence of a substantial sediment yield. In our simulation, sediment concentrations greater than $0.02\,\mathrm{kg\,m^{-3}}$ would be sufficient to create a temporary accumulation of sediment, which is two orders of magnitude smaller than typically measured values (e.g. Riihimaki and others, 2005). In the case of an actively eroding glacier where till cover is thought to be sparse or till storage minimal, we propose that two main types of sediment storage could be differentiated: (1) sediment pockets scattered over the bed resulting from overall glacial erosion and transport and (2) temporary deposition near the terminus due to the dynamics of the water and sediment flow. We suggest that peaks in sediment fluxes at the beginning of the melt-season could be the result of subglacial channels tapping into pre-existing sediment pockets. In the second part of a melt-season it may be difficult to identify whether the channel would tap into a pre-existing sediment pocket or whether the temporary accumulation of sediment at the terminus is responsible

for variations in sediment flux, unless other tracers, for example water conductivity, are used (Anderson, 2005).

5.4.3 Implications for esker deposition

Esker studies have addressed the spatial controls on esker location and their implication for water and sediment supply (e.g. Brennand, 1994, 2000; Burke and others, 2012, 2015; Clark and Walder, 1994; Knight, 2003; Storrar and others, 2014). It is, however, rare to find an explanation as to why the subglacial channelized water flow would deposit sediment. Esker sediments are recognized to originate from highly dynamic water flow (e.g. Brennand, 1994, 2000; Burke and others, 2012, 2015; Clark and Walder, 1994), and flood-like flows are invoked to explain a sudden increase in the transport capacity of the water that would move the sediment and deposit it as the flood terminates. Using a simple theory of subglacial water flow along hydraulic potential gradients (Shreve, 1972) would indicate that water flow speed increases toward the terminus as the slope of the ice steepens (e.g. Alley and others, 1997; Clark and Walder, 1994), promoting sediment evacuation rather than deposition.

The results presented here provide a simple mechanism for sediment deposition near a glacier terminus: a bottleneck in sediment transport inherent to the dynamics of water flow in subglacial channels. In the presence of a sufficient sediment supply, this bottleneck leads to sediment deposition in the vicinity of the terminus, which can be interpreted as an incipient esker. The waning of water discharge in a forcing cycle (synthetic melt-season) is particularly conducive to sediment deposition. Decreasing discharge over the course of $\sim 1-4$ weeks (Figs 5.5, 5.6 and 5.9) results in the largest sediment volumes deposited. On these timescales, discharge can decrease faster than creep-closure can compensate to sustain hydraulic pressure gradients, but leaves a significant amount of time for sediment to accumulate. With water input fluctuations of period smaller than a week, the window for sediment deposition is limited as the following rise in discharge will flush the sediment again. When input discharge decreases over longer periods of time, the constriction of the channel by creep is large enough that hydraulic potential gradients only drop slightly, inhibiting the bottleneck effect. These results thus suggest that sudden water flow velocity changes are not necessary for sediment deposition, and that flood flows are also not needed to explain the presence of large clasts (e.g. Brennand, 1994; Burke and others, 2012) as we show that boulder-size sediment is flushed out of the channel bed.

We propose that esker deposition is a natural feature of channelized water flow under land-terminating glaciers. Provided that the sediment supply is sufficient, we expect that an esker would, at least temporarily, be deposited at the end of a melt-season (Fig. 5.9). The fate of such an esker would be determined by the subsequent state of the subglacial environment near the terminus. For example, a retreating ice sheet would exhibit a thinning terminus, favourable for further sediment deposition and the growth of an esker. On the other hand, an advancing ice sheet would exhibit a steepened terminus resulting in higher

shear stresses caused by water flow and flushing of previously stored sediment. Our results, thus support time-trangressive deposition of eskers by retreating ice sheets (e.g. Brennand, 2000; Burke and others, 2012, 2015; Clark and Walder, 1994) and suggest that sudden deposition of esker segments longer than a few kilometres is unlikely (e.g. Brennand, 1994).

5.5 Conclusions

We present the first one-dimensional framework for morphodynamics in R-channels, by combining water- and sediment flow for both alluvial and mixed alluvial / bedrock conditions. We show that channelized water flow under a land-terminating glacier inherently creates a bottleneck in sediment transport near the terminus. In the presence of a sufficient sediment supply, this bottleneck leads to an accumulation of sediment near the terminus, whereas the rest of the channel experiences supply-limited conditions. The bottleneck is accentuated by temporal fluctuations in water discharge, in particular when these fluctuations have periods greater than several days and up to several weeks. As a result the waning phase of a melt-season is particularly prone to temporary sediment accumulation and deposition of an incipient esker. This temporary sediment deposition can drive proglacial sediment fluxes and, as a result, can challenge our current interpretations of glacial erosion rates based on proglacial sediment yields. This model establishes a framework for exploring the physical processes driving proglacial sediment fluxes and esker deposition. Future work involving more extensive numerical modelling combined with field observations is therefore required to extract information about subglacial conditions from sediment fluxes or esker characteristics.

Chapter 6

Synthesis

The work conducted in this thesis represents the first attempt at quantifying the indirect and direct roles of subglacial water flow in glacial erosion with numerical models. Despite the widely acknowledged importance of water flow in glacial erosion (see Chapter 1), studies exploring such importance remain rare. In Chapter 1, the importance of subglacial hydrology for glacial erosion is stressed and the dearth of research on the topic is emphasized. I chose to study the direct and indirect roles of subglacial hydrology on erosion at subseasonal to annual timescales with process-based numerical models to address three main questions: (1) What are the indirect effects of subglacial hydrology on abrasion and quarrying patterns? (Chapter 2) (2) How important is the direct effect of subglacial hydrology on bedrock erosion? (Chapters 3 and 4) (3) What are the dynamics of sediment transport in a channelized drainage system over a hard bed? (Chapter 5). First the research that I undertook during my PhD is summarized, the main findings are highlighted and questions that arose from each of them are identified. Question (1) is addressed in Section 6.1.1, Question (2) in Sections 6.1.2 and 6.1.3 and Question (3) in Section 6.1.4. I then put my work in the context of glacial erosion studies and discuss the implications for assumptions commonly made about subglacial hydrology. Finally, I discuss the implications for future work and propose research areas that I believe should be prioritized within glacial geomorphology.

6.1 Summary of research

6.1.1 Subglacial hydrology, sliding laws and erosion patterns

In Chapter 2, I use a numerical model to compare abrasion and quarrying patterns and determine how they are affected by the type of subglacial drainage system, the frequency and amplitude of water input and the type of sliding law. Due to the empirical and un-validated nature of existing erosion laws, I discuss only erosion patterns and avoid calculating rates.

Including a subglacial drainage system captures the influence of variable melt-water input on basal water pressures and yields seasonally-enhanced modelled sliding where ex-

tensive amounts of water can reach the bed, namely below the ELA. Fluctuations in water input over periods of several days have the greatest effect on modelled sliding patterns. The choice of sliding law (sliding proportional to shear stress or Coulomb-type friction) has also a significant impact on sliding patterns, and in particular their sensitivity to changes in effective pressure. Enhanced sliding results in enhanced abrasion rates; however, the low associated effective pressures and large calculated cavity sizes lead to a decrease in quarrying rates calculated with Iverson's (2012) law. In summary, modelled abrasion patterns are particularly affected by the implementation of a subglacial drainage system and its morphology, the frequency of the water input and the choice of sliding law. In contrast, quarrying patterns are mostly controlled by effective pressure patterns, although the low calculated quarrying rates associated with high sliding speed and low effective pressures are at odds with previous theories (e.g. Hallet, 1996). In addition, the location of the highest modelled water-pressure fluctuations coincides with the location of lowest calculated quarrying rates, possibly contradicting previous theories (e.g. Cohen and others, 2006; Hallet, 1996; Iverson, 1991; Röthlisberger and Iken, 1981).

The results concerning abrasion patterns corroborate the findings of Herman and others (2011), that introducing a simple subglacial hydrology model (Flowers and Clarke, 2002) leads to a maximum in erosion below the ELA that can explain the formation of overdeepenings, in particular if erosion scales with the sliding velocity raised to a power close to two (Herman and others, 2015; Koppes and others, 2015). These results are in agreement with thermochonological studies showing the bi-modal aspect of glacial erosion, where valleys are excavated faster than the surrounding topography (e.g. Shuster and others, 2005; Steer and others, 2012; Valla and others, 2011, see Fig. 1.3). Such bi-modality would be further enhanced if quarrying rates were controlled by fluctuations in effective pressure rather than values of effective pressure (Chapter 2, Fig. 2.12).

Two of the main limitations of the study presented in Chapter 2 are the limited spatial dimension and timescale of the numerical modelling. Flow-line modelling of subglacial hydrology may be representative of ice-sheet margins (e.g. Hewitt, 2013; Werder and others, 2013; Werder, 2016), but the topography of a valley would influence water flow significantly (Werder and others, 2013; Werder, 2016). To investigate how topography affects erosion rates and explore the possible long-term feedbacks between erosion patterns and landscape evolution it is necessary to test erosion laws with numerical models as developed by Hewitt (2013) or Werder and others (2013). The timescale explored in such studies would, however, remain of the order of a few years with the current state of the numerical modelling methods. Two recent studies attempt to bridge this gap, yet their goal remains landscape evolution on the scale of several glacial cycles (Brædstrup and others, 2016; Ugelvig and others, 2016). Brædstrup and others (2016) test the influence of different sliding laws on shear stresses at the glacier bed, although subglacial hydrology is not considered. Ugelvig and others (2016) use a parametrization of subglacial hydrology and explore how quarrying calculated

with Iverson's (2012) law impacts the evolution of valley topography. The role of subglacial hydrology is, however, not particularly emphasized in the presentation of results. The numerical model used in Brædstrup and others (2016) and Ugelvig and others (2016) (see also Egholm and others, 2011b,a, 2012, 2009; Pedersen and Egholm, 2013) is nevertheless the most complete to date in representing the processes of glacial erosion and simulating its long term effects.

The work in Chapter 2 is the first to discuss sub-annual patterns of both abrasion and quarrying and their relation to subglacial hydrology. This work shows that integrating subglacial hydrology in landscape evolution models is necessary. It also provides with a basis to discuss assumptions on the type of subglacial drainage system implemented in landscape evolution models.

6.1.2 Erosion by subglacial water flow

Erosion caused by subglacial water flow had never been studied using a processed based approach. In Chapter 3 I adapt a model of fluvial erosion by abrasion in rivers (Lamb and others, 2008a; Sklar and Dietrich, 2004) to subglacial water flow. The abrasion model uses the tools and cover principle: particles transported by water flow act as tools chipping the bedrock, while an over-abundance of particles will cover and shield the bedrock. Abrasion rates show a maximum when the relative sediment transport—the ratio between sediment supply and transport capacity—is optimum. Another limitation of abrasion rates comes from particle trajectories. When the shear stress created by water flow is too low, a particle is immobile; larger shear stress will lead to rolling, then saltation and eventually suspension. When suspended, a particle will only impact the bed because of turbulent eddies. Abrasion rates, for a given sediment supply, are thus maximum in the saltation regime, nil in the absence of motion and relatively low when particles are suspended (Lamb and others, 2008a).

Using this erosion model, I test the effect of fluctuations in water input, ice-surface geometry and sediment availability on subglacial meltwater erosion (SME) patterns and rates. When the subglacial drainage system is permitted to evolve between distributed and channelized, erosion occurs primarily at the base of subglacial channels; erosion in the distributed drainage system is comparatively negligible. Significant volumes of sand-sized or smaller particles could, nonetheless, be transported in the sole presence of a distributed drainage system (Appendix 3). In the channelized drainage system, the calculated transport stages are an order of magnitude higher than those expected for sub-aerial water flow at similar discharges (e.g. Sklar and Dietrich, 2004) and it becomes necessary to account for the erosion by the suspended sediment load as well as the bed load (Lamb and others, 2008a; Sklar and Dietrich, 2004). The glacier-catchment-averaged erosion rates calculated are at least an order of magnitude less that those expected for warm-based glaciers (e.g. Gurnell and others, 1996; Hallet and others, 1996; Koppes and Montgomery, 2009), suggesting that SME is volumetrically negligible. Nonetheless, SME is concentrated at the bed of narrow

channels and a few to several decimetres of incision can occur over a single melt season. Such rates could explain the incision of tunnel valleys or inner gorges in bedrock over timescales commensurate with ice ages.

This study suffers from similar spatio-temporal limitations as Chapter 2. Extending the numerical model of SME to two dimensions and including variable bedrock topography will be necessary in the future to explore more realistic SME patterns. Further limitations of the model presented in Chapter 3 are the omission of sediment transport and plucking caused by water flow. I discuss the omission of water-born plucking in the Section 6.1.3, while sediment transport is introduced in Chapter 5.

Chapter 3 is the first study that aims at understanding the underlying processes of SME. This erosion mechanism is largely acknowledged in textbooks, yet process-based studies are absent. The quantification of the physical processes of subglacial water flow, sediment mobilization and bedrock erosion combined provides with a strong basis to discuss current assumptions and theories about SME, which, to the present day, have been built almost uniquely on observations.

6.1.3 Landform excavation by subglacial melt-water erosion

In Chapter 4, I use the model of SME to test current theories on the excavation of bedrock tunnel valleys and inner gorges. Subglacial floods of a wide range of magnitudes are often invoked to explain the erosive power of subglacial water flow (e.g. Kehew and others 2012; van der Vegt and others 2012; see also Chapter 4). Due to the limitation of erosion at high shear stresses, I show that floods yield less erosion by abrasion than seasonally produced meltwater. Then using the model in concert with a simple model of ice dynamics over several thousand years around the maximum extent of a glacial cycle, I show that erosion by abrasion resulting from seasonally produced meltwater can explain the formation of bedrock tunnel valleys and inner gorges.

Although this numerical modelling work is novel and presents a process-based explanation for water-born subglacial erosional landforms, it suffers from several limitations. Most importantly, sediment transport and plucking are lacking. The assumption of a supply-limited bed is common in bedrock erosion studies and used to justify the omission of sediment transport (e.g. Tucker and Hancock, 2010). In the subglacial environment, shear stresses can vary by an order of magnitude in a given reach or over distances of several kilometres thus leading to channel conditions alternating between supply- and transport limited. The justification of a supply-limited bed is more complicated and this assumption is discussed in Chapter 5 and Section 6.1.4.

In rivers where the joint spacing is less than 1–2 m, plucking is expected to be the dominant process of erosion and can lead to rapid canyon formation during floods (e.g. Baynes and others, 2015; Bretz, 1969; Lamb and Fonstad, 2010; Larsen and Lamb, 2016). Plucking is, however, limited by the depth of what Chatanantavet and Parker (2009) call

a "battering layer", namely the layer of rock sufficiently affected by weathering that blocks loosen and can be toppled by water flow. The maximum depth of erosion resulting from a single flood will thus be limited by the depth of the battering layer. Lamb and Fonstad (2010) infer that shear stresses of $\sim 600\,\mathrm{Pa}$ sustained for 2–3 days excavated the $\sim 15\,\mathrm{m}$-deep Box Canyon in Texas. I calculate shear stresses larger than 600 Pa for periods of 10–50 days during individual meltseasons over the simulated glacial cycles. The high frequency at which these powerful flows occur would continuously remove the battering layer, leaving little material for subsequent subglacial floods to remove and therefore limiting the erosional efficiency of these flood.

In situations where the battering layer is particularly deep because bedrock blocks are already loosened, for example in the presence of basalt columns (e.g. Baynes and others, 2015; Bretz, 1969; Larsen and Lamb, 2016), plucking would be limited by the transport capacity of the flow (e.g. Dubinski and Wohl, 2013; Lamb and others, 2015). Streams tend to adjust their beds in a fashion that shear stresses remain above, yet close to, the threshold for motion (Parker, 1978). This bed adjustment would also limit the efficiency of floods, as suggested by Larsen and Lamb (2016). In summary, although the simulated rates of SME are likely underestimated due to the omission of plucking, seasonal meltwater production may still be more conducive to bedrock channel excavation than floods.

Two main novel ideas arise from Chapter 4: (1) the unnecessary aspect of flood-flows to explain geomorphic changes caused by SME and (2) the possible widespread subglacial origin of inner gorges. An idea widely accepted in geomorphology is that medium- to low-frequency (return times of more than several decades) events drive geomorphic changes. Subglacial seasonal meltwater flow can lead to sufficiently high shear stresses to explain geomorphic changes attributed to SME, suggesting that in this setting, in opposition with previous theories in geomorphology, high frequency events can constitute the most important drivers of geomorphic change. As SME is expected to occur in the vicinity of the terminus of glaciers and ice sheets experiencing significant surface melt, the subglacial incision of inner gorges should occur extensively during extensive alpine glaciations, therefore the fluvial origin of such features is perhaps much less prominent than previously thought.

6.1.4 Sediment transport by subglacial water flow

In Chapter 5, I develop the first model of 1-D morphodynamics in R-channels suited for channel bed conditions ranging from fully exposed bedrock to fully alluviated. The model is used to explore subglacial sediment transport patterns and sediment delivery to the proglacial area. The shear stresses calculated over most of the bed are sufficiently large that supply-limited or mixed bedrock /alluvial conditions occur at the bed of the channel, but a bottleneck in sediment transport develops close to the terminus as expected from Chapters 3 and 4. The results support the idea that subglacial water flow produces suffi-

ciently large transport capacities to easily evacuate the volume of sediment that is expected to be produced by rapidly-eroding glaciers.

The bottleneck in sediment transport near the glacier terminus can lead to a temporary accumulation of sediment that is relevant to both esker formation and the interpretation of pro-glacial sediment yields. The bottleneck is consistent with esker deposition as a glacier thins and retreats or at the end of a meltseason as water discharge decreases in a well-established channel. These results provide the first process-based explanation of esker deposition. The temporary accumulation and flushing of sediment can have a significant impact on the interpretation of proglacial sediment yields. For example, the hysteresis between sediment concentration and water discharge in the proglacial stream is often used to infer conditions at the bed of a glacier; this hysteresis may instead be the signal produced by temporary sediment accumulation. More work is needed to test the effect of different ice geometries and rates and patterns of water and sediment input on esker formation and on sediment delivery to the proglacial environment. This work would help to improve the methods used to infer subglacial conditions from these deposits and sediment fluxes.

6.2 Implications for future work

6.2.1 Caveats of quarrying theories

I suggest that there are two main reasons that discrepancies have arisen between previous theories of quarrying and the results of Iverson's (2012) law: (1) previous theories have overlooked the role of large effective pressures associated with low sliding rates on bedrock obstacles and they actually control the process more than rapid water pressure fluctuations or (2) some aspect of the process is not properly captured by Iverson's (2012) quarrying law. Iverson (2012) developed an expression for quarrying rates to be used in landscape evolution models for long time-scales and not necessarily to capture sub-annual behaviour of the process. I performed some preliminary numerical experiments with the help of Olivier Gagliardini to simulate the stress gradients in a bedrock obstacle caused by flowing ice, with a similar set-up as described in Gagliardini and others (2007). I tested three scenarios using the bed conditions (effective pressure and sliding speed) that I calculated with the numerical model in the reference experiment described in Chapter 2: (1) high effective pressure and low sliding speed resulting in no lee-side cavity formation, (2) low effective pressure and high sliding speed resulting in lee-side cavity formation but with uniform water pressure in the cavity and across bed and (3) the same as (2), but with lower water pressure in the cavity. The stress gradients in the bedrock obstacle calculated were larger in (1) than in (2), but largest in (3).

Quarrying requires fracture growth, dislodgement and entrainment of a block. If a block breaks in the presence of a large enough cavity it may not be entrained immediately thereafter by sliding ice, as could be the case in Scenario (3). Water pressure and sliding

speed fluctuations are expected to occur over less than several days and it is likely that the freshly quarried block would be evacuated within such a timeframe. Thus, unless fractures are already particularly well developed, the limiting factor for quarrying would be fracture growth. The conditions observed in Scenario (1) are expected to occur almost continuously, whereas the conditions in Scenario (3) are limited to a several-week period of high meltwater production during the meltseason (e.g. Bartholomew and others, 2011, 2012; Iken and others, 1983; Sole and others, 2011; Van De Wal and others, 2015). Determining whether Scenario (1) or (3) leads to the most crack growth in a bedrock obstacle will be key to further our understanding of quarrying. The result will nevertheless likely be a function of the density and development of pre-existing cracks.

In a competent bedrock obstacle, large water pressure fluctuations are perhaps necessary to create large enough pressure gradients for fractures to grow (e.g. Cohen and others, 2006). However, for a bedrock obstacle with a high fracture density, moderate pressure gradients may be sufficient to quarry blocks as suggested by the research on plucking in rivers (Dubinski and Wohl, 2013; Lamb and others, 2015). Ultimately, it is possible that in the presence of particularly well-developed fractures, for example in columnar basalt, the rate of quarrying would be very close to that of entrainment and scale directly with sliding speed (e.g. Clarke, 2005; Iverson and Iverson, 2001). Iverson (2012) incorporates the importance of fracture homogeneity in bedrock, although stresses in a bedrock step may be overestimated in his parametrization. The quarrying law applies a parametrization that Hallet (1996) proposed for the ledge of a step to the whole contact area between the ice and the bed. The transferred stress may thus be overestimated.

Studies of sediment budgets of glacial catchments suggest that only a small fraction of the sediment present at a glacier bed originates from sub-aerial sources (e.g. rock falls), even for small cirque glaciers (Riihimaki and others, 2005; Sanders and others, 2013, 2012). The tools available for abrasion are thus mainly produced by quarrying, as suggested by Riihimaki and others (2005). This points towards abrasion patterns being controlled by quarrying and clast production. A better understanding of the drivers of quarrying is crucial to better understand glacial erosion and landscape evolution. Using a glacial erosion law based on the abrasion process may yield realistic landscapes, but whether the actual processes are faithfully captured remains questionable. For example, assuming that quarrying is the dominant mechanism of glacial erosion and accounting for subglacial hydrology, does not necessarily lead to the excavation of a U-shaped valley (Ugelvig and others, 2016, Figs. 13 and 14).

6.2.2 Landforms

The necessity of subglacial floods is often invoked to explain either the ability to transport boulders or the erosive power of subglacial water flow. The numerical modelling work presented in this thesis shows that seasonal water flow under glaciers can produce shear

stresses commensurate with extreme sub-aerial floods, and that shear stresses produced during subglacial floods may be detrimental to the excavation of landforms. Reproducing subglacial conditions in a laboratory experiment can be challenging because of the high water pressures that must be achieved, but a few studies have been successful in exploring pressurized water flow between sand and glass (Catania and Paola, 2001; Lelandais and others, 2016). Finally, resolving the discrepancies between field observation of erosional landforms created by SME (e.g. tunnel valleys and inner gorges), descriptions of landforms deposited by subglacial water flow (e.g. eskers), observations of proglacial sediment yields, observations of subglacial water flow and sediment transport (Bartholomaus and others, 2015; Gimbert and others, 2016), numerical modelling and laboratory experiments, will be necessary to better understand subglacial water flow, SME and measurements of glacial erosion.

6.2.3 Glacial erosion and landscape evolution

The work presented in this thesis is limited to 1-D numerical modelling primarily targeting annual to sub-annual timescales. The novelty of the approach resides in testing how these sub-annual processes might impact long-term erosion rates and patterns, and in examining some of the assumptions made in numerical studies of glacial erosion and landscape evolution.

Abrasion, water pressure fluctuations and evacuation of sediment by subglacial water flow are most pronounced below the ELA, yet this efficiency decreases in the vicinity of the terminus. Erosion rates should therefore be fastest between the ELA and the terminus, and not at or above the ELA. If quarrying is most efficient at high effective pressures, hence in general where the subglacial drainage system undergoes only small temporal changes and ice is thick, the process would be limited by the lack of evacuation of the sediment. The hypsometry of glacial landscapes has been used to infer that glacial erosion is most effective at and above the ELA. I posit that this signal has been incorrectly interpreted based on early numerical modelling of glacial erosion in the absence of subglacial hydrology. When overdeepenings, which are ubiquitous in glacial landscapes (e.g. Cook and Swift, 2012; Haeberli and others, 2016; Preusser and others, 2010), are accounted for in hypsometric analysis, a second peak in the elevation distribution arises at low elevations (Dürst-Stucki and Schlunegger, 2013; Herman and others, 2011). The ability of climate to control average mountain height in certain mountain ranges through the action of repeated glaciations is not challenged by the presented results, but I believe that this problem warrants further study of the mechanisms of glacial erosion.

The importance of considering subglacial hydrology

The effect of subglacial hydrology on glacial erosion is compelling (Chapters 1–5). One of the goals of this thesis was to explore how subglacial hydrology influences glacial erosion in order to test some of the common assumptions made in landscape evolution models and, if necessary, propose new approaches. Subglacial hydrology is crucial for understanding effective pressure and sliding patterns, and therefore must be either parametrized or implemented in a simple fashion (e.g. Arnold and Sharp, 2002; Egholm and others, 2012; Herman and others, 2011; Hildes and others, 2004; Ugelvig and others, 2016).

I suggest that the representation of the morphology of a particular distributed drainage system is of secondary importance for landscape evolution models. For example, there are significant differences between considering a distributed drainage system as a sheet or network of cavities (Hewitt, 2013, see also Chapter 2), although these differences occur at the sub-daily to sub-weekly timescale (Fig. A.2) and the resulting differences in sliding and abrasion patterns remain small (Fig. A.6), in particular when compared to the importance of the choice of sliding law (Fig. 2.8). The implementation of the transition between distributed and channelized drainage systems leads to significant pattern changes compared to using a distributed system only. This transition is, however, not observed for every glacier (e.g. Iken and Bindschadler, 1986). Implementing this transition is computationally expensive, and may also be of secondary importance until computer simulation times decrease. It is nonetheless important to parametrize an enhanced drainage efficiency as water pressures rise in order to avoid water pressures reaching unrealistic values. Unrealistic water pressures would results in unrealistically high sliding speeds and abrasion rates.

When a subglacial drainage system is implemented, a Coulomb-type friction law (e.g. Gagliardini and others, 2007; Lliboutry, 1968; Schoof, 2005) is perhaps a better choice than a law in which sliding is proportional to basal shear stress (e.g. Bindschadler, 1983; Sanders and others, 2013; Weertman, 1964) to accommodate water pressures close to overburden pressure (Chapter 2). Coulomb-type behaviour is furthermore expected for sliding over soft beds (e.g. Clarke, 2005; Iverson and Iverson, 2001).

Assumptions about the role of subglacial water flow in studies of glacial erosion

The assumption that subglacial meltwater erosion (SME) is negligible compared to glacial erosion by abrasion and quarrying is corroborated in Chapters 3 and 4. Further work on SME is necessary to understand specific landforms such as tunnel valleys and inner gorges, but SME can probably be omitted in models of landscape evolution at the scale of a mountain range. The assumption that subglacial water has the capacity to evacuate all the sediment produced subglacially is also substantiated by numerical simulations (Chapter 5). Over most of a channel bed it is safe to assume supply-limited conditions and omit sediment transport by subglacial water flow, although this assumption may fail close to the terminus

and perhaps where large adverse bed slopes are present (Werder, 2016). The tendency of subglacial water flow to deposit sediment near the terminus may lead to significant sediment accumulation and shielding of bedrock. Further work, in particular the coupling sediment transport by sliding ice and flowing water and glacial erosion, should be conducted to improve our comprehension of sediment dynamics close to the terminus.

6.2.4 Research priorities

Understanding glacial erosion requires the comprehension of processes at a broad range of spatial (from less than a meter to a continent) and temporal (from a day to a few million years) scales, while direct observations are particularly challenging to obtain. Numerous methods are available to study these processes (Chapter 1) and can be relevant for a specific range of spatio-temporal scales. Most of these methods are indirect and it can be difficult to identify what processes are captured. A better integration between these methods at different spatio-temporal scales is key to further explore glacial erosion.

I will use three examples to illustrate this thinking and highlight the work that should be prioritized. First, numerical modelling can be used to study that broad range of spatio-temporal scales, yet there remains a gap between studies of specific erosion processes and the mechanisms of landscape evolution. Physical laws describing abrasion and quarrying rates exist (Hallet, 1979, 1981; Iverson, 2012) and have been used directly in landscape evolution models (e.g. Brocklehusrt and Whipple, 2002; Egholm and others, 2009, 2011b, 2012; Herman and others, 2011; MacGregor and others, 2000, 2009; Tomkin and Braun, 2002), while the assessment of these laws in the laboratory (Byers and others, 2012; Iverson, 1990), in the field (Cohen and others, 2005, 2006) or with numerical models (Beaud and others, 2014; Cohen and others, 2005) yields conflicting interpretations. In addition, recent calculations of erosion rates are still based on Hallet's (1979) abrasion law and only a function of sliding speed and an erosion constant (Herman and others, 2015; Koppes and others, 2015), although the role of quarrying is widely recognized as an erosive process and what controls it remains unclear. The assumptions leading to the use of erosion laws at large spatio-temporal scales warrant to be better tested, verified or updated which requires several methods to be united.

Another example of a possible improvement of the integration of various methods is the use of sediment yields in proglacial environments to quantify glacial erosion rates. These yields are informative on timescales of hours to decades and on spatial scales of a glacier catchment. The roles of subglacial transport and erosion by quarrying, abrasion, subglacial meltwater flow and weathering are amalgamated in the monitored sediment flux, often that of suspended sediment only. The mechanisms of subglacial sediment transport remain little studied (e.g. Clarke 2005; Creyts and others 2013; Gimbert and others 2016; Lelandais and others 2016; Ng 2000a; Walder and Fowler 1994; Chapter 5) and the dynamics of sediment evacuation may drive proglacial sediment yields (e.g. Orwin and Smart 2004; Chapter 5).

Empirical validations of glacial erosion laws are rare but extremely valuable (Herman and others, 2015; Koppes and others, 2015). However, applying these specific validations generally may be premature considering the caveats in our current knowledge of glacial erosion processes (e.g. using Humphrey and Raymond, 1994 to justify $l = 1$ in Eq. 1.4; see Chapter 2, Section 2.5.2). Combining the current studies of subglacial sediment transport and proglacial sediment yield will be key for the mutual improvement of areas of research.

The last example is related to the integration of observations of paleo-landforms and studies of present-day subglacial processes based on observations, numerical modelling and laboratory experiments. Glacio-fluvial paleo-landforms, such as tunnel valleys (e.g. Ó Cofaigh, 1996; Kehew and others, 2012; van der Vegt and others, 2012) or eskers (e.g. Burke and others, 2012, 2015; Livingstone and others, 2015; Storrar and others, 2014) contain unique information about the large-scale structure of subglacial drainage systems under past ice sheets (e.g. channel spacing; Hewitt, 2011; Livingstone and others, 2015) and could thus inform our understanding of the drainage systems under modern ice sheets. Extracting such information requires that the mechanisms responsible for the formation of glacio-fluvial landforms, namely sediment transport and erosion by subglacial water flow, are well understood. To date, most studies have encompassed at most a few methods (e.g. Beaud and others 2016; Catania and Paola 2001; Gimbert and others 2016; Kehew and others 2012; Lelandais and others 2016; van der Vegt and others 2012; Chapters 4 and 5) and the understanding of paleo-landforms remains limited. Bridging the gaps between these different observational and numerical methods will be key for future studies.

There is a gap between observations of landscapes, landscape evolution models and understanding of specific processes of glacial erosion. The current descriptions of erosion processes still suffer from significant caveats. The direct integration of these processes in landscape evolution models should hence be accomplished carefully and the outputs of such landscape evolution models be interpreted cautiously. A better process-based understanding of glacial erosion and the verification of theories on these processes will be key to advance our understanding of landscape evolution by glacial erosion.

Bibliography

Alley, R. B., K. M. Cuffey, E. B. Evenson, J. C. Strasser, D. E. Lawson and G. J. Larson, 1997. How glaciers entrain and transport basal sediment: Physical constraints, *Quaternary Science Reviews*, **16**(9), 1017–1038.

Alley, R. B., D. E. Lawson, G. J. Larson, E. B. Evenson and G. S. Baker, 2003. Stabilizing feedbacks in glacier-bed erosion, *Nature*, **424**(6950), 758–760.

Anderson, B., I. C. Willis, B. Goodsell, A. Banwell, I. Owens, A. Mackintosh and W. Lawson, 2014. Annual to daily ice velocity and water pressure variations on Ka Roimata o Hine Hukatere (Franz Josef Glacier), New Zealand, *Arctic, Antarctic, and Alpine Research*, **46**(4), 919–932.

Anderson, R. S., 2014. Evolution of lumpy glacial landscapes, *Geology*, doi:10.1130/G35537.1.

Anderson, R. S. and S. P. Anderson, 2010. Geomorphology: the Mechanics and Chemistry of Landscapes, Cambridge University Press, Cambridge, UK.

Anderson, R. S., S. P. Anderson, K. R. MacGregor, E. D. Waddington, S. O'Neel, C. A. Riihimaki and M. G. Loso, 2004. Strong feedbacks between hydrology and sliding of a small alpine glacier, *Journal of Geophysical Research*, **109**(F3), F03005.

Anderson, R. S., B. Hallet, J. Walder and B. F. Aubry, 1982. Observations in a cavity beneath Grinnell Glacier, *Earth Surface Processes and Landforms*, **7**(1), 63–70.

Anderson, R. S., P. Molnar and M. A. Kessler, 2006. Features of glacial valley profiles simply explained, *Journal of Geophysical Research*, **111**(F1), F01004.

Anderson, S. P., 2005. Glaciers show direct linkage between erosion rate and chemical weathering fluxes, *Geomorphology*, **67**(1), 147–157.

Arnold, N. and M. Sharp, 2002. Flow variability in the Scandinavian ice sheet: modelling the coupling between ice sheet flow and hydrology, *Quaternary Science Reviews*, **21**(4-6), 485–502.

Baker, V. R., 1973. Paleohydrology and sedimentology of Lake Missoula flooding in eastern Washington, *Geological Society of America Special Papers*, **144**, 1–73.

Bartholomaus, T. C., J. M. Amundson, J. I. Walter, S. O'Neel, M. E. West and C. F. Larsen, 2015. Subglacial discharge at tidewater glaciers revealed by seismic tremor, *Geophysical Research Letters*, **42**(15), 6391–6398.

Bartholomaus, T. C., R. S. Anderson and S. P. Anderson, 2007. Response of glacier basal motion to transient water storage, *Nature Geoscience*, **1**(1), 33–37.

Bartholomaus, T. C., R. S. Anderson and S. P. Anderson, 2011. Growth and collapse of the distributed subglacial hydrologic system of Kennicott Glacier, Alaska, USA, and its effects on basal motion, *Journal of Glaciology*, **57**(206), 985–1002.

Bartholomew, I., P. Nienow, A. Sole, D. Mair, T. Cowton and M. A. King, 2012. Short-term variability in Greenland Ice Sheet motion forced by time-varying meltwater drainage: Implications for the relationship between subglacial drainage system behavior and ice velocity, *Journal of Geophysical Research*, **117**, F03002.

Bartholomew, I. D., P. W. Nienow, A. Sole, D. Mair, T. Cowton, M. A. King and S. Palmer, 2011. Seasonal variations in Greenland Ice Sheet motion: Inland extent and behaviour at higher elevations, *Earth and Planetary Science Letters*, **307**(3), 271–278.

Baynes, E. R. C., M. Attal, S. Niedermann, L. A. Kirstein, A. J. Dugmore and M. Naylor, 2015. Erosion during extreme flood events dominates Holocene canyon evolution in northeast Iceland, *Proceedings of the Natural Academy of Sciences of the United States of America*, **112**(8), 2255–2360.

Beaud, F., G. E. Flowers and S. Pimentel, 2014. Seasonal-scale abrasion and quarrying patterns from a two-dimensional ice-flow model coupled to distributed and channelized subglacial drainage, *Geomorphology*, **219**, 176–191.

Beaud, F., G. E. Flowers and J. G. Venditti, 2016. Efficacy of bedrock erosion by subglacial water flow, *Earth Surface Dynamics*, **4**, 125–145.

Bennett, M. R. and N. F. Glasser, 2009. Glacial Geology: Ice Sheets and Landforms, John Wiley & Sons Ltd, The Atrium, Chichester, West Sussex, UK, 2nd ed.

Bindschadler, R., 1983. The importance of pressurized subglacial water in separation and sliding at the glacier bed, *Journal of Glaciology*, **29**(101), 3–19.

Björnsson, H., 2002. Subglacial lakes and jökulhlaups in Iceland, *Global and Planetary Change*, **35**(3), 255–271.

Björnsson, H., 2010. Understanding jökulhlaups: from tale to theory, *Journal of Glaciology*, **56**(200), 1002–1010.

Blache, J., 1952. La sculpture glaciaire, *Revue de géographie alpine*, **40**(1), 31–123.

Blatter, H., 1995. Velocity and stress fields in grounded glaciers: a simple algorithm for including deviatoric stress gradients, *Journal of Glaciology*, **41**(138), 333–344.

Bogen, J., 1996. Erosion rates and sediment yields of glaciers, *Annals of Glaciology*, **22**(1), 48–52.

Boulton, G. S., 1974. Process and patterns of glacial erosion, *Glacial Geomorphology: Proceedings of Fifth Annual Geomorphology Symposia*, 41–87.

Boulton, G. S., 1979. Processes of glacier erosion on different substrata, *Journal of Glaciology*, **23**(89), 15–38.

Boulton, G. S., P. E. Caban and K. Van Gijssel, 1995. Groundwater flow beneath ice sheets: Part I—Large scale patterns, *Quaternary Science Reviews*, **14**(6), 545–562.

Boulton, G. S. and R. C. A. Hindmarsh, 1987. Sediment deformation beneath glaciers: rheology and geological consequences, *Journal of Geophysical Research*, **92**(B9), 9059–9082.

Brædstrup, C. F., D. L. Egholm, S. V. Ugelvig and V. K. Pedersen, 2016. Basal shear stress under alpine glaciers: insights from experiments using the iSOSIA and Elmer/Ice models, *Earth Surface Dynamics*, **4**(1), 159–174.

Brennand, T. A., 1994. Macroforms, large bedforms and rhythmic sedimentary sequences in subglacial eskers, south-central Ontario: implications for esker genesis and meltwater regime, *Sedimentary Geology*, **91**(1), 9–55.

Brennand, T. A., 2000. Deglacial meltwater drainage and glaciodynamics: inferences from Laurentide eskers, Canada, *Geomorphology*, **32**(3), 263–293.

Bretz, J. H., 1969. The Lake Missoula floods and the channeled scabland, *The Journal of Geology*, **77**, 505–543.

Brocklehusrt, S. H. and K. X. Whipple, 2002. Glacial erosion and relief production in the Eastern Sierra Nevada, California, *Geomorphology*, **42**, 1–24.

Brozovic, N., D. W. Burbank and A. J. Meigs, 1997. Climatic Limits on Landscape Development in the Northwestern Himalayas, *Science*, **276**, 571–574.

Budd, W. F., P. L. Keage and N. A. Blundy, 1979. Empirical studies of ice sliding, *Journal of Glaciology*, **23**(89), 157–170.

Burke, M. J., T. A. Brennand and A. J. Perkins, 2012. Transient subglacial hydrology of a thin ice sheet: insights from the Chasm esker, British Columbia, Canada, *Quaternary Science Reviews*, **58**, 30–55.

Burke, M. J., T. A. Brennand and D. B. Sjogren, 2015. The role of sediment supply in esker formation and ice tunnel evolution, *Quaternary Science Reviews*, **115**, 50–77.

Burt, T. P., R. J. Chorley, D. Brundsen, N. J. Cox and A. S. Goodie, eds., 2008. The History of the Study of Landforms or the Development of Geomorphology, vol. 4: Quaternary and Recent Processes and Forms (1890–1965) and the Mid-Century Revolutions, The Geological Society of London.

Byers, J., D. Cohen and N. R. Iverson, 2012. Subglacial clast/bed contact forces, *Journal of Glaciology*, **58**(207), 89–98.

Catania, G. and C. Paola, 2001. Braiding under glass, *Geology*, **29**(3), 259–262.

Champagnac, J.-D., F. Schlunegger, K. Norton, F. von Blanckenburg, L. M. Abbühl and M. Schwab, 2009. Erosion-driven uplift of the modern Central Alps, *Tectonophysics*, **474**(1), 236–249.

Champagnac, J.-D., P. G. Valla and F. Herman, 2014. Late-Cenozoic relief evolution under evolving climate: A review, *Tectonophysics*, **614**, 44–65.

Chatanantavet, P. and G. Parker, 2009. Physically based modeling of bedrock incision by abrasion, plucking, and macroabrasion, *Journal of Geophysical Research*, **114**(F4), F04018.

Church, M. and J. M. Ryder, 1972. Paraglacial sedimentation: a consideration of fluvial processes conditioned by glaciation, *Geological Society of America Bulletin*, **83**(10), 3059–3072.

Clark, P. U. and J. S. Walder, 1994. Subglacial drainage, eskers, and deforming beds beneath the Laurentide and Eurasian ice sheets, *Geological Society of America Bulletin*, **106**(2), 304–314.

Clarke, G. K. C., 1987. Subglacial till: a physical framework for its properties and processes, *Journal of Geophysical Research*, **92**(B9), 9023–9036.

Clarke, G. K. C., 1996. Lumped-element analysis of subglacial hydraulic circuits, *Journal of Geophysical Research*, **101**(B8), 17547–17559.

Clarke, G. K. C., 2003. Hydraulics of subglacial outburst floods: new insights from the Spring–Hutter formulation, *Journal of Glaciology*, **49**(165), 299–313.

Clarke, G. K. C., 2005. Subglacial Processes, *Annual Review of Earth and Planetary Sciences*, **33**, 247–276.

Clarke, Garry K. C., D. W. Leverington, J. T. Teller, A. S. Dyke and S. J. Marshall, 2005. Fresh arguments against the Shaw megaflood hypothesis. A reply to comments by David Sharpe on "Paleohydraulics of the last outburst flood from glacial Lake Agassiz and the 8200 BP cold event", *Quaternary Science Reviews*, **24**(12-13), 1533–1541.

Cohen, D., T. S. Hooyer, N. R. Iverson, J. F. Thomason and M. Jackson, 2006. Role of transient water pressure in quarrying: A subglacial experiment using acoustic emissions, *Journal of Geophysical Research*, **111**(F3), F03006.

Cohen, N. R., D.and Iverson, T. S. Hooyer, U. H. Fischer, M. Jackson and P. L. Moore, 2005. Debris-bed friction of hard-bedded glaciers, *Journal of Geophysical Research*, **110**(F2), F02007.

Cook, K. L., J. M. Turowski and N. Hovius, 2013. A demonstration of the importance of bedload transport for fluvial bedrock erosion and knickpoint propagation, *Earth Surface Processes and Landforms*, **38**(7), 683–695.

Cook, S. J. and D. A. Swift, 2012. Subglacial basins: Their origin and importance in glacial systems and landscapes, *Earth-Science Reviews*, **115**, 332–372.

Cowton, T., P. Nienow, I. Bartholomew, A. Sole and D. Mair, 2012. Rapid erosion beneath the Greenland ice sheet, *Geology*, **40**(4), 343–346.

Creyts, T. T., G. K. C. Clarke and M. Church, 2013. Evolution of subglacial overdeepenings in response to sediment redistribution and glaciohydraulic supercooling, *Journal of Geophysical Research*, **118**, 1–24.

Creyts, T. T. and C. G. Schoof, 2009. Drainage through subglacial water sheets, *Journal of Geophysical Research*, **114**, F04008.

Crompton, J. W., G. E. Flowers, D. Kirste, B. Hagedorn and M. J. Sharp, 2015. Clay mineral precipitation and low silica in glacier meltwaters explored through reaction-path modelling, *Journal of Glaciology*, **61**(230), 1061–1078.

Cruikshank, J., 2005. Do Glaciers Listen? Local Knowledge, Colonial Encounters, and Social Imagination, UBC Press.

Cuffey, K. and R. B. Alley, 1996. Is erosion by deforming subglacial sediments significant?(Toward till continuity), *Annals of Glaciology*, **22**, 17–24.

Cuffey, K. M and W. S. B. Paterson, 2010. The Physics of Glaciers, Academic Press.

Denton, G. H. and D. E. Sugden, 2005. Meltwater Features That Suggest Miocene Ice-Sheet Overriding of the Transantarctic Mountains in Victoria Land, Antarctica, *Geografiska Annaler. Series A. Physical Geography*, **87**, 67–85.

Dietrich, W. E., 1982. Settling velocity of natural particles, *Water Resources Research*, **18**(6), 1615–1626.

Dubinski, I. M. and E. Wohl, 2013. Relationships between block quarrying, bed shear stress, and stream power: a physical model of block quarrying of a jointed bedrock channel, *Geomorphology*, **180**, 66–81.

Dühnforth, R. S., M.and Anderson, D. Ward and G. M. Stock, 2010. Bedrock fracture control of glacial erosion processes and rates, *Geology*, **38**(5), 423–426.

Dürst-Stucki, M., R. Reber and F. Schlunegger, 2010. Subglacial tunnel valleys in the Alpine foreland: an example from Bern, Switzerland, *Swiss Journal of Geosciences*, **103**(3), 363–374.

Dürst-Stucki, M. and F. Schlunegger, 2013. Identification of erosional mechanisms during past glaciations based on a bedrock surface model of the central European Alps, *Earth and Planetary Science Letters*, **384**, 57–70.

Dürst-Stucki, M., F. Schlunegger, F. Christener, J.-C. Otto and J. Götz, 2012. Deepening of inner gorges through subglacial meltwater—An example from the UNESCO Entlebuch area, Switzerland, *Geomorphology*, **139**, 506–517.

Egholm, D. L., M. F. Knudsen, C. D. Clark and J. E. Lesemann, 2011a. Modeling the flow of glaciers in steep terrains: the integrated second-order shallow ice approximation (iSOSIA), *Journal of Geophysical Research*, **116**(F2), F02012.

Egholm, D. L., M. F. Knudsen and M. Sandiford, 2013. Lifespan of mountain ranges scaled by feedbacks between landsliding and erosion by rivers, *Nature*, **498**(7455), 475–478.

Egholm, D. L., S. B. Nielsen, V. K. Pedersen and J.-E. Lesemann, 2009. Glacial effects limiting mountain height, *Nature*, **460**(13), 884–888.

Egholm, D. L., V. K. Pedersen, M. F. Knudsen and N. K. Larsen, 2011b. On the importance of higher order ice dynamics for glacial landscape evolution, *Geomorphology*, **141–142**, 67–80.

Egholm, D. L., V. K. Pedersen, M. F. Knudsen and N. K. Larsen, 2012. Coupling the flow of ice, water, and sediment in a glacial landscape evolution model, *Geomorphology*, **141–142**(0), 47–66.

Einstein, H. A., 1950. The bed-load function for sediment transportation in open channel flows, *Tech. Rep. 1026*, US Department of Agriculture, Soil Conservation Service.

England, P. and P. Molnar, 1990. Surface uplift, uplift of rocks, and exhumation of rocks, *Geology*, **18**(12), 1173–1177.

Evans, I. S., 2008. Chapter 11: Glacial Erosional Processes and Forms: Mountain Glaciation and Glacier Geography, Burt, T. P., R. J. Chorley, D. Brundsen, N. J. Cox and A. S. Goodie, eds., The History of the Study of Landforms or the Development of Geomorphology, The Geological Society of London, vol. 4: Quaternary and Recent Processes and Forms (1890–1965) and the Mid-Century Revolutions, 413–494.

Fernandez-Luque, R. and R. van Beek, 1976. Erosion and transport of bed-load sediment, *Journal of Hydraulic Research*, **14**(2), 127–144.

Ferraccioli, F., C. A. Finn, T. A. Jordan, R. E. Bell, L. M. Anderson and D. Damaske, 2011. East Antarctic rifting triggers uplift of the Gamburtsev Mountains, *Nature*, **479**(7373), 388–392.

Fischer, U. H., A. Bebiolka, J. Brandefelt, S. Follin, S. Hirschorn, M. Jensen, S. Keller, L. Kennell, J.-O. Naslund, S. Normani, J.-O. Selroos and P. Vidstrand, 2015. Chapter 11: Radioactive Waste Under Conditions of Future Ice Ages, Haeberli, W. and C. Whiteman, eds., Snow and Ice-Related Hazards, Risks, and Disasters, Elsevier, Hazard and Disasters Series.

Fischer, U. H., D. Mair, J. L. Kavanaugh, I. Willis, P. Nienow and B. Hubbard, 2011. Modelling ice–bed coupling during a glacier speed-up event: Haut Glacier d'Arolla, Switzerland, *Hydrological Processes*, **25**(9), 1361–1372.

Flowers, G. E., 2008. Subglacial modulation of the hydrograph from glacierized basins, *Hydrological Processes*, **22**(19), 3903–3918.

Flowers, G. E., 2015. Modelling water flow under glaciers and ice sheets, *Proceedings of the Royal Society of London A: Mathematical, Physical and Engineering Science*, **471**(2176), 1–41.

Flowers, G. E., H. Björnsson, F. Pálsson and G. K. C. Clarke, 2004. A coupled sheet-conduit mechanism for jökulhlaup propagation, *Geophysical Research Letters*, **31**, L05401.

Flowers, G. E. and G. K. C. Clarke, 2002. A multicomponent coupled model of glacier hydrology: 1. Theory and synthetic examples, *Journal of Geophysical Research*, **107**(2287), 10–1029.

Flowers, G E, N Roux, S Pimentel and C. G. Schoof, 2011. Present dynamics and future prognosis of a slowly surging glacier, *The Cryosphere*, **5**(1), 299–313.

Fountain, A. G. and J. S. Walder, 1998. Water flow through temperate glaciers, *Reviews of Geophysics*, **36**(3), 299–328.

Fowler, A. and J. Walder, 1993. Creep closure of channels in deforming subglacial till, *Proceedings of the Royal Society of London A: Mathematical, Physical and Engineering Science*, **441**, 17–31.

Fox, M., F. Herman, E. Kissling and S. D. Willett, 2015. Rapid exhumation in the Western Alps driven by slab detachment and glacial erosion, *Geology*, **43**(5), 379–382.

Fox, M., F. Herman, S. D. Willett and D. A. May, 2014. A linear inversion method to infer exhumation rates in space and time from thermochronometric data, *Earth Surface Dynamics*, **2**(1), 47–65.

Gagliardini, O., D. Cohen, P. Raback and T. Zwinger, 2007. Finite-element modeling of subglacial cavities and related friction law, *Journal of Geophysical Research*, **112**(F2), F02027.

Garcia, M. H., 2000. The Legend of A.F. Shields., *Journal of Hydraulic Engineering*, **126**(9), 718–720.

García, M. H., 2008. Sedimentation Engineering: Processes, Measurements, Modeling, and Practice No. 110, ASCE Publications.

Gimbert, F., V. C. Tsai, J. M. Amundson, T. C. Bartholomaus and J. I. Walter, 2016. Subseasonal changes observed in subglacial channel pressure, size, and sediment transport, *Geophysical Research Letters*, **43**(8), 3786–3794.

Glasser, N. F. and M. R. Bennett, 2004. Glacial erosional landforms: origins and significance for palaeoglaciology, *Progress in Physical Geography*, **28**(1), 43–75.

Glen, J. W., 1955. The creep of polycrystalline ice, *Proceedings of the Royal Society of London A: Mathematical, Physical and Engineering Science*, **228**(1175), 519–538.

Greenwood, S. L., C. C. Clason, C. Helanow and M. Margold, 2016. Theoretical, contemporary observational and palaeo-perspectives on ice sheet hydrology: Processes and products, *Earth-Science Reviews*, **155**, 1–27.

Gulley, J. D., M. Grabiec, J. B. Martin, J. Jania, G. Catania and P. Glowacki, 2012. The effect of discrete recharge by moulins and heterogeneity in flow-path efficiency at glacier beds on subglacial hydrology, *Journal of Glaciology*, **58**(211), 926–940.

Gurnell, A. M., D. Hannah and D. Lawler, 1996. Suspended sediment yield from glacier basins, *IAHS Publications-Series of Proceedings and Reports-Intern Assoc Hydrological Sciences*, **236**, 97–104.

Haeberli, W., A. Linsbauer, A. Cochachin, C. Salazar and U. H. Fischer, 2016. On the morphological characteristics of overdeepenings in high-mountain glacier beds, *Earth Surface Processes and Landforms*, **41**(13), 1980–1990.

Hallet, B., 1976. Deposits formed by subglacial precipitation of CaCO3, *Geological Society of America Bulletin*, **87**(7), 1003–1015.

Hallet, B., 1979. A theoritical model of glacial abrasion, *Journal of Glaciology*, **17**, 209–222.

Hallet, B., 1981. Glacial abrasion and sliding: their dependence on the debris concentration in basal ice, *Annals of Glaciology*, **2**(1), 23–28.

Hallet, B., 1996. Glacial quarrying: a simple theoretical model, *Annals of Glaciology*, **22**, 1–8.

Hallet, B., L. Hunter and J. Bogen, 1996. Rates of erosion and sediment evacuation by glaciers: A review of field data and their implications, *Global and Planetary Change*, **12**(1-4), 213–235.

Harbor, J. M., 1992. Numerical modeling of the development of U-shaped valleys by glacial erosion, *Geological Society of America Bulletin*, **104**(10), 1364–1375.

Harbor, J. M., B. Hallet and C. F. Raymond, 1988. A numerical model of landform development by glacial erosion, *Nature*, **333**(6171), 347–349.

Herman, F., F. Beaud, J. D. Champagnac, J. M. Lemieux and P. Sternai, 2011. Glacial hydrology and erosion patterns: A mechanism for carving glacial valleys, *Earth and Planetary Science Letters*, **310**(3), 498–508.

Herman, F., O. Beyssac, M. Brughelli, S. N. Lane, S. Leprince, T. Adatte, J. Y. Y. Lin, J.-P. Avouac and S. C. Cox, 2015. Erosion by an Alpine glacier, *Science*, **350**(6257), 193–195.

Herman, F. and M. Brandon, 2015. Mid-latitude glacial erosion hotspot related to equatorial shifts in southern Westerlies, *Geology*, **43**(11), 987–990.

Herman, F. and J. Braun, 2008. Evolution of the glacial landscape of the Southern Alps of New Zealand: Insights from a glacial erosion model, *Journal of Geophysical Research*, **113**, F02009.

Herman, F. and J.-D. Champagnac, 2016. Plio-Pleistocene increase of erosion rates in mountain belts in response to climate change, *Terra Nova*, **28**(1), 2–10.

Herman, F., E. J. Rhodes, J. Braun and L. Heiniger, 2010. Uniform erosion rates and relief amplitude during glacial cycles in the Southern Alps of New Zealand, as revealed from OSL-thermochronology, *Earth and Planetary Science Letters*, **297**(1), 183–189.

Herman, F., D. Seward, P. G. Valla, A. Carter, B. Kohn, S. D. Willett and T. A. Ehlers, 2013. Worldwide acceleration of mountain erosion under a cooling climate, *Nature*, **504**(7480), 423–426.

Hewitt, I. J., 2011. Modelling distributed and channelized subglacial drainage: the spacing of channels, *Journal of Glaciology*, **57**(202), 302–314.

Hewitt, I. J., 2013. Seasonal changes in ice sheet motion due to melt water lubrication, *Earth and Planetary Science Letters*, **371**, 16–25.

Hewitt, I. J. and A. C. Fowler, 2008. Seasonal waves on glaciers, *Hydrological Processes*, **22**(19), 3919–3930.

Hewitt, I. J., C. Schoof and M. A. Werder, 2012. Flotation and free surface flow in a model for subglacial drainage. Part 2. Channel flow, *Journal of Fluid Mechanics*, **702**, 157–187.

Hildes, D. H. D., G. K. C. Clarke, G. E. Flowers and S. J. Marshall, 2004. Subglacial erosion and englacial sediment transport modelled for North American ice sheets, *Quaternary Science Reviews*, **23**(3-4), 409–430.

Hindmarsh, R. C. A., 1996. Sliding of till over bedrock: scratching, polishing, comminution and kinematic-wave theory, *Annals of Glaciology*, **22**(1), 41–47.

Hoffman, M. and S. Price, 2014. Feedbacks between coupled subglacial hydrology and glacier dynamics, *Journal of Geophysical Research: Earth Surface*, **119**(3), 414–436.

Hooke, R. L., 1991. Positive feedbacks associated with erosion of glacial cirques and overdeepenings, *Bulletin of the Geological Society of America*, **103**(8), 1104–1108.

Hooke, R. L., P. Calla, P. Holmlund, M. Nilsson and A. P. Stroeven, 1989. A 3 year record of seasonal variations in surface velocity, Storglaciären, Sweden, *Journal of Glaciology*, **35**(120), 235–247.

Hooyer, T. S., D. Cohen and N. R. Iverson, 2012. Control of glacial quarrying by bedrock joints, *Geomorphology*, **153**, 91–101.

Humphrey, N. F. and C. F. Raymond, 1994. Hydrology, erosion and sediment production in a surging glacier: Variegated Glacier, Alaska, 1982-83, *Journal of Glaciology*, **40**(136), 539–552.

Hutter, K, 1983. Theoretical Glaciology: Material Science of Ice and the Mechanics of Glaciers and Ice Sheets, vol. 1, Springer.

Iken, A., 1981. The effect of the subglacial water pressure on the sliding velocity of a glacier in an idealized numerical model, *Journal of Glaciology*, **27**(97), 407–421.

Iken, A. and R. A. Bindschadler, 1986. Combined measurements of subglacial water pressure and surface velocity of Findelengletscher, Switzerland: conclusions about drainage system and sliding mechanism, *Journal of Glaciology*, **32**(110), 101–119.

Iken, A., H. Rothlisberger, A. Flotron and W. Haeberli, 1983. The uplift of Unteraargletscher at the beginning of the melt season, a consequence of water storage at the bed?, *Journal of Glaciology*, **29**(101), 28–47.

Inoue, T., N. Izumi, Y. Shimizu and G. Parker, 2014. Interaction among alluvial cover, bed roughness, and incision rate in purely bedrock and alluvial-bedrock channel, *Journal of Geophysical Research*, **119**(10), 2123–2146.

Iverson, N. R., 1989. Theoretical and experimental analyses of glacial abrasion and quarrying, (PhD thesis), University of Minesota, Minneapolis.

Iverson, N. R., 1990. Laboratory simulations of glacial abrasion: comparison with theory, *Journal of Glaciology*, **36**(124), 304–314.

Iverson, N. R., 1991. Potential effects of subglacial water-pressure fluctuations on quarrying, *Journal of Glaciology*, **37**(125), 27–36.

Iverson, N. R., 1993. Regelation of ice through debris at glacier beds: Implications for sediment transport, *Geology*, **21**(6), 559–562.

Iverson, N. R., 2002. Processes of Glacial Erosion, Menzies, J., ed., Modern and Past Glacial Environments, Butterworth-Heinemann, chap. 5, 131–146.

Iverson, N. R., 2012. A theory of glacial quarrying for landscape evolution models, *Geology*, **40**(8), 679–682.

Iverson, N. R. and R. M. Iverson, 2001. Distributed shear of subglacial till due to Coulomb slip, *Journal of Glaciology*, **47**(158), 481–488.

Iverson, N. R. and M. Person, 2012. Glacier-bed geomorphic processes and hydrologic conditions relevant to nuclear waste disposal, *Geofluids*, **12**(1), 38–57.

Iverson, N. R. and B. B. Petersen, 2011. A new laboratory device for study of subglacial processes: first results on ice–bed separation during sliding, *Journal of Glaciology*, **57**(206), 1135–1146.

Jansen, J. D., A. T. Codilean, A. P. Stroeven, D. Fabel, C. Hättestrand, J. Kleman, J. M. Harbor, J. Heyman, P. W. Kubik and S. Xu, 2014. Inner gorges cut by subglacial meltwater during Fennoscandian ice sheet decay, *Nature Communications*, **5**(3815).

Jørgensen, F. and P. B. E. Sandersen, 2006. Buried and open tunnel valleys in Denmark–erosion beneath multiple ice sheets, *Quaternary Science Reviews*, **25**(11), 1339–1363.

Kamb, B., 1987. Glacier surge mechanism based on linked cavity configuration of the basal water conduit system, *Journal of Geophysical Research*, **92**(B9), 9083–9100.

Kehew, A. E., J. A. Piotrowski and F. Jørgensen, 2012. Tunnel valleys: Concepts and controversies—A review, *Earth-Science Reviews*, **113**(1), 33–58.

Kessler, M. A. and R. S. Anderson, 2004. Testing a numerical glacial hydrological model using spring speed-up events and outburst floods, *Geophysical Research Letters*, **18**(31), L18503.

Kessler, M. A., R. S. Anderson and J. P. Briner, 2008. Fjord insertion into continental margins driven by topographic steering of ice, *Nature Geoscience*, **1**(6), 365–369.

Kirchner, J. W., R. C. Finkel, C. S. Riebe, D. E. Granger, J. L. Clayton, J. G. King and W. F. Megahan, 2001. Mountain erosion over 10 yr, 10 k.y., and 10 m.y. time scales, *Geology*, **29**(7), 591–594.

Knight, J., 2003. Bedform patterns, subglacial meltwater events, and Late Devensian ice sheet dynamics in north-central Ireland, *Global and Planetary Change*, **35**(3), 237–253.

Koppes, M. and B. Hallet, 2006. Erosion rates during rapid deglaciation in Icy Bay, Alaska, *Journal of Geophysical Research*, **111**(F2), F02023.

Koppes, M., B. Hallet, E. Rignot, J. Mouginot, J. S. Wellner and K. Boldt, 2015. Observed latitudinal variations in erosion as a function of glacier dynamics, *Nature*, **526**(7571), 100–103.

Koppes, M. N. and B. Hallet, 2002. Influence of rapid glacial retreat on the rate of erosion by tidewater glaciers, *Geology*, **30**(1), 47–50.

Koppes, M. N. and D. R. Montgomery, 2009. The relative efficacy of fluvial and glacial erosion over modern to orogenic timescales, *Nature Geoscience*, **2**(9), 644–647.

Kor, P. S. G., J. Shaw and D. R. Sharpe, 1991. Erosion of bedrock by subglacial meltwater, Georgian Bay, Ontario: a regional view, *Canadian Journal of Earth Sciences*, **28**(4), 623–642.

Korup, O. and F. Schlunegger, 2007. Bedrock landsliding, river incision, and transience of geomorphic hillslope-channel coupling: Evidence from inner gorges in the Swiss Alps, *Journal of Geophysical Research*, **112**(3), F03027.

Krabbendam, M. and T. Bradwell, 2011. Lateral plucking as a mechanism for elongate erosional glacial bedforms: explaining megagrooves in Britain and Canada, *Earth Surface Processes and Landforms*, **36**(10), 1335–1349.

Kyrke-Smith, T. M. and A. C. Fowler, 2014. Subglacial swamps, *Proceedings of the Royal Society of London A: Mathematical, Physical and Engineering Science*, **470**(2171), 20140340.

Lajeunesse, P., 2014. Buried preglacial fluvial gorges and valleys preserved through Quaternary glaciations beneath the eastern Laurentide Ice Sheet, *Geological Society of America Bulletin*, **126**(3-4), 447–458.

Lamb, M. P., W. E. Dietrich and L. S. Sklar, 2008a. A model for fluvial bedrock incision by impacting suspended and bed load sediment, *Journal of Geophysical Research*, **113**(F3), F03025.

Lamb, M. P., W. E. Dietrich and J. G. Venditti, 2008b. Is the critical Shields stress for incipient sediment motion dependent on channel-bed slope?, *Journal of Geophysical Research: Earth Surface (2003–2012)*, **113**, F02008.

Lamb, M. P., N. J. Finnegan, J. S. Scheingross and L. S. Sklar, 2015. New insights into the mechanics of fluvial bedrock erosion through flume experiments and theory, *Geomorphology*, **244**, 33–55.

Lamb, M. P. and M. A. Fonstad, 2010. Rapid formation of a modern bedrock canyon by a single flood event, *Nature Geoscience*, **3**(7), 477–481.

Larsen, I. J. and M. P. Lamb, 2016. Progressive incision of the Channeled Scablands by outburst floods, *Nature*, **538**(7624), 229–232.

Le Brocq, A. M., A. J. Payne, M. J. Siegert and R. B. Alley, 2009. A subglacial water-flow model for West Antarctica, *Journal of Glaciology*, **55**(193), 879–888.

Lelandais, T., R. Mourgues, É. Ravier, S. Pochat, P. Strzerzynski and O. Bourgeois, 2016. Experimental modeling of pressurized subglacial water flow: Implications for tunnel valley formation, *Journal of Geophysical Research*, **121**(11), 2022–2041.

Lister, H., A. Pendlington and J. Chorlton, 1968. Laboratory experiments on abrasion of sandstones by ice, *Snow and Ice. Reports and Discussions*, 98–106.

Livingstone, S. J., R. D. Storrar, J. K. Hillier, C. R. Stokes, C. D. Clark and L. Tarasov, 2015. An ice-sheet scale comparison of eskers with modelled subglacial drainage routes, *Geomorphology*, **246**, 104–112.

Lliboutry, L, 1962. L'erosion glaciaire, *International Association of Scientific Hydrology Publication*, **59**.

Lliboutry, Luis, 1965. Traité de glaciologie, vol. 1, Masson.

Lliboutry, L., 1968. General theory of subglacial cavitation and sliding of temperate glaciers, *Journal of Glaciology*, **7**(49), 21–58.

Lliboutry, L., 1976. Physical processes in temperate glaciers, *Journal of Glaciology*, **16**(74), 151–158.

Lliboutry, L. A, 1994. Monolithologic erosion of hard beds by temperate glaciers, *Journal of Glaciology*, **40**(136), 433–450.

Loso, M. G., R. S. Anderson and S. P. Anderson, 2004. Post–Little Ice Age record of coarse and fine clastic sedimentation in an Alaskan proglacial lake, *Geology*, **32**(12), 1065–1068.

MacGregor, K. R., R. S. Anderson, S. P. Anderson and E. D. Waddington, 2000. Numerical simulations of glacial longitudinal profile evolution, *Geology*, **28**, 1031–1034.

MacGregor, K. R., R. S. Anderson and E. D. Waddington, 2009. Numerical modeling of glacial erosion and headwall processes in alpine valleys, *Geomorphology*, **103**(2), 189–204.

Mair, D., P. Nienow, M. Sharp, T. Wohlleben and I. Willis, 2002. Influence of subglacial drainage system evolution on glacier surface motion: Haut Glacier d'Arolla, Switzerland, *Journal of Geophysical Research*, **107**(B8), 10–1029.

Mair, D., I. Willis, U. H. Fischer, B. Hubbard, P. Nienow and A. Hubbard, 2003. Hydrological controls on patterns of surface, internal and basal motion during three "spring events": Haut Glacier d'Arolla, Switzerland, *Journal of Glaciology*, **49**(167), 555–567.

Mao, L., A. Dell'Agnese, C. Huincache, D. Penna, M. Engel, G. Niedrist and F. Comiti, 2014. Bedload hysteresis in a glacier-fed mountain river, *Earth Surface Processes and Landforms*, **39**(7), 964–976.

de Martonne, M. E., 1910. Sur la théorie méchanique de l'érosion glaciaire, *Comptes rendus hebdomadaires des scéances de l'Académie des sciences*, **Séance du 10 Janvier 1910**.

Mathews, W. H., 1964. Water pressure under a glacier, *Journal of Glaciology*, **5**(38), 235–40.

Mathews, W. H., 1979. Simulated glacial abrasion, *Journal of Glaciology*, **23**(89), 51–56.

McCall, J. G., 1960. The flow characteristics of a cirque glacier and their effect on glacial structure and cirque formation, *Norwegian Cirque Glacier. London: The Royal Geographic Society Research Series*, 39–62.

Meier, M. F., 1958. Vertical profiles of velocity and the flow of glacier ice, International Association of Scientific Hydrology Publication 47, Symposium of Chamonix 1958 – Physics of the Movement of the Ice, 169–170.

Meierbachtol, T., J. Harper and N. Humphrey, 2013. Basal Drainage System Response to Increasing Surface Melt on the Greenland Ice Sheet, *Science*, **341**(6147), 777–779.

Meyer-Peter, E. and R. Müller, 1948. Formulas for bed-load transport, Proceedings of the 2nd Meeting of the International Association for Hydraulic Structures Research, Stockholm, 39–64.

Mitchell, S. G. and D. R. Montgomery, 2006. Influence of a glacial buzzsaw on the height and morphology of the Cascade Range in central Washington State, USA, *Quaternary Research*, **65**(1), 96–107.

Molnar, P. and P. England, 1990. Late Cenozoic uplift of mountain ranges and global climate change: chicken and egg?, *Nature*, **346**, 29–34.

Montgomery, D. R. and O. Korup, 2010. Preservation of inner gorges through repeated Alpine glaciations, *Nature Geoscience*, **4**(1), 62–67.

Mooers, H. D., 1989. On the formation of the tunnel valleys of the Superior lobe, central Minnesota, *Quaternary Research*, **32**(1), 24–35.

Morland, L. W. and E. M. Morris, 1977. Stress in an elastic bedrock hump due to glacier flow, *Journal of Glaciology*, **18**(78), 67–75.

Müller, F. and A. Iken, 1973. Velocity fluctuations and water regime of Arctic valley glaciers, *International Association of Scientific Hydrology Publication*, **95**, 165–182.

Nelson, P. A. and G. Seminara, 2011. Modeling the evolution of bedrock channel shape with erosion from saltating bed load, *Geophysical Research Letters*, **38**(17), L17406.

Nelson, P. A. and G. Seminara, 2012. A theoretical framework for the morphodynamics of bedrock channels, *Geophysical Research Letters*, **39**(6), L06408.

Ng, F. S. L., 2000a. Canals under sediment-based ice sheets, *Annals of Glaciology*, **30**(1), 146–152.

Ng, F. S. L., 2000b. Coupled ice–till deformation near subglacial channels and cavities, *Journal of Glaciology*, **46**(155), 580–598.

Nienow, P., M. Sharp and I. Willis, 1998. Seasonal changes in the morphology of the subglacial drainage system, Haut Glacier d'Arolla, Switzerland, *Earth Surface Processes and Landforms*, **23**(9), 825–843.

Nye, J. F., 1976. Water flow in glaciers: jökulhlaups, tunnels and veins, *Journal of Glaciology*, **17**, 181–207.

Ó Cofaigh, C., 1996. Tunnel valley genesis, *Progress in Physical Geography*, **20**(1), 1–19.

Orwin, J. F. and C. C. Smart, 2004. Short-term spatial and temporal patterns of suspended sediment transfer in proglacial channels, Small River Glacier, Canada, *Hydrological Processes*, **18**(9), 1521–1542.

Østrem, G., 1975. Sediment transport in glacial meltwater streams, *Special Publications of SEPM*, 101–122.

Parker, G., 1978. Self-formed straight rivers with equilibrium banks and mobile bed. Part 2. The gravel river, *Journal of Fluid Mechanics*, **89**(1), 127–146.

Pattyn, F., 2002. Transient glacier response with a higher-order numerical ice-flow model, *Journal of Glaciology*, **48**(162), 467–477.

Pedersen, V. K. and D. L. Egholm, 2013. Glaciations in response to climate variations preconditioned by evolving topography, *Nature*, **493**(7431), 206–210.

Pimentel, S. and G. E. Flowers, 2011. A numerical study of hydrologically driven glacier dynamics and subglacial flooding, *Proceedings of the Royal Society of London A: Mathematical, Physical and Engineering Science*, **467**(2126), 537–558.

Pimentel, S., G. E. Flowers and C. G. Schoof, 2010. A hydrologically coupled higher-order flow-band model of ice dynamics with a Coulomb friction sliding law, *Journal of Geophysical Research*, **115**, F04023.

Preusser, F., J. M. Reitner and C. Schlüchter, 2010. Distribution, geometry, age and origin of overdeepened valleys and basins in the Alps and their foreland, *Swiss Journal of Geosciences*, **103**(3), 407–426.

Riihimaki, C. A., K. R. MacGregor, R. S. Anderson, S. P. Anderson and M. G. Loso, 2005. Sediment evacuation and glacial erosion rates at a small alpine glacier, *Journal of Geophysical Research*, **110**(F3), F03003.

Robin, G., 1976. Is the basal ice of a temperate glacier at the pressure melting point?, *Journal of Glaciology*, **16**(74), 183–196.

Roe, G. H., 2011. What do glaciers tell us about climate variability and climate change?, *Journal of Glaciology*, **57**(203), 567–578.

Roe, G. H. and M. A. O'Neal, 2009. The response of glaciers to intrinsic climate variability: observations and models of late-Holocene variations in the Pacific Northwest, *Journal of Glaciology*, **55**(193), 839–854.

Rose, K. C., N. Ross, R. G. Bingham, H. FJ. Corr, F. Ferraccioli, T. A. Jordan, A. M. Le Brocq, D. M. Rippin and M. J. Siegert, 2014. A temperate former West Antarctic ice sheet suggested by an extensive zone of subglacial meltwater channels, *Geology*, **42**(11), 971–974.

Röthlisberger, H., 1968. Erosive processes which are likely to accentuate or reduce the bottom relief of valley glaciers, *International Association of Hydrological Sciences Publication*, **79**, 87–97.

Röthlisberger, H., 1972. Water pressure in intra– and subglacial channels, *Journal of Glaciology*, **11**(62), 177–203.

Röthlisberger, H. and A. Iken, 1981. Plucking as an effect of water-pressure variations at the glacier bed, *Annals of Glaciology*, **2**, 57–62.

Sanders, D., L. Wischounig, A. Gruber and M. Ostermann, 2014. Inner gorge–slot canyon system produced by repeated stream incision (eastern Alps): Significance for development of bedrock canyons, *Geomorphology*, **214**, 465–484.

Sanders, J. W., K. M. Cuffey, K. R. MacGregor and B. D. Collins, 2013. The sediment budget of an alpine cirque, *Geological Society of America Bulletin*, **125**(1-2), 229–248.

Sanders, J. W., K. M. Cuffey, J. R. Moore, K. R. MacGregor and J. L. Kavanaugh, 2012. Periglacial weathering and headwall erosion in cirque glacier bergschrunds, *Geology*, **40**(9), 779–782.

Scheingross, J. S., F. Brun, D. Y. Lo, K. Omerdin and M. P. Lamb, 2014. Experimental evidence for fluvial bedrock incision by suspended and bedload sediment, *Geology*, **42**(6), 523–526.

Scheingross, J. S., E. W. Winchell, M. P. Lamb and W. E. Dietrich, 2013. Influence of bed patchiness, slope, grain hiding, and form drag on gravel mobilization in very steep streams, *Journal of Geophysical Research*, **118**, 1–20.

Schoof, C., 2005. The effect of cavitation on glacier sliding, *Proceedings of the Royal Society of London A: Mathematical, Physical and Engineering Science*, **461**(2055), 609–627.

Schoof, C., 2010. Ice-sheet acceleration driven by melt supply variability, *Nature*, **468**(7325), 803–806.

Schoof, C., I. J. Hewitt and M. A. Werder, 2012. Flotation and free surface flow in a model for subglacial drainage. Part 1. Linked cavities, *Journal of Fluid Mechanics*, **702**, 126–156.

Sharpe, D., 2005. Comments on: "Paleohydraulics of the last outburst flood from glacial Lake Agassiz and the 8200 BP cold event" by Clarke et al. [Quaternary Science Reviews 23 (2004) 389–407], *Quaternary Science Reviews*, **24**(12-13), 1529–1532.

Shaw, J. and R. Gilbert, 1990. Evidence for large-scale subglacial meltwater flood events in southern Ontario and northern New York State, *Geology*, **18**(12), 1169–1172.

Shields, A., 1936. Awendung der Aehnlichkeitsmechanik und der Turbulenzforschung auf die Geschiebebewegung, *Mitteilungen der Preussischen Versuchsanstalt für Wasserbau und Schiffbau*, **26**(26).

Shreve, R. L., 1972. Movement of water in glaciers, *Journal of Glaciology*, **11**, 205–214.

Shuster, D. L., T. A. Ehlers, M. E. Rusmoren and K. A. Farley, 2005. Rapid Glacial Erosion at 1.8 Ma Revealed by 4He/3He Thermochronometry, *Science*, **310**(5754), 1668–1670.

Sklar, L. S. and W. E. Dietrich, 2001. Sediment and rock strength controls on river incision into bedrock, *Geology*, **29**(12), 1087–1090.

Sklar, L. S. and W. E. Dietrich, 2004. A mechanistic model for river incision into bedrock by saltating bed load, *Water Resources Research*, **40**(6), W06301.

Sklar, L. S. and W. E. Dietrich, 2006. The role of sediment in controlling steady-state bedrock channel slope: Implications of the saltation–abrasion incision model, *Geomorphology*, **82**(1), 58–83.

Sklar, L. S. and W. E. Dietrich, 2008. Implications of the saltation–abrasion bedrock incision model for steady-state river longitudinal profile relief and concavity, *Earth Surface Processes and Landforms*, **33**(7), 1129–1151.

Sole, A. J., D. W. F. Mair, P. W. Nienow, I. D. Bartholomew, M. A. King, M. J. Burke and I. Joughin, 2011. Seasonal speedup of a Greenland marine-terminating outlet glacier forced by surface melt–induced changes in subglacial hydrology, *Journal of Geophysical Research: Earth Surface*, **116**, F03014.

Steer, P., R. S. Huismans, P. G. Valla, S. Gac and F. Herman, 2012. Bimodal Plio-Quaternary glacial erosion of fjords and low-relief surfaces in Scandinavia, *Nature Geoscience*, **5**(9), 635–639.

Storrar, R. D., C. R. Stokes and D. J. A. Evans, 2014. Increased channelization of subglacial drainage during deglaciation of the Laurentide Ice Sheet, *Geology*, **42**(3), 239–242.

Stumm, D., 2010. Deep glacial erosion. Review with focus on tunnel valleys in northern Europe, *Technical report NAB 10-33*, National Genossenschaft für die Lagerung radioaktiver Abfälle.

Swift, D. A., P. W. Nienow and T. B. Hoey, 2005. Basal sediment evacuation by subglacial meltwater: suspended sediment transport from Haut Glacier d'Arolla, Switzerland, *Earth Surface Processes and Landforms*, **30**(7), 867–883.

Thomson, S. N., M. T. Brandon, J. H. Tomkin, P. W. Reiners, C. Vásquez and N. J. Wilson, 2010. Glaciation as a destructive and constructive control on mountain building, *Nature*, **467**(7313), 313–317.

Tomkin, J. H. and J. Braun, 2002. The influence of alpine glaciation on the relief of tectonically active mountain belts, *American Journal of Science*, **302**, 169–190.

Tucker, G. E. and G. R. Hancock, 2010. Modelling landscape evolution, *Earth Surface Processes and Landforms*, **35**(1), 28–50.

Turowski, J. M., D. Lague and N. Hovius, 2007. Cover effect in bedrock abrasion: A new derivation and its implications for the modeling of bedrock channel morphology, *J. Geophys. Res.-Earth*, **112**, F04006.

Turowski, J. M., E. M. Yager, A. Badoux, D. Rickenmann and P. Molnar, 2009. The impact of exceptional events on erosion, bedload transport and channel stability in a step-pool channel, *Earth Surface Processes and Landforms*, **34**(12), 1661–1673.

Ugelvig, S. V., D. L. Egholm and N. R. Iverson, 2016. Glacial landscape evolution by subglacial quarrying: A multiscale computational approach, *Journal of Geophysical Research: Earth Surface*, **121**(11), 2042–2068.

Valla, P. G., D. L. Shuster and P. A. van der Beek, 2011. Significant increase in relief of the European Alps during mid-Pleistocene glaciations, *Nature Geoscience*, **4**(10), 688–692.

Valla, P. G., P. A. Van Der Beek and J. Carcaillet, 2010. Dating bedrock gorge incision in the French Western Alps (Ecrins-Pelvoux massif) using cosmogenic 10Be, *Terra Nova*, **22**(1), 18–25.

Van De Wal, R. S. W., C. J. P. P. Smeets, W. Boot, M. Stoffelen, R. van Kampen, S. H. Doyle, F. Wilhelms, M. R. van den Broeke, C. H. Reijmer, J. Oerlemans and others, 2015. Self-regulation of ice flow varies across the ablation area in south-west Greenland, *The Cryosphere*, **9**(2), 603–611.

van der Vegt, P., A. Janszen and A. Moscariello, 2012. Tunnel valleys: current knowledge and future perspectives, *Geological Society, London, Special Publications*, **368**(1), 75–97.

Vivian, R., 1970. Hydrologie et erosion sous-glaciaires, *Revue de géographie alpine*, **58**(2), 241–264.

Vivian, R. A and J. Zumstein, 1973. Hydrologie sous-glaciaire au glacier d'Argentière (Mont-Blanc, France), Symposium on the Hydrology of Glaciers, IAHS Publ, vol. 95, 53–64.

Walder, J. and B. Hallet, 1979. Geometry of former subglacial water channels and cavities, *Journal of Glaciology*, **23**, 335–346.

Walder, J. S. and A. Fowler, 1994. Channelized subglacial drainage over a deformable bed, *Journal of Glaciology*, **40**, 3–15.

Warburton, J., 1990. An alpine proglacial fluvial sediment budget, *Geografiska Annaler. Series A. Physical Geography*, 261–272.

Ward, D. J., R. S. Anderson and P. J. Haeussler, 2012. Scaling the Teflon Peaks: Rock type and the generation of extreme relief in the glaciated western Alaska Range, *Journal of Geophysical Research*, **117**(F1), F01031.

Weertman, J., 1964. The theory of glacier sliding, *Journal of Glaciology*, **5**, 287–303.

Weertman, J., 1972. General theory of water flow at the base of a glacier or ice sheet, *Reviews of Geophysics*, **10**(1), 287–333.

Werder, M. A., 2016. The hydrology of subglacial overdeepenings: A new supercooling threshold formula, *Geophysical Research Letters*, **43**(5), 2045–2052.

Werder, M. A., I. J. Hewitt, C. Schoof and G. E. Flowers, 2013. Modeling channelized and distributed drainage in two dimensions, *Journal of Geophysical Research*, **118**, 2140–2158.

Wheler, B. A., A. H. MacDougall, G. E. Flowers, E. I. Petersen, P. H. Whitfield and K. E. Kohfeld, 2014. Effects of Temperature Forcing Provenance and Extrapolation on the Performance of an Empirical Glacier-Melt Model, *Arctic, Antarctic, and Alpine Research*, **46**(2), 379–393.

Whipple, K. X., R. A. DiBiase and B. T. Crosby, 2013. Bedrock Rivers, Shroder, J. and E. Wohl, eds., Fluvial geomorphology, Academic Press, San Diego, CA, vol. 9 of *Treatise on Geomorphology*.

Whipple, K. X., G. S. Hancock and R. S. Anderson, 2000. River incision into bedrock: Mechanics and relative efficacy of plucking, abrasion, and cavitation, *Geological Society of America Bulletin*, **112**(3), 490–503.

Willenbring, J. K. and D. J. Jerolmack, 2016. The null hypothesis: globally steady rates of erosion, weathering fluxes and shelf sediment accumulation during Late Cenozoic mountain uplift and glaciation, *Terra Nova*, **28**(1), 11–18.

Willett, S. D., 1999. Orogeny and orography: the effects of erosion on the structure of mountain belts, *Journal of Geophysical Research*, **104**(B12), 28,928–957,981.

Willis, I. C., K. S. Richards and M. J. Sharp, 1996. Links between proglacial stream suspended sediment dynamics, glacier hydrology and glacier motion at Midtdalsbreen, Norway, *Hydrological Processes*, **10**(4), 629–648.

Wingfield, R., 1990. The origin of major incisions within the Pleistocene deposits of the North Sea, *Marine Geology*, **91**(1-2), 31–52.

Wolman, M. G. and J. P. Miller, 1960. Magnitude and frequency of forces in geomorphic processes, *The Journal of Geology*, **68**(1), 54–74.

Wright, H. E., 1973. Tunnel valleys, glacial surges, and subglacial hydrology of the Superior Lobe, Minnesota, *Geological Society of America Memoirs*, **136**, 251–276.

Yager, E. M., W. E. Dietrich, J. W. Kirchner and B. W. McArdell, 2012. Prediction of sediment transport in step-pool channels, *Water Resources Research*, **48**, W01541.

Zhang, L., G. Parker, C. P. Stark, T. Inoue, E. Viparelli, X. Fu and N. Izumi, 2015. Macroroughness model of bedrock-alluvial river morphodynamics, *Earth Surface Dynamics*, **3**(1), 113–138.

Zhang, P., P. Molnar and W. R. Downs, 2001. Increased sedimentation rates and grain sizes 2–4 Myr ago due to the influence of climate change on erosion rates, *Nature*, **410**(6831), 891–897.

Appendix A

Appendix to Chapter 2

A.1 Drainage system represented as a cavity continuum

A.1.1 Formulation of the cavity system

The following provides short overview of the rationale for and formulation of the cavity system. This theory was originally developed by Kamb (1987) and further used by Schoof (2010) as the formulation for the distributed drainage system. Note that models by Hewitt and others (2012), Hewitt (2013) and Werder and others (2013) use similar formulations to represent the distributed drainage system. When ice slides over bedrock obstacles cavities may form in the lee side of bedrock obstacles, cavities which may be filled with water. The presence of small linking canals allows water to flow from one cavity to the other. Opening of a cavity occurs as ice is sliding over an obstacle and is enhanced if the water is pressurized, and closing occurs by creep of the ice. Rather than modelling each individual cavity, it is assumed that the cavity system forms a continuum. If the water flow in that system is turbulent, it is possible that the resulting heat dissipation melts the ice walls and an R-channel can form (Kamb, 1987; Schoof, 2010). We however neglect the viscous heat dissipation in the cavity system (Hewitt and others, 2012; Hewitt, 2013; Werder and others, 2013) and do not account for the channels here. We choose here to focus on distributed drainage systems and to compare a macroporous sheet and a system of cavities.

The temporal evolution of the cavity system can be expressed as (e.g., Kamb, 1987):

$$\frac{\partial h_{\mathrm{ca}}}{\partial t} = v_{\mathrm{o}}(h_{\mathrm{ca}}) - v_{\mathrm{c}}(h_{\mathrm{ca}}, N) \tag{A.1}$$

with h_{ca} the areally-averaged water volume in the system, $N = p_{\mathrm{i}} - p_{\mathrm{s}}$ the effective pressure, v_{o} the opening rate and v_{c} the closure rate of the cavities that can be expressed respectively as:

$$v_{\mathrm{o}}(h_{\mathrm{ca}}) = \begin{cases} u_{\mathrm{b}}(h_{\mathrm{r}} - h_{\mathrm{ca}})/l_{\mathrm{r}} \text{ if } h_{\mathrm{ca}} < h_{\mathrm{r}} \\ 0 \text{ otherwise} \end{cases}, \tag{A.2}$$

$$v_{\mathrm{c}}(h_{\mathrm{ca}}, N) = \tilde{A} h_{\mathrm{ca}} |N|^{n-1} N. \tag{A.3}$$

Here $\tilde{A}$ is the rheological constant of ice corrected for the shape of the cavities and n is Glen's flow law exponent. The conservation of water in the system of cavities reads:

$$\frac{\partial h_{\mathrm{ca}}}{\partial t} + \nabla \cdot \boldsymbol{q}_{\mathrm{ca}} = \dot{b}_{\mathrm{ca}}, \tag{A.4}$$

where $\dot{b}_{\mathrm{ca}}$ is a source term. The flux can be written as:

$$\boldsymbol{q}_{\mathrm{ca}} = -K_{\mathrm{ca}} h_{\mathrm{ca}}^{\alpha} |\nabla \psi_{\mathrm{ca}}|^{\beta-1} \nabla \psi_{\mathrm{ca}}, \tag{A.5}$$

where K_{ca} is the effective hydraulic conductivity and $\psi_{\mathrm{ca}} = p_{\mathrm{ca}} + \rho_{\mathrm{w}} g z_{\mathrm{b}}$ is the hydraulic potential, with p_{ca} the water pressure in the system of cavities and z_{b} the elevation of the bed. For turbulent flow, the Darcy-Weisbach relation requires that $\alpha = 5/4$ and $\beta = 3/2$. Note that if $\alpha = 1$ and $\beta = 1$, equation A.5 reduces to equation 2.10 which is Darcy's law for laminar flow. The system is assumed to be saturated, hence the height of the cavities is equal to the height of water flow. To account for the water that can be stored englacially, one can assume an areally-averaged thickness of englacially stored water h_{e} and the mass conservation equation (A.4) becomes:

$$\frac{\partial h_{\mathrm{ca}}}{\partial t} + \frac{\partial h_{\mathrm{e}}}{\partial t} + \nabla \cdot \boldsymbol{q}_{\mathrm{ca}} = \dot{b}_{\mathrm{ca}}. \tag{A.6}$$

The englacial aquifer is assumed to have a void ratio e_{v} such that (e.g., Werder and others, 2013):

$$h_{\mathrm{e}}(p_{\mathrm{ca}}) = e_{\mathrm{v}} \frac{\psi_{\mathrm{ca}} - \rho_{\mathrm{w}} g z_{\mathrm{b}}}{\rho_{\mathrm{w}} g}. \tag{A.7}$$

The governing equations for the system of cavities can be rewritten as (Werder and others, 2013):

$$\frac{e_{\mathrm{v}}}{\rho_{\mathrm{w}} g} \frac{\partial \psi_{\mathrm{ca}}}{\partial t} + \nabla \cdot \boldsymbol{q}_{\mathrm{ca}} + v_{\mathrm{o}} - v_{\mathrm{c}} - \dot{b}_{\mathrm{ca}}, \tag{A.8}$$

$$\frac{\partial h_{\mathrm{ca}}}{\partial t} = v_{\mathrm{o}} - v_{\mathrm{c}}. \tag{A.9}$$

Equations A.8 and A.9 form a parabolic system of equations and can be solved for ψ_{ca} and h_{ca}.

Unless mentioned otherwise the experiments performed with the cavity system are setup identically to those performed with the macroporous sheet and share the same boundary conditions (see Section 2.2.1). For the experiments where an annual cycle is shown, the actual duration of the simulations is two years but only the second is shown, as the first year serves as a spin-up. A summary of the model variables, constants and simulations can be found respectively in Tables A.1, A.2, A.3.

A.1.2 Implications of using a cavity model

Spatio-temporal steady input and system steady state

The interest in testing the steady state of the model is to understand its basic behaviour and determine whether significant differences arise between the macroporous sheet and the

Table A.1: Model variables

Symbols	Names	Units
$\dot{b_{\mathrm{ca}}}$	Source term to cavity system	$\mathrm{m\,s^{-1}}$
h_{ca}	Areally-averaged volume of water in cavity system	m
h_{e}	Englacial storage	m
N	Effective pressure	Pa
p_{ca}	Water pressure in cavities	Pa
q_{ca}	Water flux in cavities	$\mathrm{m^2\,s^{-1}}$
u_{b}	Sliding velocity	$\mathrm{m\,a^{-1}}$
v_{o}	Cavity opening rate	$\mathrm{m\,s^{-1}}$
v_{o}	Cavity closure rate	$\mathrm{m\,s^{-1}}$
ψ_{ca}	Fluid potential in cavity system	Pa

Table A.2: Model constants and parameters

Symbols	Names	Values	Units
$\tilde{A}$	Ice flow-law coefficient corrected for cavity shape	5×10^{-25}	$\mathrm{Pa^{-3}\,s^{-1}}$
e_{v}	Englacial void ratio	1×10^{-3}	-
K_{ca}	Conductivity in the cavity system	$1 \times 10^{-4} - 4.5 \times 10^{-2}$	$\mathrm{m^{7/4}\,kg^{-1/2}}$ or $\mathrm{m\,s^{-1}}$
l_{r}	Length of bed obstacles	3	m
h_{r}	Height of bed obstacles	0.12	m
α	Empirical exponent	1, 5/4	-
β	Empirical exponent	1, 3/2	-

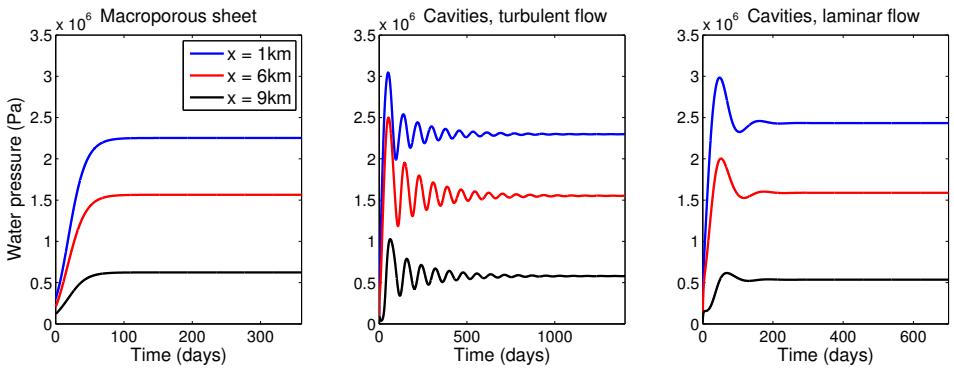

Figure A.1: Water pressure timeseries for three simulations to steady state at three different locations along the bed. (a) Macroporous sheet (CST_sheet)); (b) Cavities with turbulent flow (CST_tur)); (c) Cavities with laminar flow (CST_lam).

system of cavities. In this first experiment, water input is constant in both time and space. When a macroporous sheet is considered, there is no feedback between the water pressure and the maximum thickness of flow, hence the system reaches a steady state relatively quickly. In contrast, with the cavity system, feedbacks between water pressure and adjustment of the size of cavities cause equilibrium to be reached significantly later. This behaviour is illustrated in Figure A.1. The parameters were chosen so that the water pressure at steady state corresponds to ∼70% of the ice overburden pressure. The macroporous sheet model reaches steady state after only ∼120 d while it takes ∼1000 d for the cavity model with turbulent flow and ∼200 d for the cavity model with laminar flow. This is may be due to the feedbacks between the opening and closure of the cavity system that are not in phase with the pressure changes. A large pressure peak causes the cavities to open which then facilitates flow, however, when the cavities close the pressure increases again.

Spatially varying input

Model comparison

To compare transient results with each formulation of the distributed drainage system we use the same parameters as in the previous experiment (Figure A.1). Figure A.2a shows the flotation fraction and the normalized water input rate at $x = 7.4$ km for the cavities with laminar and turbulent flow and the sheet. When the flow in the cavity system is assumed turbulent, it leads to larger peak pressures but lower winter pressures. The maximum water pressure is reached later with the macroporous sheet, due to the necessity of filling the sheet for the pressure to rise significantly. The daily fluctuations in water pressure are however in phase across the different models (Figure A.2a) and the daily maximum rate of water pressure matches the daily maximum water input. The averaged thickness of the sheet or averaged cavity heights (Figure A.2b) are, however, significantly different. With the macroporous sheet, the maximum mean sheet thickness is in phase with the maximum water pressure, while in either formulation of the cavity model, the maximum water pressures are attained while the size of the cavities is increasing. These differences in phasing between mean sheet thicknesses arise from the respective model constructions. In the macroporous sheet, the pressure is a direct function of the sheet thickness, while in the cavity system the

Simulation	Purpose	Hydrology	Frequency	h_c^s or h_r (m)	K_s ($m\,s^{-1}\,orm^{7/4}\,kg^{-1/2}$)	α	β	u_b ($m\,a^{-1}$)
CST_tur	Steady state	turbulent cavities	Steady	0.12	5×10^{-3}	5/4	3/2	1
CST_lam	Steady state	laminar cavities	Steady	0.12	1×10^{-4}	1	2	1
CST_sheet	Steady state	macroporous sheet	Steady	0.6	4.5×10^{-2}	1	2	1
CAV_tur_SD	Transient	turbulent cavitites	SD	0.12	5×10^{-3}	5/4	3/2	1
CAV_lam_SD	Transient	laminar cavitites	SD	0.12	1×10^{-4}	1	2	1
SH_SD	Transient	macroporous sheet	SD	0.6	4.5×10^{-2}	1	2	1
CAV_tur_SD_ub5	Transient	turbulent cavitites	SD	0.12	1×10^{-3}	5/4	3/2	5
CAV_tur_SD_ub10	Transient	turbulent cavitites	SD	0.12	1×10^{-3}	5/4	3/2	10
CAV_tur_SD_ub20	Transient	turbulent cavitites	SD	0.12	1×10^{-3}	5/4	3/2	20
CAV_ref	Sliding feedback	turbulent cavities	SD	0.15	1.2×10^{-3}	5/4	3/2	coupled

Table A.3: Summary of the simulations performed with the distributed hydraulic system.

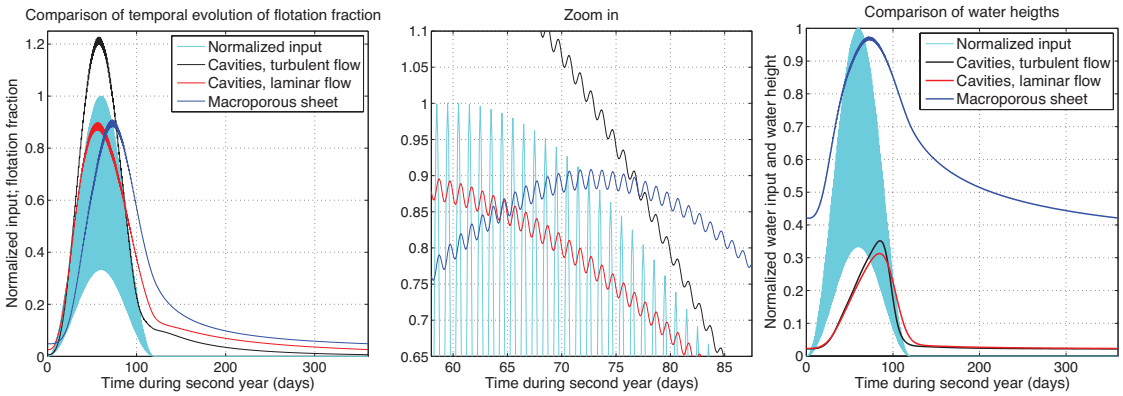

(a) Temporal evolution of flotation fraction (b) Changes in h_w

Figure A.2: Timeseries of (a) flotation fraction and (b) normalized water height for the second year of the run at the location $x = 7.4\,\mathrm{km}$. The normalized water input is plotted in light blue. The thickness of flow is normalized by the maximum obstacle size or the critical sheet thickness for the cavity model and macroporous sheet, respectively. The simulations presented are CAV_tur_SD in black, CAV_lam_SD in red and SH_SD in blue (see Table A.3)

size of the cavities changes as a function of water pressure and sliding speed (Equations A.1–A.3). The behaviour of the cavity system reproduces the processes inferred by Iken (1981) and later Bartholomaus and others (2011), as already found by Hewitt (2013).

A significant difference that arises between the cavity and macroporous sheet models is the spatial distribution of water thickness. In the macroporous sheet, the critical sheet thickness is constant and therefore the water thickness is mainly controlled by the hydraulic potential. In the cavity system, the thickness of flow depends not only on the size of bed obstacles, but also on sliding speed (Equations A.1–A.3). Figure A.3 shows longitudinal profiles of normalized sheet thickness. In the macroporous sheet (Figure A.3, blue curves) normalized sheet thicknesses do not change monotonically, reflecting the fact that water pressure coincides with sheet thickness ($p_s \propto {h_s}^k$). In the cavity system (Figure A.3, black curves), the sheet thickness increases monotonically with distance down-glacier. The sliding speed is assumed constant although the ice thickness, hence the creep closure, decreases toward the terminus, resulting in larger cavity sizes. In the cavity system the maximum water pressure coincides with the maximum rate of cavity opening (Figure A.2) and not with the maximum cavity size, explaining the monotonic character of the longitudinal profile of cavity height (Figure A.3, black curve with crosses).

Changes in sliding speed

As shown by Equations A.5 and A.1–A.3, the behaviour of the cavity system is highly dependent on sliding speed. To test this sensitivity, we compare the pressure regime obtained with turbulent flow in the cavity system for different sliding speeds. All the hydrology-related parameters are kept constant (Table A.3).

As expected from Equations A.5 and A.1–A.3, the greater the sliding speed, the lower the water pressure in the system (Figure A.4a). Interestingly, the greater the sliding speed, the

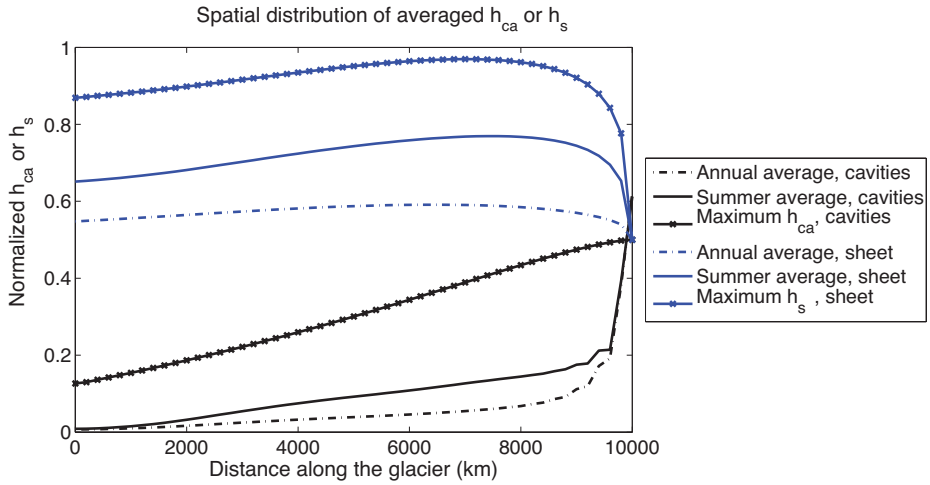

Figure A.3: Longitudinal profiles of normalized sheet thickness for the macroporous sheet (blue) and the cavity system (black). The normalization if done using the critical sheet thickness and the height of bed obstacles with respect to the relevant system. Dash-dotted lines represent the average over the simulation, full lines the average over the melt-season and the line with crosses the maximum thickness of flow observed in the simulation.

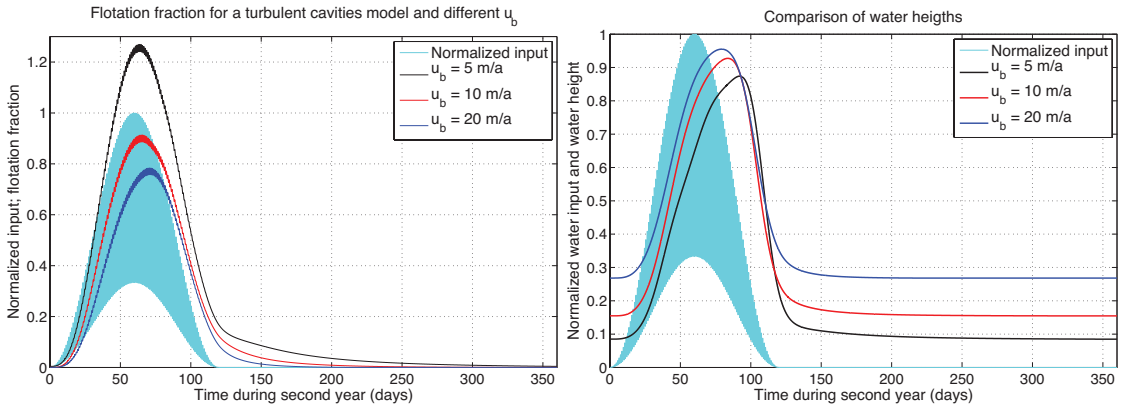

(a) Flotation fraction for different u_b at $x = 7.4$ (b) Normalized h_w and for different u_b at $x = 7.4$

Figure A.4: Timeseries of (a) flotation fraction and (b) normalized water height for the second year of the run at the location $x = 7.4\,\mathrm{km}$ plotted for different sliding speeds. In black: $u_\mathrm{b} = 5\,\mathrm{m\,a^{-1}}$; red: $u_\mathrm{b} = 10\,\mathrm{m\,a^{-1}}$; and blue: $u_\mathrm{b} = 20\,\mathrm{m\,a^{-1}}$. The normalized water input is plotted in light blue. The cavity height is normalized by the maximum obstacle size. Note that the hydrology parameters are kept constant throughout these simulations, however they differ from the previous simulations (CAV_tur_SD_ub5, CAV_tur_SD_ub10 and CAV_tur_SD_ub20 in Table A.3).

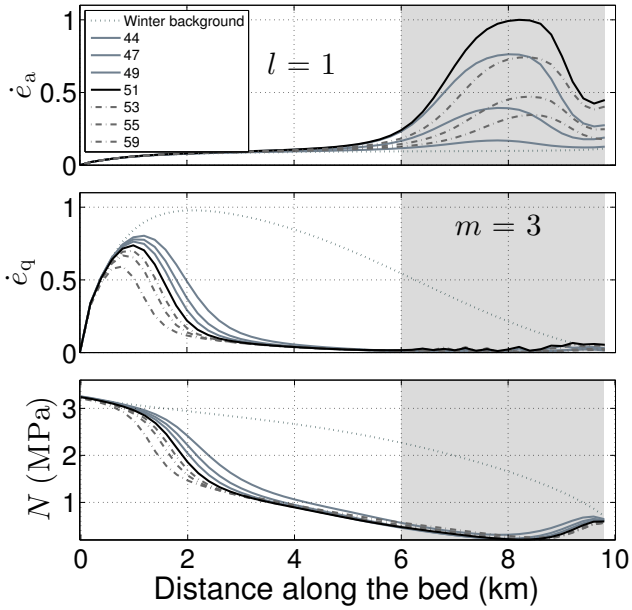

Figure A.5: Profiles of normalized abrasion rate, normalized quarrying rate and basal effective pressure during the seasonal sliding enhancement in cavities-only simulation CAV_ref; (a) Abrasion rates $\dot{e}_a$ for $l = 1$; (b) Quarrying rates $\dot{e}_q$ for $m = 3$; (c) Effective pressure $N = p_i - p_{ca}$. Lines are snapshots corresponding to different sliding phases (day number during melt season in legend): increasing sliding (solid grey), maximum sliding (solid black), decreasing sliding (dot-dashed grey) and winter background (dotted). Shading highlights region most affected by spring "speed-up". This figure is to be compared with Figure 2.5 and 2.6.

later the peak in water pressure is attained and the closer it is from the peak in maximum cavity size (Figure A.4ab). When sliding speed is large, cavities are large regardless of the water pressure, and the behaviour of the cavity system tends toward that of a macroporous sheet. This trend is, however, probably caused by both the lack of feedback between pressure and sliding in these simulations and the consideration of only a single bedrock obstacle size. As in Creyts and Schoof (2009), considering different obstacle sizes may render the model more realistic.

Interactions with ice dynamics

The interplay between water flow and sliding speed is inherent to the formulation of the system of cavities, therefore the coupling with ice dynamics is necessary if we are to generalize the conclusions we have drawn so far. We reproduce a similar experiment to that used in simulations SH_ref and SC_ref (see Table 2.3 and Section 2.3.2) with the system of cavities (Table A.3).

Figure A.5 shows the speed-up obtained. The patterns of abrasion are similar to those obtained with the sheet-only model (Figure 2.5). A significant difference in effective pressure can be observed in the upper two kilometres of the flowline as it remains large compared to

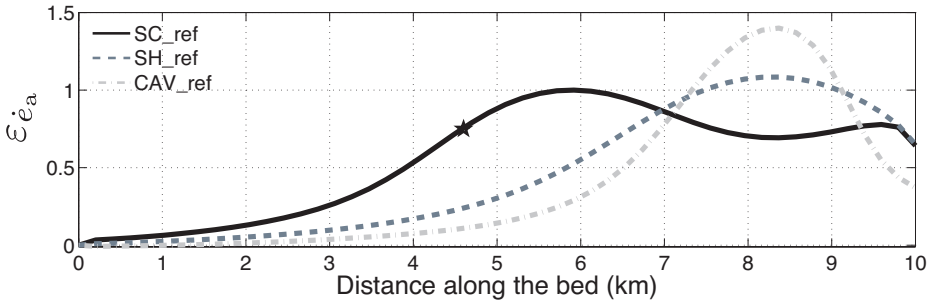

Figure A.6: Comparison of excess abrasion $\varepsilon_{\dot{e}_a}$ for different drainage morphologies: macroporous sheet and channels (solid black), macroporous sheet only (dashed grey), cavities only (dash-dotted light grey). Excess abrasion is normalized with respect to its maximum in simulation SC_ref. Stars marks maximum up-glacier position of channel head (here defined as $S(x) = 0.1\text{m}^2$) in multi-morphology simulations.

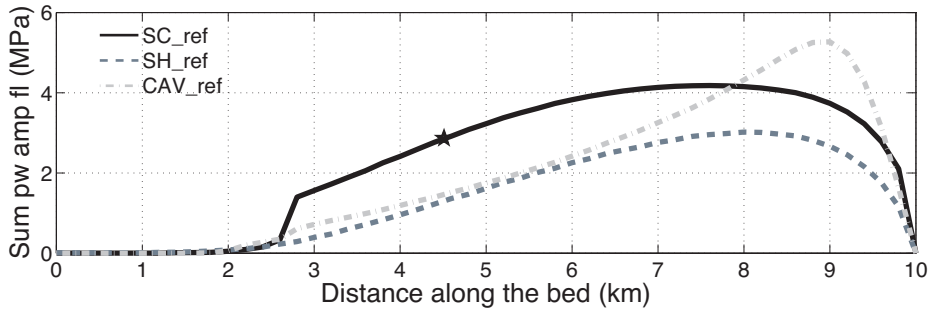

Figure A.7: Comparison of time-integrated daily reduction in water pressure for different drainage morphologies: macroporous sheet and channels (solid black), macroporous sheet only (dashed grey), cavities only (dash-dotted light grey). The star marks the maximum up-glacier position of channel head (here defined as $S(x) = 0.1\text{m}^2$) in multi-morphology simulations.

that obtained with the sheet only (Figure 2.5c and A.5). Quarrying rates therefore remain high in the upper reaches even throughout the melt-season. This is most likely due to the lack of water input to that area of the bed (Figure 2.4, black curve), although this behaviour is not observed with laminar flow in the cavities (not shown).

To test whether different hydrology models yield significantly different results, we compare excess abrasion (Equation 2.17) obtained with the system of cavities, sheet only and sheet and channels, as shown in Figure A.6. The maximum in excess abrasion obtained with the cavity model is located very close to that obtained with the sheet model, although the peak is sharper. The differences in magnitude between the simulations originate in model tuning.

In order to assess the differences in water pressure fluctuations caused by model formulation, we compare the integrated drop in water pressure (Figure A.7). The resulting peak in integrated pressure fluctuations in the system of cavities is more localized and ∼1 km further down-glacier from the peak in the simulations where distributed drainage is represented by a macroporous sheet.

A.1.3 Summary

This brief comparison shows that the differences in behaviour between the macroporous sheet and the system of cavities mostly result in a more localized speed-up and sharper peak in pressure fluctuations when the system of cavities is used. The other significant difference is the lag for the macroporous sheet to reach its maximum water pressure compared to the system of cavities, although this lag is probably much less evident when channels are integrated (see Figure 2.6 maximum sliding and minimum N reached on day 46 of the simulation).

The feedbacks between water pressure and cavity size may render the system of cavities more stable to varying water input than the macroporous sheet, as the increase in cavity size and resulting decrease in water pressure partially reduces the tendency of the system to exceed flotation water pressures. We still find that excess abrasion increases significantly with the period of forcing (for example see Figure 2.10a) and that, for example, a Seasonal + Weekly forcing leads to much higher excess abrasion than the Seasonal + Daily forcing (results not shown, see Figure 2.3 for a summary of forcings). In light of these results, the conclusions drawn about erosion patterns while using a macroporous sheet to represent the distributed drainage system would hold with a system of cavities.

Appendix B

Appendix to Chapter 3

B.1 Subglacial water flow model

B.1.1 Channelized drainage

The rate of channel closure is given by:

$$v_{\mathrm{cc}}(S, N_{\mathrm{ch}}) = \tilde{A}_{\mathrm{ch}} S |N_{\mathrm{ch}}|^{n-1} N_{\mathrm{ch}}, \tag{B.1}$$

where $\tilde{A}_{\mathrm{ch}}$ is the ice flow-law coefficient adapted for a semi-circular channel, S is the cross-sectional area of the channel, n is the flow-law exponent, $N_{\mathrm{ch}} = \phi_0 - \phi_{\mathrm{ch}}$ is the effective pressure in the channel, ϕ_{ch} is the hydraulic potential in the channel and $\phi_0 = \rho_{\mathrm{w}} g z_{\mathrm{b}} + \rho_{\mathrm{i}} g h_{\mathrm{i}}$ is the hydraulic potential at the ice surface, with g the gravitational acceleration, z_{b} the elevation of the bed, ρ_{w} and ρ_{i} the density of water and ice respectively, and h_{i} the ice thickness. The discharge Q_{ch} in a semi-circular channel reads

$$Q_{\mathrm{ch}} = -k_{\mathrm{ch}} S^{\alpha_{\mathrm{c}}} |\nabla \phi_{\mathrm{ch}}|^{\beta_{\mathrm{c}}-2} \nabla \phi_{\mathrm{ch}}, \tag{B.2}$$

where k_{ch} is the effective conductivity of a channel and α_{c} and β_{c} are constants chosen for turbulent flow conditions (see Table B.1). The dissipation of potential energy is expressed as

$$\Xi = \left| Q_{\mathrm{ch}} \frac{\partial \phi_{\mathrm{ch}}}{\partial x} \right|, \tag{B.3}$$

with x the coordinate along the flowline. The energy required to maintain the water at the pressure melting point is given by

$$\Pi = -c_{\mathrm{t}} c_{\mathrm{w}} \rho_{\mathrm{w}} Q_{\mathrm{ch}} \frac{\partial}{\partial x} (\phi_{\mathrm{ch}} - \phi_{\mathrm{b}}), \tag{B.4}$$

where c_{t} is the pressure-melting coefficient for ice, c_{w} is the heat capacity of water and ϕ_{b} the hydraulic potential at the bed.

B.1.2 Network of linked cavities

Cavity opening is a function of sliding speed u_b and bedrock obstacle size:

$$v_\mathrm{o}(h_\mathrm{ca}) = \begin{cases} u_\mathrm{b}(h_\mathrm{r} - h_\mathrm{ca})/l_\mathrm{r} \text{ if } h_\mathrm{ca} < h_\mathrm{r} \\ 0 \text{ otherwise,} \end{cases} \tag{B.5}$$

where h_r and l_r are, respectively, the maximum height and length of characteristic bedrock obstacles and h_ca is the average height of the cavities. Cavity closure is caused by ice creep:

$$v_\mathrm{c}(h_\mathrm{ca}, N_\mathrm{ca}) = \tilde{A}_\mathrm{ca} h_\mathrm{ca} |N_\mathrm{ca}|^{n-1} N_\mathrm{ca}, \tag{B.6}$$

where $\tilde{A}_\mathrm{ca}$ is the ice flow-law coefficient adjusted for cavity geometry and $N_\mathrm{ca} = \phi_0 - \phi_\mathrm{ca}$ is the water effective pressure in the cavity network, with ϕ_ca the pressure in the network of cavities. The flux through the cavity system is expressed as

$$\boldsymbol{q}_\mathrm{ca} = -K_\mathrm{ca} h_\mathrm{ca}^{\alpha} |\nabla \phi_\mathrm{ca}|^{\beta-2} \nabla \phi_\mathrm{ca}, \tag{B.7}$$

where K_ca is the effective conductivity of the cavity system, and α and β are again chosen to satisfy turbulent flow conditions (see Table B.1).

Table B.1: Summary of hydrological model parameters.

Parameter	Description	Value
M	Number of grid points	101
$\mathrm{d}x$	Cell size	$500\,\mathrm{m}$
$\mathrm{d}t$	Time step	$600\,\mathrm{s}$
W	System width	$1000\,\mathrm{m}$
X_L	Glacier length	$50\,\mathrm{km}$
ρ_w	Water density	$1000\,\mathrm{kg\,m^{-3}}$
ρ_i	Ice density	$910\,\mathrm{kg\,m^{-3}}$
c_w	Heat capacity of water	$4.22\times10^{3}\,\mathrm{J\,kg^{-1}\,K^{-1}}$
c_t	Pressure melting coefficient	$7.5\times10^{-8}\,\mathrm{K\,Pa^{-1}}$
L	Latent heat of fusion	$3.34\times10^{5}\,\mathrm{J\,kg^{-1}}$
$\tilde{A}_\mathrm{ch}$	Flow-law coefficient for channels †	$5\times10^{-25}\,\mathrm{Pa^{-n}\,s^{-1}}$
$\tilde{A}_\mathrm{ca}$	Flow-law coefficient for cavity network †	$5\times10^{-25}\,\mathrm{Pa^{-n}\,s^{-1}}$
n	Flow-law exponent	3
K_cav	Conductivity of linked cavity system	$1-25\times10^{-3}\,\mathrm{m^{7/4}\,kg^{-1/2}}$
k_ch	Channel conductivity	0.1225 (i.e. $\langle n'\rangle = 0.321$)
k_ex	Exchange coefficient between cavities and channel	$5\times10^{-13}\,\mathrm{m^{3/2}\,kg^{-1/2}}$
$\langle n'\rangle$	Manning roughness averaged	0.0321
n'_i	Manning roughness for ice	0.01
n'_b	Manning roughness for bed	0.05
e_v	Englacial void ratio †	1×10^{-3}
h_r	Height of bed obstacles	$0.2\,\mathrm{m}$
l_r	Length of bed obstacles †	$2\,\mathrm{m}$
u_b	Sliding speed	$5\ \mathrm{m\,a^{-1}}$
α	Flux exponent for the cavity network †	5/4
α_c	Flux exponent for the R-channel †	5/4
β	Flux exponent for the cavity network †	3/2
β_c	Flux exponent for the R-channel †	3/2
γ	Numerical compressibility parameter	$10^{-9}\,\mathrm{Pa^{-1}}$

†Parameter values from Werder and others (2013)

B.2 Shear stress partitioning

To compute the viscous heat dissipation in semi-circular R-channels, the roughness of the bed and ice walls is averaged (Clarke, 2003). If u is the average flow velocity in a channel or network of cavities, and $u = Q_{\mathrm{ch}}/S$ or $u = q_{\mathrm{ca}}/h_{\mathrm{ca}}$, respectively, the total shear stress on the ice walls and bed can be written

$$\tau_{\mathrm{tot}} = \frac{1}{8} \langle f_{\mathrm{R}} \rangle \, \rho_{\mathrm{w}} u^2. \tag{B.8}$$

To account for the difference in roughness between the ice and bed, the averaged Darcy-Weisbach friction coefficient $\langle f_{\mathrm{R}} \rangle$ is given by (Clarke, 2003):

$$\langle f_{\mathrm{R}} \rangle = \frac{f_{\mathrm{i}} P_{\mathrm{i}} + f_{\mathrm{b}} P_{\mathrm{b}}}{P_{\mathrm{w}}}, \tag{B.9}$$

where f_{i} and f_{b} are, respectively, the friction coefficients of the ice and bed, and P_{i}, P_{b} and P_{w} are the ice, bed and total wetted perimeters, respectively. Given that $f_a = (8 g {n'_a}^2)/R_{\mathrm{H}}^{1/3}$, with a representing either the ice i or the bed b and R_{H} being the hydraulic radius. After substitution the averaged Manning roughness is

$$\langle n' \rangle = \left(\frac{{n'_{\mathrm{i}}}^2 P_{\mathrm{i}} + {n'_{\mathrm{b}}}^2 P_{\mathrm{b}}}{P_{\mathrm{w}}} \right)^{1/2}. \tag{B.10}$$

Here, n'_{i} and n'_{b} are the Manning roughnesses of the ice and the bed, respectively. The partitioning of the shear stress is obtained through the sum of the shear stresses weighted by the normalized wetted perimeters of the respective materials:

$$\tau_{\mathrm{tot}} = \frac{\tau_{\mathrm{i}} P_{\mathrm{i}}}{P_{\mathrm{w}}} + \frac{\tau_{\mathrm{b}} P_{\mathrm{b}}}{P_{\mathrm{w}}}. \tag{B.11}$$

The shear stress on either the ice (τ_{i}) or bed (τ_{b}) is computed using Eq. (B.8) replacing $\langle f_{\mathrm{R}} \rangle$ by f_{i} or f_{b} . For the shear stress on the bed this leads to

$$\tau_{\mathrm{b}} = \frac{1}{8} f_{\mathrm{b}} \rho_{\mathrm{w}} u^2. \tag{B.12}$$

We use a formulation of the discharge in a channel that is not a direct function of the Manning roughness or the Darcy-Weisbach friction coefficient, but rather an effective channel conductivity k_{ch} (Table B.1) given by

$$k_{\mathrm{ch}} = \left(\rho_{\mathrm{w}} g {n'}^2 \left(\frac{2}{\pi} \right)^{2/3} (\pi + 2)^{4/3} \right)^{-1/2} \tag{B.13}$$

as a function of the Manning roughness n', or

$$k_{\mathrm{ch}} = \left(\frac{8}{\rho_{\mathrm{w}} f_{\mathrm{R}} \left(\frac{2}{\pi} \right)^{1/2} (\pi + 2)} \right)^{1/2} \tag{B.14}$$

as a function of Darcy-Weisbach roughness f_{R}.

B.3 Erosion model details

B.3.1 Saltation erosion model (SEM)

Hop height H_{s} and length L_{s}

Sklar and Dietrich (2004) determined that the best empirical fit for the hop height could be written

$$H_{\mathrm{s}} = 1.44D\left(\frac{\tau^*}{\tau_{\mathrm{c}}^*} - 1\right)^{0.5}, \tag{B.15}$$

and the hop length as

$$L_{\mathrm{s}} = 8.0D\frac{(\tau^*/\tau_{\mathrm{c}}^* - 1)^{0.88}}{(1-(u^*/w_{\mathrm{f}})^2)^{1/2}} \quad \text{for} \quad u^*/w_{\mathrm{f}} < 1, \tag{B.16}$$

where D is the particle diameter, w_{f} is the terminal settling velocity of a particle, τ^* is the Shields stress, τ_{c}^* its critical value for sediment motion and u^* the shear velocity. When the shear velocity exceeds the settling velocity ($u^*/w_{\mathrm{f}} \geq 1$) the particle is in suspension and the hop length becomes infinite. The settling velocity of a particle is computed following Dietrich (1982), who defines a dimensionless fall velocity W_* and particle diameter D_* as:

$$W_* = \frac{\rho_{\mathrm{w}} w_{\mathrm{f}}^3}{(\rho_{\mathrm{s}} - \rho_{\mathrm{w}})g\nu} \tag{B.17}$$

$$D_* = \frac{(\rho_{\mathrm{s}} - \rho_{\mathrm{w}})gD^3}{\rho_{\mathrm{w}}\nu}, \tag{B.18}$$

where ν is the kinematic viscosity of water and ρ_{s} is the density of the particle. The dimensionless fall velocity is found empirically to be

$$W_* = R_3 \times 10^{R_1+R_2}, \tag{B.19}$$

where

$$\begin{aligned} R_1 = -3.76715 + 1.92944\log(D_*) - 0.09815\log(D_*)^{2.0} \\ -0.00575\log(D_*)^{3.0} + 0.00056\log(D_*)^{4.0}, \end{aligned} \tag{B.20}$$

$$\begin{aligned} R_2 = \log\left(1 - \frac{1-\mathrm{CSF}}{0.85}\right) - (1-\mathrm{CSF})^{2.3}\tanh(\log(D_*) - 4.6) \\ +0.3(0.5-\mathrm{CSF})(1-\mathrm{CSF})^{2.0}(\log(D_*) - 4.6) \end{aligned} \tag{B.21}$$

and

$$R_3 = \left[0.65 - \left(\frac{\mathrm{CSF}}{2.83}\tanh(\log(D_*) - 4.6)\right)\right]^{1+(3.5-P_{\mathrm{nb}})/2.5}. \tag{B.22}$$

Here P_{nb} is the Powers number and CSF the Corey shape factor. Together these numbers define the shape of the particle. The dimensional fall velocity can then be computed by

Table B.2: Summary of parameter values for the SEM (Sect. 3.2.2) and TLEM (Sect. 3.2.2).

Parameter	Description	Value
ν	Kinematic viscosity of water	$10^{-6}\,\mathrm{m^2\,s^{-1}}$
P_{nb}	Powers number	3.5
CSF	Corey shape factor	0.8

inverting Eq. (B.17):

$$w_{\mathrm{f}} = \left(\frac{W_*(\rho_{\mathrm{s}} - \rho_{\mathrm{w}})g\nu}{\rho_{\mathrm{w}}}\right)^{1/3}. \tag{B.23}$$

Impact velocity w_{si}

From the fall velocity, Sklar and Dietrich (2004) compute the mean particle descent velocity w_{sd} as

$$w_{\mathrm{sd}} = \frac{3H_{\mathrm{s}}U_{\mathrm{s}}}{2L_{\mathrm{s}}} = 0.4(rgD)^{1/2}\left(\frac{\tau^*}{\tau_{\mathrm{c}}^*} - 1\right)^{0.18}\left(1 - \left(\frac{u^*}{w_{\mathrm{f}}}\right)^2\right)^{1/2}, \tag{B.24}$$

where $r = \rho_{\mathrm{s}}/\rho_{\mathrm{w}} - 1$ is the buoyant density of sediment and the along-path velocity of particles travelling as bedload is given by

$$U_{\mathrm{s}} = 1.56\,(rgD)^{1/2}\left(\frac{\tau^*}{\tau_{\mathrm{c}}^*} - 1\right)^{0.56}. \tag{B.25}$$

Sklar and Dietrich (2004) further estimate that the impact velocity is twice the mean descent velocity:

$$w_{\mathrm{si}} \approx 2w_{\mathrm{sd}}. \tag{B.26}$$

B.3.2 Total load erosion model (TLEM)

For the suspended load, the sediment concentration can be written

$$c = c_{\mathrm{b}}\left(\frac{(1-\zeta_{\mathrm{z}})/\zeta_{\mathrm{z}}}{(1-\zeta_{\mathrm{b}})/\zeta_{\mathrm{b}}}\right)^{P_{\mathrm{R}}}, \tag{B.27}$$

where we define $\zeta_{\mathrm{z}} = z/H$ and $\zeta_{\mathrm{b}} = H_{\mathrm{s}}/H$, H is the height of the flow and $P_{\mathrm{R}} = w_{\mathrm{st}}/(\kappa u^*)$ is the Rouse parameter while κ is von Karman's constant. The near-bed sediment concentration c_{b} is defined as:

$$c_{\mathrm{b}} = \frac{q_{\mathrm{s}}}{uH\chi + U_{\mathrm{s}}H_{\mathrm{s}}}, \tag{B.28}$$

where q_{s} is the sediment supply per unit width. The integral relating the flux of sediment to c_{b}, H and u is given by:

$$\chi = \frac{1}{uH}\int_{H_{\mathrm{s}}}^{H}\left(\frac{(1-\zeta_{\mathrm{z}})/\zeta_{\mathrm{z}}}{(1-\zeta_{\mathrm{b}})/\zeta_{\mathrm{b}}}\right)^{P_{\mathrm{R}}}\frac{u^*}{\kappa}\ln\left(\frac{z}{z_0}\right)\mathrm{d}x, \tag{B.29}$$

and the bed load transport capacity is expressed as

$$q_{\mathrm{b}} = c_{\mathrm{b}} U_{\mathrm{s}} H_{\mathrm{s}} = \frac{q_{\mathrm{s}} U_{\mathrm{s}} H_{\mathrm{s}}}{u H \chi + U_{\mathrm{s}} H_{\mathrm{s}}}. \tag{B.30}$$

Because the effect of turbulence on sediment concentration has been introduced, the equation for the impact velocity (Eq. (B.26)) proposed by Sklar and Dietrich (2004) is no longer valid. Instead, the effective impact velocity is written as a function of velocity fluctuations w' close to the bed:

$$w_{\mathrm{i,eff}} = \left(\int_{-w_{\mathrm{s}}}^{6\sigma_{\mathrm{w}}} \left(w' + w_{\mathrm{s}} \right)^3 P \mathrm{d}w' \right)^{1/3}, \tag{B.31}$$

where $\sigma_{\mathrm{w}} = \sqrt{\overline{w'^2}}$ is the standard deviation of velocity fluctuations (the over line denotes averaging; as an approximation for open flows $\sigma_{\mathrm{w}} = u^*$) and P is a probability density function of the velocity fluctuations such that

$$P(w') = \frac{1}{\sqrt{2\pi}\sigma_{\mathrm{w}}} \exp\left(-\frac{w'^2}{2{\sigma_{\mathrm{w}}}^2} \right). \tag{B.32}$$

Note that w' is taken as a variable such that $w' \in [-w_{\mathrm{s}}, 6\sigma_{\mathrm{w}}]$. The velocity normal to the bed of a falling particle w_{s} is given by

$$w_{\mathrm{s}} = w_{\mathrm{st}} \cos(\theta) \sqrt{1 - \exp\left(-\frac{3 C_{\mathrm{d}} \rho_{\mathrm{w}} H_{\mathrm{f}}}{2 \rho_{\mathrm{s}} D \cos(\theta)} \right)}, \tag{B.33}$$

where w_{st} is the terminal settling velocity, θ is the slope of the bed, C_{d} is the drag coefficient and H_{f} is the particle fall distance. The terminal settling velocity is computed as

$$w_{\mathrm{st}} = \left(\frac{4}{3} \frac{r g D}{C_{\mathrm{d}}} \right)^{1/2} \tag{B.34}$$

and the drag coefficient as

$$C_{\mathrm{d}} = \frac{4}{3} \frac{(\rho_{\mathrm{s}} - \rho_{\mathrm{w}}) g D}{\rho_{\mathrm{w}} {w_{\mathrm{f}}}^2}. \tag{B.35}$$

Finally, the fall distance is a function of the sediment concentration throughout the water column (c):

$$H_{\mathrm{f}} = \frac{1}{c_{\mathrm{b}}} \int_{H}^{H_{\mathrm{s}}} z \frac{\mathrm{d}c}{\mathrm{d}z} \mathrm{d}z, \tag{B.36}$$

where z is the height above the bed.

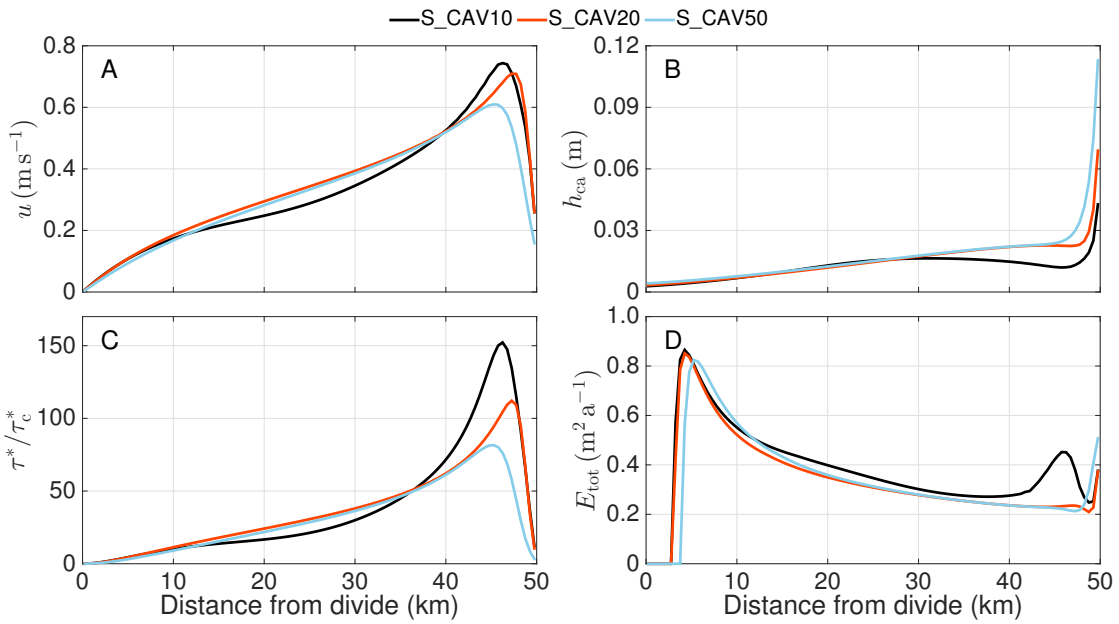

Figure B.1: Comparison of the hydraulic conditions, transport stage and erosion in a network of cavities for different sliding speeds ($u_{\mathrm{b}} = 10 - 50\,\mathrm{m/a}$, S_CAV10 – 50, Table B.3; Sect. B.4.1). (A) Water velocity u; (B) Height of cavities h_{ca}; (C) Transport stage $\tau^*/\tau_{\mathrm{c}}^*$; (D) Total erosion ($E_{\mathrm{tot}} = \dot{e}_{\mathrm{tot}} W$) computed with the TLEM. Transport stage and erosion are computed for sand particles with a diameter $D = 1\,\mathrm{mm}$.

B.4 Supplementary steady-state simulations

B.4.1 Linked cavities

Here we ask whether water flow through a network of linked cavities is capable of bedrock erosion, in tests using a fixed ice geometry and surface melt profile, but variable sliding speeds. The opening term in the cavity evolution equation (Eq. (B.5)) is a function of effective pressure, sliding speed and geometry of bed obstacles. Since the latter is poorly defined and we prescribe ice geometry, we choose to vary only the sliding speed in these tests (Table B.3). We assume a sediment size corresponding to coarse sand ($D = 1\,\mathrm{mm}$) in anticipation of much lower transport capacities than in a channel. We also divide the reference reach-averaged sediment supply ($q_{\mathrm{s,ref}}$; Table 3.2) by the width of the glacier (W) such that $q_{\mathrm{s,cav}} = q_{\mathrm{s,ref}}/W$.

The flow velocity through the cavity network (Fig. B.1A) shows similar features to the simulation S_MOULIN (see Fig. 3.2B). Close to the terminus the ice thins rapidly (Fig. 3.1), reducing creep closure and leading to larger cavities (Fig. B.1B; Eq. (B.5)). The increase in cavity size over the last 2 km of the bed is accentuated if sliding speeds are relatively large (largest cavities for S_CAV50 simulation, Table B.3), and the increase in cavity size drives the drop in velocity (Fig. B.1B; $u = q_{\mathrm{w}}/h_{\mathrm{cav}}$). In turn the larger the sliding speed, the larger the transport stage (Fig. B.1C).

Table B.3: Summary of steady-state simulations. For simulations in which meltwater input is a function of ice-surface elevation z_s, we compute $f(z_s(x)) = \dot{b}_{ss\,max} \times (1 - (z_s(x) - z_{s,min})/z_{s,max})$, where $\dot{b}_{ss\,max} = 8.5 \times 10^{-7}\,m\,s^{-1}$ is the maximum meltwater input rate to the channelized drainage system, and $z_{s,min}$ and $z_{s,max}$ are, respectively, the minimum and maximum ice-surface elevations. Note that $\dot{b}_{ss\,max} = 8.5 \times 10^{-7}\,m\,s^{-1}$ corresponds to 7.6 cm of ice melt per day assuming $\rho_i = 910\,kg\,m^{-3}$. The reference sediment supply used for the steady-state simulations is: $q_{s,ref} = 3.6 \times 10^{-3}\,m^2\,s^{-1}$.

Simulation	Purpose	Forcing	Difference from reference run	Section
S_MOULIN	R-channel only	$Q_{ch}(x=0,t) = 4.25\,m^3\,s^{-1}$	Localized input upstream boundary	3.4.1
S_CAV10–50	Cavities only	$\dot{b}_{cav}(x,t) = f(z_s(x))$	Network of cavities only with $u_b = 10-50$, $D = 1\,mm$	B.4.1
S_REF	Reference	$\dot{b}_{ch,ref}(x,t) = f(z_s(x))$		3.4.1
S_CST	Water input	$\dot{b}_{ch}(x,t) = 4.25 \times 10^{-7}\,m\,s^{-1}$	$\dot{b}_{ch}$ constant in space	B.4.2
S_CSTx2	Water input	$\dot{b}_{ch}(x,t) = 8.5 \times 10^{-7}\,m\,s^{-1}$	$2 \times \dot{b}_{ch}$ from S_CST	B.4.2
S_SURFx2	Water input	$\dot{b}_{ch}(x,t) = \dot{b}_{ch,ref} \times 2$	$2 \times \dot{b}_{ch}$ from REF	B.4.2
S_SSZ	Sediment size	$\dot{b}_{ch}(x,t) = \dot{b}_{ch,ref}$	$D = 1$–$550\,mm$	B.4.3
S_MR23	Manning roughness	$\dot{b}_{ch}(x,t) = \dot{b}_{ch,ref}$	$n'_i = 0.010$, $n'_b = 0.035$, $< n' >= 0.023$	B.4.4
S_MR35	Manning roughness	$\dot{b}_{ch}(x,t) = \dot{b}_{ch,ref}$	$n'_i = 0.020$, $n'_b = 0.050$, $< n' >= 0.035$	B.4.4
S_MR38	Manning roughness	$\dot{b}_{ch}(x,t) = \dot{b}_{ch,ref}$	$n'_i = 0.010$, $n'_b = 0.060$, $< n' >= 0.038$	B.4.4
S_MR46	Manning roughness	$\dot{b}_{ch}(x,t) = \dot{b}_{ch,ref}$	$n'_i = 0.020$, $n'_b = 0.070$, $< n' >= 0.046$	B.4.4

Particle motion is initiated over most of the bed ($\tau^*/\tau^*_c > 1$; Fig. B.1C) and transport stages are particularly high ($\tau^*/\tau^*_c > 2$; Fig. B.1C), hence erosion rates are limited by the decrease in relative sediment supply (q_s/q_{tc}). As a result, erosion peaks between km 4 and 5 (Fig. B.1D) and decreases thereafter until near the terminus. Close to the terminus, transport stage drops while remaining above 5, thus erosion increases again. In simulation S_CAV10, the local peak in erosion at km 48 (Fig. B.1D) occurs due to the peak in transport stage (Fig. B.1C) that allows the high impact velocity to offset the low relative sediment supply rate.

B.4.2 Water input

Subglacial discharge is largely controlled by the amount and distribution of melt water reaching the bed. Alley and others (1997) suggest that the transport capacity of a subglacial channel is an exponential function of discharge ($Q_{tc} \propto Q_{ch}^{9/2}$). We compare the effect of (1) feeding the system through a single moulin at the upstream domain boundary (S_MOULIN, Table B.3), (2) a constant water input throughout the profile (S_CST and S_CSTx2, Table B.3) and (3) water input varying inversely with ice-surface elevation

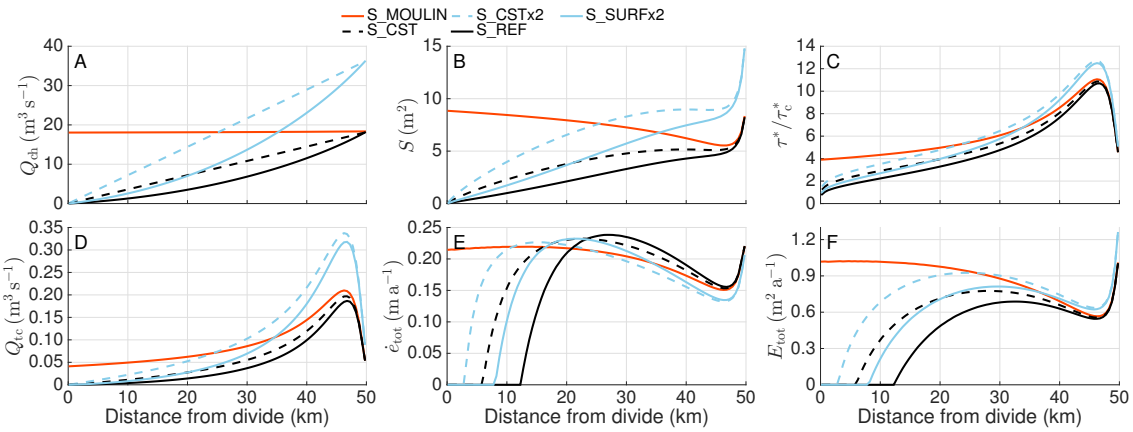

Figure B.2: Comparison of steady-state results for varying surface melt scenarios, reference ice geometry (Fig. 3.1) and drainage through one R-channel (Table 3.3, reference and water input; Sect. 3.4.1). The legend applies to all panels. (A) Discharge in the R-channel, Q_{ch}; (B) Cross-sectional area of the channel, S; (C) Transport stage, τ^*/τ_c^*; (D) Total transport capacity in the channel, $Q_{tc} = q_{tc} \times W_{ch}$; (E) Erosion rate per unit width calculated with the TLEM, $\dot{e}_{tot}$; Total erosion computed with the TLEM, $E_{tot} = \dot{e}_{tot} \times W_{ch}$.

(S_REF and S_SURFx2, Table B.3). In tests S_CSTx2 and S_SURFx2 the water input rate is doubled compared to S_CST and S_REF, respectively.

Water velocity in a channel is dependent on channel discharge and cross-sectional area. The latter is controlled by the ratio of melt opening to creep closure and is thus sensitive to ice thickness (Eqs (3.1)–(B.2)). As expected, the larger the water input, and hence the discharge (Fig. B.2A), the larger the cross-sectional area of the channel (Fig. B.2B). Peaks in transport stage (τ^*/τ_c^*; Fig. B.2C) coincide with the kink in the channel size profile (between km 46 and 47) similarly to what is seen in Fig. 3.2.

Since the channel cross-sectional area increases by about an order of magnitude along the profile (except for S_MOULIN since $Q_{ch} = \text{cst}$), the amplitude of total transport capacity (Q_{tc}, Fig. B.2D) is enhanced by about an order of magnitude compared to that of the reach-averaged transport capacity (q_{tc}, not shown). Despite the large increase in channel size close to the terminus, the decrease in transport stage (τ^*/τ_c^*; Fig. B.2C) is large enough that the total transport capacity still declines by a factor of two to three (Q_{tc}, Fig. B.2D).

All simulations in Fig. B.2 but S_MOULIN show a sharp increase in erosion rate per unit width ($\dot{e}_{tot}$, Fig. B.2E) and total erosion (E_{tot}, Fig. B.2F) commensurate with the increase of total transport capacity Q_{tc} from zero near the divide (km 3 for S_CSTx2 and km 12 for S_REF). A local maximum in erosion rates ($\dot{e}_{tot}$, Fig. B.2E) occurs when the bed-fraction exposed F_e reaches 0.7 (not shown); for higher transport stages, due to the constant sediment supply, the lack of tools ($c_b < 9 \times 10^{-3}$ and $q_s/q_{tc} < 0.3$, not shown; see Fig. 3.2) drives erosion rates down until km 47 (Fig. B.2E). Closer to the terminus, the transport stage drops (τ^*/τ_c^*, Fig. B.2C), the number of tools increases and so does erosion. Because of the feedback by which the number of tools in the vicinity of the bed and the erosion rates

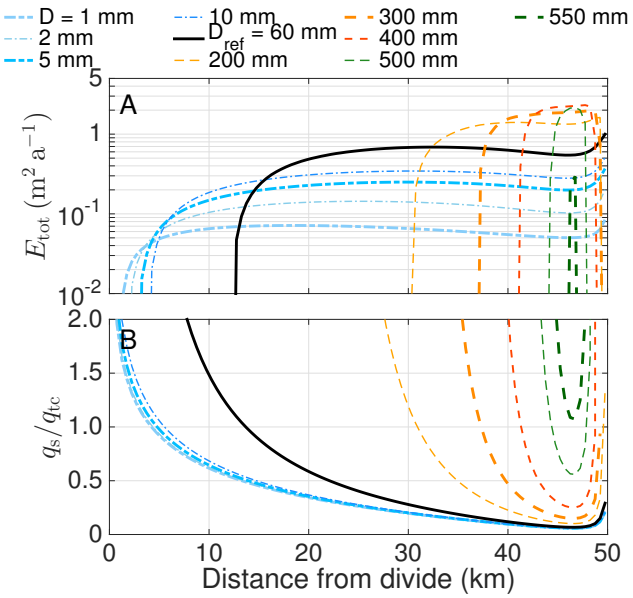

Figure B.3: Influence of sediment size D (S_SSZ, Table B.3) on total erosion with the TLEM for the same hydrology as in the reference simulation (S_REF, Table B.3). (A) Total erosion rate computed with the TLEM (E_{tot}); (B) Relative sediment supply ($q_{\text{s}}/q_{\text{tc}}$).

decrease with increasing transport stage, the erosion per unit width is highest for S_REF (Table 3.3) and lowest for S_CSTx2 and S_MOULIN (Table B.3).

Profiles of total erosion (E_{tot}, Fig. B.2F) are very similar to profiles of erosion rate per unit width (Fig. B.2E). For a given ice geometry, increased steady-state discharge leads to larger channels and thus larger peaks in total erosion. The doubling in surface melt between S_REF and S_SURFx2 (Table B.3) leads to an increase of only $\sim$ 33% in total erosion integrated over the glacier length.

B.4.3 Sediment size

Increasing the particle size is equivalent to a reduction in transport capacity (Eqs. (3.13) and (3.12)) and will affect rates and patterns of erosion (Fig. 15 in Sklar and Dietrich (2004); Fig. 7 in Lamb and others (2008a)). We show in Fig. B.3 that varying the particle diameter from sand- to boulder-sized leads to similar patterns as variations in sediment supply rate (Fig. B.3). When explained in terms of the relative sediment supply ($q_{\text{s}}/q_{\text{tc}}$), the feedbacks are those described in Fig. 3.4. In the case of particle size it is the decrease in transport capacity, rather that the increase in sediment supply, that yields larger relative sediment supply. We do not display the results of the SEM since the patterns are similar, despite the fact that little to no erosion occurs for the smallest particles (D= 1–2 mm) which travel mostly in suspension.

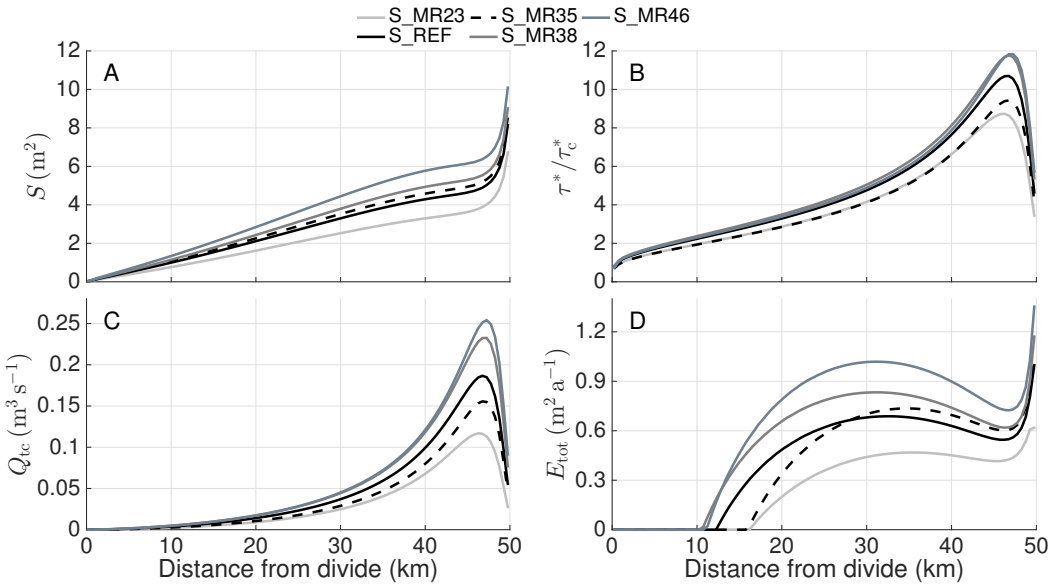

Figure B.4: Influence of bed and channel wall roughness on erosion and transport capacity. (A) Channel cross-sectional area S; (B) Transport stage τ^*/τ_c^*; (C) Total transport capacity Q_{tc}; (D) Total erosion computed with the TLEM E_{tot}.

B.4.4 R-channel roughness and steady-state conditions

We discuss here the effect of the roughness of the ice walls and of the bed material (Clarke, 2003) since the roughness parameters are poorly constrained. A smaller roughness would lead to less viscous heat dissipation and less melt of the channel, but also to a lower shear stress on the bed. We test different roughness combinations (see Table B.3; Eqs. (B.8)–(B.12); Fig. B.4), while discharge is kept constant (see Fig. B.2A, solid black), to differentiate the effect of bed and ice wall roughness.

As expected, the larger the average roughness, the larger the channel (Fig. B.4A). The transport stage (Fig. B.4B), on the other hand, is dependent on bed roughness (Eq. (3.6)). When we increase only the ice wall roughness (S_MR35) the channel grows larger, but the transport stage remains lower than in the reference simulation (S_REF) because the average water flow velocity is lower. The total transport capacity (Fig. B.4C) follows the same general hierarchy between simulations as the transport stage. In terms of the total erosion rates (Fig. B.4D), simulations with larger averaged Manning roughness (e.g. S_MR23 vs. S_MR46) produce more erosion.

Appendix C

Appendix to Chapter 4

We explore the formation of bedrock channels, such as tunnel valleys and inner gorges, with a numerical model. This study is largely based on the numerical model of subglacial meltwater erosion (SME) of bedrock that is described in Beaud and others (2016), to which we have made the following additions: (1) an investigation of erosion during floods (in contrast to melt-season or steady-state conditions only) and (2) the extension of the model to time scales commensurate with glacial cycles.

The two research questions that we address in this paper are: 1) Is flood-SME or seasonal-SME more effective at carving bedrock channels? 2) Can seasonal-SME over a glacial cycle explain the formation of the range of bedrock channels we observe in glaciated terrain?

In this appendix we provide an explanation for the classification of subglacial water flow events given in the main text, and describe the model set up for subglacial flood simulations and simulations spanning a glacial cycle. We also provide a visual comparison of our results with observed bedrock channels, and discuss our choice of parameterization for the lateral spreading of erosion in the long-term simulations.

C.1 Classification of subglacial water flow events

We define frequent, small magnitude events as those capable of producing enough meltwater to form R-channels in a temperate glacier. When surface melting occurs, the subglacial drainage system undergoes dramatic changes throughout a melt season, and the increase in water discharge between winter and summer can be up to a few orders of magnitude. Each day of surface melting will drive a pulse in discharge, which may happen a few tens of times or more each season. A rainfall event during the melt season could have a similar effect. We also treat the rapid drainage of small supraglacial lakes on an ice sheet (e.g. southwestern Greenland) as frequent events. Several lakes are likely to drain into the same outlet, and the resulting meltwater pulse is likely to remain relatively small (e.g. Bartholomew et al., 2012).

We define moderate magnitude, infrequent floods as those typically described as jökulhlaups (e.g. Bartholomaus and others, 2007; Björnsson, 2002; Clarke, 2003; Nye, 1976). Such floods require either a high geothermal flux at the base of the ice, or the presence of a relatively

Table C.1: Classification of subglacial water flow event frequency.

	Frequent events	Moderate frequency events	Rare events
Frequency of occurrence	≥ 10 times per year	Once a year to every 100 yrs	Once every 100 to 10000 yrs
Event examples	- Diurnal melt - Small surface lake drainage - Rainfall	- Large supraglacial lake drainage - Ice-dammed lake drainage - Melt-water from subglacial volcanism	- Mega-floods inferred from the geological record such as drainage of Lake Missoula or Agassiz

Table C.2: Classification of subglacial water flow event magnitude.

	Small magnitude	Moderate magnitude	Large magnitude
Event peak discharges	$\sim$ 10 to $\sim 5 \times 10^2\,\mathrm{m^3\,s^{-1}}$	$\sim 5 \times 10^2$ to $\sim 5 \times 10^4\,\mathrm{m^3\,s^{-1}}$	$> 5 \times 10^4\,\mathrm{m^3\,s^{-1}}$
Event examples	- Diurnal melt - Small surface lake drainage - Rainfall	- Large supraglacial lake drainage - Ice-dammed lake drainage - Subglacial volcanism	- Mega-floods inferred from the geological record such as drainage of Lake Missoula or Agassiz

large supraglacial or ice-dammed lake to act as a reservoir. In many cases, ice-dammed lakes tend to drain annually, however, conditions allowing for the formation of such lakes in a mountain glacier environment may not persist for more than a few decades.

Finally, we use the classification of large magnitude and rare events to represent paleo-mega-floods that have not been observed directly but are inferred from the geological record, thus making peak discharge determination very difficult (e.g. Baker, 1973; Bretz, 1969; Larsen and Lamb, 2016). The classification of event frequency and magnitude, along with some event examples, are summarized in Tables C.1 and C.2.

C.2 Modelling methodology

In order to standardize the flood simulations, we use the general shape of the hydrograph described in Nye (1976) and scale the duration and maximum volume of water released. The reference water volume ($\sim 1 \times 10^8\,\mathrm{m^3}$) is set equal to that of our reference synthetic melt season: a sinusoid with a 120-day period superimposed with daily sinusoidal fluctuations and a maximum discharge of ($\sim 20\,\mathrm{m^3\,s^{-1}}$) (see Beaud and others, 2016). The hydrograph is used as a flux boundary condition imposed at the upstream end of the model domain. For

the flood simulations, we use a subglacial hydraulic system comprising only an R-channel, and omit the distributed system (e.g. Clarke, 2003). According to Björnsson (2002, Table 2), a typical duration for a jökulhlaup travelling 50km from Grìmsvötn under Vatnajökull, Iceland, is 2–30 days with peak discharges ranging from $5 \times 10^3 - 1 \times 10^6\,\mathrm{m^3\,s^{-1}}$. The larger floods tend to have shorter durations than the smaller ones. We choose our reference flood (Fig. 4.1B) so that its duration is 20 days and the peak discharge is $4.5 \times 10^3\,\mathrm{m^3\,s^{-1}}$. Peak discharge during the simulated floods ranges from $20\,\mathrm{m^3\,s^{-1}}$ to $8.6 \times 10^3\,\mathrm{m^3\,s^{-1}}$. Note that we limit the range of floods tested, because larger floods would require a more sophisticated hydrology model that accounts for overpressure in the channel and the hydromechanical response of the glacier.

The parameters used for the erosion model are the same as those described in Beaud and others (2016), based originally on parameters used in Sklar and Dietrich (2004) and Lamb and others (2008a). The rock properties (Young's modulus and tensile strength) have been experimentally determined (Sklar and Dietrich, 2001, 2004) and correspond to those of unfractured limestone. Parameter choices were made to facilitate comparison between Beaud et al. (2016) and the original studies that developed the erosion models (Lamb and others, 2008a; Sklar and Dietrich, 2004); we have retained most of the same values for simplicity and comparability with previous work. Only the sediment size ($D = 60$ or $256\,\mathrm{mm}$) and sediment supply per unit width ($q_\mathrm{s} = 9.1 \times 10^{-3}\,\mathrm{m^3\,s^{-1}}$) have been modified.

In the present study we omit the role of plucking in SME, although plucking has been argued to be the dominant erosion mechanism in highly fractured bedrock (Whipple and others, 2000, 2013). We limit our model to abrasion for two reasons. First, when the quarried block is larger than a few decimetres in diameter, the assumption that changes in bed elevation are much slower than the evolution of the R- channel in the ice fails. Such a situation would require the development of new governing equations. Second, plucking is limited by weathering efficiency, which determines the thickness of the layer of loosened blocks (Chatanantavet and Parker, 2009; Lamb and others, 2015); this layer can limit the efficiency of quarrying unless blocks are particularly loose, for example in columnar basalt. We suggest that, with the exception of the latter condition, our findings related to the limits of erosion at very large shear stresses would hold.

C.3 Subglacial meltwater erosion on long timescales

We perform two long-term simulations: a tunnel valley and an inner gorge scenario. In both cases, we use the shallow-ice approximation (Hutter, 1983) in the ice-flow model and we impose a mass-balance profile as a function of ice-surface elevation.

C.3.1 Tunnel valley scenario

We model an ice sheet advancing across a gently sloping bed such that the length of the ice sheet is about 1200 km, mimicking the scale of a continental ice sheet (e.g. Laurentide ice sheet). We select the lowermost $\sim 250\,\mathrm{km}$ of the profile to apply the SME model. This model geometry permits us to avoid the impact of complex basal topography, and to focus on the margins of the ice sheet where the effect of the glacial advance–retreat cycle would

be largest. Throughout the simulated glacial cycle, thick ice inhibits the development of channelized subglacial drainage beyond ~ 300 km upstream of the maximum ice extent. Due to the relatively large time span between profiles for which SME is calculated (250 yrs), we interpolate the SME pattern between each time slice. Laterally, we distribute the erosion over 200 m to obtain a bedrock channel aspect ratio (width-to-depth) of ~ 10 (van der Vegt and others, 2012).

C.3.2 Inner gorge scenario

For the inner gorge simulation, we run the ice-flow model on a real longitudinal valley profile from the Swiss Alps. The profile starts near the summit of the Höch Gumme, Canton Bern, follows the valley downstream and passes through the Lammschlucht gorge (see Dürst-Stucki and others, 2012) to terminate in Willisau, canton Luzern. In this scenario, the glacier is only 35 km long and we omit the uppermost 5 km. The upper part of the profile is very steep and this causes the hydrology model not to converge. With this simulation we can test the effect of longitudinal variation in basal topography and the effect of glacier scale on the bedrock channel excavated. In this simulation we also assume that the topography of the valley will laterally constrain water flow more than in the TV scenario. We therefore distribute the erosion over only 50 m instead of 200 m.

C.4 Effect of lateral spreading on bedrock channel topography

Drainage pathways under glaciers and ice sheets are determined by hydraulic potential gradients (e.g. Shreve, 1972) and the locations of water injection points such as moulins (e.g. Gulley and others, 2012). These pathways are therefore subject to migration as glacier geometry evolves. In the case of IGs, they would be relatively constrained by steep walls in an alpine valley, and in the case of TVs, more mobile close to the terminus of a gently sloping ice sheet (e.g. Werder and others, 2013).

We impose the width over which we distribute erosion throughout a glacial cycle, assuming that it represents the lateral migration of R-channels. However, this width is poorly constrained and we show how different ways of distributing erosion change the resulting bedrock channel. A significant bedrock channel is obtained for all prescribed widths, with the maximum depth of the simulated channel ranging from several metres to several decametres (Fig. C.2).

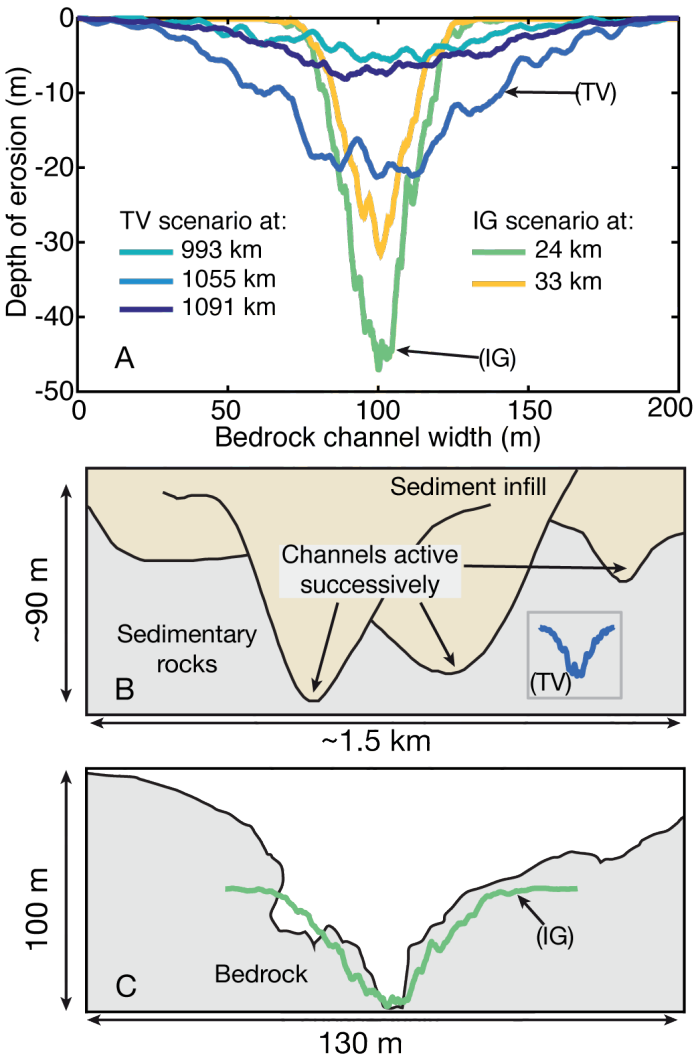

Figure C.1: Comparison of simulations (A) with observations (B, C) of bedrock channels. (A) Selected cross-sections from TV and IG simulations. (B) Cross-section of the Hornsyld Valley, Denmark, redrawn from Jørgensen and Sandersen (2006). (C) Cross-section of a gorge in Péribonka, Québec, Canada, redrawn from Lajeunesse (2014). The insets (TV) and (IG) in (B) and (C) represent selected profiles from (A) plotted at the scale of the corresponding observations.

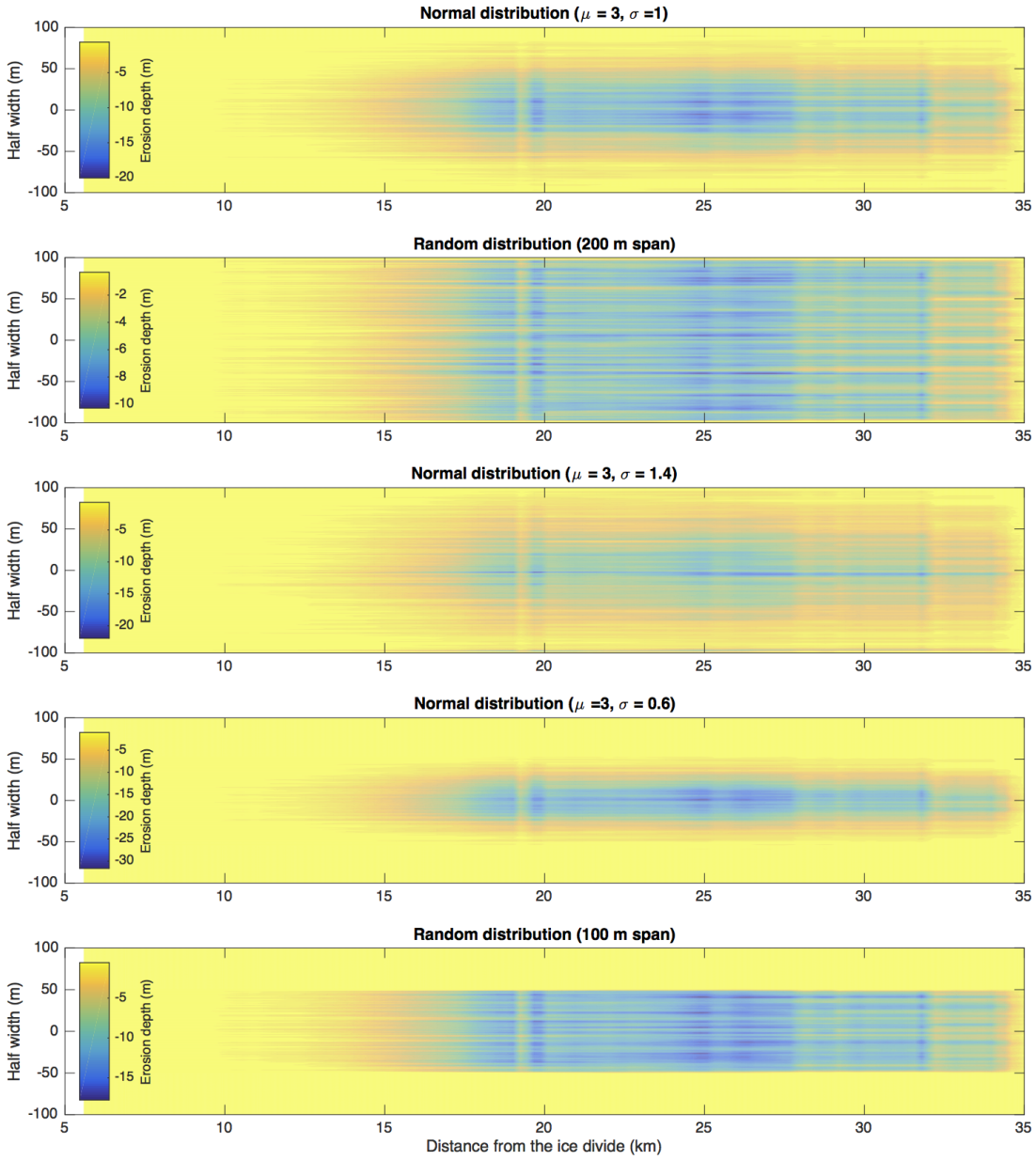

Figure C.2: Effect of prescribed lateral variation in channel position on the resulting bedrock channel. The random distribution means that all lateral positions are uniformly distributed and a specific random location is selected in that distribution for each simulated year. The simulation used is the inner gorge scenario with D = 256 mm.

Appendix D

Appendix to Chapter 5

D.1 Notation

$\tilde{A}$ Flow-law coefficient for channels ($5 \times 10^{-25}\,\mathrm{Pa^{-n}\,s^{-1}}$)

$\dot{b}_{\mathrm{ch}}$ Local water input to the channel ($\mathrm{m^2\,s^{-1}}$)

c_{t} Pressure melting coefficient ($\mathrm{K\,Pa^{-1}}$)

c_{w} Heat capacity of water ($\mathrm{J\,kg^{-1}\,K^{-1}}$)

D Particle diameter (m)

$\mathrm{d}t$ Time step (s)

$\mathrm{d}x$ Grid cell size (m)

f_{b} Darcy-Weisbach roughness of the bed

f_{i} Darcy-Weisbach roughness of the ice

f_{R} Channel-averaged Darcy-Weisbach roughness

F_{c} Fraction of covered bedrock

g Gravitational acceleration ($9.8\,\mathrm{m\,s^{-2}}$)

h_{i} Ice thickness (m)

M Number of grid cells

$[m_{\mathrm{s}}]$ Sediment mass concentration ($\mathrm{kg\,m^{-3}}$)

L Latent heat of fusion ($\mathrm{J\,kg^{-1}}$)

n Exponent of Glen's flow law

n'_{i} Manning roughness of ice

n'_{b} Manning roughness of the bed

$\langle n' \rangle$ Channel-avereaged Manning roughness

N_{ch} Effective pressure in the channel (Pa)

p_{ch} Water pressure in the channel (Pa)

p_{i} Ice overburden pressure (Pa)

P_{b} Bed perimeter of channel (m)

P_{i} Ice perimeter of channel (m)

P_{W} Wetted perimeter of channel (m)

q_{ls} Local source of volumetric sediment flux per unit width ($\mathrm{m^3\,s^{-1}}$)

q_{t} Volumetric rate of sediment transport per unit width ($\mathrm{m^2\,s^{-1}}$)

q_{tt} Volumetric rate of sediment transport ($\mathrm{m^3\,s^{-1}}$)

q_{tc} Volumetric transport capacity per unit width ($\mathrm{m^2\,s^{-1}}$)

q_{ttc} Volumetric transport capacity ($\mathrm{m^3\,s^{-1}}$)

Q_{ch} Water discharge ($\mathrm{m^3\,s^{-1}}$)

r Buoyant density of submerged particle

R_{H} Hydraulic radius of channel (m)

R_{i} Radius of ice-walled channel (m)

r_{V} Ratio between available sediment volume and volume at transport capacity

S_{ch} Channel cross-sectional area ($\mathrm{m^2}$)

v Water velocity in channel ($\mathrm{m\,s^{-1}}$)

u_{s} Depth-averaged streamwise bed load velocity ($\mathrm{m\,s^{-1}}$)

v_{oc} Channel opening rate by viscous heat dissipation ($\mathrm{m^2\,s^{-1}}$)

v_{cc} Channel creep closure rate ($\mathrm{m^2\,s^{-1}}$)

v_{s} Channel closure rate by sediment deposition ($\mathrm{m^2\,s^{-1}}$)

V_{s} Volume of sediment per unit length ($\mathrm{m^2}$)

V_{b} Volume of transient sediment per unit width and length (m)

V_{bal} Balance between sediment input and output fluxes per time step ($\mathrm{m^3}$)

V_{tc} Volume of sediment per unit width and length at saturation for transport ($\mathrm{m^2}$)

W_{ch} Channel width (m)

X_{L} Glacier length (m)

z_{b} Elevation of bed surface (alluvium and bedrock) (m)

z_i	Elevation of glacier surface (m)
λ	Porosity of bed sediment
γ	Fluid compressibility factor
η_a	Thickness of sediment above bedrock (m)
η_br	Elevation of bedrock surface (m)
ρ_i	Ice density ($\mathrm{kg\,m^{-3}}$)
ρ_s	Particle density ($\mathrm{kg\,m^{-3}}$)
ρ_w	Water density ($\mathrm{kg\,m^{-3}}$)
Π	Sensible heat change of water ($\mathrm{W\,m^{-1}}$)
τ_b	Basal shear stress (Pa)
τ_tot	Total shear stress at the flow boundary (Pa)
τ^*	Non-dimensional boundary shear stress
τ_c^*	Threshold non-dimensional boundary shear stress for particle motion
ϕ_ch	Hydraulic potential in the channel (Pa)
Ξ	Dissipation of potential energy ($\mathrm{W\,m^{-1}}$)

D.2 Supplementary equations

The hydraulic radius of the channel is

$$R_{\mathrm{H}} = \frac{S_{\mathrm{ch}}}{P_{\mathrm{W}}} = \frac{S_{\mathrm{ch}}}{P_{\mathrm{i}} + P_{\mathrm{b}}}, \tag{D.1}$$

where P_{W}, P_{i} and P_{b} are, respectively, the wetted perimeters of the whole channel, the ice walls and the bed. The second equality is only valid under the assumption of water filled conduits. The wetted ice perimeter for a semi-circular channel is given by

$$P_{\mathrm{i}} = \pi R_{\mathrm{i}} = \pi \sqrt{\frac{2S_{\mathrm{ch}}}{\pi}} \tag{D.2}$$

and the wetted perimeter of the bed is

$$P_{\mathrm{b}} = 2R_{\mathrm{i}}. \tag{D.3}$$

The effective pressure in the channel is

$$N_{\mathrm{ch}} = p_{\mathrm{i}} - p_{\mathrm{ch}} = \rho_{\mathrm{i}} g(z_{\mathrm{i}} - z_{\mathrm{b}}) - p_{\mathrm{ch}}. \tag{D.4}$$

The elevation of the channel bed is

$$z_{\mathrm{b}} = \eta_{\mathrm{br}} + \eta_{\mathrm{a}}. \tag{D.5}$$

The shear stress produced by water flow on the channel walls is

$$\tau_{\mathrm{tot}} = \frac{1}{8} \langle f_{\mathrm{R}} \rangle \, \rho_{\mathrm{w}} v|v|, \tag{D.6}$$

where $v = Q_{\mathrm{ch}}/S_{\mathrm{ch}}$ is the water velocity and the friction coefficient averaged over the channel walls is

$$\langle f_{\mathrm{R}} \rangle = \frac{f_{\mathrm{i}} P_{\mathrm{i}} + f_{\mathrm{b}} P_{\mathrm{b}}}{P_{\mathrm{i}} + P_{\mathrm{b}}} = \frac{f_{\mathrm{i}} P_{\mathrm{i}} + f_{\mathrm{b}} P_{\mathrm{b}}}{P_{\mathrm{W}}}. \tag{D.7}$$

The second equality is only valid for saturated channels. The friction coefficient for the ice wall and bed, respectively, is

$$f_{\mathrm{i}} = \frac{8g{n_{\mathrm{i}}}'^2}{R_{\mathrm{H}}^{1/3}} \text{ and } f_{\mathrm{b}} = \frac{8g{n_{\mathrm{b}}}'^2}{R_{\mathrm{H}}^{1/3}} \tag{D.8}$$

and the shear stress exerted on the bed is

$$\tau_{\mathrm{b}} = \frac{1}{8} f_{\mathrm{b}} \rho_{\mathrm{w}} v|v|. \tag{D.9}$$

D.3 Model testing and sediment conservation

We perform a number of uncoupled tests with different sediment configurations and a steady-state hydrology to examine the model sensitivity to the time step and grid size, and to asses the ability of the model to capture both alluvial and mixed alluvial / bedrock conditions at the channel bed.

D.3.1 Sediment conservation and time stepping

To test whether the model conserves sediment volume, we plot the volume change per time step in the whole system (Fig. D.1) for the simulation shown in Fig. 5.2 (see Section 5.3.2) for two different time steps. The comparison of the volume change computed as ΔV_{s} and as the balance between

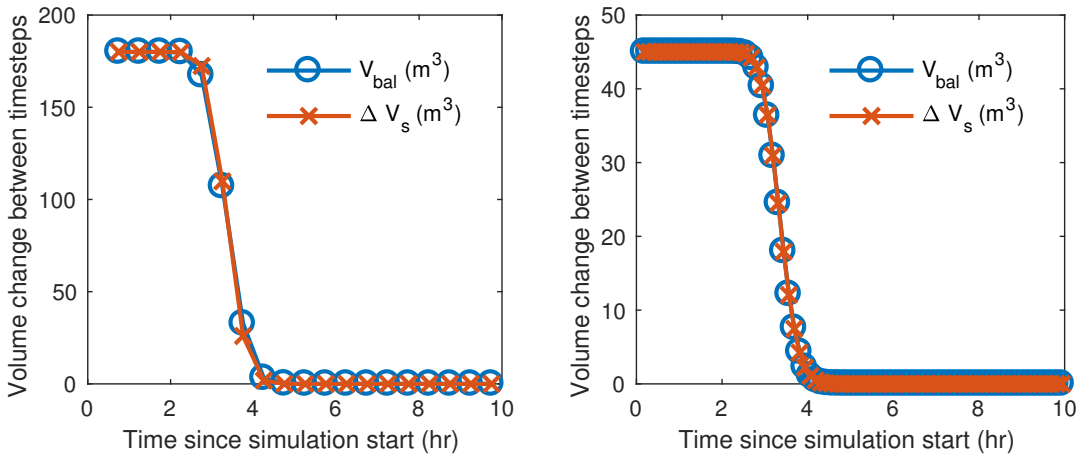

Figure D.1: Comparison between sediment flux budgets per time step ($V_{\mathrm{bal}} = (q_{\mathrm{ls}}(x = 0) - q_{\mathrm{tt}}(x = X_{\mathrm{L}})) \times \mathrm{d}t$) and the change in sediment volume per time step (ΔV_{s}), for the simulation shown in Fig. 5.2 with solver outputs requested at intervals of 1800 s (a) and 450 s (b).

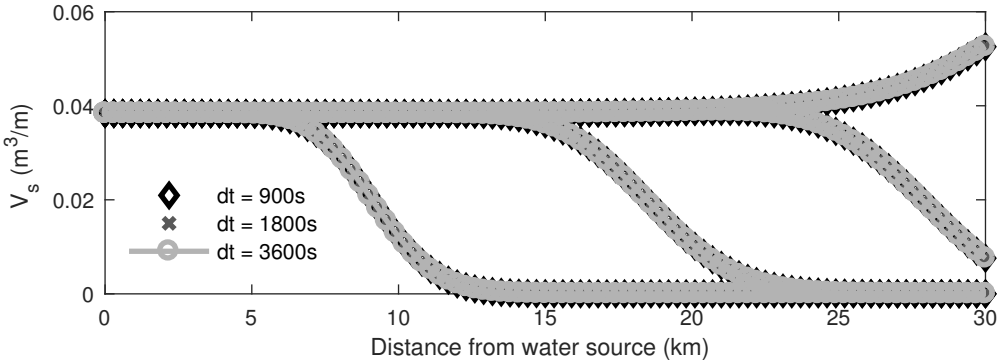

Figure D.2: Comparison of the solution for V_{s} computed for the simulation set-up shown in Fig. 5.2 for three different time steps: $\mathrm{d}t = 900$, 1800 and 3600 s. The simulations are uncoupled and the solutions are shown for $t = 1$, 2, 3 and 4 hours.

sediment input and output fluxes per time step ($V_{\mathrm{bal}} = (q_{\mathrm{ls}}(x = 0) - q_{\mathrm{tt}}(x = X_{\mathrm{L}})) \times \mathrm{d}t$) shows a good visual match for either time step, but the match is better for the smaller time step. The Matlab `ode15s` solver uses an adaptive time step; the solution is thus the same regardless of the time interval at which the solver output is requested (Fig. D.2). We argue that the poorer match in volume change results from the loss of accuracy in the calculated flux due to the coarser temporal resolution.

D.3.2 Grid size

We perform a grid refinement test with three different grid sizes ($\mathrm{d}x = 600$, 300 and 150 m) with the same model set-up as in the previous section (see Section 5.3.2 and Fig. 5.2; $Q_{\mathrm{ch}}(x = 0) = 50\,\mathrm{m}^3\,\mathrm{s}^{-1}$ and $q_{\mathrm{ls}}(x = 0) = 0.1\,\mathrm{m}^3\,\mathrm{s}^{-1}$). The grid size has a visible effect on V_{s} (Fig. D.3A) patterns, although this effect is small when looking at S_{ch} or p_{ch} (Fig. D.3B and C). We suggest that the role played by the grid size is the result of the resolution in sediment flux gradients. The finer the grid the better these changes are resolved. With a coarser grid the longitudinal distribution of V_{s} is smoothed, in particular when a wave of sediment is travelling through the system. The grid size also influences the hydraulic potential gradients near the terminus, where surface slopes and ice thickness changes are larger. The finer the grid, the larger the channel at the terminus and the smaller the transport capacity (q_{tc}; Fig. D.3B and C). These conditions enhance the bottleneck effect and leads to larger sediment volumes (V_{s}) near the terminus.

D.3.3 Initial sediment layer

Once the R-channel reaches a steady-state with an upstream water discharge of $Q_{\mathrm{ch}}(x = 0) = 50\,\mathrm{m}^3\,\mathrm{s}^{-1}$, we introduce a sediment layer of 0.5 m along the channel ($V_{\mathrm{s}} = 0.5(1 - \lambda)W_{\mathrm{ch}}$). Sediment removal occurs as a wave travelling down-glacier (Fig. D.4A), as no additional sediment is introduced during the simulation and the transport capacity per unit width (q_{tc}) decreases monotonically along the profile (Fig. D.4B). This test highlights in particular the sediment bottleneck at the terminus as it takes $\sim$ 100 hours to remove sediment from the whole profile but the last kilometre (Fig. D.4A), and another $\sim$ 100 hours to completely rid the system of sediment.

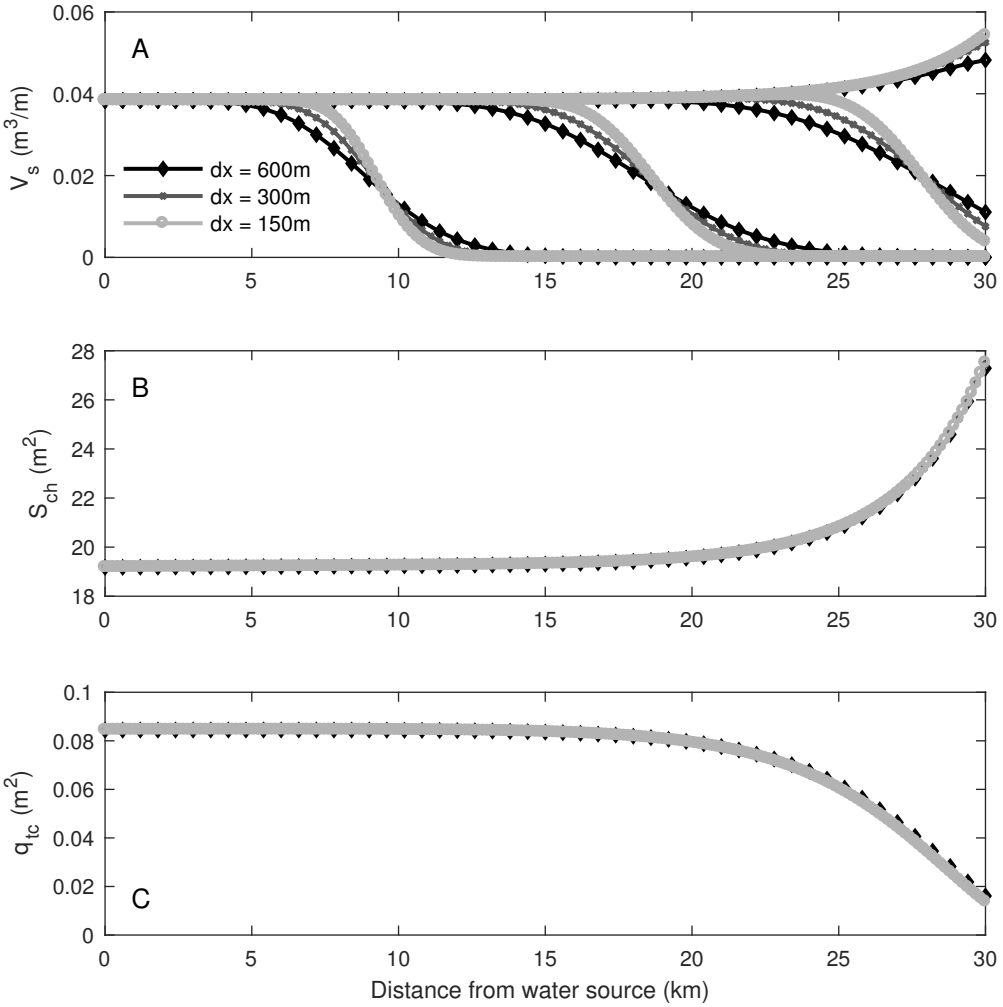

Figure D.3: Comparison of the solution for three different grid sizes: $\mathrm{d}x$ = 600, 300 and 150 m and computed for the simulation set-up shown in Fig. 5.2. (A) Sediment volume per unit length, V_s; (B) Channel cross-sectional area, S_ch; (C) Transport capacity per unit width, q_tc. The solutions are shown for t = 1, 2, 3 and 4 hours, and $\mathrm{d}t = 900$s.

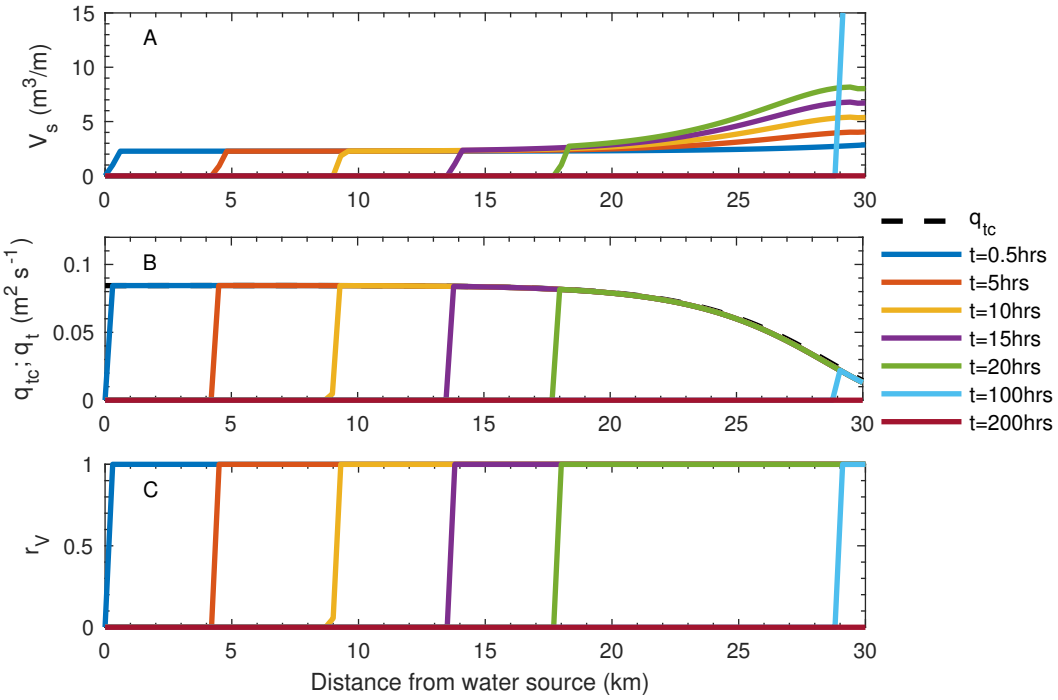

Figure D.4: Evolution of sediment transport in an uncoupled simulation with steady-state hydrology (Fig. 5.1) and an initial layer of sediment. (A) Volume of sediment per unit length V_s; (B) Volumetric transport capacity q_{tc} (dashed) and sediment flux q_t (solid lines) per unit width; (C) Ratio between volume of sediment in a reach and volume transported at capacity r_V.